Impacts of cosmic inhomogeneities on the CMB : primordial perturbations in two-field bouncing cosmologies and cosmic magnetism in late-time structures

Nadège Lemarchand

université PARIS-SACLAY

UNIVERSITÉ PARIS SUD
Comprendre le monde, construire l'avenir

NNT : 2019SACLS510

Thèse de doctorat

Impacts of cosmic inhomogeneities on the CMB: primordial perturbations in two-field bouncing cosmologies and cosmic magnetism in late-time structures

Thèse de doctorat de l'Université Paris-Saclay
préparée à l'Université Paris-Sud

École doctorale n°127 Astronomie et astrophysique d'Ile-de-France (AAIF)
Spécialité de doctorat : astronomie et astrophysique

Thèse présentée et soutenue à Orsay, le 12 décembre 2019, par

NADÈGE LEMARCHAND

Composition du Jury :

Nabila Aghanim Directrice de recherche, CNRS (Institut d'Astrophysique Spatiale)	Présidente
Carlos Hernández-Monteagudo Tenure scientist, Centro de Estudios de Física del Cosmos de Aragón	Rapporteur
Hiroyuki Tashiro Associate Professor, Nagoya University (Cosmology Group)	Rapporteur
Aurélien Barrau Professeur des Universités, Université Grenoble Alpes (Laboratoire de Physique Subatomique et de Cosmologie)	Examinateur
Giulio Fabbian Research fellow, University of Sussex (Physics and Astronomy, Astronomy Centre)	Examinateur
Julien Grain Chargé de recherche, CNRS (Institut d'Astrophysique Spatiale)	Directeur de thèse

Contents

Synthèse

Le Fond Diffus Cosmologique (FDC) est une sonde cosmologique clé mettant des contraintes étroites sur le modèle ΛCDM de l'Univers. Emis 380000 ans après le big bang, il montre de petites anisotropies en température et en polarisation qui tracent les inhomogénéités cosmiques à différentes époques de l'Univers. En effet, d'une part les anisotropies primaires, imprimées au moment de son émission, donnent accès à la phase d'inflation ayant lieu au tout début de l'Univers et durant laquelle les perturbations primordiales sont générées. D'autre part, les anisotropies secondaires, imprimées depuis lors, tracent les inhomogénéités dans l'Univers récent, qui ont évolué en grandes structures sous l'action de la gravité à partir des inhomogénéités primordiales, et interagissant alors avec le FDC. Ainsi les anisotropies du FDC sont une sonde puissante à la fois de l'origine des inhomogénéités dans l'Univers très jeune, et de leur état évolué dans l'Univers récent. Cette thèse porte sur deux aspects des inhomogénéités: d'abord leur production dans une extension du scénario inflationnaire, puis la prédiction de l'impact des champs magnétiques des grandes structures sur les anisotropies secondaires polarisées du FDC.

Malgré ses succès, l'inflation ne résout pas le problème de la singularité initiale du big bang, où l'interaction gravitationnelle pourrait être quantifiée. En Cosmologie Quantique à Boucles (CQB), cette singularité est remplacée par un rebond quantique. La CQB à un champ avec potentiel quadratique a déjà été étudiée et prédit une phase d'inflation suivant le rebond avec une probabilité proche de un. Dans ce cadre, les perturbations primordiales ne sont plus seulement produites pendant l'inflation, mais aussi pendant le rebond et la contraction le précédant. Dans ma thèse, j'ai considéré une extension à deux champs de la CQB avec un champ massif comme inflaton, et un champ sans masse servant d'horloge interne. J'ai d'abord étudié l'évolution globale de l'Univers de manière analytique et numérique, montrant que loin dans la contraction, le champ massif domine le contenu énergétique. J'ai aussi vérifié que l'inflation reste probable, malgré la présence du champ sans masse. Puis, j'ai examiné la production de perturbations: contrairement au cas à un champ, en plus de la composante adiabatique standard, elles sont ici décrites par une composante isocourbe, caractéristique des modèles multi-champs et pour laquelle Planck a mis des limites supérieures. Loin dans la contraction, ces deux composantes sont hautement couplées. J'ai montré comment fixer leurs conditions initiales en utilisant des variables combinant les deux types de perturbations, rendant le couplage sous-dominant. Il reste maintenant à les propager à travers le rebond jusqu'à la fin de l'inflation pour obtenir leurs spectres de puissance respectifs ainsi que leur spectre de puissance croisé, à comparer ensuite aux contraintes observationnelles.

Depuis son émission, le FDC a voyagé à travers les grandes structures avant de nous atteindre. Son interaction avec les structures engendre des anisotropies secondaires, comme celles dues à l'effet Sunyaev-Zel'dovich dans les amas. Or, des plasmas magnétisés ont été observés dans les galaxies et les grandes structures. Cela devrait engendrer de la rotation Faraday de la polarisation linéaire primordiale, transformant des modes E en B, et de la conversion Faraday de la polarisation linéaire en circulaire. J'ai revisité ces sources d'anisotropies en calculant les spectres de puissance angulaires de l'angle de rotation Faraday et du taux de conversion Faraday par les

grandes structures. Pour cela, j'ai utilisé le modèle de halo en prêtant une attention particulière à l'impact des projections des champs magnétiques. Les spectres piquent à des multipoles $\ell \sim 10^4$ et sont proportionnels à σ_8^3, en supposant un champ magnétique indépendant de la masse du halo. Cette dépendance est cependant dégénérée avec celle qui existe entre les champs magnétiques et la masse des halos. Ensuite, je détaille le calcul des spectres de puissance angulaires totaux des anisotropies polarisées, à partir de ceux de la rotation Faraday et de la conversion Faraday. Enfin, je montre comment reconstruire les champs de rotation Faraday et de conversion Faraday à partir du FDC en adaptant les estimateurs développés pour la reconstruction du lentillage gravitationnel.

Introduction

Modern cosmology is born in the XX$^{\text{th}}$ century, soon after the formulation of the theory of General Relativity (GR) in 1915 by Albert Einstein to describe the gravitational interaction. The general cosmological solutions to the Einstein equations were introduced by Alexander Friedmann and Georges Lemaître independently in 1922 and 1927 respectively. These solutions allow the Universe to be expanding and indeed, Hubble in 1929 observed that galaxies were receding from us all the more fast that they were far. It has been interpreted as the expansion of the Universe. This observation involves that the Universe has a thermal history: its temperature has decreased during its expansion. This led Gamow in 1948 to draw the conclusion that there must be a relic radiation from the early Universe, which is the first light it has released. Its temperature was computed shortly afterwards, the very same year, by Alpher and Herman to be around 5 K. Its first detection by chance in 1964 by Penzias and Wilson confirmed the theoretical prediction and was another evidence for the expansion of the Universe. Since then, there have been three satellite missions to observe the CMB in details and many other ground based or balloon born observations. For the past 30 years, the CMB has become an important probe to test our modern understanding of cosmology built upon the Friedmann-Lemaître solutions: indeed, it contains information not only on the origin of the Universe and therefore about its initial conditions, but also on its history from the release of the CMB 380 000 years after the big bang up to now, since it took this long for the light to reach us. This information is actually contained in the temperature and polarisation anisotropies of the CMB: the primary anisotropies, imprinted at the CMB release, trace the production of the primordial inhomogeneities in the very early Universe while the secondary anisotropies result of the interaction of the primary anisotropies with the large-scale structures, which are nothing more than the evolved state of the primordial perturbations which have collapsed under gravity, so that secondary anisotropies probe the recent structuration of the Universe. The observation of the CMB anisotropies allows a better understanding of the production and evolution of the cosmic inhomogeneities but also to set tight constraints on the parameters of the standard model of cosmology ΛCDM (Planck Collaboration et al., 2018b). It turns out that the hot big bang model, in reference to the thermal history of the Universe, is in remarkable agreement with the observations and in particular the one of the CMB anisotropies.

No matter how well-fitted it is to observations, the model raises questions about its formulation. The first satellite mission dedicated to the CMB, COBE launched in 1989, already observed the incredible uniformity of the CMB over the whole sky by detecting only very small temperature anisotropies. It has been further confirmed until Planck in 2013 which observed them to be of the order of $\Delta T/T_0 \sim 10^{-5}$, with ultimate precision. The observation of the CMB thus supports the cosmological principle, that is the homogeneity and isotropy hypotheses underpinning the model. Nonetheless, the hot big bang scenario is incomplete as it does not explain the origin of the homogeneity and isotropy of the model, nor the origin of the tiny fluctuations observed in the CMB. It is therefore completed with the inflationary paradigm, a phase of accelerated expansion in the very early Universe that answers the initial condition 'problems' of the

Universe. Indeed, the gaussian statistics of the CMB anisotropies suggest that they must have quantum origin. Thus, the vacuum quantum fluctuations in the very early Universe are expected to be amplified during inflation, giving rise to the primordial scalar and tensor inhomogeneities which later leave their imprints on the temperature and polarisation anisotropies, explaining the origin of the fluctuations. For now, this paradigm remains to be definitely confirmed, as only an upper bound has been set on the energy scale of inflation, mostly through the observation of the temperature anisotropies by Planck (see Planck Collaboration et al., 2018d). Nonetheless, the tensorial quantum perturbations of the metric, or gravitational waves, are expected to be amplified during this phase but have never been detected so far. Thus, the detection of a gravitational wave background originating from the primordial Universe would back up this paradigm. At the level of CMB anisotropies, this translates into polarisation anisotropies. The linear polarisation anisotropies of the CMB draw two kinds of polarisation patterns on the sky: the E modes which are parity invariant corresponding to the curl-free component of the vector field, and the B modes which are not and correspond to the divergence-free component of the vector field. It is useful to introduce these two modes to describe linear polarisation because they are basis invariant unlike the polarisation vector field. As the B modes are parity variant, scalar perturbations cannot produce them and they are the unique signature of the tensor perturbations, contrary to the E modes which can be produced by both scalar and tensor perturbations.

Inflation is expected to occur at very high energies very close to the Planck energy scale, when the Universe was still very hot, shortly after the initial unphysical singularity predicted by GR. However, the inflationary paradigm does not solve the initial big bang singularity issue: it is believed that a quantum theory of gravitation might do so, like the Loop Quantum Gravity (LQG) theory (see Gambini & Pullin, 2011, for an introduction). The application of its techniques to the system Universe led to the field of Loop Quantum Cosmology (LQC) and replaces the big bang singularity by a quantum bounce. Linking the inflationary paradigm to a quantum model of the very early Universe that solves the initial singularity might answer some of the questions raised by the hot big bang model. Such a model of the very early Universe may change the production of the primordial inhomogeneities: in particular, they are now not only produced during inflation, but also during the bounce and the contraction previous to it. This change may leave its footprints on the CMB anisotropies, allowing further tests of these high energy physics models. A simple model of LQC with a single massive scalar field with a quadratic potential has already been studied and is compatible with an inflation phase following the bounce. Furthermore, the primordial power spectra of its scalar and tensor perturbations show distinguishing features as compared to a standard inflation phase, see Barrau et al. (2014a). Now, this model of the very early Universe can be enriched by adding more fields, as suggested by the use of scalar fields as reference fields Gielen & Oriti (2018). Indeed, even though the most favoured models of inflation involve a single scalar field, we have reasons to consider more fields. In my thesis, I have been interested in a two-field extension of LQC with a massive scalar field with quadratic potential as being the inflaton and a massless scalar field parameterising time. Two kinds of motivations lie behind this model: first, fundamental physics considerations coming from LQG, since in this theory, time is not defined at the quantum level, but at the classical level a scalar field without potential is a monotonic function of time and so can be used as a relational emergent time to parameterize our equations. However, a field without potential cannot give rise to inflation. Thus, we also need a scalar field with potential in order to have an inflation phase. Moreover, all the fields of the Standard Model of particle physics make up the Universe. Thus, there is no reason that there should be only one field during the contraction either. These reasons therefore suggest to investigate bouncing cosmologies with at least two fields. My approach has been to study the scalar perturbations produced in such a model, where an isocurvature component is expected in addition to the standard adiabatic one, to be later propagated into primary induced anisotropies.

Finally, the CMB is the superposition of the first light released by the Universe and of its interaction with the large-scale structures on its way to our detectors. Thus, both primordial and late-time effects leave their imprint on this relic radiation one receives today. This can be good or bad news: either it can be used to extract information on the structures of the Universe or it can be seen as polluting the primordial signal which is one of the only windows we have on the primordial physics. It is thus relevant to characterise precisely the secondary effects impacting the CMB, either to extract cosmological and astrophysical information on its own, or to remove a foreground contamination. An example of secondary anisotropies are those due to the lensing of the CMB by the gravitational potentials of large-scale structures, which deforms the primordial image of the Universe. Both temperature and polarisation anisotropies are impacted by this effect but in particular, it turns some E modes into B modes. While the primordial B modes, signature of the primordial gravitational waves produced during inflation, have not been observed yet and are actually expected to be very low, their secondary component, the lensed B modes, have. Thus, a precise modeling of all the possible secondary B modes is needed to subtract it to the observed CMB in order to recover the primordial signal and to extract information about the early phases of the Universe. Conversely, these secondary anisotropies could also be used to probe the standard model of cosmology or the structure formation of the Universe, as shown for example with the reconstruction of the lensing potential map Planck Collaboration et al. (2018c). Now, observations show that large-scale structures contain magnetic fields of the order of the microGauss, as well as free electrons. These magnetised plasmas should lead to magneto-optic effects like Faraday Rotation (FR) and Faraday Conversion (FC) of the CMB. FR rotates the primordial linear polarisation of the CMB, and turns some E modes into B modes, in a similar way to the gravitational lensing, while FC converts the primordial linear polarisation into circular polarisation, which has no primordial component in the standard model of cosmology. The second part of my thesis has consisted in making a full sky modelisation of these two effects, in a way similar to what has already been done for the angular power spectra of the thermal Sunyaev-Zel'dovich (tSZ) effect or lensing, as a first step to predict the induced secondary polarised anisotropies of the CMB.

The PhD manuscript is organised as follows: I first introduce the context and background needed to this thesis in Part I, starting from the background standard model of cosmology to the production of anisotropies in the CMB, going through early Universe physics and the treatment of perturbations within it. The Part II is then dedicated to predicting primordial power spectra in an early Universe model within the LQC framework. For this purpose, I first present the mother LQG theory and then its LQC application and a review of previous results useful for the model of the early Universe I considered. I will solve both analytically and numerically its dynamics and explore the consequences for an inflationary phase. I will also tackle the dynamics for its coupled adiabatic and isocurvature perturbations by first solving it in the uncoupled case. Finally, Part III is devoted to the prediction of secondary polarised anisotropies that could spoil the detection of the primordial ones. I will focus on two effects impacting primary polarisation anisotropies: the FR and FC effects. As a first step, I compute the angular power spectra of these effects occurring in galaxy clusters and study their cosmological and astrophysical dependencies. The angular power spectra of CMB secondary polarised anisotropies are also given as well as quadratic estimators to reconstruct the FR and FC fields thanks to CMB secondary polarised anisotropies, which could be used to probe both cosmology and the astrophysics of clusters.

Part I

Cosmology: some basics

Chapter 1

The standard model of cosmology: ΛCDM

This chapter presents the standard model of cosmology and its theoretical foundation, namely the theory of General Relativity. Indeed, the modern theory of gravitation developed by Albert Einstein in 1915 was used no later than in 1917 to build the first (static) model of the Universe by Einstein himself. Contrary to original Einstein's idea, the Universe is observed as expanding. Today, observations enable us to measure the parameters of the current model of our Universe with unprecedented precision. This gives a particular model of our Universe named ΛCDM, after its two main constituents. However minimalistic and well-fitted this model can be to observations, it also raises open questions on its theoretical framework, that is about General Relativity but maybe also about particle physics.

1.1 From General Relativity to cosmology

1.1.1 From the principle of stationary action to Einstein's equations

Modern formulations of physics are based on analytical mechanics and in particular the Hamiltonian formalism for its quantum part, or the Lagrangian formalism for General Relativity (abbreviated GR hereafter). Classical GR is formulated with a Lagrangian L and an action S that is required to be stationary to get the equations of motion of space-time itself that depends on its energy density content. The action is related to the Lagrangian by an integration

$$S = \int L \, \mathrm{d}t. \tag{1.1}$$

The absolute space and time of Newtonian mechanics are no longer independent in GR: it forms one single entity called space-time. Actually, it is even more than that: it is coupled to its energy density content. In GR, the Euclidean 3-space of Newtonian mechanics is replaced by a pseudo-Riemannian manifold of dimension 4 that locally looks like $\mathbb{R}^4$ but that is globally curved by the presence of energy densities. To give coordinates to events in such space-times and measure lengths or durations, one needs what is called a metric. Metrics are not unique to pseudo-Riemannian manifolds, it is just a formal way to write lengths or durations within a coordinate system: for example, there is a metric for cartesian coordinates and another one for spherical coordinates. Formally, a metric is a rank-2 tensor written $g_{\mu\nu}$. This metric allows to define

a particular derivative on a manifold called covariant derivative: as the manifold representing space-time is globally curved, one cannot easily compare objects such as tensors in two different space-time points labelled by coordinates x^μ. Therefore, one needs to parallel transport objects between points, however close they are, in order to compare them, and all the more so to compute derivatives. The covariant derivative, indicated by ∇_μ, differentiates objects that are parallel transported between infinitesimally closed points

$$\nabla_\mu V^\nu = \partial_\mu V^\nu + \Gamma^\nu_{\mu\alpha} V^\alpha, \tag{1.2}$$

where V^μ is a vector, ∂_μ is the usual partial derivative with respect to the space-time coordinate x^μ and $\Gamma^\nu_{\mu\alpha}$ is the connection (also known as Christoffel symbol) because it 'connects' two neighbour points: this connection is said to be metric compatible, meaning that it can be univocally computed given the metric. As the covariant derivative is precisely needed to differentiate objects on curved geometries, one can understand that it can be used to define a curvature tensor $R^\mu_{\nu\alpha\beta}$ of rank 4, also called Riemann tensor, following

$$(\nabla_\alpha \nabla_\beta - \nabla_\beta \nabla_\alpha) V^\mu = R^\mu_{\nu\alpha\beta} V^\nu, \tag{1.3}$$

where V^μ is any vector. Using Einstein's summation convention one can define a rank-2 tensor called the Ricci tensor as: $R_{\mu\nu} = R^\alpha_{\mu\alpha\nu}$ and the Ricci scalar $R = R_{\mu\nu} g^{\mu\nu}$ or the curvature scalar. As metric describes the geometry of a space-time, the action of GR depends in particular on the metric and its derivatives

$$S = \frac{1}{2\kappa} \int (R - 2\Lambda) \sqrt{-g}\, \mathrm{d}^4 x + \int \mathcal{L}_\mathrm{m} \sqrt{-g}\, \mathrm{d}^4 x, \tag{1.4}$$

where $\mathcal{L}_\mathrm{m}$ is the Lagrangian density of matter fields related to the Lagrangian of matter by an integration over space: $L = \int \mathrm{d}^3 x\, \mathcal{L}$, Λ is the so called cosmological constant, g is the determinant of the metric and $\kappa = 8\pi \mathrm{G}/c^4$. The first term is named the Einstein-Hilbert action, after the two physicists. The equations of motion for this space-time -the equations of motion of the theory of GR- are then given by extremising the action following the least action principle, which is central in modern formulations of physics. It leads to the Euler-Lagrange equations which are in this context called the Einstein's equations

$$G_{\mu\nu} + \Lambda g_{\mu\nu} = \kappa T_{\mu\nu}, \tag{1.5}$$

where $G_{\mu\nu} = R_{\mu\nu} - R g_{\mu\nu}/2$ is the Einstein tensor and $T_{\mu\nu}$ is the energy-momentum tensor obtained by varying the matter action with respect to the metric, or equivalently by differentiating the Lagrangian of matter with respect to the metric. The energy momentum tensor is symmetric and such a rank-2 tensor can be decomposed uniquely as follows

$$T_{\mu\nu} = \rho u_\mu u_\nu + P \gamma_{\mu\nu} + 2 q_{(\mu} u_{\nu)} + \pi_{\mu\nu}, \tag{1.6}$$

where u^μ is the velocity of an observer belonging to the fluid, $\rho = T_{\mu\nu} u^\mu u^\nu$ is the energy density measured by a comoving observer with the fluid, $\gamma_{\mu\nu}$ is the spatial metric of surfaces perpendicular to the flow i.e. $\gamma_{\mu\nu} = g_{\mu\nu} + u_\mu u_\nu$, $P = T_{\mu\nu}\gamma^{\mu\nu}/3$ is the pressure, $q^\mu = -T_{\alpha\beta} u^\alpha \gamma^{\beta\mu}$ is the energy flow with respect to u^μ and $\pi_{\mu\nu}$ is the anisotropic pressure tensor which is symmetric. These quantities satisfy the following properties

$$q_\mu u^\mu = 0,\ \pi_{\mu\nu} u^\mu = 0,\ \pi_{\mu\nu} u^\mu = \pi_{\mu\nu} \gamma^{\mu\nu} = 0.$$

This is the most general form the energy-momentum tensor can have, but in cosmology one only needs a reduced version of it, that of a perfect fluid where we do not use the anisotropic pressure

tensor. In the following, we explain how a model of the Universe has been built in the years following the construction of GR in 1915, under this theoretical framework, among other things. It led to a domain of physics called (modern) Cosmology so that our current understanding of the Universe is rather recent.

1.1.2 Application to the whole Universe: cosmology

1.1.2.1 The symmetries behind the model

The gravitational interaction is well described by the theory of GR on solar system scales (e.g. Hoyle et al., 2004; Will, 2014). We have seen it is a manifestation of the geometry of space-time, hence it led Einstein to use it to build a model of the Universe as soon as in 1917, by assuming space-time would be well described by GR on the Universe scale. The current model of our Universe relies on two additional hypotheses, based on observations, simplifying the construction of the model:

The Copernican principle We do not occupy a special place in the Universe, let alone its centre. This principle refers to Nicolas Copernic, who promoted the heliocentric model of the Solar system, at a time when people thought the Earth was at the centre of the Universe.

The isotropy hypothesis The Universe is isotropic: there is no privileged direction in the Universe. It is based on many observations: the distribution of galaxies is isotropic around us as is the Comic Microwave Background (CMB) which is a relic radiation from the beginning of the Universe.

Together, these two hypotheses form the cosmological principle: as the Universe is isotropic around us and we do not occupy a special place within it, then it is isotropic around every position in the Universe and it is therefore homogeneous. As a homogeneous Universe can be anisotropic (for example if there is a flow of objects), the cosmological principle is often summarised as follows: the Universe is spatially homogeneous and isotropic. These symmetries on the geometry of the Universe restrict the possible solutions to the Einstein's equations that can be used to build a model of our Universe. These solutions are the Friedmann-Lemaître space-times, discovered independently by the two astronomers in 1922 and 1927. Note that this space-time goes well beyond our observable universe and describes the whole Universe.

The Friedmann-Lemaître solutions are given by metrics $g_{\mu\nu}$ expressed through space-time intervals by $\mathrm{d}s^2 = g_{\mu\nu}\mathrm{d}x^\mu x^\nu$ where x^μ are space-time coordinates. The space-time intervals in these solutions are

$$\mathrm{d}s^2 = -\mathrm{d}t^2 + a(t)^2\gamma_{ij}(x^k)\mathrm{d}x^i\mathrm{d}x^j, \tag{1.7}$$

where t is called the cosmic time, $a(t)$ is the scale factor, γ_{ij} is the spatial metric of the hypersurfaces of constant time Σ_t and the indices i, j, k are spatial indices running from 1 to 3. The spatial metric has three possible expressions

$$\mathrm{d}\sigma^2 = \gamma_{ij}\mathrm{d}x^i\mathrm{d}x^j = \mathrm{d}\chi^2 + f_K^2(\chi)\mathrm{d}\Omega^2 = \frac{\mathrm{d}r^2}{1-Kr^2} + r^2\mathrm{d}\Omega^2, \tag{1.8}$$

with $\mathrm{d}\Omega^2 = \mathrm{d}\theta^2 + \sin^2\theta\mathrm{d}\varphi^2$ is the infinitesimal solid angle, and χ and r are radial coordinates

related by a function of the curvature constant K, $r = f_K(\chi)$ where

$$f_K(\chi) = \begin{cases} K^{-1/2}\sin\left(\sqrt{K}\chi\right) & K > 0, \\ \chi & K = 0, \\ (-K)^{-1/2}\sinh\left(\sqrt{-K}\chi\right) & K < 0. \end{cases} \tag{1.9}$$

Indeed, the surface of a comoving sphere of radius χ is given by $S(\chi) = 4\pi f_K^2(\chi)$, which depends on the spatial curvature radius $1/\sqrt{|K|}$. Thus, one can also identify $f_K(\chi) = r$ as a radial coordinate, by analogy with the expression of the surface of a sphere in flat space. Indeed, in the flat space case $K = 0$, one recovers the usual expression for the surface of a sphere $S(\chi) = 4\pi\chi^2$ and the two radial coordinates coincide $\chi = r$, which also holds for distances small compared to the curvature radius: $\chi \ll 1/\sqrt{|K|}$. The curvature constant is related to the Riemann tensor on spatial surfaces Σ_t, also known as the spatial curvature tensor

$${}^{(3)}R_{ijkl} = 2K\gamma_{k[i}\gamma_{j]l}. \tag{1.10}$$

1.1.2.2 An expanding Universe

The x^i are called comoving coordinates, meaning that an observer for which $x^i = constant$ moves along with the Universe: it does not move in space once the motion of the Universe has been removed, but moves 'with time' $x^0 = t$. To illustrate this, consider two comoving observers with spatial coordinates $\boldsymbol{x}_1$ and $\boldsymbol{x}_2$, their physical separation is not given by the difference of the two vectors but by

$$\boldsymbol{r}_{12} = a(t)(\boldsymbol{x}_1 - \boldsymbol{x}_2), \tag{1.11}$$

so that the scale factor $a(t)$ translates the expansion of the Universe. Then, one has

$$\dot{\boldsymbol{r}}_{12} = H(t)\boldsymbol{r}_{12}, \tag{1.12}$$

with $H(t) = \dot{a}(t)/a(t)$ is the Hubble parameter, and this relation is called the Hubble-Lemaître law, which states that the moving away speed between two objects is all the more high as they are remote, if $H > 0$. This is also called the recession speed and is due to the motion of the Universe, also known as Hubble flow. The expansion of the Universe has been observed through this Hubble-Lemaître law, by Hubble himself in 1929 by measuring independently the distance and velocity of 24 galaxies: see the Hubble diagram in Fig. 1.1. The original observations by Hubble overestimated the Hubble constant H_0, which is the value of the Hubble parameter today, by an order of magnitude, finding $H_0 = 500$ km·s^{-1}·Mpc^{-1} where it is now measured to be of the order of $H_0 \approx 70$ km·s^{-1}·Mpc^{-1}.

Analogously to the spatial comoving coordinates x^i, one can define a conformal time η as

$$\mathrm{d}\eta = \frac{\mathrm{d}t}{a(t)}, \tag{1.13}$$

so that the metric Eq. (1.7) can be rewritten like

$$\mathrm{d}s^2 = a(\eta)^2(-\mathrm{d}\eta^2 + \gamma_{ij}(x^k)\mathrm{d}x^i\mathrm{d}x^j). \tag{1.14}$$

1.1.2.3 The energy content of the Universe

Finally, one needs to model the energy content of the Universe in order to have a complete model. With the above space-time symmetries, the energy-momentum tensor Eq. (1.6) has the following expression

$$T_{\mu\nu} = \rho(t)u_\mu u_\nu + P(t)a(t)\widehat{\gamma}_{\mu\nu}, \tag{1.15}$$

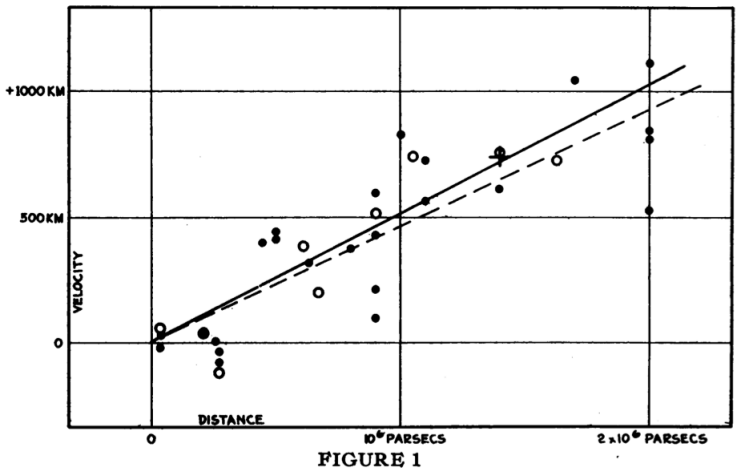

FIGURE 1

Velocity-Distance Relation among Extra-Galactic Nebulae.

Figure 1.1: The original Hubble diagram from the Hubble (1929) publication. Radial velocities of 'extra-galactic nebulae', today known as galaxies, are plotted against their distances. Black disks and plain line represent individual galaxies where circles and dashed line correspond to galaxies gathered in groups.

where $\widehat{\gamma}_{\mu\nu} = g_{\mu\nu} + u_\mu u_\nu$ so that $\widehat{\gamma}_{ij} = a(t)^2\gamma_{ij}$. This expression corresponds to the energy-momentum tensor of a perfect fluid, i.e. one for which $\pi_{\mu\nu} = 0$ and $q^\mu = 0$. The fact that the energy content of the Universe is modeled by such a perfect fluid is a consequence of the hypotheses on space-time symmetries.

The possible solutions to the Einstein's equations Eq. (1.5) that could model our Universe are given by the Friedmann-Lemaître-Robertson-Walker metrics and are derived by considering the cosmological principle only, and similarly for the energy-momentum tensor of its content. The relation between the geometry of space-time and its energy content, that is, the Einstein's equations, would model different possible universes. In order to study these different models, it is useful to rewrite the Einstein's equations Eq. (1.5) given the hypotheses on spatial isotropy and homogeneity

$$\begin{aligned} H^2 &= \frac{\kappa}{3}\rho - \frac{K}{a^2} + \frac{\Lambda}{3}, \\ \frac{\ddot{a}}{a} &= -\frac{\kappa}{6}(\rho + 3P) + \frac{\Lambda}{3}. \end{aligned} \tag{1.16}$$

These equations are called the Friedmann's equations and the second one is often called the Raychaudhuri equation. One needs to solve these equations to study the possible models of the Universe. However this is not possible without describing more the fluids making up the Universe. For this, let us introduce another equation called the equation of state which relates the pressure of a fluid to its energy density

$$P = w\rho. \tag{1.17}$$

The equation of state depends on the kind of matter considered. Here are the values for w for some fluids

- pressureless matter: $w = 0$,

- radiation: $w = 1/3$,

- cosmological constant Λ: $w = -1$,

- curvature K: $w = -1/3$.

The remaining question to build a model of our Universe by solving Eq. (1.16) is: in which proportions these different fluids fill up the Universe?

1.2 ΛCDM: a model with only five independent parameters

The proportions of the different fluids

To answer this question, it is useful to introduce what are called the density parameters Ω

$$\Omega = \frac{\kappa\rho}{3H^2}, \quad \Omega_\Lambda = \frac{\Lambda}{3H^2}, \quad \Omega_K = -\frac{K}{H^2a^2}. \tag{1.18}$$

The first parameter is actually a sum over different fluids with their own equation of state: $\Omega = \sum_i \Omega_i$. Among them is the pressureless matter for which $w = 0$: this kind of matter can be further decomposed into baryonic matter Ω_b and Cold Dark Matter (CDM) Ω_CDM. The baryonic matter is all matter mainly made up with baryons: atoms, molecules and all observables objects in the Universe like stars, galaxies and galaxy clusters. Electrons are not baryonic matter but as they are three orders of magnitude lighter than baryons, baryonic matter corresponds to essentially all observable matter in the Universe. On the contrary, CDM corresponds to a kind of matter which is described as collisionless matter only sensitive to the gravitational interaction (dark, as it does not interact electromagnetically and so is not observable). Another component of the Universe is radiation Ω_r for which $w = 1/3$. Radiation can be either photons Ω_γ or neutrinos Ω_ν. With these parameters at hand, the first of Friedmann's equations Eq. (1.16) is rewritten as a dimensionless equation

$$\sum_i \Omega_i + \Omega_\Lambda + \Omega_K = 1. \tag{1.19}$$

Having a concrete model of the Universe means solving the dynamics of the Friedmann's equations Eq. (1.16) and this requires knowledge of which fluids make up the Universe and in which proportions: that is, knowing the 'initial conditions' for the energy density of the different fluids making up the Universe. These initial conditions are given by the cosmological parameters measured today: Ω^0_K, Ω^0_Λ, Ω^0_r, Ω^0_b, Ω^0_CDM (the density parameter for the neutrinos is related to the density parameter for photons in a simple way, so only one parameter is needed for radiation). One also needs an initial condition for the scale factor a or equivalently for H, as the two are related by an integration: thus the value of the Hubble parameter today H_0, also known as the Hubble constant, is also one of the cosmological parameter. At the end of the day, given the constraint Eq. (1.19) on the sum of the Ω parameters, only five independent parameters are needed to solve for the dynamics of the Universe and build a model.

Observations and measurements of the parameters of the model would then give the best fit solution to model our Universe. Our current understanding of observations of the Universe is based on the ΛCDM model. The acronym stands for the two main components of our Universe: a cosmological constant Λ already appearing in the Einstein-Hilbert action whose nature is still not understood currently, but is believed to be some kind of energy, called 'Dark Energy' (DE), and its main matter content being CDM.

The need to split matter into two different kinds and to introduce CDM, a matter that is collisionless and does not interact electromagnetically was indicated by the visible matter

composed of baryons not behaving the way it was expected by GR. The most known example of this is the rotation curves of galaxies, traced by the rotational velocities of galaxies as a function of their distances to the galaxy centre, see red plain curve (B) of Fig. 1.2. The mass inferred from the visible light is not enough to explain such high rotational velocities at the periphery of galaxies, one indeed would expect the blue dashed curve (A). Therefore, there must be some invisible, hence Dark Matter, mass surrounding galaxies. One distinguishes typically three types of DM depending on how fast their particles travel: 'cold' corresponds to subrelativistic particles, 'hot' to ultrarelativistic ones and 'warm' is between these two regimes. The high velocity of hot DM prevents it to form small scale structures while CDM can be the source of the observed galaxy-sized lumps. Therefore CDM is currently preferred. Finally, regarding the fact that DM is collisionless, it has been hinted by Chandra observations of the so-called bullet cluster (e.g. Markevitch et al., 2004). This corresponds to an undergoing high-velocity merger in which the positions of the various mass components were analysed. X-ray observations show that the hot gas forms a shock due to the collision while lensing observations show that most of the mass (which is dark) went through the shock, lying at the same place as the galaxies which are collisionless (negligible probability of merging). This suggests that DM is collisionless itself.

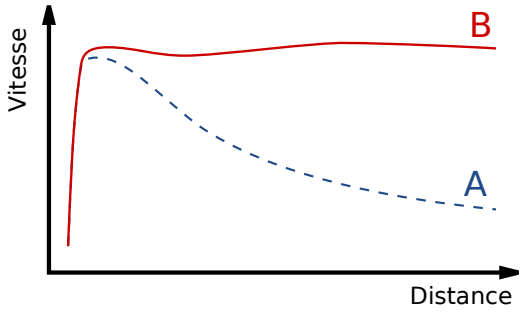

Figure 1.2: A typical so-called galaxy 'rotation curve', representing rotational velocities of stars within a galaxy as a function of their distance to its centre. The full red (B) curve is what is typically observed in a galaxy, where the dashed blue (A) curve is what is expected from Newtonian dynamics. Credit: William Crochot.

The observation suggesting that there is a cosmological constant in the model of our Universe and that it is actually the main component of our Universe comes from an improvement of the Hubble diagram presented in Fig. 1.1. Indeed, two teams Perlmutter et al. (1999) and Riess et al. (1998) observed Ia supernovae and made a Hubble diagram which extends to further distances. The velocity-distance relation Eq. (1.12) is no longer linear for high distances, and their analysis showed that the expansion of the Universe is accelerating. They found that the deceleration parameter defined by $q_0 \equiv -\ddot{a}/(aH^2)|_{t=t_0} = \Omega_{\rm m}^0/2 - \Omega_\Lambda^0 + \Omega_{\rm r}^0$ is negative. Combining this result with observations of the relic radiation today, which shows in particular that the radiation density parameter is negligible, proves that the main content of the Universe is a cosmological constant and that its spatial sections are almost flat.

As an example, we give in Table 1.1 the cosmological parameters obtained by the Planck collaboration in Planck Collaboration et al. (2018b). Of course, other probes than the relic radiation (CMB) can be used to determine these parameters, such as Supernovae (SNe) or Baryon Acoustic Oscillations (BAO). Fig. 1.3 shows contours at 68.3%, 95.4%, and 99.7% confidence level on the Ω_Λ and $\Omega_{\rm m}$ parameters obtained from these three probes, as well as their combination.

$h = H_0/100$	Hubble constant	0.64 ± 0.02
Ω_k^0	curvature density parameter	-0.01 ± 0.01
$\Omega_{\rm CDM}^0 h^2$	CDM density parameter	0.119 ± 0.002
$\Omega_{\rm b}^0 h^2$	baryon density parameter	0.0225 ± 0.0002
$\Omega_{\rm r}^0 h^2$	radiation density parameter	4.148×10^{-5}
Ω_Λ^0	cosmological constant density parameter	0.66 ± 0.02

Table 1.1: Values of the cosmological parameters of the ΛCDM model measured or derived by the Planck collaboration, as in Table 5 of Planck Collaboration et al. (2018b) except for $\Omega_{\rm r}^0 h^2$ which was derived thanks to the measurement of the temperature of the relic radiation by the FIRAS instrument on board of the COBE satelite; Ω_Λ^0 is derived thanks to the constraint of Eq. (1.19).

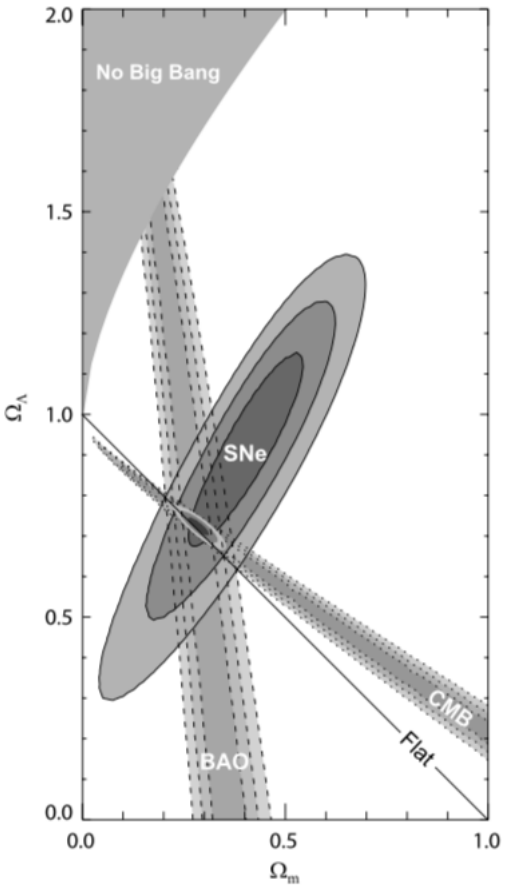

Figure 1.3: Contours at 68.3%, 95.4%, and 99.7% confidence level on the Ω_Λ and $\Omega_{\rm m}$ parameters obtained from the relic radiation (CMB), Baryon Acoustic Oscillations (BAO), and Supernovae (SNe), as well as their combination. Figure taken from Kowalski et al. (2008).

1.3 Chronology of the Universe

Domination eras and key moments in the history of the Universe

Another useful equation to study the dynamics of the Universe is the continuity or conservation equation for the fluids. It comes from the conservation of the total energy momentum tensor $T_{\mu\nu}$ of Eq. (1.6) with respect to the covariant derivative. The conservation of $T_{\mu\nu}$ is actually not a requirement but a consequence of the theory of GR: the Bianchi's identities (a set of identities on the derivative of the Riemann tensor that can be derived from its explicit expression) involve that the Einstein's tensor Eq. (1.5) is also conserved, and given the connection Eq. (1.2), so is the metric. Then, the Einstein's equations Eq. (1.5) directly gives the conservations of the energy-momentum tensor. Therefore, this equation is not independent from the Einstein's equations Eq. (1.5). With our symmetries on space implying that the fluids are perfect, the conservation of the energy-momentum tensor translates into

$$\dot{\rho} + 3H(\rho + P) = 0. \tag{1.20}$$

One can indeed check that this equation is not independent from the Friedmann's equations (1.16) but is obtained by differentiating the first with respect to time and then using the original equations. Using the equation of state (1.17), one can solve for the density of the different fluids i making up the Universe and finds that

$$\rho \propto a^{-3(1+w)} \quad \text{or} \quad \Omega_i = \Omega_i^0 \left(\frac{a}{a_0}\right)^{-3(1+w)} \left(\frac{H_0}{H}\right)^2, \tag{1.21}$$

for w constant, where $H^2 = \kappa \sum_i \rho_i/3$. Thus, the energy density for the fluids listed above behaves like

- pressureless matter: $w = 0$, $\rho \propto a^{-3}$,
- radiation: $w = 1/3$, $\rho \propto a^{-4}$,
- cosmological constant Λ: $w = -1$, $\rho \propto a^0 = \text{cst}$,
- curvature K: $w = -1/3$, $\rho \propto a^{-2}$.

As the Universe is expanding, as shown by the Hubble diagram in Fig. 1.1 with $H_0 = \dot{a}_0/a_0 > 0$, it means that the scale factor is increasing, so that it has been smaller in the past. With the behaviours of the different fluids with the scale factor, one finds that if a is decreasing going backwards in time, the energy density of all these fluids increase, see Fig. 1.4. The energy density increases all the more so as the inverse power in the scale factor is high. Thus, even though we know today the cosmological constant or DE dominates, see Table 1.1, as matter is the second most abundant fluid in the Universe, it must have dominated in the past and far enough, radiation must have dominated the Universe content, as illustrated in Fig. 1.4.

Today, the energy density of radiation is negligible compared to the main components of the Universe: CDM and the cosmological constant. However, the radiation filling up the Universe has been observed to follow a black body spectrum (Fixsen et al., 1996). This means a temperature can be assigned to it, and this will define the temperature of the Universe. The FIRAS instrument on board of COBE has measured it with the best precision to date to be $T_0 = 2.725$ K. We will see in the next chapter that the energy density of radiation is related to it as $\rho_r \propto T^4$. Given that the energy density of radiation goes like $\rho \propto a^{-4}$, then temperature is inversely proportional to the scale factor: $T \propto 1/a$. Thus, the denser the Universe, the hotter it is. At the time where radiation dominated the Universe, the temperature was greater than $T_{eq} = 9283$ K. This value

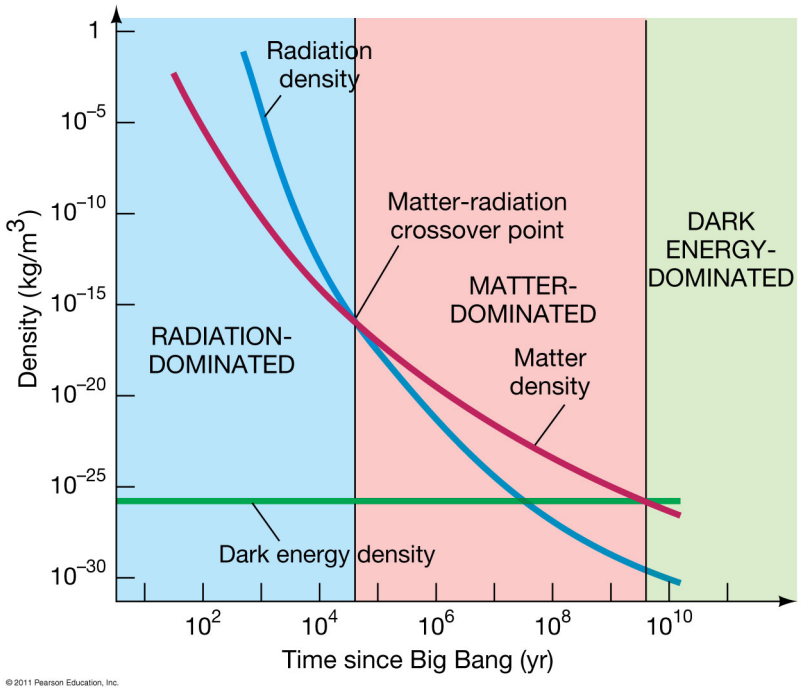

Figure 1.4: Behaviour of the energy density parameters of the three main fluids making up the Universe content: radiation, matter and a cosmological constant or DE. Figure taken from the University of Oregon website.

can be found by equating the energy density of matter with that of radiation to find the moment where radiation starts dominating the Universe (going backwards in time); the temperature is then deduced. When the temperature is high enough, atoms cannot form and consequently, there were no structures as we see them today. For example, at this temperature, the Universe is a plasma made of 75% hydrogen and 25% helium nuclei with free electrons and photons: matter and radiation are thermodynamically coupled. We will detail this primordial phase of the Universe and what happened before in Chapter 2. We now run through the chronology of the Universe -as in Fig. 1.5, showing the timeline of the Universe- starting from this primordial phase, which can be defined to end around 380 000 years after the 'beginning of times'. From this stage on, as the Universe expands, it cools down. While the energy density of the Universe is dominated by matter, the first neutral atoms form at a temperature of $T \sim 3500$ K, this period is known as the recombination epoch. The radiation decouples from matter and the first photons are consequently released, forming the relic radiation we still see today whose temperature is T_0. Small energy density perturbations in this early phase of the Universe, with typical value $\delta\rho/\rho \approx 10^{-5}$, evolved under gravity and are the seeds for the later formation of structures in the Universe. We mention only briefly here the history of the Universe: after recombination, there was a period called 'Dark Ages', which lasted about one hundred million years where the Universe became dark as the expansion cooled the radiation down to infrared light. Then the first stars known as pop III stars formed, followed by galaxies and then quasars, whose emitted light reionised the Universe: this is the reionisation epoch which lasted about 8 hundred million years. The Universe then became more and more structured, with galaxies clumping together

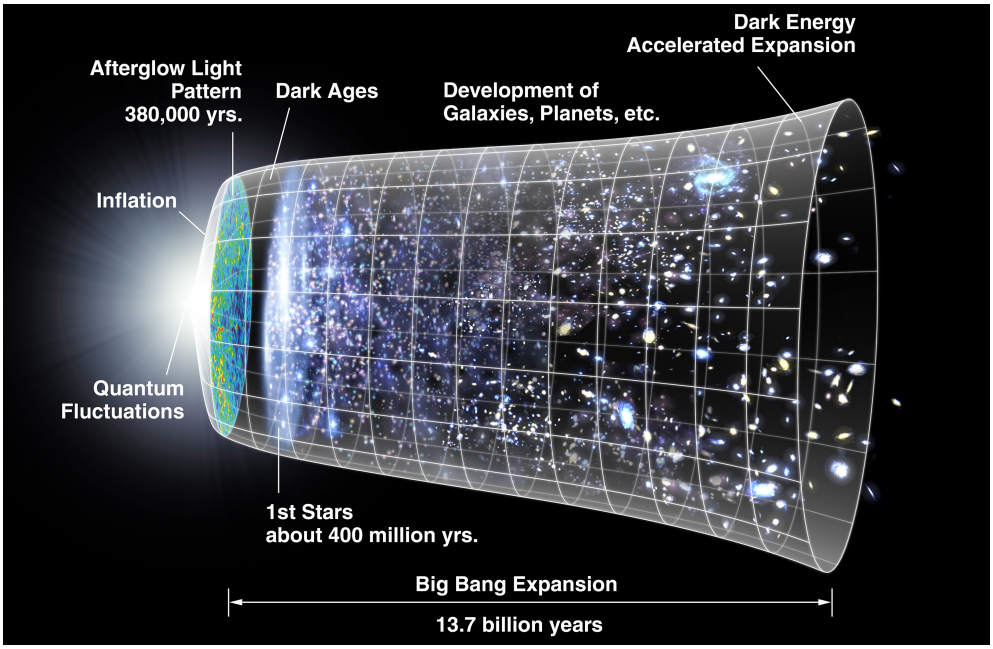

Figure 1.5: Timeline of the Universe. By NASA/WMAP Science Team - Original version: NASA; modified by Cherkash.

to form the first proto-clusters, then clusters and superclusters so that the cosmic web began emerging with a structure made of walls, filaments and nodes hosting the most virialised objects just mentioned. During this evolution of the Universe, the cosmological constant, or DE, starts dominating its evolution, exceeding that of matter.

1.4 Limitations of the model

The ΛCDM model is a minimalistic model that fits well to the observations. However, it shows what can be seen to some people as limitations, which are actually more questions raised by the model: these are open questions on the theoretical framework underlying the model that we will mention now.

One of the biggest of these limitations is probably the unknown nature of DM. Indeed, there is no particle in the Standard Model (SM) of particle physics with the properties described in Section 1.2. This kind of matter is only seen through its gravitational effects, so a possibility is that it could be a new particle, not discovered yet, the same way as neutrinos are only sensitive to the weak interaction and the gravitational interaction, or that electrons do not feel the strong interaction. Indeed, it has even been postulated that neutrinos could be DM but its very small mass prevents it from explaining the whole missing mass of the Universe, as they are still relativistic while DM is cold. Therefore, some people think it could be a more massive neutrino, a particle yet to be discovered, not pertaining to the SM of particle physics. There is a whole domain of particle physics/astroparticles searching for a new particle explaining DM. Another approach is a modification of the gravitational law on galaxy scales in the weak field regime of GR, known as MOND for Modified Newtonian Dynamics, an idea introduced by

Milgrom (1983).

In the same vein there is modified gravity, a modified formulation of GR, to account for the problems in the standard model of cosmology, like the unknown nature of DM and DE. Indeed, some people see the cosmological constant as an unsatisfactory explanation for the acceleration of the expansion of the Universe and think that it needs to be explained. For this, the modified gravity people think that GR must be modified on cosmological scales, for example by replacing the Ricci scalar by a function of R in the Lagrangian. Other theories explain the acceleration of the expansion of the Universe by the introduction of a new fluid, of still unknown nature, with negative pressure: the Dark Energy. Such theories include for example quintessence or other scalar fields. Another explanation is that it could be the observable effect of the backreaction of inhomogeneities on the simple homogeneous and isotropic model of the Universe. However, some other people like Bianchi & Rovelli (2010) think that having a cosmological constant is a sufficient explanation for the recent accelerated expansion of the Universe. For detailed reviews on these topics see for example Clifton et al. (2012); Joyce et al. (2015); Brax (2018).

Another problem dealing now with the cosmological constant is that it is sometimes interpreted as the vacuum energy density of the Universe. Calculations made within the SM of particle physics predict a value of 10^{74} GeV^4 where it is observed to be 10^{-47} GeV^4. There are thus 120 orders of magnitude between the theoretical prediction and the observed value.

Some other problems have to do with the initial conditions of the Universe. We will detail them in the next chapter when dealing with a solution to solve these issues. In just a few words, we can mention them: the flatness problem or why the curvature density parameter is so small, meaning it should have been very close to zero in the primordial Universe; the horizon problem or why the Universe is so homogeneous with density fluctuations not exceeding $\delta\rho/\rho \approx 10^{-5}$ while they were not causally connected; the structure origin problem or what is the mechanism for the origin of the perturbations in a Universe described as being spatially homogenous and isotropic (the simplicity being its own limitation) and finally, the monopoles problem which is a particle physics problem, related to a break in the symmetry underlying the Grand Unification of the three other interactions than gravity in a group G, namely the strong interaction and the electromagnetic and weak ones.

Finally, a serious problem that we will also detail in the next chapter is the initial singularity. Indeed, we have seen that the Universe is expanding, therefore when looking backwards in time, the scale factor is decreasing: $\dot{a} < 0$, and if one looks at the Friedmann's equations Eq. (1.16) and incorporates the solution for the radiation (which is the kind of content that dominates the further away one goes in the past) Eq. (1.21) into it, nothing prevents the scale factor to decrease down to zero. Thus, the energy density should be infinite when the scale factor reaches 0, which is quite unphysical: this is what is called a singularity. This kind of singularity is also found elsewhere in GR, for example at the centre of black holes. This raises a question of fundamental physics and may ask for the quantisation of GR.

Chapter 2

The early Universe

2.1 The hot Big Bang scenario

The standard model of cosmology is sometimes called the big bang model or hot big bang scenario. Why is this so? As mentioned in the previous chapter, the Universe is observed to be expanding, resulting in an increasing scale factor $\dot{a} > 0$. Thus, the scale factor decreases down to zero when looking backwards in time: hence, the current Universe is seen as the result of a 'big-bang' at its origin. As the temperature of the Universe is inversely proportional to the scale factor, the younger the Universe, the hotter it is: hence the 'hot big-bang scenario'. We will now detail a bit why the Universe was hot in the past and what it looked like when it was very young, a phase known as the (very) early Universe.

2.1.1 A bit of thermodynamics in an expanding Universe

As far as one can go in the remote past where the laws of physics are still valid, that is, until the temperature reaches $T \sim 10$ TeV $\sim 10^{19}$ K, which is the highest temperature where particle physics has been tested experimentally in the Large Hadron Collider (LHC), the energy density of the Universe is dominated by radiation. To show that at these temperatures radiation dominates, let us assume that far away enough in the past the Universe is made of particles in thermal equilibrium only, not yet bound into structures, so that they constitute a perfect gas whose distribution functions are given by the Fermi-Dirac (+) and Bose-Einstein (-) statistics for the fermions and bosons respectively in state i

$$F_i(E_i, T_i) = \frac{g_i}{(2\pi)^3} \frac{1}{\exp((E_i - \mu_i)/T_i) \pm 1}, \tag{2.1}$$

where μ_i and T_i are respectively the chemical potential and the temperature of the species and g_i is the degeneracy of the energy level i. Let us also assume that at some point everything in the Universe was radiation (meaning all particles were relativistic so $T \gg m$ and $E \approx pc$), thus one can compute its energy density to be

$$\rho_r(T) \approx g_*(T) \left(\frac{\pi^2}{30}\right) T^4, \tag{2.2}$$

where we have taken the chemical potential to be zero for the SM particles of interest, and the effective number of relativistic degrees of freedom is

$$g_*(T) = \sum_{i=\mathrm{b}} g_i \left(\frac{T_i}{T}\right)^4 + \frac{7}{8}\sum_{i=\mathrm{f}} g_i \left(\frac{T_i}{T}\right)^4, \tag{2.3}$$

where we have summed over all particles b=bosons and f=fermions.

The entropy of the thermodynamical system can be derived given its differential

$$\mathrm{d}S = \frac{\mathrm{d}E}{T} + \frac{P\mathrm{d}V}{T}. \tag{2.4}$$

Now using the variable T instead of E, one can rewrite $\mathrm{d}E$ as

$$\mathrm{d}E = \mathrm{d}(\rho V) = \rho \mathrm{d}V + V\frac{\mathrm{d}\rho}{\mathrm{d}T}\mathrm{d}T, \tag{2.5}$$

as the energy density does not depend on the volume, by definition. Therefore

$$\mathrm{d}S = \frac{\rho + P}{T}\mathrm{d}V + \frac{V}{T}\frac{\mathrm{d}\rho}{\mathrm{d}T}\mathrm{d}T, \tag{2.6}$$

which can be integrated to give

$$S = \frac{V}{T}(\rho + P). \tag{2.7}$$

As the physical volume of the Universe V is proportional to the scale factor to the third, then the energy $E \propto \rho a^3$ and if we let $S \propto sa^3$, where s is the entropy density then

$$T\mathrm{d}S = T\mathrm{d}(sa^3) = \mathrm{d}(\rho a^3) + P\mathrm{d}a^3. \tag{2.8}$$

Recalling the continuity equation Eq. (1.20) which can be rewritten as $\mathrm{d}(\rho a^3) = -P\mathrm{d}a^3$ then one has finally

$$\mathrm{d}(sa^3) = 0. \tag{2.9}$$

One has just shown the conservation of entropy during the Early Universe. Given that for radiation $P = \rho/3$, one can easily express the entropy density as

$$s \approx \frac{2\pi^2}{45} q_* T^3, \tag{2.10}$$

with

$$q_*(T) = \sum_{i=\mathrm{b}} g_i \left(\frac{T_i}{T}\right)^3 + \frac{7}{8}\sum_{i=\mathrm{f}} g_i \left(\frac{T_i}{T}\right)^3. \tag{2.11}$$

The conservation of total entropy therefore translates into $q_*(T)T^3a^3$ being a constant. For a decoupled species from the rest of the plasma i, its own entropy is also conserved. Therefore, the difference $S - S_i = (2\pi^2/45)q_\gamma(T)T^3a^3$ represents the entropy of the particles in the thermal bath, made in particular of photons, is also conserved. Hence, the temperature of the Universe, defined as the temperature of the photons follows

$$T \propto q_\gamma^{-1/3} a^{-1}, \tag{2.12}$$

where q_γ is given by Eq. (2.11) summing only over relativistic particles in thermal equilibrium with the photons.

Now let us see that radiation indeed dominates when temperatures are of the order of the highest one reached at the LHC. Radiation starts to dominate in the past when its energy density equals that of matter

$$\Omega_{\rm m} = \Omega_{\rm r} \;\Leftrightarrow\; \Omega_{\rm m}^0 \left(\frac{a_{\rm eq}}{a_0}\right)^{-3} \left(\frac{H_0}{H}\right)^2 = \Omega_{\rm r}^0 \left(\frac{a_{\rm eq}}{a_0}\right)^{-4} \left(\frac{H_0}{H}\right)^2 \;\Leftrightarrow\; \frac{a_{\rm eq}}{a_0} = \frac{\Omega_{\rm r}^0}{\Omega_{\rm m}^0}, \tag{2.13}$$

where $a_{\rm eq}$ is the scale factor at matter-radiation equality. The temperature at equality is thus given by

$$T_{\rm eq} = T_0 \left(\frac{q_\gamma^0}{q_{\gamma,{\rm eq}}}\right)^{1/3} \frac{a_0}{a_{\rm eq}} = T_0 \left(\frac{q_\gamma^0}{q_{\gamma,{\rm eq}}}\right)^{1/3} \frac{\Omega_{\rm m}^0}{\Omega_{\rm r}^0}. \tag{2.14}$$

Today there are only two relativistic degrees of freedom $q_\gamma^0 = 2$, i.e. only photons are in thermal equilibrium with themselves but as we do not know yet what is the composition of the Universe at equality, let us assume that all particles have decoupled from the photons at equality so that $q_{\gamma,{\rm eq}} = 2$, to get an upper bound on $T_{\rm eq}$. This gives

$$T_{\rm eq} < 9296 \text{ K}, \tag{2.15}$$

which is way below temperatures reached at the LHC. In fact, the right computation gives $T_{\rm eq} = 9282$ K, so our approximation is not too far. Thus, one can safely assume that when temperatures are as high as in the LHC, radiation dominates the Universe. Starting from these very high temperatures, one can now run through the chronology of the Early Universe.

2.1.2 Chronology in the early Universe

The chronology of the early Universe is summarized in Fig. 2.1 and we will now detail it. I present here a sequencing in terms of energy (or equivalently, temperature) which follows the chronology of the Universe, since temperature decreases as the Universe expands.

Different sequencing of the early Universe can be made. A first one is regarding the four fundamental interactions of nature. At energies above 10^{16} TeV, this is the Planck epoch: we expect that at these energy scales, our physical theories may no longer be valid and one cannot extrapolate them to explain what happened. Indeed, because of the large energy densities at play when the Universe was at the Planck temperature, one is approaching the Big-Bang singularity of the standard model, so that one might no longer be in the regime of validity of GR. GR might need to be quantised at these energies: this will be detailed a bit more in the last section. Then, until energy reaches $\sim 10^{13}$ TeV, the three interactions of the SM of particle physics are expected to be unified in one interaction: this is the so-called Grand Unification Theory (GUT) scale. This GU theory has not been tested yet and we actually do not even know if the SM of particle physics can be described by such a theory. Nonetheless, from energies of $\sim 10^{13}$ TeV and above energies of $\sim 10^6$ TeV, we know that the electromagnetic and weak interactions form only one called the electroweak interaction.

Then, at the highest temperatures where the laws of physics have been tested experimentally, the Universe content is different than it is today. I detail here a second way of sequencing the early Universe period from what we know about the SM of particle physics. Indeed, at these temperatures, matter is in a plasma state and the energies are so high that atoms are not yet bound, nor even the nucleons inside it. It is therefore expected that until the temperature cools down to energies of ~ 100 MeV, the primordial Universe is a quark-gluon plasma. This period is simply called the quark epoch. As the Universe expands, the temperature drops and for energies lower than ~ 100 MeV, quarks and gluons bind to form hadrons like neutrons and protons: this

is the hadron epoch which lasts until energy reaches ~ 1 MeV. At this temperature happens the neutrino decoupling: neutrinos stop interacting with the thermal plasma because the interaction rate Γ of the following weak interactions

$$\nu + \bar{\nu} \leftrightarrow e + \bar{e} \quad \text{and} \quad \nu + e \leftrightarrow \nu + e \tag{2.16}$$

becomes smaller than the expansion rate of the Universe H. In parallel and until the energy reaches ~ 100 keV, leptons and antileptons are in thermal equilibrium in the primordial plasma: this is, without surprise, called the lepton epoch. Then happens the Big Bang Nucleosynthesis (BBN) where protons and neutrons, formed during the hadron epoch, bind to finally form the first atomic nuclei by fusion reactions: at this stage the Universe is mainly composed of the hydrogen nuclei p formed during the hadron epoch, and now other nuclei form like helium 4, but also deuterium, helium-3 and lithium-7 in smaller amounts. Then all of these particles (leptons, atomic nuclei and photons) remain in thermal equilibrium, forming a plasma of radiation: this is the photon epoch, which lasts until the energy drops to ~ 0.4 eV where it is no longer high enough for the photons to break the forming neutral atoms. Therefore, atomic nuclei 'recombine' with electrons to form neutral atoms. Then photons can no longer interact with electrons which are bound with nuclei and as atoms are neutral, photons do not have any particle left to interact with. Therefore they decouple from matter and propagate freely in the Universe with their temperature decreasing as the inverse of the scale factor (see Eq. (2.12)), so that we observe them today at a temperature of $T_0 = 2.725$ K all around us, giving the first picture of the Universe, at the end of recombination. Given that the decoupling of photons occurs right after the recombination, one can use the temperature to compute $a(t)/a_0$ and inverse this function to get the time at which this event happens. The first release of photons then happens at $t = 380\,000$ yrs after the Big-Bang phase where the Universe originates from.

During this early phase of the Universe which lasts over 380 000 years, another paradigm takes place. This is not really a theory nor a phase predicted by our current knowledge of the laws of physics, but more a model that gives an explanation to solve some of the problems of the standard model mentioned in Chapter 1. In the next section, we will detail the original motivations for such a paradigm.

2.2 The inflationary paradigm

2.2.1 Motivations: problems of the hot Big Bang scenario

Some of the problems of the hot big bang mentioned in the previous chapter like the curvature or the horizon problems are deduced from the observation of the CMB. These with other 'initial conditions' problems are detailed here and are the original motivations for the inflationary paradigm that we will describe afterwards.

2.2.1.1 Flatness problem or why the Universe is so flat?

One has found that the evolution of the curvature density parameter is given by Eq. (1.21)

$$\Omega_{\rm K} = \Omega_{\rm K}^0 \left(\frac{a}{a_0}\right)^{-2} \left(\frac{H_0}{H}\right)^2 . \tag{2.17}$$

Observations show that today, the curvature density parameter is compatible with zero $\Omega_{\rm K}^0 = -0.01 \pm 0.01$, see Table 1.1. Given Eq. (2.17), it means that in the past, curvature must have

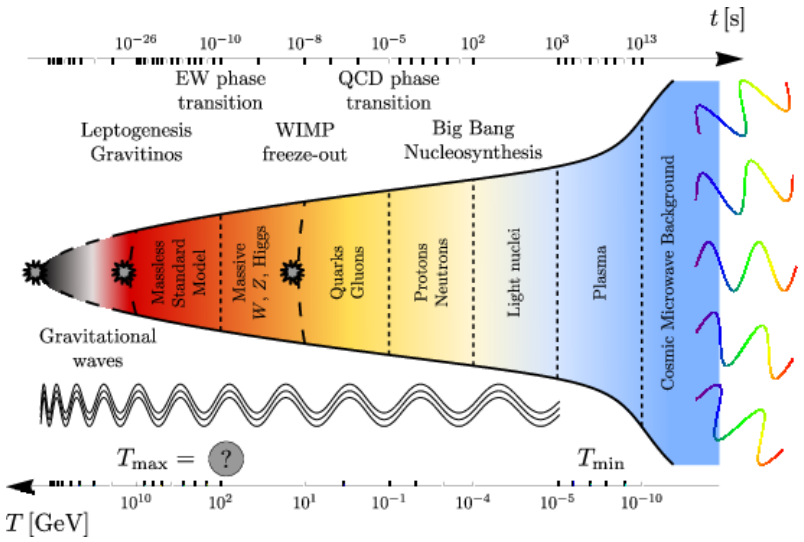

Figure 2.1: A timeline of the primordial Universe. Figure from Pralavorio (2013).

been even closer to zero, for example at matter-radiation equality

$$\Omega_{\rm K}^{\rm eq} = \frac{\Omega_{\rm K}^0}{2\Omega_{\rm r}^0}\left(\frac{\Omega_{\rm r}^0}{\Omega_{\rm m}^0}\right)^2 = -4\times 10^{-6}, \tag{2.18}$$

where we have used Eq. (2.13) and Eq. (1.19) to derive this expression. At the Planck epoch where radiation dominates the energy content of the Universe this gives

$$\Omega_{\rm K}^{\rm Pl} = \frac{\Omega_{\rm K}^0}{\Omega_r^0}\left(\frac{T_0}{T_{\rm Pl}}\right)^2\left(\frac{q_\gamma^0}{q_\gamma^{\rm Pl}}\right)^{2/3} \lesssim -10^{-62}, \tag{2.19}$$

where $q_\gamma^{\rm Pl} > 106.75$ (106.75 is the effective number of degrees of freedom when all known particles of the SM of particle physics are relativistic) and $T_{\rm Pl} \sim 10^{16}$ TeV $\sim 10^{32}$ K and we have used Eq. (2.12) to derive this expression. The very small value of Ω_K means that the Universe is very close to critical, i.e. $\Omega \approx \kappa\rho_c/(3H^2) = 1$ (where $\rho_c = 3H^2/\kappa$ is the critical density of the Universe). It is argued in Peter & Uzan (2009) and Peacock (1999), by rewriting the Friedmann equations in the form of a dynamical system, that a Universe with $\Omega_K = 0$ is unstable for any matter content with equation of state $w \geq 0$. This means that if one starts from a Universe with $\Omega_K = 0$, it soon evolves to a Universe with Ω_K departing significantly from zero, as shown in Fig. 2.2, except if the Universe is only filled with a cosmological constant Λ (and no matter). Therefore one is naturally led to ask himself the question: if a flat Universe is unstable, then why ours is so flat? More precisely, we have shown that the curvature density parameter must have been precisely constrained close to zero so that it has the value one observes today. If $K \neq 0$ and $\Omega_K \sim 1$, then our Universe would have been very different: $K > 0$ means an overdense Universe with $\rho > \rho_c$ and would lead to a recollapse of the Universe soon after the big-bang, into a 'big-crunch' (the Universe collapses in a very dense state similar to the big-bang); on the contrary $K < 0$ means an underdense Universe which expands so fast that it reaches the temperature we observe today but in much less time, so that structures do not have time to form under the action of gravity on density perturbations: the Universe would therefore just contains atoms diluted

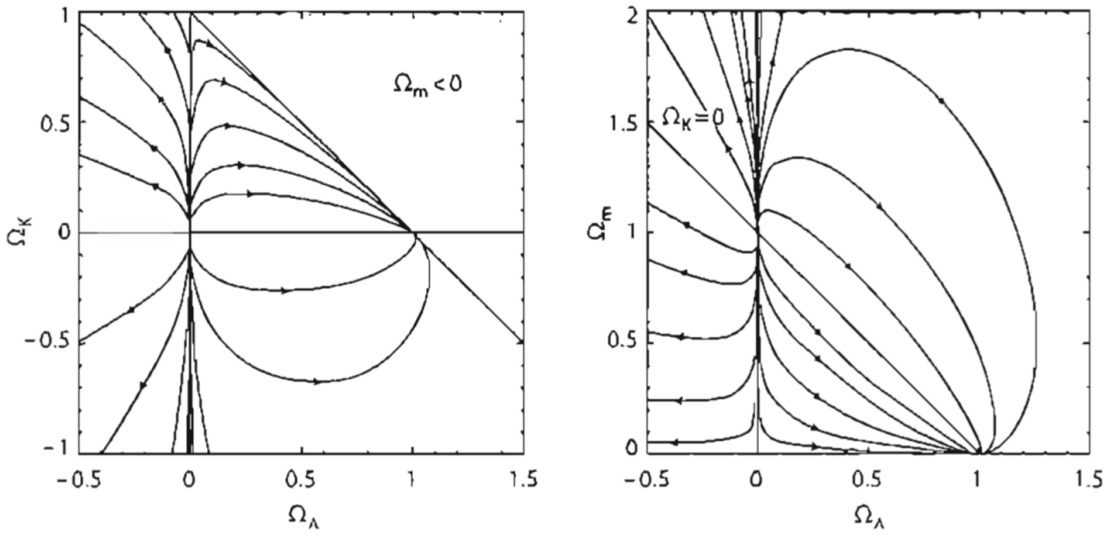

Figure 2.2: Dynamical evolution in the plane $(\Omega_K, \Omega_\Lambda)$ (left) and $(\Omega_m, \Omega_\Lambda)$ (right) for a matter content with equation of state $w = 0$. Figure from Peter & Uzan (2009).

through space. This problem is thus an initial value problem or fine-tuning problem to some cosmologists because the standard model of cosmology do not explain why the initial value for the curvature is so precisely constrained to give the complex Universe one observes today. This problem is sometimes rephrased as the 'oldness problem': as the Universe expands, the value of Ω_K departs from zero. However, today Ω_K is still very close to zero thus one can rather ask 'why our Universe is so young?'.

2.2.1.2 Horizon problem or why the Universe is so homogeneous?

As we will see in Chapter 4 on the Cosmic Microwave Background (CMB), this relic radiation is very uniform with an average temperature measured today of $T_0 = 2.725$ K and even though there are some fluctuations in temperature, there are so tiny $\langle(\delta T/T)^2\rangle^{1/2} \sim 10^{-5}$ that one can safely say that the Universe was in a state of thermal equilibrium at recombination. Now, this should not be the case in the hot big bang model. Indeed, photons in our past light cone have not been causally connected in the primordial Universe, so they could not equilibrate thermally, see Fig. 2.3. To see this, let us compute the size of the horizon at decoupling. The horizon of an observer is the distance (proper or comoving, measured with respect to the observer) at which photons which have been emitted are received by the observer at a given time of reception t_R. It is computed by considering null geodesics of the metric Eq. (1.7), i.e. $\mathrm{d}s^2 = 0$, which gives, for a homogenous and isotropic Universe and flat space

$$r_{\rm H} \equiv \int_0^{t_R} \frac{\mathrm{d}\tau}{a(\tau)}, \tag{2.20}$$

this is the comoving horizon. The proper horizon is given by multiplying by the scale factor at reception a_R

$$d_{\rm H} \equiv a_R \int_0^{t_R} \frac{\mathrm{d}\tau}{a(\tau)}. \tag{2.21}$$

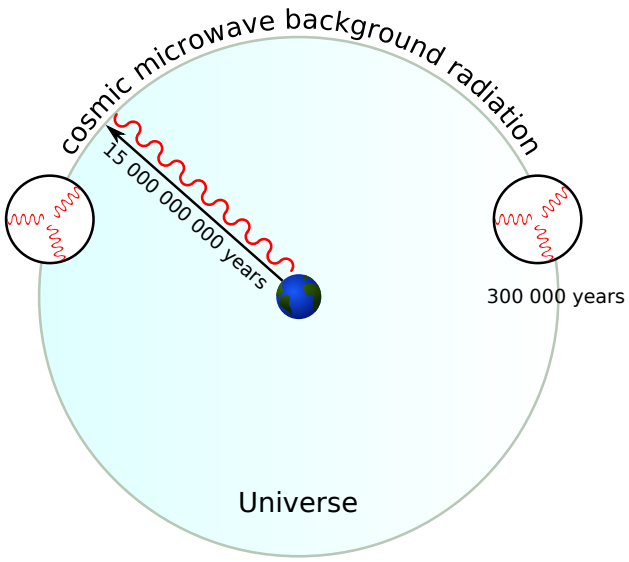

Figure 2.3: A visualisation of the horizon problem. The original uploader was Theresa knott at English Wikipedia. Derivative work: chris - CC BY-SA 3.0.

If the time of reception is today: $t_R = t_0 = 13,8$ Gyr, the above formulae would give our horizon. The horizon when photons decouple from matter, i.e. at decoupling, is given by setting $t_R = t_{\rm LSS} = 380\,000$ yr, where LSS stands for Last Scattering Surface, i.e. the spatial hypersurface where photons last scattered with the electrons of the primordial bath so that they can wander freely afterwards. Let D be the physical size of the horizon at decoupling

$$D = a_{\rm LSS} \int_0^{t_{\rm LSS}} \frac{{\rm d}\tau}{a(\tau)}. \tag{2.22}$$

Now one can compute the angular size $\delta\theta$ of such an 'object' on the sky today. The LSS is located at a comoving distance $r_{\rm LSS}$ and at the time when photons were emitted, they had to travel the physical distance $a_{\rm LSS}\, r_{\rm LSS}$ before reaching us. Therefore, the angular size of the horizon on the sky today is

$$\delta\theta = \left(a_{\rm LSS} \int_0^{t_{\rm LSS}} \frac{{\rm d}\tau}{a(\tau)} \right) \Big/ (a_{\rm LSS}\, r_{\rm LSS}) = \int_0^{t_{\rm LSS}} \frac{{\rm d}\tau}{a(\tau)} \Big/ r_{\rm LSS} = \int_0^{t_{\rm LSS}} \frac{{\rm d}\tau}{a(\tau)} \Big/ \int_{t_{\rm LSS}}^{t_0} \frac{{\rm d}\tau}{a(\tau)}. \tag{2.23}$$

It is computed by solving for the scale factor thanks to the first of the Friedmann's equations Eq. (1.16) in the matter dominated era and in the radiation dominated era (as $0 < t_{\rm eq} < t_{\rm LSS}$) and then by integrating. This gives $\delta\theta \sim 1°$: the horizon at decoupling has a size of 1° on the sky today. Now the horizon encompasses the volume of a causally connected region which means that regions larger than the angular size of 1° on the sky today have not been causally connected at decoupling. Stated otherwise: causally connected regions at decoupling are smaller than the observable Universe today, as seen in Fig. 2.3. There are thus $\sim (4\pi)/(\pi/180)^2 \sim 10^5$ causally disconnected regions on the sky. If one assumes that the homogeneous temperature of the sky is due to photons which have thermally equilibrate at decoupling, for example through the Compton scattering process, then observations prove this hypothesis to be wrong. One would

instead expect fluctuations of order unity on angular scales larger than 1°. Then one asks 'what can be the physical reason for the Universe being so homogeneous?'.

2.2.1.3 Structure formation problem

The fact that the Universe is so homogeneous seems to be a philosophical problem to some cosmologists although it is at the root of our model, in the very hypotheses underlying it. Nonetheless, it is thought that the tiny density inhomogeneities in the primordial plasma lead to the large-scale structures one observes today through the collapse of such overdensities under the attraction of gravity once matter dominates the Universe content. The problem is that our model does not explain the origin of such primordial inhomogeneities. Worse: there is no causal mechanism that can account for producing inhomogeneities on scales larger than the horizon at decoupling, i.e. today one observes in the CMB perturbations with wavelengths larger than the size of the horizon at decoupling, so these perturbations should not exist if they were formed by a causal physical process during this epoch. In fact, as one approaches the singularity, every perturbations are outside of the horizon. Thus, in the standard cosmological model, the initial conditions for these perturbations cannot have been set by a causal physical process at this moment of the Early Universe. This problem is thus intimately linked to the horizon problem.

2.2.1.4 Relic problem

Finally, another problem is the relic problem. As mentioned in the previous chapter, this is a problem related to particle physics, but as the SM of particle physics is used to describe the early stages of the Universe, one can consider it as an inconsistency of the hot big-bang model. As explained in Section 2.1.2, one has a reliable history of the Universe until temperature reaches energies of ~ 10 TeV. In particular, the Universe underwent a phase transition corresponding to the spontaneous symmetry breaking of the electroweak interaction: this is the electroweak phase transition. In the SM of particle physics, for energies above ~ 300 GeV, the electromagnetic and weak interactions are unified into a single one known as the electroweak interaction whose symmetry is described by the group $SU(2)_L \otimes U(1)_Y$. However, for lower energies, the electroweak interaction split in two, whose symmetry is described by the group $U(1)_{EM}$, producing at the same time the $W^{\pm}$ and Z^0 bosons and the photon γ. Particle physicists think that at higher energies, the three interactions of the SM of particle physics should also be unified, i.e. that the electroweak interaction and the strong interaction are unified with a symmetry described by a group G. Such theories are called Grand Unified Theories (GUT) and are expected to describe physics at energies higher than $\sim 10^{16}$ GeV (this is called the GUT energy scale). The Spontaneous Symmetry Breaking (SSB) of G into $SU(3)_c \otimes SU(2)_L \otimes U(1)_Y$, where $SU(3)_c$ describes the symmetry of the strong interaction, is expected to produce stable heavy particles. This is where lies the problem: one does not observe these particles today. To be more precise, for example, some of these particles are expected to be produced massively during this SSB so that they should dominate the Universe today. These ones are point-like topological defects and correspond to magnetic monopoles, that is, some kind of magnetic field 'charge'. The density parameter for these magnetic monopole relics is

$$\Omega_M h^2 \sim 10^{17} \left(\frac{T_{GUT}}{10^{16}\,\mathrm{GeV}} \right)^3 \left(\frac{m_M}{10^{16}\,\mathrm{GeV}} \right), \tag{2.24}$$

where T_{GUT} is the temperature of the SSB from GUT to the SM of particle physics and m_M is the mass of the magnetic monopoles which are predicted to be of the order $\sim 10^{16}$ GeV in GUT models, see Section 4.5.2 of Peter & Uzan (2009) or 7.4 of Kolb & Turner (1990) for more

details. Now, if one lets Ω be the total energy content of the Universe (excluding curvature), one has that Ω is of order unity because of the constraint Eq. (1.19). Thus, magnetic monopoles are overproduced during this phase transition and would drastically change the evolution of the Universe if they had been there. Moreover, one does not detect any of these monopoles today. The standard model of cosmology does not explain why, when extrapolating particle physics to very high energies, these particles are at least so rare in the Universe one does not detect them.

All these considerations about problems of the big bang model are actually considerations about the initial conditions of our Universe. The hot big bang scenario well describes facts such as the abundance of light elements or the temperature of the Universe but does not explain the origin of the value of the curvature density parameter, the smallness of the relative temperature fluctuations or the density perturbations that give rise to the structures we observe today. These initial conditions seem very special, 'fine-tuned', to some of the cosmologists and this is why a new paradigm has been proposed to bring answers. We will describe how this paradigm solves the initial condition problems of the standard model of cosmology in the next section.

2.2.2 Solving these problems: the inflationary paradigm

A way to solve these problems is to have an accelerated phase of expansion in the early Universe. Let us see how the above mentioned three problems are solved in this way.

2.2.2.1 Flatness problem

As we have seen in Section 2.2.1.1, the flatness problem is related to the value of the cosmological parameter Ω_K measuring the curvature density of the Universe, that is constrained to be so close to zero in the very early Universe. The so-called 'inflation' is a mechanism that solves, among other things, the flatness problem by starting from a random value of Ω_K of order unity in the very early Universe and bringing it to the very special and constrained value one observes in the early Universe. To see that a phase of accelerated expansion in the early Universe solves the flatness problem, let us rewrite the Friedmann's equations Eq. (1.16) as

$$\frac{3K}{\kappa} = a^2\rho\left(1 - \frac{3H^2}{\kappa\rho}\right) = a^2\rho\,(1-\Omega^{-1}), \tag{2.25}$$

so that $a^2\rho\,(1-\Omega^{-1})$ is a constant. Now $\Omega = 1-\Omega_K$, so the smaller Ω_K, the closer to 1 Ω is. As the very special value of Ω_K in the Early Universe is believed to be fine-tuned within the standard model of cosmology that we have presented up to now, one would prefer a value of Ω not so constrained to be close to 1. Let us compare its value at an initial time $t_{\rm i}$ with its value at some later time $t_{\rm f}$ in the early Universe

$$a_{\rm i}^2\rho_{\rm i}\,(1-\Omega_{\rm i}^{-1}) = a_{\rm f}^2\rho_{\rm f}\,(1-\Omega_{\rm f}^{-1}), \tag{2.26}$$

if we let $t_{\rm f} = t_{\rm eq}$, we know from Eq. (2.18) that $\Omega_K^{\rm eq}$ is very close to zero and so is $(1-\Omega_{\rm eq}^{-1}) = -\Omega_K^{\rm eq}/\Omega_{\rm eq}$. Starting from a random value of Ω_K of order unity in the very early Universe and bringing it to the very special and constrained value one observes in the early Universe, one has $1-\Omega_{\rm i}^{-1} \gg 1-\Omega_{\rm f}^{-1}$. Therefore, solving the flatness problem requires that

$$a_{\rm f}^2\rho_{\rm f} \gg a_{\rm i}^2\rho_{\rm i}, \tag{2.27}$$

which also means that, given Eq. (2.25),

$$\dot{a}_{\rm f}(t) > \dot{a}_{\rm i}(t). \tag{2.28}$$

Thus, the inflation is a mechanism during which the expansion of the Universe accelerates

$$\ddot{a}(t) > 0. \tag{2.29}$$

2.2.2.2 Horizon problem

This phase of inflation also solves the horizon problem. Indeed, let us consider the comoving Hubble radius. The Hubble radius, or Hubble distance, is defined by noticing that H has the dimension of the inverse of a time. Thus the Hubble distance is $D_H \equiv c/H$, with c the speed of light; this is a physical distance. The comoving Hubble radius is therefore given by $c/(aH)$. One can show that close to the decoupling time, this comoving Hubble radius well approximates the comoving size of the particle horizon. With the requirement that inflation is a phase of accelerated expansion of the Universe, see Eq. (2.29), the comoving Hubble radius decreases with time during this phase

$$\frac{\mathrm{d}}{\mathrm{d}t}(aH)^{-1} < 0. \tag{2.30}$$

This means that the comoving distance between two points that have been causally connected at the beginning of inflation, i.e. within the comoving Hubble radius, might be larger than the comoving Hubble radius at the end of inflation. Thus, they may appear causally disconnected if one does not consider this early accelerated phase, as the comoving Hubble radius always increases with time for all known sources of matter. Thus, an accelerated phase of expansion in the early Universe might also be required to solve the horizon problem.

2.2.2.3 Relic problem

Finally, a period of inflation simply solves the relic problem by diluting the monopoles drastically since the Universe expands exponentially, removing them from the observable Universe. This mechanism can lower their observed density by many orders of magnitude, similarly to $\Omega_K \to 0$ and the geometry goes to flatness. Note that it is possible only if inflation happens below the temperature where magnetic monopoles are produced.

2.2.2.4 Duration of inflation

Then, to quantify this accelerated phase of expansion, one usually computes its duration as the ratio of the value of the scale factor at the end of inflation with that at the beginning of inflation

$$N \equiv \ln\left(\frac{a_\mathrm{f}}{a_\mathrm{i}}\right), \tag{2.31}$$

N is called the e-folds number and quantifies how much the scale factor increases during the inflation phase. Now, Eq. (2.29) translates into $\rho + 3P < 0$ given the second of the Friedmann's equations Eq. (1.16): one says that the strong energy condition $\rho + 3P > 0$ is violated, i.e. $w < -1/3$, so that during inflation the Universe is filled with a fluid of negative pressure. Thus, if one assumes that the inflation phase is due to a fluid with equation of state parameter $w = -1$ that lasts from t_i to t_f, one has

$$\left|\frac{\Omega_K(t_\mathrm{f})}{\Omega_K(t_\mathrm{i})}\right| = \left(\frac{a_\mathrm{f}}{a_\mathrm{i}}\right)^{-2} = \mathrm{e}^{-2N}. \tag{2.32}$$

As the inflaton (the fluid dominating the Universe during the inflation) has not been observed yet in any high energy particle physics experiment, it is expected to be part of the Universe

content around the GUT scale. Recalling that in order to solve the flatness problem, inflation is a mechanism that starts from a random value of $\Omega_K(t_\mathrm{i}) \sim \mathcal{O}(1)$ and bring it the closer possible to zero, we will get a lower bound for the duration of inflation by taking t_f to be prior to the Planck time so that $|\Omega_K(t_\mathrm{f})| \lesssim 10^{-60}$ and

$$N \gtrsim 69. \tag{2.33}$$

Likewise, for the horizon problem to be solved, one thus needs that the comoving Hubble radius of today's observable Universe is smaller than the comoving Hubble radius at the beginning of inflation, so that all observable points on the CMB have been causally connected in the past, i.e.

$$\frac{1}{a_0 H_0} \leq \frac{1}{a_\mathrm{i} H_\mathrm{i}}. \tag{2.34}$$

This implies that

$$\mathrm{e}^N \geq \frac{H_\mathrm{i}}{H_\mathrm{f}} \frac{a_\mathrm{f} H_\mathrm{f}}{a_0 H_0} = \frac{a_\mathrm{f} H_\mathrm{f}}{a_0 H_0} \approx \frac{T_0 H_\mathrm{f}}{T_\mathrm{f} H_0}, \tag{2.35}$$

where we have used the fact that $H_\mathrm{f} = H_\mathrm{i}$ because $\dot{H} = -\kappa(\rho + P)/2 = 0$ as we assumed inflation was governed by a fluid with equation of state $w = -1$, and the fact that the temperature of the Universe is inversely proportional to the scale factor Eq. (2.12). Taking the end of inflation at the GUT scale $T_\mathrm{f} \sim 10^{16}$ GeV and that the Universe is later dominated by radiation to express H_f, one has

$$\mathrm{e}^N \gtrsim \frac{T_0}{T_\mathrm{f}} \left(\frac{T_\mathrm{f}}{T_0}\right)^2 \Omega_\mathrm{r}^0 \sqrt{2}, \tag{2.36}$$

with the temperature of the Universe today being $T_0 = 10^{-4}$ eV. Thus

$$N \gtrsim \ln\left(\frac{T_\mathrm{f}}{T_0} \Omega_\mathrm{r}^0 \sqrt{2}\right), \tag{2.37}$$

i.e. numerically

$$N \gtrsim 58; \tag{2.38}$$

one notices that if the end of inflation is taken during the Planck epoch, the lower bound for N increases while an inflation ending at lower energies will give a smaller value. Finally, a long enough phase of inflation solves the horizon problem, with a value for its duration compatible with the one found to solve the flatness problem, as solving the two problems give only a lower bound for the number of e-folds.

2.2.3 The simplest model: inflation with one scalar field

In the previous section we have chosen an inflaton field with $w = -1$ to solve two of the problems of the standard model of cosmology. We know from Chapter 1 that the cosmological constant Λ fulfills this condition. However, by definition, the cosmological constant is a constant, so it cannot be used to describe the dynamics of the inflation phase as it would lead to a forever accelerated expansion of the Universe. Thus we rely on another fluid that can produce an accelerated phase of expansion and then stops it: this is done thanks to a scalar field, the inflaton field. There are many models of inflation: some with several fields known under the name of multifield inflation, that could interact with each other, or with more or less complicated potentials. The simplest models of inflation involve one scalar field φ with a potential $V(\varphi)$ and are also the ones favored

by the Planck data (Planck Collaboration et al., 2018d). The action of such a scalar field is then simply given by

$$S = -\int \sqrt{-g}\left(\frac{1}{2}\partial_\mu\varphi\partial^\mu\varphi + V(\varphi)\right)\mathrm{d}^4x, \tag{2.39}$$

which, once varied with respect to the metric, gives its energy-momentum tensor

$$T_{\mu\nu} = \partial_\mu\varphi\partial_\nu\varphi - \left(\frac{1}{2}\partial_\alpha\varphi\partial^\alpha\varphi + V(\varphi)\right)g_{\mu\nu}. \tag{2.40}$$

From this, one can deduce the energy density in the scalar field and its pressure

$$\rho_\varphi = \frac{\dot{\varphi}^2}{2} + V(\varphi), \quad \text{and} \quad P_\varphi = \frac{\dot{\varphi}^2}{2} - V(\varphi). \tag{2.41}$$

Such a field is usually called the inflaton field, because it fills up the Universe during the inflation phase. One recalls that the inflaton field must violate the strong energy condition Eq. (2.29) in order to solve the 'initial conditions' problems of the standard model of cosmology

$$P_\varphi < -\frac{\rho_\phi}{3}, \tag{2.42}$$

which implies that

$$\dot{\varphi}^2 < V. \tag{2.43}$$

Thus, providing that this last condition is fulfilled, such a scalar field dominating the energy content of the Universe enables a phase of accelerated expansion.

A way to ensure that condition Eq. (2.43) is fulfilled is if the potential energy of the inflaton dominates over its kinetic energy

$$V \gg \frac{\dot{\varphi}^2}{2}, \tag{2.44}$$

which translates into either a relatively very large potential as in Fig. 2.4 (a) (convex potential) or small kinetic energy (b) (concave potential), constraining the shape of the possible potentials.

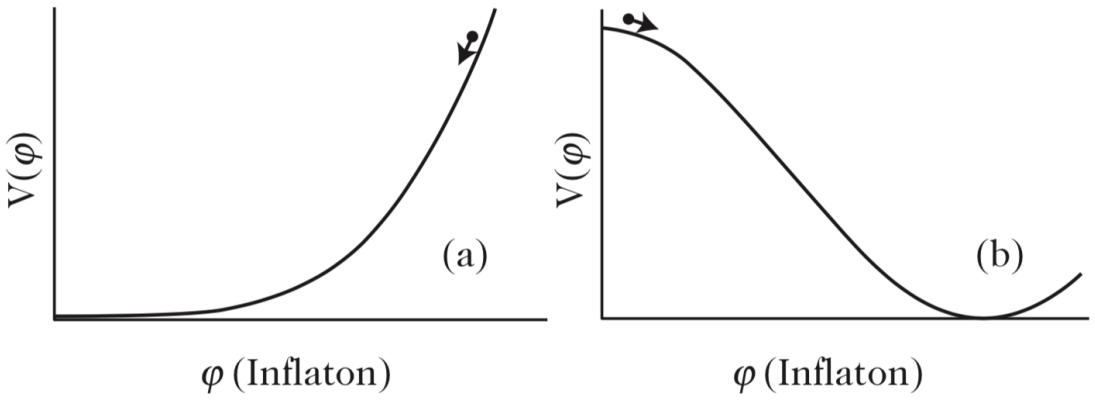

Figure 2.4: Two examples of inflationary potentials with large field values (a) and small field values (b). Figure adapted from Peter & Uzan (2009).

With the inflaton being the dominant constituent of the Universe, the Friedmann's equations (1.16) are thus

$$\begin{aligned} H^2 &= \frac{\kappa}{3}\left(\frac{1}{2}\dot{\varphi}^2 + V(\varphi)\right) - \frac{K}{a^2}, \\ \frac{\ddot{a}}{a} &= -\frac{\kappa}{3}(\dot{\varphi}^2 - V(\varphi)), \end{aligned} \tag{2.45}$$

and the continuity equation (1.20) can be replaced by the Klein-Gordon (KG) equation by simplifying by $\dot{\varphi}$

$$\ddot{\varphi} + 3H\dot{\varphi} + V_{,\varphi} = 0, \tag{2.46}$$

where $_{,\varphi}$ means derivative with respect to the field. As for any fluid, the three above equations are not independent from each other, see Eq. (1.20). Now, a way that the inflation phase lasts long enough is if the kinetic energy of the inflaton stay small compared to the inflationary potential, that is, if the field does not evolve too rapidly. Stated otherwise, if the acceleration of the inflaton $\ddot{\varphi}$ is small, the inflation phase can last. This is ensured by the friction term $3H\dot{\varphi}$ in Eq. (2.46) to be dominant over the acceleration of the field

$$3H\dot{\varphi} \gg \ddot{\varphi}. \tag{2.47}$$

These last two conditions Eq. (2.44) and Eq. (2.47) define the slow-roll regime of inflation. The slow-roll scenario allows to make predictions for most of the potentials without precising their shape. Slow-roll means that the field is slowly rolling on its potential during the inflation phase, i.e. that $\dot{\varphi}$ is small, so that the condition $\dot{\varphi}^2 < V$ is more likely satisfied. Furthermore, we know that inflation must be long enough in order to solve the flatness and horizon problems at least, thus, if one wants to describe the whole inflation with the slow-roll formalism, $\dot{\varphi}$ must be kept small so the acceleration of the field $\ddot{\varphi}$ is also small. With these conditions, the equations of motion for the dynamics of the Universe and the scalar field become

$$\begin{aligned} H^2 &\approx \frac{\kappa}{3}V(\varphi), \\ \frac{\ddot{a}}{a} &\approx \frac{\kappa}{3}V(\varphi), \\ 3H\dot{\varphi} + V_{,\varphi} &\approx 0, \end{aligned} \tag{2.48}$$

where we have neglected the spatial curvature as by definition, the inflaton dominates the energy content of the Universe during inflation. Noticing that $\dot{H} = \ddot{a}/a - H^2$ the second equation is

$$\dot{H} \approx -\frac{\kappa}{2}\dot{\varphi}^2 \approx 0, \tag{2.49}$$

so that H is nearly constant and one can solve for the scale factor

$$a(t) = \mathrm{e}^{Ht}. \tag{2.50}$$

This is the reason why inflation is often referred to as a phase of exponential expansion of the Universe.

To go beyond the exponential expansion of the Universe, one defines the slow-roll parameters

$$\begin{aligned} \varepsilon &= -\frac{\dot{H}}{H^2}, \\ \delta &= \varepsilon - \frac{\dot{\varepsilon}}{2H\varepsilon}, \end{aligned} \tag{2.51}$$

which in the case of single field inflation reduce to

$$\begin{aligned} \varepsilon &= \frac{3\dot{\varphi}^2}{2(\dot{\varphi}^2/2+V)} = \frac{2}{\kappa}\left(\frac{H_{,\varphi}}{H}\right)^2, \\ \delta &= -\frac{\ddot{\varphi}}{H\dot{\varphi}} = \frac{2}{\kappa}\frac{H_{,\varphi\varphi}}{H}, \end{aligned} \tag{2.52}$$

the first parameter would thus quantify the first of the slow-roll conditions while the second one relates to the second. Indeed, the slow-roll conditions Eq. (2.44) and Eq. (2.47) are equivalent to

$$\varepsilon \ll \frac{3}{2} \quad \text{and} \quad \delta \ll 3, \tag{2.53}$$

given the expressions Eq. (2.52) for the slow-roll parameters ε and δ. One can define other sets of slow-roll parameters

$$\begin{aligned} \varepsilon_H &= \frac{2}{\kappa}\left(\frac{H_{,\varphi}}{H}\right)^2, & & & \varepsilon_V &= \frac{1}{2\kappa}\left(\frac{V_{,\varphi}}{V}\right)^2, \\ \delta_H &= \frac{2}{\kappa}\frac{H_{,\varphi\varphi}}{H}, & \text{and} & & \delta_V &= \frac{1}{\kappa}\frac{V_{,\varphi\varphi}}{V}, \end{aligned} \tag{2.54}$$

and one can show that these different sets of slow-roll parameters are not independent to each other but are related by

$$\varepsilon = \varepsilon_H = \varepsilon_V \quad \text{and} \quad \delta = \delta_H = \delta_V - \varepsilon_V. \tag{2.55}$$

These small parameters are thus useful to Taylor expand the potential V or the expansion rate H with the variable φ, in the equations of motion Eq. (2.45) and Eq. (2.46) and thus find perturbative series approximations to their solutions. For example, the number of e-folds is given by

$$N = \ln\left(\frac{a_\mathrm{f}}{a_\mathrm{i}}\right) = \int_{t_\mathrm{i}}^{t_\mathrm{f}} \frac{\mathrm{d}a}{\mathrm{d}t}\frac{1}{a(t)}\mathrm{d}t = \int_{t_\mathrm{i}}^{t_\mathrm{f}} H(t)\mathrm{d}t. \tag{2.56}$$

By making a change of variable $t(\varphi)$, it becomes

$$N = \int_{\varphi_\mathrm{i}}^{\varphi_\mathrm{f}} \frac{H(\varphi)}{\dot{\varphi}}\mathrm{d}\varphi = \int_{\varphi_\mathrm{i}}^{\varphi_\mathrm{f}} \sqrt{\frac{\kappa}{2\varepsilon}}\mathrm{d}\varphi. \tag{2.57}$$

Observations enable to directly measure these parameters in order to constrain the different models of inflation, i.e. potentials, without testing them one by one.

Finally, inflation needs to stop to let radiation dominates the energy content of the Early Universe. Inflation ends when the slow-roll conditions Eq. (2.53) are not fulfilled anymore, that is $\varepsilon \sim 1$ or $\delta \sim 1$. At the end of inflation, the field oscillates in the bottom of its potential. Thus, there is on average as much kinetic energy in the field as potential energy so that $\langle P \rangle = 0$ and the inflation behaves like pressureless matter or dust, contrary to the inflation phase where almost all the energy of the field was in the potential. As we do not observe any inflaton field today, it must decay into the particles of the SM of particle physics, so the inflaton must be coupled to these particles. This phase is called the 'reheating' phase because the energy of the inflaton is transferred to the particles making up the Early Universe.

2.3 Pre-inflationary physics

The inflationary paradigm does not solve the initial singularity issue already mentioned at the end of Chapter 1. However, high energies are reached during this early phase of the Universe and it is therefore relevant to connect it to very early Universe high energy models that cure this problem: it is expected as a phase following the Planck epoch.

We recall here that one big issue with the standard model of cosmology is that when extrapolated to the most ancient times of the Universe, and therefore to higher temperatures than those reached experimentally (for example, at the LHC), a space-time singularity is found. This singularity takes the form of several quantities going to infinity in a finite amount of time, like the energy densities ρ and consequently the Hubble parameter H, and comes from a singularity of the metric $g^{\mu\nu}$. Of course the singularity is not physical, meaning one enters a region of space-time which is beyond the regime of validity of GR. Indeed, the very early Universe is a region of space-time described by the strong field regime of GR, where the space-time curvature goes to infinity so that GR is necessarily needed (or a modification of it) to describe this epoch, as well as quantum mechanics, given the very high energies assumed to be involved. We stress that describing this epoch is a quite speculative exercise as neither GR nor the other interactions have been tested in these physical conditions. Because both quantum mechanics and GR are needed to make predictions about this epoch, it is usually expected that GR must be quantized at these energy densities. Anyway, a well-formulated description of quantum fields in curved space is done through a 'semi-classical' formulation of the usual quantum fields (those of the SM of particle physics) in curved space-time, as developed in Birrell & Davies (1984), where gravitation is treated classically, so that the resulting quantum theory of gravitation should recover this as a limiting case.

One of the ideas to solve the initial singularity, based on the intuition that gravitation must be quantised and that we need both gravitation and quantum mechanics to describe this epoch, is the unification of the gravitational interaction with the three other fundamental interactions (strong, weak and electromagnetic), quantizing it in the process. Such theories are for example Kaluza-Klein theories, whose approach is to have a geometrical formulation of the three interactions of the SM of particle physics, so as to mimic our geometrical understanding of gravitation. This is done through the introduction of additional compactified spatial dimensions that should be very small as compared to the three known ones today, but should have been of comparable size at the Planck epoch. However, the link to the gauge theories of the SM of particle physics has still to be done. Another similar idea, which also aims to unify the four fundamental interactions, is superstring theory which unifies them in a quantum field theory described by strings (one-dimensional objects). The gravitational interaction is modeled by a massless spin-2 field. The superstring theory also requires the introduction of extra spatial dimensions that are compactified. Similarly, the link to the classical description of gravitation remains to be done.

A somehow less ambitious approach consists in quantising GR only, without unifying it with the three other interactions. Attempts have been made in the context of cosmology leading to the quantum cosmology field, in order to solve the initial singularity. The idea is to use the canonical quantisation procedure to derive the wave function of the Universe describing both the space-time geometry and matter content of the Universe. The Wheeler-DeWitt quantisation was the first historical attempt but failed to remove the initial singularity. In Chapter 5 we will present a theory that attempts to quantize gravitation only: the Loop Quantum Gravity (LQG) theory, which essentially works by considering different canonical variables than the historically considered one in the Wheeler-DeWitt equation. We will then see in Chapter 6 that when applied to cosmology, and in particular to the early Universe, it gives rise to the field of Loop Quantum Cosmology (LQC) and this time succeeds in removing the initial space-time singularity, replacing

the big bang by a big bounce. We will see that this model naturally leads to an inflation phase, justifying the paradigm.

To finish, there actually exists alternatives to inflation (like ekpyrotic cosmology or bouncing universes). Indeed, one of the criticism about this paradigm is that it requires more fine-tuning than no-inflation (Penrose, 1989; Hollands & Wald, 2002), supported by the father of inflation Steinhardt himself in Ijjas et al. (2013), so that it is sometimes said that the inflationary paradigm is not well motivated. Also, some people think that a proper treatment of the Planck epoch (which is not doable currently with the most fundamental physical theories we have) where quantum gravity effects are expected would lead to the classical initial conditions of our Universe.

Chapter 3

Cosmological perturbations

As mentioned in the previous chapter with the structure formation problem, the Universe is not perfectly homogeneous and isotropic as it already contained some density fluctuations at the time of the decoupling of photons from the primordial plasma, which later led to the structures one observes today: stars, galaxies and galaxy clusters among others. They formed through the gravitational collapse of primordial matter density perturbations in the matter dominated era. However, the Universe was not far from being homogeneous and isotropic (until recombination) as can attest the smallness of the relative density fluctuations in the primordial Universe seen through the value of the relative temperature fluctuations with $\langle(\delta T/T)^2\rangle \sim 10^{-5}$, and still is statistically at the largest scales. In this chapter we will see that these inhomogeneities are in fact produced during inflation. It is expected that there are both density and gravity perturbations in this primordial phase so we are going to study them in this context. In practice, as the Einstein's equations couple metric to matter, deriving the equations governing their dynamics requires to perturb both the metric and the energy content of the Universe. After discussing their quantum origin, we will extend this idea to a primordial phase with two scalar fields and give the expressions of the primordial power spectra, and finally see how the measurement of the parameters of the power spectra gives access to the model of inflation describing the early Universe.

3.1 Dynamical equations for the perturbations

3.1.1 Perturbations of the metric: SVT decomposition

In order to give a more accurate model of our Universe, the fluctuations have been incorporated in the model as first order perturbations around a homogeneous and isotropic Universe: $g_{\mu\nu} = \bar{g}_{\mu\nu} + \delta g_{\mu\nu}$, where $\bar{g}_{\mu\nu}$ is the FLRW metric. This translates into a perturbed metric

$$\mathrm{d}s^2 = a^2(\eta)\left(-(1+2A)\mathrm{d}\eta^2 + 2B_i\mathrm{d}x^i\mathrm{d}\eta + (\gamma_{ij}+h_{ij})\mathrm{d}x^i\mathrm{d}x^j\right), \tag{3.1}$$

where the first order perturbations are thus modeled by a scalar perturbation A, a vector perturbation B^i (3 degrees of freedom) and a tensor perturbation h_{ij} (symmetric, so 6 degrees of freedom). Therefore, the perturbed part of the metric has a total of 10 degrees. However, the vector and tensor perturbation variables in Eq. (3.1) can be decomposed themselves following a scalar-vector-tensor (SVT) decomposition, where vectors are divergence-free and tensors are transverse and traceless. For instance, any vector field can be decomposed as the gradient of

a scalar B and a divergence free vector $\bar{B}_i$ (in the following bars will indicate divergence free quantities)

$$B^i = D^i B + \bar{B}^i \quad \text{with} \quad D^i \bar{B}_i = 0, \tag{3.2}$$

where D is the covariant derivative on the spatial hypersurfaces. Thus, the 3 vector degrees of freedom in Eq. (3.1) are decomposed into 1 scalar and 2 vector. Similarly, any symmetric rank-2 tensor can be decomposed like

$$h_{ij} = 2C\gamma_{ij} + 2D_i D_j E + 2D_{(i}\bar{E}_{j)} + 2\bar{E}_{ij} \quad \text{with} \quad D_i \bar{E}^{ij} = 0 \text{ and } \bar{E}^i_i = 0, \tag{3.3}$$

with the symmetrized tensor $D_{(i}\bar{E}_{j)} = (D_i\bar{E}_j + D_j\bar{E}_i)/2$, so that the 6 degrees of freedom are decomposed into 2 scalar (C, E), 2 vector ($\bar{E}_i$) and 2 tensor ($\bar{E}_{ij}$). Thus, the 10 degrees of freedom of the metric have finally been decomposed into 4 scalar (A, B, C, and E), 4 vector ($\bar{B}^i$ and $\bar{E}^i$) and 2 tensor ($\bar{E}^{ij}$). This decomposition is useful as the three kinds of perturbations are decoupled at first order.

3.1.2 Gauge fixing

Although the perturbation variables seem to have been introduced quite simply in the previous section, defining perturbations in GR is actually a difficult task. Indeed, the GR theory is used to model space-time, thus the scene on which other physical interactions take place Therefore, perturbations of physical quantities are referred to this background scene. But what about perturbing the background scene itself? To what these perturbations should be referred to? Actually, one cannot refer the perturbations of the metric to the unperturbed one describing homogeneous and isotropic Universe as GR is background independent. There is no preferred set of coordinates, hence no preferred metric in GR so that there is no hierarchy between the unperturbed metric and the perturbed one: they are equivalent and one cannot use a metric to refer to the other.

Therefore, a problem arising with the perturbations of the metric is that some of them can be seen as 'real' perturbations around a homogeneous and isotropic Universe modeled by the FLRW metric, while a change of coordinates of the FLRW metric itself like $x^i \to y^i = x^i - \xi^i(x^j, \eta)$ would lead to a metric which looks like the perturbed one Eq. (3.1)

$$\mathrm{d}s^2 = a^2(\eta)\left(-\mathrm{d}\eta^2 + 2\xi_i'\mathrm{d}y^i\mathrm{d}\eta + (\gamma_{ij} + 2D_{(i}\xi_{j)})\mathrm{d}y^i\mathrm{d}y^j\right), \tag{3.4}$$

so that one can identify B_i with ξ_i' and E_i with ξ_i and a $'$ means derivative with respect to the conformal time η. These two perturbation variables thus do not correspond to 'real' ones, in the sense of physical perturbations. One can instead build a set of so-called gauge invariant perturbations, that do not change under a change of coordinates like the previous one. These gauge invariant perturbations are obtained by making a change of coordinates of the perturbed metric Eq. (3.1) and by considering how the first order perturbations change. The gauge invariant variables are then built by making combinations of the first order perturbations that do not contain the unphysical perturbation degrees of freedom of ξ^μ. Doing so leads to the following gauge-invariant perturbations

$$\Psi, \quad \Phi, \quad \bar{\Phi}^i \quad \text{and} \quad \bar{E}^{ij}, \tag{3.5}$$

where

$$\begin{aligned} \Psi &\equiv -C - \mathcal{H}(B - E'), \\ \Phi &\equiv A + \mathcal{H}(B - E') + (B - E')', \\ \bar{\Phi}^i &\equiv \bar{E}^{i'} - \bar{B}^i, \end{aligned} \tag{3.6}$$

and $\mathcal{H} = a'/a = aH$ is the comoving Hubble factor. These are 'real' space-time perturbations in the sense that they cannot be removed by a change of coordinates. Notice that these perturbations are described by 6 degrees of freedom, rather than 10, as 4 degrees of freedom of the perturbations of the metric can be removed by a change of coordinates (ξ^μ). The tensor perturbations $\bar{E}^{ij}$ are the gravitational waves and Φ and Ψ are called the Bardeen potentials.

Fixing a gauge means choosing a system of coordinates. An appropriate gauge fixing is when the gauge invariant perturbations Eq. (3.6) coincide with the perturbation variables of the metric or energy content. A gauge that will be useful for us in the following (in Chapter 7 and the next section) is the flat gauge, in which the scalar part of the curvature perturbation of spatial hypersurfaces, $\delta^{(3)}R$, vanishes. Now, it can be shown that $\delta^{(3)}R = -4(\Delta + 3K)C/a^2$, so that this gauge is completely set by

$$C = 0, \quad E = 0, \quad \bar{E}_i = 0, \tag{3.7}$$

and the 6 remaining metric perturbations correspond to the following gauge invariant perturbations

$$A = \Psi + \Phi + \left(\frac{\Psi}{\mathcal{H}}\right)', \quad B = -\frac{\Psi}{\mathcal{H}}, \quad \bar{B}^i = \bar{\Phi}^i, \quad \text{and} \quad \bar{E}^{ij}. \tag{3.8}$$

Another noteworthy gauge, useful when dealing with only one scalar field, is the Newtonian or longitudinal gauge in which the expansion appears as isotropic. It is completely set by

$$B = 0, \quad E = 0, \quad \text{and} \quad \bar{B}^i = 0, \tag{3.9}$$

so that the 6 remaining metric perturbations

$$A = \Phi, \quad C = -\Psi, \quad \bar{E}^i = \int \bar{\phi}^i \mathrm{d}\eta, \quad \text{and} \quad \bar{E}^{ij}, \tag{3.10}$$

also correspond to gauge invariant perturbations. Here, Ψ is related to the scalar 3-curvature perturbation of spatial hypersurfaces and is the gravitational potential in the Poisson equation. Hence, contrary to the flat gauge, there is a non-vanishing scalar 3-curvature perturbation $\delta^{(3)}R$.

Other gauges we will encounter in this manuscript are the comoving gauge in which the fluid velocity vanishes or the gauge in which the scalar field is spatially uniform on constant time slices (spatial hypersurfaces).

3.1.3 Perturbations of matter

The linearisation of the metric implies linearisation of Einstein's tensor $G_{\mu\nu}$ and therefore of the energy-momentum tensor $T_{\mu\nu}$ by virtue of Einstein's equations. In the perfectly homogeneous and isotropic hypotheses, the energy-momentum tensor is that of a perfect fluid Eq. (1.15) and its perturbation leads to

$$\delta T_{\mu\nu} = (\delta\rho + \delta P)\bar{u}_\mu\bar{u}_\nu + \delta P\bar{g}_{\mu\nu} + 2(\rho + P)\bar{u}_{(\mu}\delta u_{\nu)} + P\delta g_{\mu\nu} + a^2 P\pi_{\mu\nu}, \tag{3.11}$$

where the notation with brackets means $\bar{u}_{(\mu}\delta u_{\nu)} = (\bar{u}_\mu\delta u_\nu + \bar{u}_\nu\delta u_\mu)/2$; $\delta\rho$ and δP are the density and pressure perturbations respectively, $u^\mu = \bar{u}^\mu + \delta u^\mu$ is the four-velocity of a comoving observer and $\pi_{\mu\nu}$ is the anisotropic pressure tensor, showing that the perturbed fluid is not perfect. However, we will later be interested in perturbations in the primordial Universe, so let us illustrate these perturbations with the energy content of the Universe being a scalar field interacting in a potential V, as this could model the energy content of the Universe in its primordial phase, during the inflation phase (cf. Chapters 2 and 6). The energy-momentum

tensor of such a scalar field is given by Eq. (2.40). Decomposing the scalar field into a spatially homogeneous part plus a first order perturbation, $\varphi = \bar{\varphi} + \delta\varphi$, the perturbation of the energy-momentum tensor is given by

$$\begin{aligned}\delta T_{\mu\nu} = \; & \partial_\mu\bar{\varphi}\partial_\nu\delta\varphi + \partial_\nu\bar{\varphi}\partial_\mu\delta\varphi - \delta g_{\mu\nu}\left(\frac{1}{2}\bar{g}^{\lambda\sigma}\partial_\lambda\bar{\varphi}\partial_\sigma\bar{\varphi} + V(\bar{\varphi})\right) \\ & - \bar{g}_{\mu\nu}\left(-\frac{\delta g^{\lambda\sigma}}{2}\partial_\lambda\bar{\varphi}\partial_\sigma\bar{\varphi} + \bar{g}^{\lambda\sigma}\partial_\lambda\bar{\varphi}\partial_\sigma\delta\varphi + \left.\frac{\partial V}{\partial\varphi}\right|_{\bar{\varphi}}\delta\varphi\right).\end{aligned} \tag{3.12}$$

Under a coordinate or gauge transformation ξ^μ, the perturbation of the scalar field transforms like

$$\delta\varphi \to \delta\varphi + \bar{\varphi}'\xi^0, \tag{3.13}$$

so, as for the perturbations of the metric, we need to build gauge invariant perturbations of the scalar field like for example

$$Q = \delta\varphi - C\frac{a\bar{\varphi}'}{a'}, \tag{3.14}$$

which is called the Mukhanov-Sasaki variable and, in the flat gauge where $C = 0$, gives the perturbation of the scalar field. Another gauge-invariant scalar field perturbation is

$$\chi = \delta\varphi + \bar{\varphi}'(B - E'), \tag{3.15}$$

which, in the Newtonian gauge where $B = E = 0$, corresponds to the scalar field perturbation. In the following, we will use this perturbation χ for the equations of motion of the scalar field perturbation. One notices that the two are related as follows

$$Q = \chi + \bar{\varphi}'\frac{\Psi}{\mathcal{H}}, \tag{3.16}$$

where $\mathcal{H} = a'/a$ is the comoving Hubble factor. We introduce one final gauge-invariant perturbation

$$\mathcal{R} = C - \mathcal{H}\frac{\delta\varphi}{\bar{\varphi}'} = -\frac{\mathcal{H}}{\bar{\varphi}'}Q, \tag{3.17}$$

which corresponds to the curvature perturbation in the comoving gauge.

3.1.4 Equations of motion

The equations of motion for the perturbations are given by the perturbed Einstein's equations

$$\delta G^\mu_\nu = \kappa\delta T^\mu_\nu, \tag{3.18}$$

which relate the perturbations of the metric with those of the energy content.

By considering the (00) and ($0i$) components of Eq. (3.18) as well as the trace of their spatial part (ij), one derives the equations of motion for the scalar modes that we will be mostly interested in

$$\begin{aligned}&\Psi = \Phi, \\ &(\Delta + 3K)\Psi - 3\mathcal{H}(\Psi' + \mathcal{H}\Phi) = \frac{\kappa}{2}\left(\bar{\varphi}'\chi' - \phi'^2\Phi + a^2\frac{\mathrm{d}V}{\mathrm{d}\bar{\varphi}}\chi\right), \\ &\Psi' + \mathcal{H}\Phi = \frac{\kappa}{2}\bar{\varphi}'\chi, \\ &\Psi'' + 2\mathcal{H}\Psi' - K\Psi + \mathcal{H}\Phi' + \left(2\mathcal{H}' + \mathcal{H}^2\right)\Phi + \frac{1}{3}\Delta(\Phi - \Psi) = \frac{\kappa}{2}\left(\bar{\varphi}'\chi' - \bar{\varphi}'^2\Phi - a^2\frac{\mathrm{d}V}{\mathrm{d}\varphi}\chi\right).\end{aligned} \tag{3.19}$$

There is no vector perturbation associated with the field, only a scalar perturbation $\delta\varphi$, so the equations of motion for the vector modes only involve those of the metric, namely

$$\begin{aligned}(\Delta + 2K)\,\bar{\Phi}_i &= 0,\\ \bar{\Phi}_i' + 2\mathcal{H}\bar{\Phi}_i &= 0.\end{aligned} \tag{3.20}$$

If the content of the Universe had vector perturbations, they would appear on the right-hand-side of these equations. The second of the above equations shows that the vector modes decrease like $\bar{\Phi}_i \propto a^{-2}$ so that one can neglect them at the end of the exponentially accelerated phase of inflation.

Similarly, the equations of motion for the tensor modes involve only the tensor modes of the metric

$$\bar{E}_{kl}'' + 2\mathcal{H}\bar{E}_{kl}' + (2K - \Delta)\bar{E}_{kl} = 0, \tag{3.21}$$

and, as for the vector modes, there would be a right-hand-side to this equation if there was anisotropic stress associated with the field. These tensor perturbations of the metric are nothing more than the gravitational waves of the Universe. The symmetric tensor $\bar{E}_{ij}$ being transverse and traceless, it only has two degrees of freedom. Going to Fourier space, it can thus be decomposed for each mode k^i like

$$\bar{E}_{ij}(k_k, \eta) = \sum_{\lambda=+,\times} \bar{E}_\lambda(k^k, \eta)\varepsilon_{ij}^\lambda(\hat{k}_k), \tag{3.22}$$

where ε_{ij}^λ are two polarisation tensors defined by

$$\varepsilon_{ij}^\lambda = \frac{e_i^1 e_j^1 - e_i^2 e_j^2}{\sqrt{2}}\delta_+^\lambda + \frac{e_i^1 e_j^2 + e_i^2 e_j^1}{\sqrt{2}}\delta_\times^\lambda, \tag{3.23}$$

which are traceless $\varepsilon_{ij}^\lambda \gamma^{ij} = 0$, transverse $\varepsilon_{ij}^\lambda k^i = 0$ and perpendicular to each other $\varepsilon_{ij}^\lambda \varepsilon_\mu^{ij} = 0$, and $\{e^1, e^2\}$ is an orthonormal basis of the subspace perpendicular to k^i. This decomposition will prove useful when quantising the two polarisation degrees of freedom of the tensor perturbations in the last section of this chapter.

One also derives the continuity or conservation equations for the perturbations of the fluid by the conservation of the perturbed energy-momentum tensor

$$\delta(\nabla_\mu T_\nu^\mu) = 0. \tag{3.24}$$

Since there is only a scalar perturbation of the scalar field, $\delta\varphi$, this only leads to the continuity equation for this perturbation

$$\chi'' + 2\mathcal{H}\chi' - \Delta\chi + a^2\frac{\mathrm{d}^2V}{\mathrm{d}\bar{\varphi}^2}\chi = 2(\bar{\varphi}'' + 2\mathcal{H}\bar{\varphi}')\Phi + \bar{\varphi}'(\Phi' + 3\Psi'), \tag{3.25}$$

i.e., written with the gauge invariant perturbation Q,

$$Q'' + 2\mathcal{H}Q' - \Delta Q + a^2\frac{\mathrm{d}^2V}{\mathrm{d}\bar{\varphi}^2}Q = \bar{\varphi}'\left(\Phi' + \Psi' + \left(\frac{\Psi}{\mathcal{H}}\right)'' - \frac{\Delta\Psi}{\mathcal{H}}\right), \tag{3.26}$$

which is actually the perturbed Klein-Gordon equation. As for Eq. (2.46), this equation is not independent from the three other equations for the scalar perturbations derived through the Einstein's equations Eq. (3.19). Actually, only two of the four equations for the scalar field perturbation are independent, so they can be cast into a single second order differential equation for the potential Φ. Indeed, using the Klein-Gordon equation Eq. (2.46) for $\bar{\varphi}$, we get

$$\Phi'' + 2\left(\mathcal{H} - \frac{\bar{\varphi}''}{\bar{\varphi}'}\right)\Phi' - \left(\Delta - 2\left(\mathcal{H}' - \mathcal{H}\frac{\bar{\varphi}''}{\bar{\varphi}'} - 2K\right)\right)\Phi = 0\ . \tag{3.27}$$

3.2 Quantum origin

In addition to solving the horizon, flatness and relic problems, the inflationnary paradigm also provides a framework to explain the origin of the small primordial inhomogeneities one can observe in the CMB. We have seen that the energy content of the Universe during inflation is mainly given by a field called the inflaton field. However, the origin of the primordial inhomogeneities cannot be classical fluctuations of the quantum field because the duration of inflation required (around $N \sim 60$ e-folds) would involve energy density fluctuations greater than the energy density of the background, breaking the perturbative approach. This is due to the fact that classical fluctuations of the scalar field are bosons and evolve as a^{-4}, see section 2.3.3 of Grain (2014). This is not the case for vacuum quantum fluctuations whose energy density remain constant during inflation, solving the problem. Furthermore, the vacuum quantum fluctuations of the inflaton field have the right statistics to explain the ones of the fluctuations of the CMB, that is, gaussian statistics (Maldacena, 2003; Planck Collaboration et al., 2016, 2018d) and lead to a scale-invariant primordial power spectrum, as is required from observations. Thus, we need the equations of motion for the quantised perturbations rather than the equations of motion for the classical perturbations as given in the previous section, so one must quantise Eq. (3.21) and Eq. (3.26). Here, we will illustrate the quantisation of perturbations with the tensor ones and postpone the procedure for the scalar perturbation(s) to the next section when dealing with two primordial fields.

Now, rather than deriving the equations of motion for the perturbations by linearising Einstein's equations as we have done in the previous section, it is more convenient to use another approach in order to see which perturbation variables should be quantised. This other approach, developed for example in Sasaki (1986), starts directly from the action of the perturbed homogeneous and isotropic Universe written up to second order and then derive the equations of motion for the first order perturbations (as when differentiating the Lagrangian written up to quadratic order into linear perturbations, one order is lost).

The second order action for the tensor perturbations is given by

$$\delta^{(2)}S = \frac{1}{2}\sum_{\lambda}\int \mathrm{d}\eta\mathrm{d}^3x\left(v'^2_{\lambda\mathrm{T}} - \delta^{ab}\partial_a v_{\lambda\mathrm{T}}\partial_b v_{\lambda\mathrm{T}} + \frac{a''}{a}v^2_{\lambda\mathrm{T}}\right), \tag{3.28}$$

where λ stands for the two polarisations of gravitational waves and $v_{\lambda\mathrm{T}}$ is a gauge invariant perturbation related to the tensor perturbations of the metric by

$$v_{\lambda\mathrm{T}} = \frac{a\bar{E}_\lambda}{\sqrt{8\pi\mathrm{G}}}, \tag{3.29}$$

where $\bar{E}_\lambda$ has been defined in Eq. (3.22). One derives the following equations of motion for the new perturbation variable from Eq. (3.28)

$$v''_{\lambda\mathrm{T}} - \left(\Delta + \frac{a''}{a}\right)v_{\lambda\mathrm{T}} = 0. \tag{3.30}$$

This is the variable $v_{\lambda\mathrm{T}}$ that will be quantised. The perturbation variable becomes a quantum field by writing

$$\hat{v}_{\lambda\mathrm{T}}(\tau,\boldsymbol{x}) = \frac{1}{(2\pi)^{3/2}}\int \mathrm{d}^3k\left(\hat{a}_{\boldsymbol{k}}v_{\lambda\mathrm{T},k}(\tau)\mathrm{e}^{i\boldsymbol{k}\cdot\boldsymbol{x}} + \hat{a}^\dagger_{\boldsymbol{k}}v^*_{\lambda\mathrm{T},k}(\tau)\mathrm{e}^{-i\boldsymbol{k}\cdot\boldsymbol{x}}\right), \tag{3.31}$$

where $\hat{a}_{\boldsymbol{k}}$ and $\hat{a}^\dagger_{\boldsymbol{k}}$ are the usual annihilation and creation operators respectively, with commutators

$$\left[\hat{a}_{\boldsymbol{k}}, \hat{a}^\dagger_{\boldsymbol{k}'}\right] = \delta^3(\boldsymbol{k}-\boldsymbol{k}') \quad \text{and} \quad [\hat{a}_{\boldsymbol{k}}, \hat{a}_{\boldsymbol{k}'}] = \left[\hat{a}^\dagger_{\boldsymbol{k}}, \hat{a}^\dagger_{\boldsymbol{k}'}\right] = 0. \tag{3.32}$$

Thus Eq. (3.30) can be rewritten in Fourier space

$$v''_{\lambda\mathrm{T}} + \left(k^2 - \frac{a''}{a}\right) v_{\lambda\mathrm{T}} = 0. \tag{3.33}$$

In order to get the primordial quantum fluctuations, the v_k in Eq. (3.33) are the functions to be solved for, and in particular one needs to find the initial conditions for these perturbations. The integrand of the second order action Eq. (3.48) defines a Lagrangian density that we will denote by $\mathcal{L}$, thus the conjugate momenta of $v_{\lambda\mathrm{T}}$ is

$$\pi_{\lambda\mathrm{T}} = \frac{\delta\mathcal{L}}{\delta v'_{\lambda\mathrm{T}}} = v'_{\lambda\mathrm{T}}. \tag{3.34}$$

Thus, the mode functions $v_k(\tau)$ must be normalised by the Klein-Gordon product or Wronskian condition

$$v_k(v_k^*)' - v_k^* v'_k = i, \tag{3.35}$$

so that $[\hat{v}(\boldsymbol{x},\eta), \hat{\pi}(\boldsymbol{y},\eta)] = i\delta^{(3)}(\boldsymbol{x}-\boldsymbol{y})$: this normalisation helps to determine the initial conditions for the perturbations, as we will now see.

The usual initial condition taken for the perturbations is the Bunch-Davies vacuum. This vacuum is used for modes that are initially smaller than the comoving Hubble radius, which is actually the case for all today's observable modes at the beginning of inflation, as the comoving Hubble radius decreased since then. As these modes are smaller than the comoving Hubble radius, they do not feel the curvature of the Universe $k^2 \gg a''/a$ and behave like in Minkowski space, so their vacuum tend to the Minkowski vacuum, that is

$$v_k(\tau) \to \frac{1}{\sqrt{k}}\exp(-ik\tau) \quad \text{when} \quad \left(\frac{k}{aH}\right) \to \infty. \tag{3.36}$$

The equation of motion Eq. (3.33) is a second order differential equation, so has two independent solutions. Therefore, only the one that coincides with the Bunch-Davies vacuum at the beginning of inflation remains with the constant of integration is appropriately taken and the solution indeed satisfies the Klein-Gordon product Eq. (3.35). Another way to have done this would have been to choose the solution that propagates in the positive time direction (remembering that to get the full mode functions one multiplies v_k by $\exp(i\boldsymbol{k}\cdot\boldsymbol{x})$, see Eq. (3.31)), so that only one of the two independent solution is kept and the constant of integration is then determined thanks to the Wronskian condition Eq. (3.35).

Finally, once the quantum perturbations have been computed, one can derive the power spectrum for these fluctuations. It is given by

$$\mathcal{P}_{v_\mathrm{T}} = \frac{k^3}{2\pi^2}\sum_\lambda |v_{\lambda\mathrm{T},k}|^2, \tag{3.37}$$

where we have summed over the two possible polarisations λ. This is all the statistics one needs to characterise the primordial fluctuations as they are gaussian because of being vacuum quantum fluctuations of the field. Moreover, this involves that $\langle v_k\rangle = 0$, so the power spectrum is really all the statistics one needs to describe the primordial fluctuations.

3.3 Perturbations with two scalar fields

3.3.1 Adiabatic and isocurvature decomposition

Although the single field model of inflation is the most favored by observations (see e.g. Planck Collaboration et al., 2016, 2018d), there are reasons to introduce more fields in early phases of

the Universe, especially in a pre-inflationnary context, as we will see in Chapter 7. Here let us consider consider two scalar fields φ - the inflaton field - and ϕ as being the energy content of the Early Universe, in the context of inflation. These two fields have their own Klein-Gordon equation Eq. (2.46), where now $V(\varphi, \phi)$ is the total potential of this system that could possibly couple the two fields. In the case where the two fields are uncoupled, the potential is just the sum of the potentials of the two fields $V(\varphi, \phi) = V_1(\varphi) + V_2(\phi)$. It is convenient to decompose the two fields into a part σ tangent to the trajectory in field space, i.e. along the field velocity $(\dot{\varphi}, \dot{\phi})$, and a part s perpendicular to this trajectory, following the idea developed in Gordon et al. (2001) for the perturbations generated by multiple scalar fields inflation in an interacting potential. This is shown in Fig. 3.1. Formally, one has

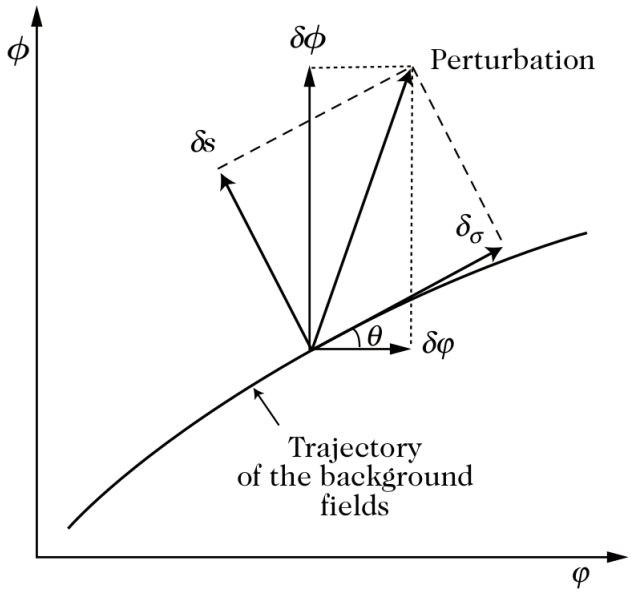

Figure 3.1: Trajectory of the background fields φ and ϕ in field space. These two fields can be decomposed into a field along the field velocity in field space, written σ and called the adiabatic component, and a field perpendicular to it, s, called the isocurvature component. It therefore leads to adiabatic and isocurvature perturbations $\delta\sigma$ and δs respectively, which are a rotation in field space of the field perturbations $\delta\varphi$ and $\delta\phi$ by an angle θ corresponding to the bending of the trajectory of the background fields. Adapted from Peter & Uzan (2009).

$$\begin{pmatrix} \dot{\sigma} \\ \dot{s} \end{pmatrix} = M(\theta) \begin{pmatrix} \dot{\varphi} \\ \dot{\phi} \end{pmatrix} \quad \text{with} \quad M(\theta) = \begin{pmatrix} \cos\theta & \sin\theta \\ -\sin\theta & \cos\theta \end{pmatrix}, \tag{3.38}$$

and the angle θ is defined by

$$\cos\theta = \frac{\dot{\varphi}}{\sqrt{\dot{\varphi}^2 + \dot{\phi}^2}} \quad \text{and} \quad \sin\theta = \frac{\dot{\phi}}{\sqrt{\dot{\varphi}^2 + \dot{\phi}^2}}\,. \tag{3.39}$$

This allows a rewriting of the equations of motion for the fields Eq. (2.46) with these new fields

$$s = \text{cst} \quad \text{and} \quad \ddot{\sigma} + 3H\dot{\sigma} + U_{,\sigma} = 0, \tag{3.40}$$

with

$$\begin{pmatrix} U_{,\sigma} \\ U_{,s} \end{pmatrix} = M(\theta) \begin{pmatrix} V_{,\varphi} \\ V_{,\phi} \end{pmatrix}. \tag{3.41}$$

This rewriting is useful to introduce the σ and s fields which are respectively the adiabatic and isocurvature components of the system of two fields (φ, ϕ). They will lead to adiabatic and isocurvature perturbations in the primordial Universe. These two fields are interesting to study perturbations. Indeed, one can intuitively understand that there will be two kinds of perturbations: as the two fields have their own scalar perturbations, resulting in energy density fluctuations, these fluctuations can be either positive (corresponding to an overdensity) or negative (corresponding to an underdense region). Therefore, the two fluctuations can either add to give a net energy density fluctuation, which corresponds to the adiabatic perturbation, or compensate each other so that there is no energy density fluctuation: this corresponds to the isocurvature perturbation perpendicular to the trajectory in fields space, and explains its name, as no curvature perturbation can be produced if there is no energy density fluctuation. Thus, $\delta\sigma$ is also called the curvature perturbation, while δs is also known as the entropy perturbation, because the field s is conserved, which is linked to the entropy conservation.

3.3.2 Dynamical equations

Then, we are interested in the perturbations of these two scalar fields $\delta\varphi$ and $\delta\phi$. The equations of motion for the perturbations are given in Eq. (3.19) for one scalar field. One can derive them adding another scalar field. Following the same steps we get

$$\begin{aligned}
&\dot{\Phi} + \mathcal{H}\Phi = \frac{\kappa}{2}(\dot{\varphi}\chi_\varphi + \dot{\phi}\chi_\phi), \\
&3\dot{\Phi} + (3H^2 + \dot{H})\Phi - \frac{\Delta}{a^2}\Phi = -\frac{\kappa}{2}\left(V_{,\varphi}\chi_\varphi + \dot{\varphi}\chi_\varphi + V_{,\phi}\chi_\phi + \dot{\phi}\chi_\phi\right), \\
&\ddot{\chi}_\varphi + 3H\dot{\chi}_\varphi - \frac{\Delta}{a^2}\chi_\varphi + V_{,\varphi\phi}\chi_\phi = -2V_{,\varphi}\Phi + 4\dot{\varphi}\dot{\Phi}, \\
&\ddot{\chi}_\phi + 3H\dot{\chi}_\phi - \frac{\Delta}{a^2}\chi_\phi + V_{,\phi\varphi}\chi_\varphi = -2V_{,\phi}\Phi + 4\dot{\phi}\dot{\Phi},
\end{aligned} \tag{3.42}$$

using the fact that $\Psi = \Phi$. We want to translate these equations of motion for the gauge invariant perturbations χ_φ and χ_ϕ into equations of motion for the adiabatic and isocurvature perturbations $\delta\sigma$ and δs. As $\dot{s} = 0$, the isocurvature perturbation is already gauge-invariant since

$$\chi_s = Q_s = \delta s, \tag{3.43}$$

but not $\delta\sigma$

$$Q_\sigma = \chi_\sigma + \dot{\sigma}\frac{\Phi}{H}. \tag{3.44}$$

A bit of calculations leads to the coupled system of equations for the adiabatic and isocurvature perturbations

$$\begin{aligned}
&\ddot{Q}_\sigma + 3H\dot{Q}_\sigma + \left(-\frac{\Delta}{a^2} - \dot{\theta}^2 + U_{,\sigma\sigma} - \frac{\kappa}{a^3}\left(\frac{a^3\dot{\sigma}^2}{H}\right)\right)Q_\sigma = 2\dot{\theta}\delta s - 2\left(\frac{U_{,\sigma}}{\dot{\sigma}} + \frac{\dot{H}}{H}\right)\dot{\theta}\delta s, \\
&\ddot{\delta s} + 3H\dot{\delta s} + \left(-\frac{\Delta}{a^2} - \dot{\theta}^2 + U_{,ss}\right)\delta s = -\frac{\dot{\theta}}{\dot{\sigma}}\frac{4\delta}{\kappa a^2}\Phi.
\end{aligned} \tag{3.45}$$

Finally, note that the curvature perturbation Eq. (3.17) written for one field generalises with two fields to

$$\mathcal{R} = C - \frac{H}{\dot{\varphi}^2 + \dot{\phi}^2}(\dot{\varphi}\delta\varphi + \dot{\phi}\delta\phi) = C - \frac{H}{\dot{\sigma}}\delta\sigma = -\frac{H}{\dot{\sigma}}Q_\sigma, \tag{3.46}$$

as $\dot{\varphi}\delta\varphi + \dot{\phi}\delta\phi = \dot{\sigma}\delta\sigma$ and $\dot{\sigma}^2 = \dot{\varphi}^2 + \dot{\phi}^2$ from Eq. (3.38). One sees directly in Eq. (3.46) that the adiabatic perturbations feed the curvature perturbations. This is the reason why the adiabatic perturbations are also often called the curvature perturbations. On the contrary, the isocurvature perturbations δs have no influence on $\mathcal{R}$, hence their name.

3.3.3 Quantum initial conditions

In order to see which perturbation variables should be quantised, we will proceed similarly to Section 3.2, as in the work of Langlois & Renaux-Petel (2008), to derive the equations of motion for the perturbations. Likewise, they start directly from the action of the perturbed homogeneous and isotropic Universe coupled to multiple fields written up to second order and then derive the equations of motion for the first order perturbations. In the following we will use the notation ϕ^I to label the fields, e.g. $\phi^1 = \varphi$, $\phi^2 = \phi$ in the two fields case. Note that they consider in full generality non-standard kinetic terms $T = -G_{IJ}\nabla_\mu\phi^I\nabla_\nu\phi^J/2$, where G_{IJ} is a metric in field space and P is an arbitrary function of T and of the fields ϕ^I, but here we will not discuss such extensions.

In the two fields case, introducing the normalised variables with conformal time

$$v_\sigma = aQ_\sigma \quad \text{and} \quad v_s = aQ_s, \tag{3.47}$$

and going to Fourier space using the wavenumber k, the second order action for the adiabatic and isocurvature perturbations is rewritten in terms of these variables

$$\delta^{(2)}S = \frac{1}{2}\int \mathrm{d}\tau\mathrm{d}^3k\left(v_\sigma'^2 + v_s'^2 - 2\xi v_\sigma' v_s - k^2c_s^2v_\sigma^2 - k^2v_s^2 + \Omega_{\sigma\sigma}v_\sigma^2 + \Omega_{ss}v_s^2 + 2\Omega_{\sigma s}v_\sigma v_s\right). \tag{3.48}$$

The functions ξ represents the coupling between the two adiabatic and isocurvature perturbations as it multiplies a term mixing them, and consequently appears in the function $\Omega_{\sigma s}$, while the functions $\Omega_{\sigma\sigma}$ and Ω_{ss} can be interpreted as time dependent effective mass terms for the adiabatic and isocurvature perturbations respectively. These functions are given by

$$\xi = a\Xi, \quad \Omega_{\sigma\sigma} = \frac{z''}{z}, \quad \Omega_{s\sigma} = \frac{z'}{z}\xi, \quad \Omega_{ss} = \frac{a''}{a} - a^2\mu_s^2, \tag{3.49}$$

and

$$\Xi = \frac{2P_{,s}}{\sqrt{2T}}, \quad z = \frac{a\sqrt{2T}}{H}, \quad \text{and} \quad \mu_s^2 = -P_{,ss} - \frac{P_{,s}^2}{2T}, \tag{3.50}$$

and, in the model we are interested in here, T is the standard kinetic energy

$$T = (\dot{\varphi}^2 + \dot{\phi}^2)/2, \tag{3.51}$$

P is the standard pressure or the Lagrangian of the model

$$P = T - V, \tag{3.52}$$

and we use the notation

$$P_{,n} \equiv e_n^I P_{,I}, \tag{3.53}$$

where $P_{,I}$ is the partial derivative of P with respect to the field ϕ^I, and $\{e_n^I\}$ is an orthonormal basis in field space, the index n going from 1 to the total number of fields. With two fields this basis is constructed as follows. The first vector is the 'adiabatic' unit vector

$$e_\sigma^I = \frac{\dot{\phi}^I}{\sqrt{2T}} \Leftrightarrow \begin{pmatrix} e_\sigma^1 \\ e_\sigma^2 \end{pmatrix} = \frac{1}{\sqrt{\dot{\varphi}(t)^2 + \dot{\phi}(t)^2}} \begin{pmatrix} \dot{\varphi}(t) \\ \dot{\phi}(t) \end{pmatrix}, \tag{3.54}$$

so that the background velocity $\dot{\phi}^I$ corresponds to the instantaneous adiabatic direction in field space. The entropy perturbations are orthogonal to the scalar field velocity so that the vector orthogonal to the adiabatic direction e_σ^I gives the entropy direction in field space. The second element e_2^I of the basis is defined as the unit vector pointing along the projection on the entropy subspace of the field acceleration $\mathcal{D}_t\dot{\phi}^I$. Here, we simply use the fact that the basis $\{e_\sigma^I, e_s^I\}$ is orthonormal so that the scalar product between the two vectors is zero, and unitarity together with right-handedness of the field basis completely set the components of e_s^I:

$$\begin{pmatrix} e_s^1 \\ e_s^2 \end{pmatrix} = \frac{1}{\sqrt{\dot{\varphi}(t)^2 + \dot{\phi}(t)^2}} \begin{pmatrix} -\dot{\phi}(t) \\ \dot{\varphi}(t) \end{pmatrix}. \tag{3.55}$$

Then, one can compute the explicit expressions of the background functions appearing in Eq. (3.48), given the shape of the potential $V(\varphi, \phi)$ as here, $P = (\dot{\varphi}(t)^2 + \dot{\phi}(t)^2)/2 - V(\varphi, \phi)$. Finally, note that from the above one sees that v_σ is simply related to the curvature perturbation (3.46) as

$$v_\sigma = -z\mathcal{R}. \tag{3.56}$$

From the action Eq. (3.48), one derives the following equations of motion for the new perturbation variables

$$\begin{aligned} &v_\sigma'' - \xi v_s' + \left(k^2 - \frac{z''}{z}\right) v_\sigma - \frac{(z\xi)'}{z} v_s = 0, \\ &v_s'' + \xi v_\sigma' + \left(k^2 - \frac{a''}{a} + a^2\mu_s^2\right) v_s - \frac{z'}{z}\xi v_\sigma = 0. \end{aligned} \tag{3.57}$$

These are the variables v_σ and v_s that will be quantised. The perturbation variables become quantum fields as in Eq. (3.31) and in order to get the primordial quantum fluctuations, the v_k in the system of coupled equations Eq. (3.57) are the functions to be solved for, and in particular one needs to find the initial conditions for these perturbations.

Here, we will consider as an example the resolution in the case where the coupling between the adiabatic and entropy perturbations vanishes ($\xi = 0$), to simplify. Indeed, in that case one can analyse the two kinds of perturbations independently, as is done in Langlois & Renaux-Petel (2008). We recall that the Lagrangian density $\mathcal{L}$ is the integrand of the second order action Eq. (3.48). In the case $\xi = 0$ the conjugate momenta of v_σ and v_s are then respectively

$$\pi_\sigma = \frac{\delta\mathcal{L}}{\delta v_\sigma'} = v_\sigma' \quad \text{and} \quad \pi_s = \frac{\delta\mathcal{L}}{\delta v_s'} = v_s', \tag{3.58}$$

and thus the mode functions $v_k(\tau)$ must be normalised by the Klein-Gordon product or Wronskian condition Eq. (3.35). When $\xi = 0$, the equations of motion for the perturbations Eq. (3.57) are decoupled

$$\begin{aligned} &v_{\sigma,k}'' + \left(k^2 - \frac{z''}{z}\right) v_{\sigma,k} = 0, \\ &v_{s,k}'' + \left(k^2 - \frac{a''}{a} + a^2\mu_s^2\right) v_{s,k} = 0. \end{aligned} \tag{3.59}$$

In the slow-roll limit we have the approximation $z''/z \approx 2/\tau^2$. Therefore, one can solve analytically for the adiabatic perturbation v_σ

$$v_{\sigma,k}(\tau) \approx -\frac{1}{\sqrt{2\pi k}}\left(C_1 \mathrm{e}^{ik\tau}\left(1+\frac{i}{k\tau}\right)+C_2\mathrm{e}^{-ik\tau}\left(1-\frac{i}{k\tau}\right)\right), \tag{3.60}$$

where C_1 and C_2 are two constants to be determined. We have just solved for the evolution of one of the primordial quantum fluctuation during inflation, but one is left with finding its initial condition. By taking the Bunch-Davies vacuum as initial condition at the beginning of inflation like in Section 3.2, only the second term in the solution for v_σ remains. The constant C_2 is appropriately taken and the solution indeed satisfies the Klein-Gordon product Eq. (3.35). As explained in Section 3.2, another way to have done this would have been to choose the solution that propagates in the positive time direction, so that only the second term in the solution for v_σ is kept and the constant C_2 is then determined thanks to the Wronskian condition Eq. (3.35). Finally

$$v_{\sigma,k}(\tau) \approx \frac{1}{\sqrt{2k}}\mathrm{e}^{-ik\tau}\left(1-\frac{i}{k\tau}\right). \tag{3.61}$$

Similarly, one can show that the approximate solution for v_s is

$$v_{s,k}(\tau) = \frac{\sqrt{\pi}}{2}\mathrm{e}^{i(\nu_s+1/2)\pi/2}\sqrt{-\tau}H^{(1)}_{\nu_s}(-k\tau), \tag{3.62}$$

where $H^{(1)}_\nu$ is the Hankel function of the first kind of order ν; the order ν_s is given by Eq. (102) in Langlois & Renaux-Petel (2008) and is a function of the Hubble factor and derivatives of the pressure P.

Finally, once the quantum perturbations have been computed, one can derive the power spectra for these fluctuations. They are given by

$$\mathcal{P}_{Q_\sigma} = \frac{k^3}{2\pi^2}\frac{|v_{\sigma,k}|^2}{a^2} \quad \text{and} \quad \mathcal{P}_{Q_s} = \frac{k^3}{2\pi^2}\frac{|v_{s,k}|^2}{a^2}. \tag{3.63}$$

In the case where the two equations are coupled Eq. (3.57), there would also be a cross power spectrum between the adiabatic and isocurvature perturbations $\mathcal{P}_{Q_sQ_\sigma}$. One final remark: in the single scalar field case, there would only be adiabatic perturbations as one can no longer compensate the perturbations of a field with another one to give a null net energy density fluctuation leading to isocurvature perturbations. Therefore, there would only be the adiabatic power spectrum, which has exactly the same expression as here.

3.4 Primordial power spectra: phenomenological parameterisation

The power spectra give all the statistics describing perturbations and they can be observed by measuring the anisotropies of the CMB or the large-scale structures statistics. Indeed, the statistical properties of the primordial inhomogeneities source the CMB anisotropies and later the large-scale structures. In order to compare the above predictions with CMB observations for example, one would need to propagate these power spectra up to the CMB to translate them in angular power spectra for the anisotropies in temperature and polarisation. This is done through the radiative transfer of the primordial anisotropies, i.e. by solving the Boltzmann equation in the expanding primordial Universe, as is done for example in Zaldarriaga & Seljak (1997). The

angular power spectra of primary anisotropies are then given by integrating over all modes k the product of the primordial power spectra of the fluctuations, which gives the initial amplitude, with the solutions of the Boltzmann equation.

In practice, in order to test the various existing models of inflation, a phenomenological parameterisation in power law is used for the primordial power spectra

$$\mathcal{P}_{\rm S}(k) = \mathcal{A}_{\rm S} \times \left(\frac{k}{k_0}\right)^{{\rm n_S}-1} \quad \text{and} \quad \mathcal{P}_{\rm T}(k) = r \times \mathcal{A}_{\rm S} \times \left(\frac{k}{k_0}\right)^{\rm n_T}, \tag{3.64}$$

where k_0 is a pivot scale so that the parameters are defined by

$$\mathcal{A}_{\rm S} = \mathcal{P}_{\rm S}(k_0), \quad r = \frac{\mathcal{P}_{\rm T}(k_0)}{\mathcal{P}_{\rm S}(k_0)}, \quad {\rm n_S} = 1 + \left.\frac{{\rm d}\ln\mathcal{P}_{\rm S}}{{\rm d}\ln(k)}\right|_{k=k_0}, \quad \text{and} \quad {\rm n_T} = \left.\frac{{\rm d}\ln\mathcal{P}_{\rm T}}{{\rm d}\ln(k)}\right|_{k=k_0}, \tag{3.65}$$

$\mathcal{A}_{\rm S}$ is called the amplitude of the scalar power spectrum and the amplitude of the tensor power spectrum is defined with respect to it by the tensor-to-scalar ratio r, $\rm n_S$ and $\rm n_T$ are the spectral indices of the scalar and tensor power spectra respectively. Using the slow-roll formalism, one can relate these phenomenological parameters to the slow-roll parameters, which at leading order gives (see e.g. Sections 7.5 and 7.7 of Liddle & Lyth (2000))

$$\mathcal{A}_{\rm S} = \frac{1}{\pi\epsilon_H}\left(\frac{H_\star}{M_{\rm Pl}}\right)^2, \quad r = 16\epsilon_H, \quad {\rm n_S} = 1 - 4\epsilon_H, \quad \text{and} \quad {\rm n_T} = -2\epsilon_H, \tag{3.66}$$

themselves related to the derivatives of the potential of inflation. Hence, the measurements of the phenomenological parameters Eq. (3.65) allows the reconstruction of the potential of inflation and therefore to discriminate between the possible models.

The latest observational constraints on the phenomenological parameters in Eq. (3.65) given by the Planck collaboration in Planck Collaboration et al. (2018d) are:

$$\ln(10^{10}\mathcal{A}_{\rm S}) = 3.044 \pm 0.014, \; r_{0.002} < 0.10, \; {\rm n_S} = 0.9649 \pm 0.0042, \; \text{and } {\rm n_T} = -\frac{r}{8} \text{ is assumed}, \tag{3.67}$$

for a pivot scale $k_0 = 0.05$ Mpc^{-1}, except for r where $k_0 = 0.002$ Mpc^{-1}. The reader acquainted with isocurvature perturbations can find upper bounds on this mode for different models in Section 9, Table 14 of Planck Collaboration et al. (2018d).

Chapter 4

The CMB: the observable of the early and late-time inhomogeneities

The CMB is a key observable for our understanding of the Universe. The generation of the relic radiation in two steps led to a black body primordial light with a very uniform temperature measured today to be $T_0 = 2.725 \pm 0.001$K. However, we argued in the previous chapter that there were perturbations to our homogeneous and isotropic model of the Universe. This translates into small relative temperature fluctuations of the order of $\Delta T/T_0 \sim 10^{-5}$. The anisotropies in temperature also induce polarisation anisotropies of the primordial light. We distinguish between two kinds of anisotropies: those stemming from inhomogeneities present at the epoch at which the CMB was generated (primary anisotropies) from those imprinted later, as photons traveled the structured Universe before reaching us (secondary anisotropies). Both types of anisotropies can be seen as a tracer of the different cosmic epochs: the primary trace the primordial physics while the secondary the large-scale structures of the Universe. These anisotropies are observed on the celestial sphere and their analysis requires to treat them statistically by predicting their angular power spectra and higher order statistics. Finally, estimators of these statistics are needed to compare the theoretical predictions to observations.

4.1 Release of the relic radiation

4.1.1 Recombination

In Chapter 2, we have explained that as the Universe expands from the hot dense state at its origin (the Big Bang), it also cools down. The equivalence between temperature and energy $E = 3k_{\rm B}T/2$ valid for relativistic particles, allows to translate the cooling down of the photons (their temperature defining the temperature of the Universe) into a decrease in their energy. Thus, we have seen in Section 2.1.2, that when their energy reaches ~ 0.4 eV, they can no longer break the binding of electrons with nuclei so that the latter combine to form neutral atoms: this moment is called the 'recombination'. The main reaction to consider to study the dynamics of recombination is the photoionisation reaction

$$p + e \longleftrightarrow \mathrm{H} + \gamma, \tag{4.1}$$

as the most abundant nuclei are the hydrogen ones p. This reaction keeps the primordial plasma in thermal equilibrium. One defines the ionisation fraction

$$X_e = \frac{n_e}{n_p + n_{\rm H}} = \frac{n_e}{n_{\rm b}}, \tag{4.2}$$

where the denominator $n_{\rm b} = n_p + n_{\rm H}$ is the total number of hydrogen nuclei, hence the name 'ionisation fraction'. By doing a bit of out-of-equilibrium thermodynamics, one can find an equation on X_e (Kolb & Turner, 1990) and its solution is plotted in Fig. 4.1 as a function of the energy of the Universe. One sees that it drops sharply below the energy value of ~ 0.4 eV so that

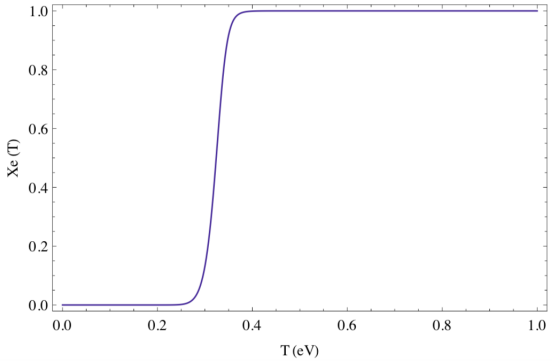

Figure 4.1: The ionisation fraction X_e as a function of temperature T expressed in units of energy (eV).

once the energy of the Universe falls below ~ 0.4 eV, all nuclei soon recombine into atoms. Thus, recombination is not clearly defined but is actually identified by a threshold: $X_e = 0.5,\ 0.1,\ 0.01$. Depending on the threshold chosen, one will find different values for the temperature of the Universe at recombination. If one defines recombination as the time when there are only 10% of free electrons left in the Universe ($X_e = 0.1$), one finds $T_{\rm rec} = 3440$ K. However, this temperature does not yet correspond to the temperature of the CMB when it was emitted. To get it, one has to consider the decoupling of the photons from the thermal bath, which is different from the stopping of reaction (4.1).

4.1.2 Decoupling

Actually, in addition for photons to interact with neutral hydrogen, they also scatter off free electrons through the Thomson scattering process so that they are tightly coupled to them. However, when nuclei combine with electrons to form neutral atoms, there are not enough free electrons left for the Thomson scattering process to take place. Indeed, the interaction rate of this process is given by

$$\Gamma_{\rm T} = n_e \sigma_{\rm T}, \tag{4.3}$$

where $\sigma_{\rm T} = 6.65 \times 10^{-25}$ cm^2 is the Thomson scattering cross-section, so that as $n_e(T)$ drops at recombination, so does the interaction rate. Therefore, the decoupling of photons occurs soon after recombination. Actually, decoupling is defined when $\Gamma_{\rm T} = H$, the Hubble parameter. As both n_e and H depend on temperature

$$n_e(T) = X_e(T) n_{\rm b}(T) \text{ with } n_{\rm b}(T) = \eta n_\gamma(T) = \eta 2 \frac{\zeta(3)}{\pi^2} T^3 \text{ and } H = H_0 \sqrt{\Omega_{\rm m}^0} \left(\frac{T}{T_0}\right)^{3/2}, \tag{4.4}$$

where we have used Eq. (2.1) to determine n_γ and the fact that the Universe is dominated by matter to derive H, one can derive the temperature at which decoupling takes place. One finds $T_{\rm dec} = 2720$ K. This temperature corresponds to the temperature of the Universe when photons scatter off electrons for the last time. These photons then make up the Cosmic Microwave Background as the Universe becomes transparent so that these photons propagate freely in the whole Universe, forming a relic radiation from that moment. This moment is also called the Last Scattering Surface (LSS) as it is a spatial hypersurface in a four dimensional space-time. Actually, the CMB as it was observed by satellites like COBE, WMAP or Planck is a two-dimensional surface: a sphere centred around us which is the intersection of the three-dimensional LSS with our past light-cone. In fact, the LSS is not properly a spatial hypersurface of the four-dimensional space-time, but has a thickness because the instant when photons stop scattering off electrons is not sharply defined. Therefore, the portion of the CMB observed also has a thickness but it is small as compared to the age of the Universe at decoupling. Given that $\dot{a}/a = H$, one can solve this equation and invert it to get the time t as a function of a and as $a = a_0 T_0/T$, one can translate $T_{\rm dec}$ in a time. The decoupling thus happens about $t = 380\,000$ yrs after the Big-Bang.

4.2 Spectral properties of the CMB

4.2.1 Best black body ever measured

Today, the mean temperature of this relic radiation over the whole sky, which is also the temperature of the Universe

$$T_0 \equiv T_{\gamma 0} = \frac{1}{4\pi}\int T(\theta,\varphi)\sin\theta {\rm d}\theta {\rm d}\varphi, \tag{4.5}$$

has been the most precisely measured by the FIRAS instrument on board of the COBE satellite to be

$$T_0 = 2.725 \pm 0.001{\rm K}. \tag{4.6}$$

Furthermore, in the hot Big-Bang model, there is no energy injected in the photons bath between the last annihilation in the primordial Universe, which is the electron-positron annihilation around ~ 100 keV, and the beginning of the reionisation of the Universe, when new photons are created by the first stars and galaxies formed. Therefore, it is expected that the CMB radiation follows a Planck spectrum

$$I(\nu,T) = \frac{2h\nu^3}{c^2}\frac{\nu^3}{{\rm e}^{h\nu/(k_{\rm B}T)}-1}, \tag{4.7}$$

where $I(\nu,T)$ is the spectral radiance, i.e. the power emitted by a surface per unit solid angle, per unit projected area, per unit of frequency. Indeed, this quantity has been measured by the FIRAS instrument and the measurement is plotted in Fig. 4.2: one clearly sees that the data follows Planck's law. This is often said that the CMB is the best black-body ever measured, as evidenced by the error bars in Fig. 4.2. This means that the radiation has thermalised, thanks to the interactions taking place in the primordial plasma, and in particular the Compton scattering process. Thus, any injection of energy in the photons bath would be seen on the measured spectrum as distortions of the black-body spectrum. As no primordial[1] distortion has been observed in the CMB spectrum yet, the observations put tight upper limits on them. We will now see what are these possible distortions.

[1] We will see later that secondary distortions can be produced, for example due to the SZ effect.

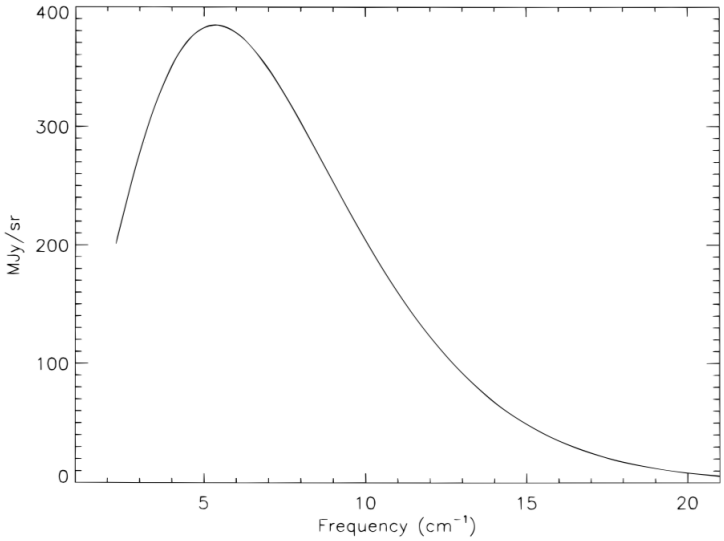

Figure 4.2: Fit to the measured spectrum of the CMB by the COBE satellite. The error bars are a fraction of the line thickness, so that they are not visible on the figure. The spectrum is that of a black-body with temperature $T_0 = 2.725 \pm 0.001$ K. Figure taken from Fixsen et al. (1996).

4.2.2 Spectral distortions y, μ and $Y_{\rm ff}$

There are three kinds of possible distortions to the black-body spectrum depending on the physical process at play and which have different effects on the spectrum.

The first of it is the Compton distortion. As its name suggests, this distortion results from the Compton scattering of photons by electrons. The distortion happens when the electrons are hotter than the photons bath, so that energy is injected in the relic radiation. Therefore, this heating of the radiation shifts the black-body spectrum to higher energies, hence frequencies, but as no new photons are injected, the low frequency part has its amplitude decreased and the resulting spectrum is no longer that of a black-body. This distortion is characterised by the Compton y parameter

$$y = \int \sigma_{\rm T} n_e \frac{(T_e - T_\gamma)}{m_e c^2} {\rm d}t, \tag{4.8}$$

being the integrated Compton optical thickness. We will come back to this distortion again when talking about the tSZ effect happening in clusters of galaxies.

Another possible distortion is due to the fact that even though the primordial plasma is thermalised thanks to the Compton scattering process, it can take some time for the spectrum to relax to Planck's law. This translates into a non-zero chemical potential μ for the photons, distorting the black-body spectrum so that they follow a Bose-Einstein one

$$I(\nu, T) = \frac{2h}{c^2} \frac{\nu^3}{{\rm e}^{(h\nu - \mu)/(k_{\rm B}T)} - 1}. \tag{4.9}$$

This is characterised by the $\tilde{\mu}$ parameter

$$\tilde{\mu} = \frac{\mu}{T_\gamma}. \tag{4.10}$$

Finally, the last kind of distortion is due to the emission of photons by the scattering of electrons on charged particles and is proportional to the following parameter

$$Y_{\rm ff} = \frac{8\sqrt{\pi}g}{3\sqrt{6}} \left(\frac{e^2}{4\pi\varepsilon_0}\right)^3 \int \frac{n_e^2}{m_e T_\gamma^3 \sqrt{m_e T_e}} \left(1 - \frac{T_\gamma}{T_e}\right) {\rm d}t, \tag{4.11}$$

where $g \sim 2$ is called the Gaunt factor. This kind of distortion is called 'free-free'.

Fig. 4.3 shows the shapes of the spectral distortions y, $\tilde{\mu}$ and $Y_{\rm ff}$. None of them have been

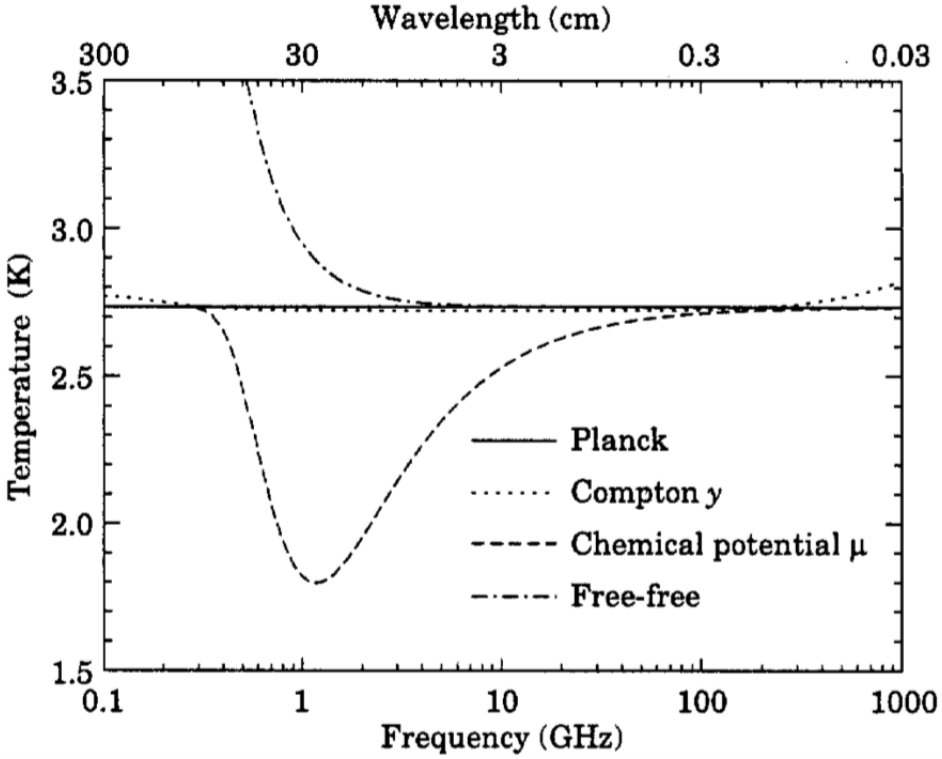

Figure 4.3: The shapes of CMB spectral distortions y, $\tilde{\mu}$ and $Y_{\rm ff}$, resulting from energy-releasing processes. Figure taken from Smoot & Scott (2000).

observed yet in the primordial CMB. In fact, observations give upper limits so that if distortions of the black-body spectrum are to be present, they must be small

$$|y| < 1.9 \times 10^{-5}, \ |\tilde{\mu}| < 9 \times 10^{-5}, \ |Y_{\rm ff}| < 1.5 \times 10^{-5}. \tag{4.12}$$

4.3 Anisotropies

So far we have only presented the mean characteristics of the CMB radiation: how it is generated, its temperature and spectrum. However due to primordial density fluctuations (themselves due to primordial quantum fluctuations, see Chapter 3), the electron density n_e is not uniform in the primordial plasma. Therefore, the LSS is not quite a hypersurface $t = {\rm cst}$, as the decoupling of photons depends on n_e through $\Gamma_{\rm T}$, but a surface for which $n_e = {\rm cst}$. As decoupling does

not happen at the same time in every point of the Universe, the LSS does not have a uniform temperature (time and temperature being related by the scale factor a: $T(t) = T_0 a_0/a(t)$) but contains so-called temperature anisotropies. The interaction rate $\Gamma_{\rm T}$ being proportional to the electron density n_e, overdense regions decouple later and should in principle correspond to slightly colder regions of the LSS. However, the Stefan-Boltzmann law relates the temperature contrast to the energy density contrast of the photons

$$\frac{\Delta T}{\overline{T}} = \frac{1}{4}\frac{\rho_\gamma - \overline{\rho}_\gamma}{\overline{\rho}_\gamma} = \frac{1}{4}\delta_\gamma, \tag{4.13}$$

so that an overdense region corresponds to a hotter region in the primordial plasma. Therefore, there is no obvious link between temperature and density at decoupling. Furthermore, other physical effects have to be considered which impact the temperature of the LSS. One of them has to do with overdense regions: these also correspond to perturbations of the gravitational potential so that if photons decouple while in a gravitational potential, they lose energy as they climb out of the potential well and are consequently colder. This effect together with Eq. (4.13), dealing with overdense regions, are collected under the name of 'Sachs-Wolf' (SW) effect. Another effect has to do with velocities in the primordial plasma or of the observer, which again change the energy of the photons received. This one is called without surprise the Doppler effect. Finally, photons travel in a perturbed Universe before reaching us and the impact of the evolution of these perturbations (like for example the gravitational potentials of forming structures) on the temperature of the photons is known as the Integrated Sachs-Wolf (ISW) effect. This last effect is part of a set sourcing secondary anisotropies of the CMB, meaning these temperature anisotropies are due to effects happening since decoupling. We will come back to it at the end of this chapter.

Here we will not detail the derivation of all the possible effects impacting the temperature of the CMB but rather focus on the formalism needed to describe these anisotropies in the CMB by focusing first on the primary anisotropies, i.e. those imprinted at the time of decoupling. Because of the vector nature of light, in addition to temperature anisotropies, there are also polarisation ones. These primordial anisotropies have Gaussian statistics and are thus completely characterised by their two-point correlation functions, or equivalently by their angular power spectra. These primary statistics are then modified by their propagation through the large-scale structures of the Universe, producing the above mentioned secondary anisotropies of the CMB.

4.3.1 Primary anisotropies

As mentioned in Chapter 3, the primary anisotropies are sourced by vacuum quantum fluctuations in the very early Universe. Indeed, the scalar perturbations of primordial fields (like the supposed inflaton field for example) result in classical energy density fluctuations, after amplification and transfer through the primordial phases of the Universe. Similarly tensor perturbations of the metric result in classical gravitational waves after amplification. We do not consider here the contribution of vector perturbations as they are expected to decay in the very early Universe, see Eq. (3.20). Both scalar and tensor perturbations have an imprint on temperature and polarisation anisotropies.

4.3.1.1 Temperature anisotropies

The two components of the temperature anisotropies, the Sachs-Wolf and Doppler effects, were described in the introduction of this section 4.3. The temperature of the CMB can be modeled by a temperature field $T(\boldsymbol{x}, t; \theta, \varphi)$ measured at the space-time point $(\boldsymbol{x}, t)$ and which depends

on the direction of observation indicated by the spherical coordinates (θ, φ). The temperature field is a scalar field: it means that a single value is assigned to it at each space-time point and this value does not change under any change of coordinates. Other examples of scalar fields are the density or pressure fields. The inflaton field described in the previous chapter is another example of a scalar field.

Such a field $T(\boldsymbol{x}, t; \theta, \varphi)$ which depends on the direction of observation, can be considered as a field belonging to the two-dimensional space being the celestial sphere. It can thus be expanded onto an orthonormal basis of the space of square-integrable functions on the unit sphere S^2: the spherical harmonics $\{Y_\ell^m(\theta, \varphi)\}$. They are called 'spherical harmonics of degree ℓ and order m', where ℓ and m are integers such that $0 \leq \ell$ and $-\ell \leq m \leq \ell$. A representation of the first real spherical harmonics is given in Fig. 4.4, with $\ell = 0$ to 3 from top to bottom and $m = -\ell$ to ℓ from left to right. As hinted by this representation, the first multipole number is thus related to the angular scale given by the polar angle: $\ell \sim \pi/\theta$ and low ℓ values correspond to large angular scales on the sky (and inversely, high ℓ values to small angular scales), while the second multipole number m corresponds to the orientation on the sphere. The spherical harmonics are

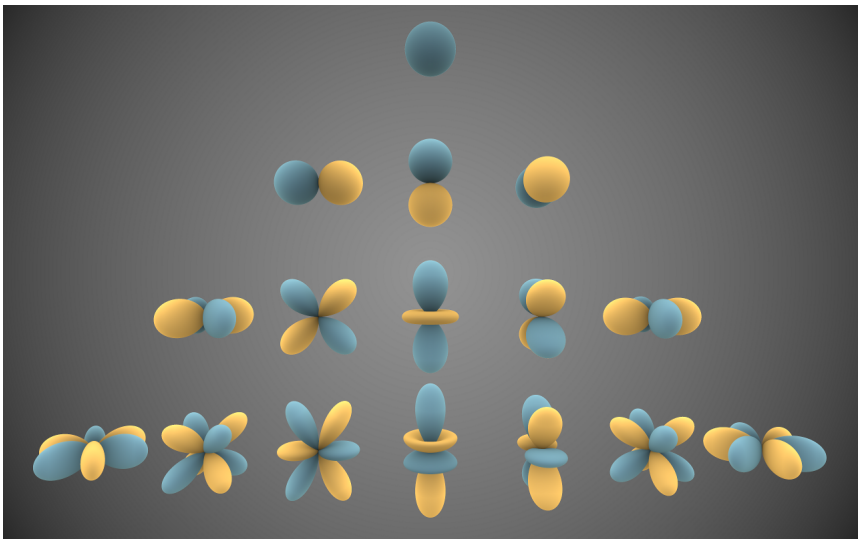

Figure 4.4: Representation of the first real spherical harmonics $Y_{\ell m}(\theta, \varphi)$ (which are combinations of the real and imaginary parts of the spherical harmonics $Y_\ell^m(\theta, \varphi)$), with $\ell = 0$ to 3 from top to bottom and $m = -\ell$ to ℓ from left to right. The distance of the surface from the origin indicates the absolute value of $Y_{\ell m}(\theta, \varphi)$ in the direction (θ, φ) and the colors indicate its sign (blue is positive, yellow is negative). Figure by Inigo.quilez.

orthonormal in the sense of the scalar product

$$\int\int_{S^2} \sin(\theta)\, \mathrm{d}\theta \mathrm{d}\varphi\ Y_{\ell'}^{m'*}(\theta, \varphi) Y_\ell^m(\theta, \varphi) = \delta_{\ell\ell'}\delta_{mm'}, \tag{4.14}$$

$*$ denoting the complex conjugate, and where we have chosen the normalisation used in quantum mechanics. Thus, any function $f(\theta, \varphi)$ can be expanded in a spherical harmonic series

$$f(\theta, \varphi) = \sum_{\ell=0}^{\infty} \sum_{m=-\ell}^{\ell} C_\ell^m Y_\ell^m(\theta, \varphi). \tag{4.15}$$

This series expansion on the 2-sphere is the analog of the Fourier series expansion on the circle with the orthonormal basis of exponentials $\{e^{inx}\}$. The C_ℓ^m are therefore often called generalised Fourier coefficients and are thus obtained similarly

$$C_\ell^m = \int\int_{S^2} \sin(\theta)\, \mathrm{d}\theta \mathrm{d}\varphi\; Y_\ell^{m*}(\theta,\varphi) f(\theta,\varphi). \tag{4.16}$$

Thus, following this formalism, the temperature field is expanded like

$$T(\boldsymbol{x},t;\theta,\varphi) = \sum_{\ell m} T_{\ell m}(\boldsymbol{x},t) Y_\ell^m(\theta,\varphi). \tag{4.17}$$

The first coefficient of the expansion T_{00} gives the mean temperature of the CMB Eq. (4.5). The other coefficients give the temperature of patches of the sky of the corresponding spherical harmonics depicted in Fig. 4.4. As the differences with the mean temperature are small (of the order of $\sim 10^{-5}$), we will rather work with the temperature fluctuation field $\Theta = (T - T_0)/T_0$ and decompose it as

$$\Theta(\boldsymbol{x},t;\theta,\varphi) = \sum_{\ell m} \Theta_{\ell m}(\boldsymbol{x},t) Y_\ell^m(\theta,\varphi), \tag{4.18}$$

so that the first coefficient of the expansion Θ_{00} vanishes.

A map of these primary temperature anisotropies on the celestial sphere is given in Fig. 4.5, detected by the Planck satellite (Planck Collaboration et al., 2018a). This is the most precise detection ever made of the temperature anisotropies, sometimes even called the 'ultimate' detection, as its precision is not limited by the sensitivity of the instrument. The red (blue) spots correspond to hotter (respectively colder) regions on the sky, with respect to the mean sky temperature Eq. (4.5).

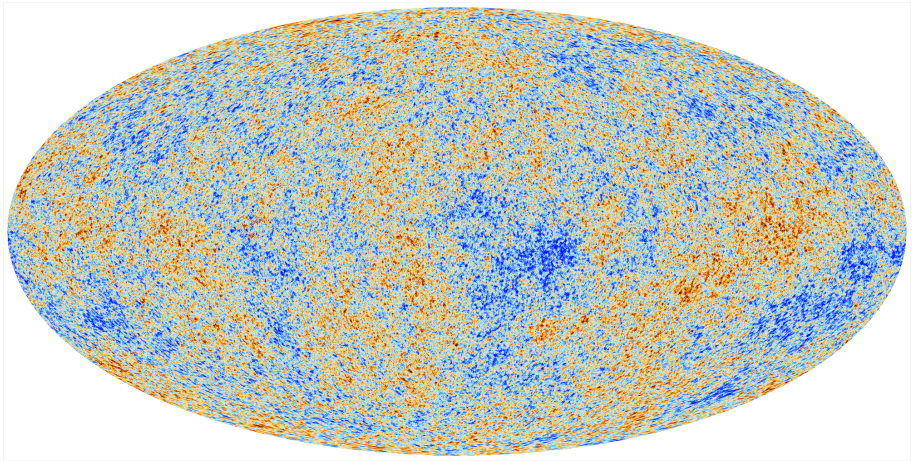

Figure 4.5: Projection of the CMB temperature anisotropies on the celestial sphere. The red (blue) spots correspond to hotter (respectively colder) regions on the sky, with respect to the mean sky temperature. This map has been observed by the Planck satellite, figure taken from the ESA website.

4.3.1.2 Polarisation anisotropies

Light as an electromagnetic wave

Light is modeled in physics by three theories having different domains of application which depend on the scale at which we are working. The simplest way to model light is to say that it is composed of light rays propagating in straight lines: this is the formalism of geometrical optics. However geometrical optics is an approximation of a more general theory called physical optics or wave optics, describing light as an electromagnetic wave. The domain of validity of geometrical optics corresponds to when the wavelength of the electromagnetic wave is small compared to the size of the objects it interacts with. Geometrical optics is recovered by saying that the light ray is the direction of propagation of the electromagnetic field describing light, or the direction of propagation of the energy carried by the electromagnetic wave. However, when going to smaller scales, we need a quantum theory of light to describe how light interacts with matter at atomic scales, i.e. the atoms or molecules: such a theory is called quantum optics and outline the corpuscular nature of light as being composed of photons. In this section, we will describe light as an electromagnetic wave.

Thus, we now present the polarisation of light. Polarisation is the property for a wave with at least two components (or two degrees of freedom, that is, at least vectorial) to have a preferred pattern for the direction of its oscillations. Electromagnetic waves, which are propagating perturbations of the electric and magnetic fields, can be polarised. When we talk about the polarisation of an electromagnetic wave, we actually talk about the direction of oscillations of the electric field. The most general form for such a field can be written in an orthonormal basis $(\hat{\boldsymbol{e}}_1, \hat{\boldsymbol{e}}_2, \hat{\boldsymbol{e}}_3)$ as

$$\boldsymbol{E}(\boldsymbol{r}, t) = \begin{vmatrix} E_1(\boldsymbol{r}, t) \\ E_2(\boldsymbol{r}, t) \\ 0 \end{vmatrix} , \tag{4.19}$$

assuming an electromagnetic wave propagating in the $\hat{\boldsymbol{e}}_3$-direction, so that the $\hat{\boldsymbol{e}}_3$-component of the electric field is null, as electromagnetic waves are of transverse nature in vacuum. If the electric field remains in the same direction while propagating, then we say the wave is *linearly* polarised. A single temporally, spatially and spectrally coherent electromagnetic wave can be polarised, and in full generality, its polarisation is elliptic: the electric field describes an ellipse as time goes by, as shown in Fig. 4.6. Depending on whether the ellipse is drawn over time in the

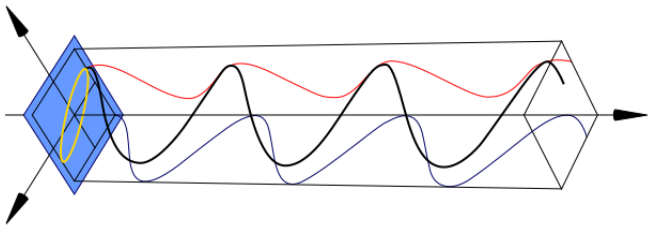

Figure 4.6: Propagation of an ellipsoidally polarized wave. The tip of the electric field follows a helical curves (in black), such that its projection on the plane perpendicular to the propagation direction draws an ellipse. This is due to the fact that its orthogonal components (which follow the blue and red curves) are phase shifted.

right(left) sense, one respectively talks about right(left)-handed elliptical polarisation. Linear

polarisation is a degenerate case of elliptical polarisation when one of the axes of the ellipse is zero. Another degenerate case is when the ellipse is actually a circle: one then talks about circular polarisation. In any case, any polarised electromagnetic wave can be decomposed either into two perpendicular linearly polarised waves, or into one right- and one left-handed circularly polarised waves. Finally, if the two components have random values over time, then the wave is said to be non-polarized.[2]

Why is most of the natural light non-polarised? If light is described by wave packets, each of them has a different random polarisation, but if the wave packets have a short coherence time, shorter than the time resolution of the detectors, its sampling frequency cannot follow this variation of polarisation and, as it is random, the average polarisation over time is null. Although natural light is composed of all the possible polarisations, some media or physical processes let only one type of polarisation pass, as is the case of the Thomson scattering process happening before decoupling. Another example is that of the optical devices called polarisers. They consist in grids which only let the light polarised in the direction perpendicular to the grid pass, see Fig. 4.7. Hence, polarisation of the light gives us information on these media or physical processes.

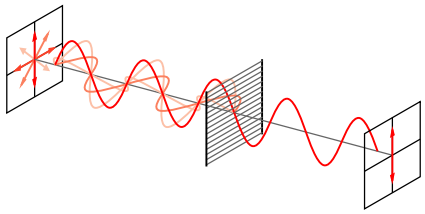

Figure 4.7: A linear polariser only lets light polarized in the direction perpendicular to its grid pass through. Figure by Bob Mellish.

Origin of CMB primary polarisation

We explain now the origin of the CMB primary polarisation anisotropies. As mentioned above, some physical processes polarise light and in particular the Thomson scattering process. The outgoing light is polarised in the perpendicular direction to the plane of scattering if the incoming radiation is anisotropic. Therefore, it is the primordial fluctuations of the plasma, resulting in temperature or intensity anisotropies, that allow the CMB to have primordial polarisation: this is the reason why one talks about 'polarisation anisotropies' and not just polarisation.

We describe here physically how the Thomson scattering process polarises light. Actually, the Thomson scattering differential cross section depends on the relative polarisation of the incoming electromagnetic wave $\boldsymbol{\varepsilon}^{\rm in}$ scattering off the electrons and the outgoing electromagnetic wave $\boldsymbol{\varepsilon}^{\rm out}$

$$\frac{\mathrm{d}\sigma}{\mathrm{d}\Omega} = \frac{3}{8\pi}\sigma_{\rm T}(\boldsymbol{\varepsilon}^{\rm in}\cdot\boldsymbol{\varepsilon}^{\rm out})^2, \tag{4.20}$$

where $\mathrm{d}\Omega$ is the elementary solid angle around the electron in the direction of scattering and $\sigma_{\rm T}$ is the total Thomson scattering cross-section; note that $\boldsymbol{\varepsilon}^{\rm in}$ and $\boldsymbol{\varepsilon}^{\rm out}$ are unit vectors. This

[2] Actually, at each instant the electric field has a definite direction and thus a polarization, but this one is changing too fast, and above all randomly, for any detector to detect a net polarization, as detectors only have access to an average over time of the electric field (for example, the sampling frequency of the detectors of the HFI instrument on the Planck mission was 180 Hz (Lamarre et al., 2010)).

expression is obtained by considering the average power radiated per unit solid angle in the polarisation state $\boldsymbol{\varepsilon}^{\text{out}}$, by the acceleration of an electron by an incident electromagnetic wave. In particular, this expression shows that the outgoing wave polarisation cannot be perpendicular to the polarisation of the incoming wave. Now, consider like in Fig. 4.8 that an incoming

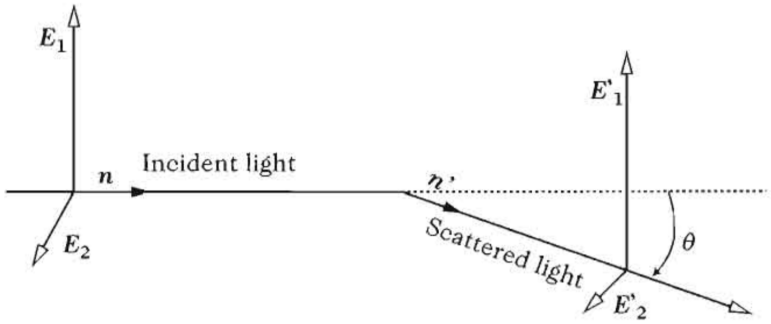

Figure 4.8: The Thomson scattering process in the reference frame of an electron. An incident electromagnetic wave propagating along $\boldsymbol{n}$ is scattered at an angle θ in the direction $\boldsymbol{n}'$. Figure taken from Peter & Uzan (2009).

electromagnetic wave propagating in the direction $\boldsymbol{n}$ in the electron reference frame, is scattered at an angle θ, resulting in an outgoing wave in the direction $\boldsymbol{n}'$, so that the scattering takes place in the plane $(\boldsymbol{n}, \boldsymbol{n}')$. The electromagnetic wave being transverse, its polarisation belongs to the plane perpendicular to $\boldsymbol{n}$, i.e. to the plane perpendicular to its direction of propagation. Then, it can always be decomposed into two linearly polarised waves in that plane: one chooses to decompose the polarisation into a linearly polarised wave in the scattering plane $(\boldsymbol{n}, \boldsymbol{n}')$ indicated by $\boldsymbol{E}_2$ and a linearly polarised wave $\boldsymbol{E}_1$ perpendicular to that plane. A similar decomposition can be made for the polarisation of the scattered wave with components $\boldsymbol{E}_2'$ in the scattering plane and $\boldsymbol{E}_1'$ perpendicular to it. Using Eq. (4.20), one can compute the scattering cross-section for the component along $\boldsymbol{\varepsilon}^{\text{out}} = \boldsymbol{E}_2'$ as $\boldsymbol{\varepsilon}^{\text{in}} \cdot \boldsymbol{E}_2' = \boldsymbol{E}_2 \cdot \boldsymbol{E}_2' = \cos\theta$. Similarly, the scattering cross-section for the component along $\boldsymbol{\varepsilon}^{\text{out}} = \boldsymbol{E}_1'$ is equal to 1 since $\boldsymbol{\varepsilon}^{\text{in}} \cdot \boldsymbol{E}_1' = \boldsymbol{E}_1 \cdot \boldsymbol{E}_1' = 1$. It thus shows that if a non-polarised incoming electromagnetic wave is scattered by an angle $\theta = \pi/2$, the outgoing wave will be linearly polarised along $\boldsymbol{E}_1'$ only, because $\boldsymbol{E}_2 \cdot \boldsymbol{E}_2' = 0$, so that the Thomson scattering process favors a particular direction of polarisation out of a non-polarised incident light.

Now, there is not a single electromagnetic wave scattering off an electron in the primordial plasma, but many at the same time. One expects that the incoming waves come from all the directions around the electron. Thus, if the primordial radiation is isotropic around the electron, that is all incident waves have the same intensity, the addition of all the outgoing polarised waves results in no net polarisation for the scattered radiation, as shown in Fig. 4.9 (a). Indeed, consider four unpolarised incident waves propagating in the $\pm x$ and $\pm y$ directions, scattered by an electron in O at an angle $\theta = \pi/2$ in the same direction $+z$. According to the mechanism polarising light described earlier, once scattered, the incident lights propagating along $\pm x$ will give an outgoing wave linearly polarised along y, while the incident light propagating along $\pm y$ will give an outgoing wave linearly polarised along x. The waves not being coherent, their sum gives an unpolarised wave. However, we know that there are anisotropies in temperature in the primordial plasma due to primordial fluctuations, which are either density fluctuations or gravitational waves. Therefore, in the reference frame of an electron in the primordial plasma,

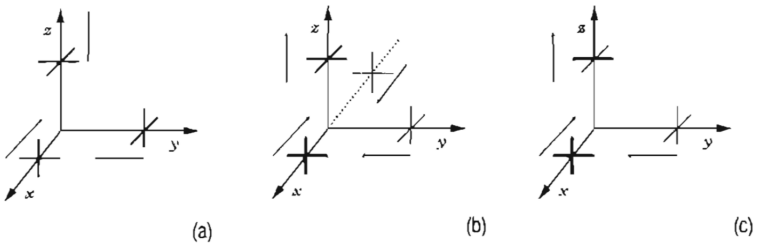

Figure 4.9: The Thomson scattering process. Figure taken from Peter & Uzan (2009).

the incoming radiation is anisotropic. Still, if the anisotropy is only dipolar, for example with a dipole intensity along x as in Fig. 4.9 (b), where the intensity of the incident waves coming from the $+$ and $-x$ directions are symmetrically hotter and colder than the mean intensity coming from the $\pm y$ direction, then the component along y of the outgoing wave is exactly equal to its component along x. Again, the two components not being coherent, there is no net polarisation for the scattered light. Finally, one has to consider a quadrupolar anisotropy as in Fig. 4.9 (c) where the intensity of the incoming waves propagating along $\pm x$ are hotter than the intensity of the incoming waves propagating along $\pm y$, to get a net outgoing linear polarisation. Indeed, the component along y of the outgoing wave results hotter than its component along x, so that the scattered light has a net polarisation along y. Thus, even though the incoming polarisations are all random, the anisotropic intensity results in a net incoming polarisation on the electron and consequently a net outgoing polarisation. Note that only a quadrupolar anisotropy can give rise to a polarised scattered wave, for some analogous symmetry reasons. Furthermore, the Thomson scattering process does not produce any circularly polarised light. The CMB indeed is not circularly polarised.

The Stokes parameters: characterising polarisation

The interested reader will find in Appendix A a presentation of the formalism of the Poincaré sphere used to describe partially polarised light (starting from the usual description of the polarisation of an electromagnetic wave), as well as the Stokes parameters (defined in terms of the spherical coordinates of this sphere) quantifying the polarisation of light. There exist other definitions of the Stokes parameters, with the components of the electric field in different basis

$$\begin{aligned} I &\equiv \langle E_x^2\rangle + \langle E_y^2\rangle = \langle E_a^2\rangle + \langle E_b^2\rangle = \langle E_l^2\rangle + \langle E_r^2\rangle, \\ Q &\equiv \langle E_x^2\rangle - \langle E_y^2\rangle, \\ U &\equiv \langle E_a^2\rangle - \langle E_b^2\rangle, \\ V &\equiv \langle |E_l|^2\rangle - \langle |E_r|^2\rangle, \end{aligned} \tag{4.21}$$

for an electromagnetic wave propagating in the $\boldsymbol{e}_z = \boldsymbol{e}_c$ direction, where $(\boldsymbol{e}_x, \boldsymbol{e}_y, \boldsymbol{e}_z)$ is the cartesian coordinates basis and $(\boldsymbol{e}_a, \boldsymbol{e}_b, \boldsymbol{e}_c)$ is the same basis rotated by an angle of $\pi/4$ about $\boldsymbol{e}_z$, and finally one defines the helicity basis $\boldsymbol{e}_{l/r} = (\boldsymbol{e}_x \pm i\boldsymbol{e}_y)/\sqrt{2}$ to get the components E_l and E_r. Actually, one cannot measure the amplitude of the two components at each instant of time, thus one measures averages of the components in the different basis over several periods.

The first Stokes parameter I is the total intensity of light. The three other ones can be seen as a measure of the intensity of light in the different polarisation states. The Q and U parameters measure the linear polarisation: the complex parameter

$$P \equiv Q + iU = |P|e^{i2\theta}, \tag{4.22}$$

gives the intensity in the linear polarisation state, θ being the angle of the direction of polarisation with respect to the basis in which Q and U are measured. Finally, V measures the intensity in the circular polarisation state: $V > 0$ for left-handed while $V < 0$ for right-handed circular polarisation. For partially polarised light as the CMB one, the Stokes parameters thus satisfy the following inequality

$$Q^2 + U^2 + V^2 = I_p^2 \leq I^2, \tag{4.23}$$

where I_p is the intensity in the polarised part of light. Fig. 4.10 shows how the sign of the Stokes parameters depends on the orientation of the semi-major axis and the sense of rotation of the polarisation ellipse.

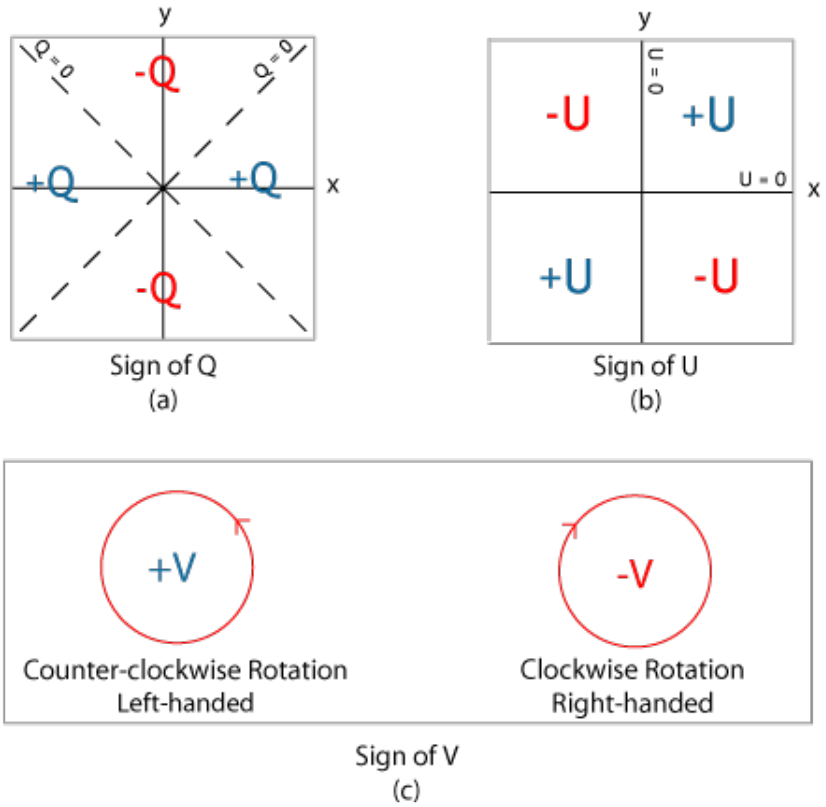

Figure 4.10: The signs of the Stokes parameters are related to the orientation of the semi-major axis and the sense of rotation of the polarisation ellipse. Figure by Dan Moulton.

One can see in Eq. (4.21) that the Stokes I parameter does not depend on the system of coordinates chosen to measure it: it is thus a scalar quantity, which is not surprising as it is related to the temperature of light. However, as suggested by the P parameter, and by the definitions of the Q and U parameters, the latter are not basis invariant. Indeed, under a rotation of angle α of the basis $(\boldsymbol{e}_x, \boldsymbol{e}_y)$ around the $\boldsymbol{e}_z$ axis

$$\begin{cases} \boldsymbol{e}'_x = \cos(\alpha)\boldsymbol{e}_x + \sin(\alpha)\boldsymbol{e}_y, \\ \boldsymbol{e}'_y = -\sin(\alpha)\boldsymbol{e}_x + \cos(\alpha)\boldsymbol{e}_y, \end{cases} \tag{4.24}$$

they become

$$\begin{cases} Q' = \cos(2\alpha)Q + \sin(2\alpha)U, \\ U' = -\sin(2\alpha)Q + \cos(2\alpha)U, \end{cases} \tag{4.25}$$

which is shown in Appendix A. Finally, the Stokes V parameter is invariant under such a rotation of the coordinate basis, as can be seen from its definition, consistent with the fact that it quantifies the circularly polarised component of light. Nonetheless, this is not a scalar quantity, but a *pseudo*-scalar one. Indeed, under a parity transformation of the coordinate system, defined as the flip in the sign of one spatial coordinate (also called reflection), like for example

$$V_x : \begin{pmatrix} x \\ y \\ z \end{pmatrix} \mapsto \begin{pmatrix} -x \\ y \\ z \end{pmatrix}, \tag{4.26}$$

the Stokes V parameter changes sign

$$V' = -V. \tag{4.27}$$

This sign flip is what distinguishes the scalar quantities from the pseudo-scalar ones.

The polarisation field of the CMB

The change in the Q and U Stokes parameters when doing a rotation of the system of coordinates by an angle α can be encoded in complex notation

$$Q' \pm iU' = (Q \pm iU)e^{\pm 2i\alpha}, \tag{4.28}$$

defining the polarisation field of the CMB as

$$P_{\pm 2}(\boldsymbol{x}, t; \theta, \varphi) = Q(\boldsymbol{x}, t; \theta, \varphi) \pm iU(\boldsymbol{x}, t; \theta, \varphi). \tag{4.29}$$

The polarisation field, when seen as a field on the celestial sphere, is what is called a spin-weighted $s = 2$ function. A spin-weighted s function ${}_sf$ of the spherical coordinates (θ, φ) transforms like

$${}_sf' = e^{is\psi}{}_sf, \tag{4.30}$$

under a rotation of the orthonormal basis $(\boldsymbol{e}_\theta, \boldsymbol{e}_\varphi)$ tangent to the sphere by an angle ψ about the radial vector $\boldsymbol{e}_r$ (Newman & Penrose (1966)). Similarly to the temperature field in Eq. (4.17), one can thus expand the polarisation field in a series, but being a spin ± 2 field, the expansion is made on the spin-weighted spherical harmonics ${}_sY_{\ell m}(\theta, \varphi)$ with $-\ell \leq s \leq \ell$, which are used to make the spherical harmonic transform of a spin-weighted s function ${}_sf(\theta, \varphi)$ on the sphere. They are defined thanks to the action of the spin raising (+) and spin lowering (-) operators $\partial^\pm$ on the usual spherical harmonics. Indeed, for a spin-weighted s function ${}_sf$, $(\partial^\pm{}_sf)$ transforms like

$$(\partial^\pm{}_sf)' = e^{i(s\pm 1)\psi}\partial^\pm{}_sf, \tag{4.31}$$

under a rotation of angle ψ. Their explicit expressions are given by

$$\partial^\pm{}_sf(\theta, \varphi) = -\sin^{\pm s}\theta \left(\partial_\theta \pm \frac{i}{\sin\theta}\partial_\varphi\right) \sin^{\mp s}\theta\partial^\pm, \tag{4.32}$$

so that the spin-weighted spherical harmonics are

$${}_sY_{\ell m} \equiv \begin{cases} \sqrt{\dfrac{(\ell - s)!}{(\ell + s)!}}(\partial^+)^s Y_{\ell m} \quad \text{for } (0 \leq s \leq \ell), \\ \sqrt{\dfrac{(\ell + s)!}{(\ell - s)!}}(-1)^s(\partial^-)^{-s}Y_{\ell m} \quad \text{for } (-\ell \leq s \leq 0). \end{cases} \tag{4.33}$$

They are normalised in a similar way than the spherical harmonics Eq. (4.14)

$$\int\int_{S^2} \sin(\theta)\,\mathrm{d}\theta\mathrm{d}\varphi\ {}_sY_{\ell'}^{m'*}(\theta,\varphi){}_sY_\ell^m(\theta,\varphi) = \delta_{\ell\ell'}\delta_{mm'}. \tag{4.34}$$

Thus, the polarisation field is written like

$$P_{\pm2}(\boldsymbol{x},t;\theta,\varphi) = \sum_{\ell m} a_{\ell m}^{\pm2}(\boldsymbol{x},t)\ {}_{\pm2}Y_\ell^m(\theta,\varphi). \tag{4.35}$$

Linear polarisation of the CMB: the E and B modes

However, the drawback of the Q and U parameters, and so of the polarisation field $P_{\pm2}$, is that they depend on the basis chosen to compute them. Indeed, we have just seen that the polarisation field changes under a rotation of the basis (it is a spin ±2 quantity). This is unconvenient as we do not want our description of polarisation to depend on the basis in which computations are done. A way to achieve this is to transform the spin ±2 polarisation field into a spin 0 field on the sphere, thus representing a scalar quantity (like temperature), thanks to the action of the spin raising and spin lowering operators

$$(\partial^\mp)^2 P_{\pm2} = \sum_{\ell m}\sqrt{\frac{(\ell+2)!}{(\ell-2)!}}a_{\ell m}^{\pm2}Y_\ell^m(\theta,\varphi), \tag{4.36}$$

where we have used the following property

$$\partial^\pm {}_sY_{\ell m} = \pm\sqrt{(\ell\mp s)(\ell+1\pm s)}{}_{s\pm1}Y_{\ell m}. \tag{4.37}$$

This way, two spin 0 and thus rotationally invariant fields with coefficients $\sqrt{(\ell+2)!/(\ell-2)!}a_{\ell m}^{\pm2}$ have been built to represent linear polarisation on the sky, but the fields are non-local as the operators $\partial^\pm$ are. These two spin 0 (scalar) fields are combined together to get fields with nice symmetries under a parity transformation

$$\begin{aligned}\chi^E(\theta,\varphi) &= -\frac{1}{2}\left((\partial^-)^2P_2(\theta,\varphi) + (\partial^+)^2P_{-2}(\theta,\varphi)\right),\\ \chi^B(\theta,\varphi) &= \frac{i}{2}\left((\partial^-)^2P_2(\theta,\varphi) - (\partial^+)^2P_{-2}(\theta,\varphi)\right),\end{aligned} \tag{4.38}$$

so that

$$\begin{aligned}\chi^E(\theta,\varphi) &= \sum_{\ell m}\sqrt{\frac{(\ell+2)!}{(\ell-2)!}}E_{\ell m}Y_{\ell m},\\ \chi^B(\theta,\varphi) &= \sum_{\ell m}\sqrt{\frac{(\ell+2)!}{(\ell-2)!}}B_{\ell m}Y_{\ell m},\end{aligned} \tag{4.39}$$

with

$$\begin{aligned}E_{\ell m} &= -\frac{1}{2}(a_{\ell m}^2 + a_{\ell m}^{-2}),\\ B_{\ell m} &= \frac{i}{2}(a_{\ell m}^2 - a_{\ell m}^{-2}).\end{aligned} \tag{4.40}$$

The E and B superscripts stand for 'electric' and 'magnetic' parts of the polarisation field. This denotes an analogy with the symmetry properties of the electric and magnetic fields. Indeed, under a parity transformation of the coordinate system, the polarisation field transforms like $P_{\pm2} \to P_{\mp2}$ because the Q Stokes parameter is unchanged while U transforms into

$-U$. This means that the coefficients of the expansion of the polarisation field transform like $a^{\pm 2}_{\ell m} \to (-1)^{\ell} a^{\mp 2}_{\ell m}$ as the spin-weighted spherical harmonics transform like ${}_sY_{\ell m} \to (-1)^{\ell}{}_{-s}Y_{\ell m}$ under a parity transformation. Therefore, the E and B coefficients transform like $E_{\ell m} \to (-1)^{\ell} E_{\ell m}$, $B_{\ell m} \to (-1)^{\ell+1} B_{\ell m}$ and χ^E is invariant under a parity transformation, while $\chi^B \to -\chi^B$. The electric part of the polarisation field is therefore a scalar, while the magnetic part is a pseudoscalar, which explains the analogy.

Equivalently, one can build similar spin 0 (scalar) fields by considering directly the coefficients $E_{\ell m}$ and $B_{\ell m}$

$$\begin{aligned} E(\theta,\varphi) &= \sum_{\ell m} E_{\ell m} Y_{\ell m}, \\ B(\theta,\varphi) &= \sum_{\ell m} B_{\ell m} Y_{\ell m}, \end{aligned} \tag{4.41}$$

known as the E and B mode polarisation fields. These fields obviously have the same symmetry properties as the $\chi^{E/B}$ fields and are also non-local. Thus, they cannot represent the polarisation field at a single point, but rather represent the polarisation patterns around a point, see Fig. 4.11. The symmetry properties of the E and B mode fields under a parity transformation are seen in these patterns: the E mode pattern is indeed invariant under a parity transformation while the B mode one is transformed into its mirror image. Furthermore, they are both invariant under rotations, as expected from a spin 0 field. Building two scalar fields with these symmetry properties starting from Eq. (4.36) is physically relevant. Indeed, density perturbations are scalar perturbations so they can only give rise to the polarisation E mode which is parity invariant, while tensor perturbations come in two polarisation states: one is parity invariant sourcing the E modes and the other being not parity invariant, only source the B modes. This is the reason why the B modes are a signature of the primordial gravitational waves, expected to be produced during inflation.

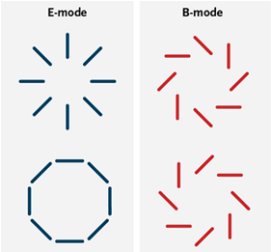

Figure 4.11: Polarisation patterns corresponding to the E and B modes of polarisation around a point, as they are non-local fields. Each bar represents the polarisation of the underlying point. The E mode pattern is indeed invariant under a parity transformation while the B mode one is transformed as its mirror image. Both are invariant under rotations, as expected from spin 0 fields.

4.3.1.3 Correlations: angular power spectrum and higher order statistics

We have described the CMB in terms of fields: temperature and polarisation fields, meaning a temperature and polarisation 'value' can be assigned at each point of space-time. Theoretically, this is an infinite amount of data. In practice, detectors divide space into pixels and assign information to these. Now, given the age (13.8 billion years) and size (93 billion light-years) of the

observable Universe, even though this amount of data is finite, it is so important that one cannot handle them separately but needs a statistical characterisation and measure of the information contained in the data. Furthermore, the theoretical predictions from inflation are only statistical and these statistics are actually nearly gaussian. This is done thanks to the $n-$point correlation functions and their derived statistics. Indeed, sometimes the only information available from the telescopes and satellites belongs to the celestial sphere so one rather deals with angular $n-$point correlation functions. For this purpose, we have already introduced all the formalism of the (spin-weighted) spherical harmonics needed to deal with fields defined on the sky.

Definitions

Let us start by a few definitions. The simplest statistics to consider, giving an unresolved and rough information on the large amount of data one has from an ensemble, is the mean value. For example Eq. (4.5) gives the mean temperature of the CMB over the whole sky. However, all the information about the temperature of the CMB measured and represented by the temperature field cannot reduce to this mean value. Indeed, we have also seen in the previous chapter that the CMB contained small relative temperature anisotropies of the order of $\Delta T/T_0 \sim 10^{-5}$, that is, the temperature is not uniform over the whole sky. This was characterised by a temperature fluctuation field defined over the whole sky: $\Theta(\theta,\varphi)$ (see Eq. (4.18)). The CMB having nearly gaussian statistics as the evolution from inflation is linear, preserving the gaussianity of the primordial inhomogeneities, all of its information can be reduced to mean values and variances of the temperature and polarisation fields. Defining $\boldsymbol{n}$ as the direction on the sky parameterised by the spherical coordinates θ and φ, one defines the angular two-point correlation function as

$$w(\boldsymbol{n},\boldsymbol{n}') \equiv \langle\Theta(\boldsymbol{n})\Theta(\boldsymbol{n}')\rangle = \sum_{\ell m}\sum_{\ell' m'}\langle\Theta_{\ell m}\Theta^*_{\ell' m'}\rangle Y_\ell^m(\boldsymbol{n})Y_{\ell'}^{m'*}(\boldsymbol{n}'), \tag{4.42}$$

where $\langle.\rangle$ is an ensemble average over universe realisations. This is the angular two-point correlation function of the temperature fluctuation field, equivalent to the angular two-point correlation function of the temperature field once the mean temperature is known, as

$$\langle\Theta(\boldsymbol{n})\Theta(\boldsymbol{n}')\rangle = \frac{\langle T(\boldsymbol{n})T(\boldsymbol{n}')\rangle}{T_0^2} - 1. \tag{4.43}$$

Thus, the angular two-point correlation function of the temperature fluctuation field is, up to a prefactor, exactly the variance of the temperature field: $T_0^2\langle\Theta(\boldsymbol{n})\Theta(\boldsymbol{n}')\rangle = \langle T(\boldsymbol{n})T(\boldsymbol{n}')\rangle - T_0^2 = \langle(T(\boldsymbol{n})-T_0)(T(\boldsymbol{n}')-T_0)\rangle$.

The writing of the angular two-point correlation function with the spherical harmonics expansion of the temperature fluctuation field shows the covariance matrix $\langle\Theta_{\ell m}\Theta^*_{\ell' m'}\rangle$. Now, we have seen in Chapter 1, Section 1.1.2 that the standard cosmological model relies on the isotropy and homogeneity hypotheses. For the two-point correlation function, this translates into the fact that w does not depend on the specific directions $\boldsymbol{n}$ and $\boldsymbol{n}'$ but only on the separation angle ψ defined by the two directions (homogeneity hypothesis), in whatever direction on the sky (isotropy hypothesis). The function w can thus be expanded like

$$w(\psi) = \sum_\ell \frac{2\ell+1}{4\pi} C_\ell P_\ell(\cos(\psi)), \tag{4.44}$$

where P_ℓ are the Legendre polynomials. Given that the coefficients of the expansion of the temperature fluctuation field are given by Eq. (4.16)

$$\Theta_{\ell m} = \int \mathrm{d}^2\boldsymbol{n}\, Y_\ell^{m*}(\boldsymbol{n})\Theta(\boldsymbol{n}), \tag{4.45}$$

one can compute the covariance matrix $\langle \Theta_{\ell m} \Theta^*_{\ell' m'} \rangle$

$$\begin{aligned} \langle \Theta_{\ell m} \Theta^*_{\ell' m'} \rangle &= \int \mathrm{d}^2 \boldsymbol{n} \int \mathrm{d}^2 \boldsymbol{n}' \, Y_\ell^{m*}(\boldsymbol{n}) Y_{\ell'}^{m'}(\boldsymbol{n}') \langle \Theta(\boldsymbol{n}) \Theta(\boldsymbol{n}') \rangle \\ &= \int \mathrm{d}^2 \boldsymbol{n} \int \mathrm{d}^2 \boldsymbol{n}' \, Y_\ell^{m*}(\boldsymbol{n}) Y_{\ell'}^{m'}(\boldsymbol{n}') \sum_{\ell''} \frac{2\ell''+1}{4\pi} C_{\ell''} P_{\ell''}(\cos(\psi)). \end{aligned} \tag{4.46}$$

Using the addition theorem for the spherical harmonics

$$P_{\ell''}(\cos(\psi)) = \frac{4\pi}{2\ell''+1} \sum_{m''=-\ell''}^{\ell''} Y_{\ell''}^{m''}(\boldsymbol{n}) Y_{\ell''}^{m''*}(\boldsymbol{n}'), \tag{4.47}$$

and the orthonormality relation for the spherical harmonics Eq. (4.14), the covariance matrix becomes

$$\langle \Theta_{\ell m} \Theta^*_{\ell' m'} \rangle = \delta_{\ell \ell'} \delta_{m m'} C_\ell, \tag{4.48}$$

so that it is a diagonal matrix whose diagonal coefficients are given by the angular power spectrum C_ℓ. The coefficients $\Theta_{\ell m}$ are thus statistically independent, as a result of statistical isotropy and homogeneity.

Similarly, one can compute the angular power spectra for the E and B modes. Having defined in Eq. (4.41) the E and B mode fields with their corresponding coefficients $E_{\ell m}$ and $B_{\ell m}$ in Eq. (4.40), the covariance matrices also reduce to angular power spectra because of the isotropy and homogeneity hypotheses

$$\langle E_{\ell m} E^*_{\ell' m'} \rangle = \delta_{\ell \ell'} \delta_{m m'} C_\ell^{EE} \quad \text{and} \quad \langle B_{\ell m} B^*_{\ell' m'} \rangle = \delta_{\ell \ell'} \delta_{m m'} C_\ell^{BB}. \tag{4.49}$$

Finally, the correlation between temperature and polarisation can be measured by the angular cross-correlation function. For example, for the correlation between temperature and the E mode, this is

$$w^{TE}(\boldsymbol{n}, \boldsymbol{n}') \equiv \langle \Theta(\boldsymbol{n}) E(\boldsymbol{n}') \rangle = \sum_{\ell m} \sum_{\ell' m'} \langle \Theta_{\ell m} E^*_{\ell' m'} \rangle Y_\ell^m(\boldsymbol{n}) Y_{\ell'}^{m'*}(\boldsymbol{n}'), \tag{4.50}$$

to which corresponds an angular cross power spectrum because of homogeneity and isotropy

$$\langle \Theta_{\ell m} E^*_{\ell' m'} \rangle = \delta_{\ell \ell'} \delta_{m m'} C_\ell^{TE}. \tag{4.51}$$

As explained in the previous section, the temperature and E modes are scalar fields, while the B mode is pseudo-scalar field. Therefore, the B mode angular power spectrum is a scalar quantity, being the product of two pseudo-scalar fields. Of course, the temperature and E mode angular power spectra are also scalar. The universe being parity invariant in the standard model of cosmology, one expects vanishing TB and EB cross-corrrelations as these are pseudo-scalar quantities.

To mention it, although at leading order the statistical predictions from inflation are gaussian, a way to quantify the deviations from gaussianity of the temperature and polarisation fields is to measure higher order correlation functions, like for example the third moment of the distribution or the angular three-point correlation function

$$\langle X(\boldsymbol{n}) Y(\boldsymbol{n}') Z(\boldsymbol{n}'') \rangle = \sum_{\ell m} \sum_{\ell' m'} \sum_{\ell'' m''} \langle X_{\ell m} Y_{\ell' m'} Z_{\ell'' m''} \rangle Y_\ell^m(\boldsymbol{n}) Y_{\ell'}^{m'}(\boldsymbol{n}') Y_{\ell''}^{m''}(\boldsymbol{n}''), \tag{4.52}$$

where X, Y and Z stand for Θ, E or B, and to which corresponds an angular bispectrum $B^{XYZ}_{\ell_1 \ell_2 \ell_3}$ which is non-vanishing if $|\ell_1 - \ell_2| \leq \ell_3 \leq \ell_1 + \ell_2$ (triangular condition) because of homogeneity and isotropy. Only the X, Y and Z combinations giving a scalar angular three-point (cross-)correlation function do not vanish, for the same reason as previously. Higher order angular correlation functions can also be defined likewise.

Predictions

The angular power spectra of the primary temperature and polarisation fields are computed once the transfer equations in the primordial Universe have been solved, as they are sourced by the primordial scalar and tensor power spectra

$$C_\ell^{XY} = \int \mathrm{d}k \left(\Delta^X_{\ell,\mathrm{S}}(k,\eta_0)\Delta^Y_{\ell,\mathrm{S}}(k,\eta_0)\mathcal{P}_\mathrm{S}(k) + \Delta^X_{\ell,\mathrm{T}}(k,\eta_0)\Delta^Y_{\ell,\mathrm{T}}(k,\eta_0)\mathcal{P}_\mathrm{T}(k) \right), \tag{4.53}$$

where X and Y stand for Θ, E or B and the $\Delta^X_{\ell,\mathrm{S/T}}$ are transfer functions that account for the evolution of the power spectrum of primordial inhomogeneities at the end of inflation during the early Universe and are integrals over the conformal time η. Some of these transfer functions vanish following the symmetry considerations developed below. The primordial power spectra contain information on the model of inflation and the initial conditions of the perturbations through the phenomenological parameters defined in Eq. (3.65) while the transfer functions are sensitive to the background cosmological parameters of Tab. 1.1.

The angular power spectra of the temperature, E and B modes with the TE cross power spectrum are plotted in Fig. 4.12. On the left the angular power spectra are generated by scalar perturbations while on the right are those generated by tensor perturbations. The B mode angular power spectrum on the left is solely due to the secondary effect of lensing by the large-scale structure, peaking at high ℓ corresponding to the angular scale of the large-scale structures in question on the sky. Indeed, let us recall that only tensor perturbations can produce a primordial component to the B mode for symmetry reasons, as explained in the previous section. In practice, one observes the superposition of the contribution from scalar and tensor perturbations. As the tensor contribution is smaller for the temperature and E mode angular power spectra from one to five orders of magnitude, it is difficult to use these to constrain the amplitude of the primordial tensor perturbations, i.e. the primordial gravitational waves, although they can be used to put upper bounds on the tensor-to-scalar ratio r. On the contrary, the primordial B modes being only produced by tensor perturbations, they are thus the unique signature of the primordial gravitational waves expected to be produced during inflation. The measurement of their power spectra at low ℓ would support the paradigm and give the amplitude of the primordial gravitational waves. Note the specific contribution of the SW, ISW and Doppler effects, introduced at the beginning of this section, on the CMB temperature power spectrum shown in Fig. 4.13.

The background cosmological parameters dictate the position of the peaks of the angular power spectra as well as their relative amplitude. Different set of cosmological parameters predict different angular power spectra, and fitting the data to these predictions enables to put constraints on the cosmological parameters, although there are some degeneracies. Similarly, the two types of initial conditions, adiabatic and isocurvature, also affect the position of the peaks and their relative amplitude, thus the Planck collaboration has put tight constraints on the possible amount of isocurvature perturbations in Planck Collaboration et al. (2018d). Fig. 4.14 shows the effect of the isocurvature mode on the CMB temperature and E mode power spectra for different models of isocurvature initial conditions: CDM, baryon, neutrino density and neutrino velocity isocurvature modes, as compared to purely adiabatic initial conditions in blue.

4.3.2 Secondary anisotropies

On top of the primary anisotropies of the CMB induced by the primordial fluctuations in the early Universe, secondary anisotropies are imprinted on the CMB radiation. Interestingly, these secondary anisotropies are also induced by the primordial fluctuations produced during inflation but which are not located where the CMB radiation we observe was emitted. Thus, these

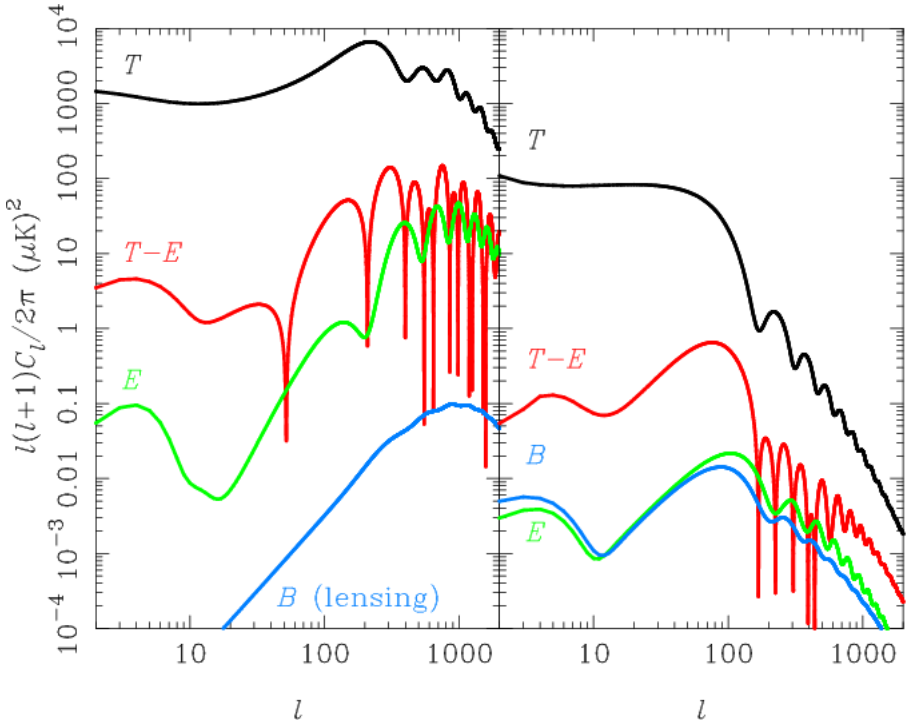

Figure 4.12: Angular power spectra of temperature and polarisation E and B mode fields. The cross power spectrum between temperature and E mode fields is also plotted (there is no TB or EB cross-correlation for symmetry reasons). On the left are the power spectra due to scalar perturbations while on the right are the power spectra due to tensor perturbations. There is no B mode generated by scalar perturbations, the one plotted is due to the secondary effect of lensing by large-scale structures. Figure taken from Challinor (2013).

primordial fluctuations have evolved into structures in the Universe before relic photons cross them on their way to us. This causes several effects on the primordial radiation: we will list some of them but this is not an exhaustive inventory (for a review see Aghanim et al., 2008).

Since decoupling, the first event in the history of the Universe that affects the primary relic radiation is Reionisation. Indeed, when the first stars and galaxies form, new photons are released in the Universe, and in particular UV photons so that they are able to reionise it. We have seen in Section 4.2.1 that this process can already affect the black body spectrum of the relic radiation because this injects energy in it. Actually, it also affects the anisotropies of the radiation because the new free electrons scattering the relic photons make it more isotropic. Reionisation affects both temperature and polarisation anisotropies through the thermal and kinetic Sunyaev-Zel'dovich (tSZ and kSZ) effects we will mention below.

We have mentioned in the introduction of this section 4.3 the Integrated Sachs-Wolf (ISW) effect, due to changing gravitational potentials: for example, forming structures have a gravitational potential that is changing over time, so that when a photon crosses it, it looses more energy when going out the potential than it earned falling in, resulting in a net negative balance. The gravitational potential also changes at late times at matter-cosmological constant equality, so that the cosmological constant leaves an imprint on the anisotropies of the CMB.

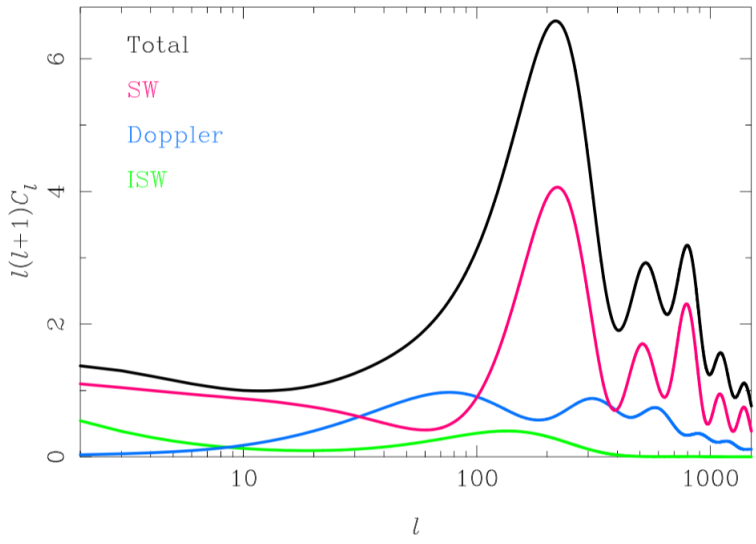

Figure 4.13: Contribution of the SW effect $\frac{\delta_\gamma}{4}+\psi$ (magenta); Doppler effect from velocity (blue); and the ISW effect (green) coming from the evolution of the potential along the line of sight. The units of the spectrum are arbitrary. Figure taken from Challinor & Peiris (2009).

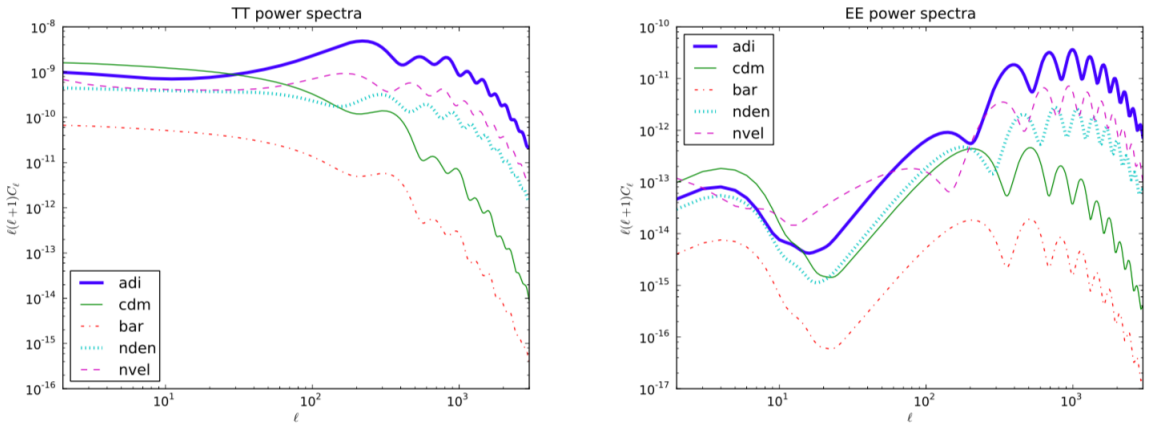

Figure 4.14: Angular power spectra for the temperature (left) and E mode (right) obtained from purely adiabatic or purely isocurvature initial conditions. Figure taken from Langlois (2012).

The tSZ effect already mentioned happens in large-scale structures like galaxy clusters or filaments. These structures are made of hot plasma with temperature around 10^7 K. Therefore, inverse Compton scattering takes place with the free electrons inside the structures: the hot electrons warm up the photons of the relic radiation. This can thus distort the black body spectrum of the photons by shifting it to higher frequencies and decrease the low frequency part of the spectrum: this is exactly the Compton distorsion described in Section 4.2.2. This effect also induces secondary anisotropies in the CMB by changing its temperature locally on the sky

by (Sunyaev & Zeldovich, 1972; Birkinshaw, 1999; Carlstrom et al., 2002)

$$\Delta T_{\rm SZ} = -2\frac{k_{\rm B}}{m_e c^2}\int_{-L_{\rm max}}^{L_{\rm max}} T_e n_e {\rm d}\ell, \tag{4.54}$$

where T_e and n_e are the temperature and number density of the free electrons respectively, and we have integrated over the line-of-sight (L.O.S.), $L_{\rm max}$ being the characteristic length of the structure along the L.O.S.. If the structure is also moving with velocity v with respect to the CMB, there is an additional Doppler effect on top of the inverse Compton scattering: this effect on the CMB is called the kSZ effect and depends on the radial component of the velocity (Rephaeli & Lahav, 1991; Nozawa et al., 1998).

Finally, other effects induce secondary polarisation anisotropies. This is the case of weak lensing, which is the deflection of the primordial light by gravitational potentials (like galaxy clusters) on their way to us. It also impacts temperature anisotropies but the effect is more important on polarised anisotropies, converting some E modes into B modes and vice-versa. The third part of this thesis is dedicated to two effects producing secondary polarised anisotropies: the Faraday Rotation and Faraday Conversion effects in galaxy clusters. These effects peak at small angular scales, typical of the size of a cluster on the sky, i.e. around $\ell \sim 10000$. The Faraday Rotation effect being very similar to the lensing one, it could bias its reconstruction, even though lensing peaks at larger angular scales $\ell \sim 1000$. Fig. 4.15 shows the impact of secondary anisotropies on the CMB temperature angular power spectrum.

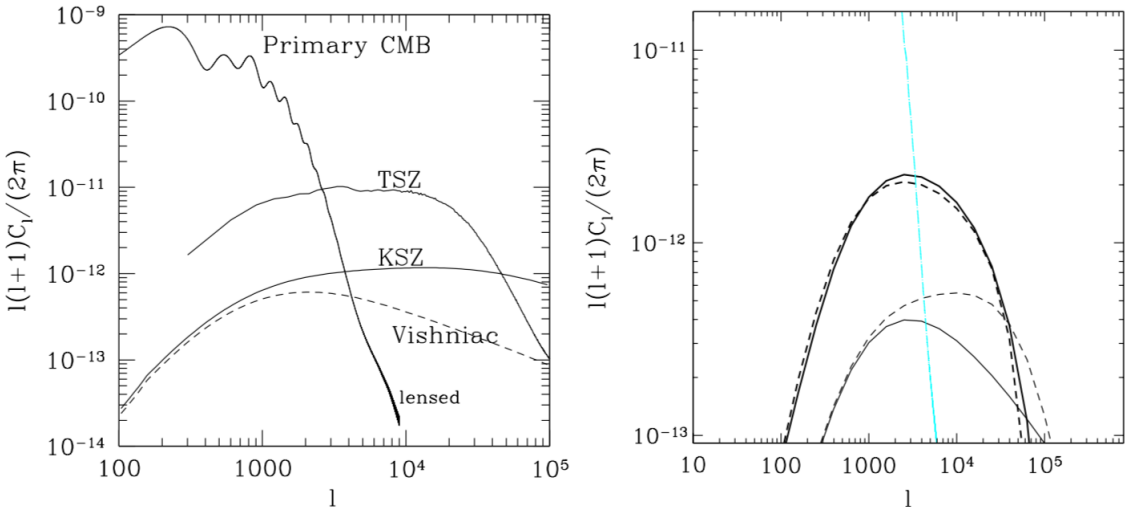

Figure 4.15: Left: the temperature anisotropies induced by the kSZ effect predicted from the numerical simulations of Zhang et al. (2004). For comparison, the contribution from the linear regime, Ostriker-Vishniac effect, is plotted in dashed line, as well as the primary power spectrum and thermal SZ spectrum. Right: secondary anisotropies produced by reionization predicted analytically by Santos et al. (2003). Top thick lines are for the inhomogeneous reionization-induced fluctuations, while bottom lines are for density-induced fluctuations. The solid thin line is for the linear Ostriker-Vishniac effect and the dashed one for the non-linear contribution to this effect. Figure taken from Aghanim et al. (2008).

Relation to spatial correlation functions

So far, we have only dealt with angular correlation functions and their corresponding angular spectra, that is correlations among directions on the celestial sphere or equivalently, deviations from uniformity at a given angular scale. However, we have argued in Section 4.1.2 that the decoupling of photons is not instantaneous and that the LSS is not properly a surface but has a relatively small thickness compared to the age of the Universe when photons were released. Thus, in full generality, one would have to consider the three dimensional spatial correlation functions of the temperature and polarisation fields. This is even more so relevant when computing the angular power spectra of the secondary anisotropies of the CMB, as one needs to integrate over the whole history of the photons since decoupling, so that there is more depth than for primary anisotropies, and we cannot only rely on the information on the celestial sphere but we need to model it in the three-dimensional space. The spatial and angular correlation functions are related by integrating along the L.O.S.. For example, for the spatial two-point (cross-)correlation function $\xi^{XY}(r_{12})$ and its angular counter-part w

$$w^{XY}(\psi) = \int \mathrm{d}r_1 F_X(r_1) \int \mathrm{d}r_2 F_Y(r_2)\, \xi^{XY}(r_{12}), \tag{4.55}$$

where $F_X(r_1)$ and $F_Y(r_2)$ are two projection kernels of three-dimensional physical effects on the sphere, X and Y stand for the two fields considered. If $\boldsymbol{r}_1$ and $\boldsymbol{r}_2$ are the position vectors of the two points 1 and 2 considered, then the difference between these two positions defines $\boldsymbol{r}_{12} \equiv \boldsymbol{r}_1 - \boldsymbol{r}_2$. Again, homogeneity tells that the spatial two-point correlation functions do not depend on the specific positions $\boldsymbol{r}_1$ and $\boldsymbol{r}_2$ but only on their difference $\boldsymbol{r}_{12}$ and isotropy tells that ξ should not depend on the direction between the two positions, so it only depends on the distance between them $r_{12} = |\boldsymbol{r}_{12}| = \sqrt{\boldsymbol{r}_1^2 + \boldsymbol{r}_2^2 - 2\boldsymbol{r}_1 \cdot \boldsymbol{r}_2} = \sqrt{\boldsymbol{r}_1^2 + \boldsymbol{r}_2^2 - 2r_1 r_2 \cos(\psi)}$. This equation is similar to the relation between the angular power spectrum of primary anisotropies and the primordial power spectra of scalar and tensor perturbations Eq. (4.53). Indeed, the projection kernels $F_X(r_1)$ and $F_Y(r_2)$ are the equivalent in real space of the transfer functions $\Delta^X_{\ell,\mathrm{S/T}}(k, \eta_0)$ accounting for the evolution since decoupling, as they contain an integration up to today of the visibility function which peaks at Recombination and Reionisation. The spatial three-point correlation function ζ and higher order statistics are related likewise to their angular counterparts.

Finally, the usual Fourier transform of the spatial two-point correlation function defines the power spectrum

$$\langle \tilde{X}(\boldsymbol{k}) \tilde{Y}^*(\boldsymbol{k}') \rangle = (2\pi)^3 \delta^3(\boldsymbol{k} - \boldsymbol{k}') P^{XY}(k), \tag{4.56}$$

where $\tilde{X}(\boldsymbol{k})$ and $\tilde{Y}(\boldsymbol{k}')$ are the Fourier transforms of the 3D fields X and Y. Statistical homogeneity requires that the Fourier components of different $\boldsymbol{k}$ are statistically independent and the power spectrum $P^{XY}(k)$ only depends on the norm of the wavevector k as a result of statistical isotropy.

The Limber approximation

A lot of the secondary effects on the CMB happen in the large-scale structures formed since then, and in particular the galaxy clusters. A useful trick when one wants to correlates two directions on the sky with small angular separation, or equivalently, large multipole ℓ, like for example the correlation between two points belonging to the same galaxy cluster (which corresponds to what is called the '1-halo' term of the two-point correlation function) is the Limber approximation (Limber, 1953; LoVerde & Afshordi, 2008). With the previous introduced notations, one can relate the angular power spectrum to the standard power spectrum by taking the

Fourier transform of the fields X and Y

$$C_\ell^{XY} = \int \mathrm{d}r_1 F_X(r_1) \int \mathrm{d}r_2 F_Y(r_2) \int \frac{\mathrm{d}^3\boldsymbol{k}}{(2\pi)^3} P^{XY}(k)(4\pi)^2 j_\ell(kr_1) j_\ell(kr_2) Y_\ell^m(\hat{\boldsymbol{k}}) Y_\ell^{m*}(\hat{\boldsymbol{k}}), \quad (4.57)$$

where we have used

$$e^{i\boldsymbol{k}\cdot\boldsymbol{r}} = 4\pi \sum_{\ell m} i^\ell j_\ell(kr) Y_\ell^{m*}(\hat{\boldsymbol{k}}) Y_\ell^m(\hat{\boldsymbol{n}}), \quad (4.58)$$

and the orthonormality relation Eq. (4.14). The j_ℓ are the spherical Bessel functions of the first kind, related to the Bessel functions of the first kind J by

$$j_\ell(z) = \sqrt{\frac{\pi}{2z}} J_{\ell+1/2}(z). \quad (4.59)$$

By performing the integral over the solid angle to remove the spherical harmonics, the angular power spectrum thus becomes

$$C_\ell^{XY} = \int k\,\mathrm{d}k P^{XY}(k) \int \mathrm{d}r_1 \frac{F_X(r_1)}{\sqrt{r_1}} J_{\ell+1/2}(kr_1) \int \mathrm{d}r_2 \frac{F_Y(r_2)}{\sqrt{r_2}} J_{\ell+1/2}(kr_2). \quad (4.60)$$

The Limber's approximation consists in the expansion of the integral of a function multiplied by a Bessel function, which leads to

$$C_\ell^{XY} = \int \frac{\mathrm{d}k}{k} P^{XY}(k) \frac{F_X(r)}{\sqrt{r}} \frac{F_Y(r)}{\sqrt{r}} \quad \text{with} \quad r = \frac{\ell + 1/2}{k}. \quad (4.61)$$

Higher order corrections exist to this approximation and can be found in LoVerde & Afshordi (2008).

The statistics introduced in this chapter are not only useful to study the temperature and polarisation random fields of the CMB, but also are almost unavoidable when doing observational cosmology to treat observations. Indeed, the large amount of data encountered when studying the CMB is not proper to this field but is characteristic of cosmology since the second part of the XX$^{\text{th}}$ century. These tools (and the Limber approximation) are thus also convoked to study other random fields like the mass density fluctuations field, the galaxy distribution (with Poissonian statistics) or the gravitational potential field $\Phi(\boldsymbol{x})$ used to describe for example the effect of weak lensing of the CMB. We will use them in Chapter 8 to study the Faraday Rotation and Faraday Conversion effects in galaxy clusters.

4.3.3 Reconstruction of the angular power spectra

Up to now we have been very theoretical in defining the statistics one can use to extract information about our Universe as they depend, among other things, on the cosmological parameters. However, the statistics observed are not quite the statistics predicted theoretically from a model. Indeed, the theoretical predictions involve averaging over an ensemble of realisations of universes, while observations only give access to a unique realisation of universes: our observable Universe. Fortunately, the isotropy hypothesis on our Universe allows to measure, for example, the angular two-point correlation function as an average over the whole sky. One thus implicitly assumes an ergodic hypothesis about our observable Universe, that is, the correlation functions computed statistically as averages over different realisations of universe are equal to the averages of measures over the whole sky. This 'spatial' ergodic hypothesis is what enables to relate the theory

to observations. As the two kind of correlation functions are not quite the same, one needs to build estimators of the statistical theoretical predictions to compare them to observations. For example, for the angular power spectrum of the CMB with primary and secondary anisotropies C_ℓ, one builds an estimator as follows

$$\hat{C}_\ell = \frac{1}{2\ell+1}\sum_m a_{\ell m} a^*_{\ell m}. \tag{4.62}$$

Indeed, statistical isotropy involves that the angular power spectrum C_ℓ does not depend on the multipole m indicating the orientation on the sphere. Thus, the observed angular power spectrum is obtained by taking the average over orientations, that is by summing over m the observed harmonic coefficients which are statistically independent, and dividing by their number equals to $2\ell+1$

$$C^{\rm obs}_\ell = \frac{1}{2\ell+1}\sum_m |a^{\rm obs}_{\ell m}|^2, \tag{4.63}$$

so that the observed angular power spectrum is a measure of the estimator $\hat{C}_\ell$. Now, taking the average of this estimator over universe realisations, one gets

$$\langle \hat{C}_\ell \rangle = C_\ell, \tag{4.64}$$

this property gives the qualifier of unbiased to the estimator. Its variance can be computed and one gets

$$\langle \hat{C}^2_\ell \rangle - \langle \hat{C}_\ell \rangle^2 = \frac{2}{2\ell+1} C^2_\ell, \tag{4.65}$$

this variance is the smallest one can get so $\langle \hat{C}_\ell \rangle$ is the best estimator of C_ℓ. However, for a given ℓ, there are only $2\ell+1$ independent modes to estimate the angular power spectrum and therefore there is a relative uncertainty on the observed one

$$\frac{\langle \hat{C}^2_\ell \rangle - \langle \hat{C}_\ell \rangle^2}{C^2_\ell} = \frac{2}{2\ell+1}, \tag{4.66}$$

which is the largest at low ℓ. This inherent statistical uncertainty is called the cosmic variance.

In practice, this comparison between theoretical predictions and observations is not so easy. The estimator above is built in the ideal case of a complete sky coverage. In real life, some proper foreground emissions pollute the CMB signal which are not secondary anisotropies, like for example the emission by our Galaxy. The easiest way to remove these is to apply a mask on the observed sky, so that one has an incomplete sky coverage. This has the effect to break the statistical isotropy so that the covariance matrix now gets off-diagonal coefficients. This is thus more difficult now to build an estimator of the angular power spectra. When the primordial scalar and tensor perturbations do not have Gaussian statistics, the angular power spectra do not characterise completely the statistics and the construction of an optimal estimator is more difficult.

Conclusion

The CMB is a cosmological observable that allows to both probe the primordial Universe with its primary anisotropies and understand its recent matter structuring thanks to the secondary anisotropies. The next part is dedicated to the prediction of primordial adiabatic and isocurvature power spectra in an LQC model of the early Universe while the third part to the prediction of secondary polarised anisotropies due to the Faraday Rotation and Faraday Conversion effects in clusters of galaxies.

Part II

Primary anisotropies of the CMB

Chapter 5

A quantum theory of gravitation: Loop Quantum Gravity

5.1 Theory: a brief introduction to LQG

5.1.1 Why quantising gravity?

Before presenting the theory of Loop Quantum Gravity (LQG hereafter), I would like to say a few words on the *need* to quantise gravity. It might seem obvious that GR has to be quantised: after all, we know that the theory has some theoretical limitations. If applied to the whole Universe through the FLRW metric, and with the help of thermodynamics, it predicts a singularity when going backwards in time: the Big Bang singularity. Indeed, we know from Hubble's observations in 1929 that the Universe is expanding, meaning that when going backwards in time, the Universe should be contracting: actually, until such a point where curvature becomes infinite. The centers of black holes are also space-time points where a singularity is predicted. Black holes are GR predicted space-time regions where the gravitational field is so strong that anything which enters cannot escape from it, even light which travels at the highest speed one can reach. Thus, matter keeps accumulating and actually concentrating inside black holes, strengthening the gravitational field which is stronger and stronger the more one gets inside it: again until such a point where the curvature becomes infinite. There are thus a lot of similarities between the very Early Universe and the inside of black holes. That GR predicts singularities with curvature becoming infinite is one thing, but another thing is that from Einstein equations, this implies that energy densities should also become infinite. Thermodynamics predicts then that these singular space-time points must be very hot, hence energetic. Thus, one would also need the usual quantum field theory of interactions (the Standard Model of particle physics) to describe what happens in these space-time regions, both with GR, since they probe the strong field regime of the theory. Anyway, one could think of a theory where one has classical GR interacting with quantum fields, like the developments of quantum field theory in curved space-times (Birrell & Davies, 1984) and semi-classical gravity. Another idea is the one of Verlinde (2011, 2017) where gravity is seen as an emergent phenomenon.

We can question the need to quantise gravity; anyway the theory I will expose below proposes a non-perturbative quantisation of GR, which has to be distinguished from other attempts to *unify* gravity with the other three fundamental interactions, that for their part are already quantised. An example of these theories is string theory, probably the most popular of them, just to cite one. LQG does not have this ambition, even though to some physicists unifying

gravity with the three other fundamental quantum field interactions may be the only way to quantise it. LQG is an attempt to quantise only gravity, without the aim of finding the underlying common symmetry that would unify it with the other three fundamental interactions. There have been other attempts in the past to quantise gravity only, one of them being the perturbative quantisation. In this attempt, GR is approximated by flat space-time plus small perturbations. It led to the problem of non-renormalisability of the quantum field theory, meaning the perturbative expansion of the theory has divergent terms. However, we must stress that quantum field theory is not perturbative by nature. Hence, the failure to quantise gravity perturbatively led to the developments of the non-perturbative quantisation of GR, and later to LQG.

5.1.2 Hamiltonian formulation of GR

We have seen in Eq. (1.4) that GR is formulated in terms of the Einstein-Hilbert action S

$$S = \frac{1}{16\pi \mathrm{G}} \int \mathrm{d}^4x\sqrt{-g}R, \tag{5.1}$$

that has to be extremised following the variational principle to get the Einstein equations. Here, g is the determinant of the metric $g_{\mu\nu}$ and R is the scalar curvature. It is an integral over space-time so that the part which is the integral over space is the Lagrangian L of the theory. GR is thus a theory treated within the Lagrangian framework. However, either quantum mechanics of particles or quantum field theories are casted in a Hamiltonian formulation. This comes from the procedure of canonical quantisation. Theories are usually[1] quantised following that procedure: to do so, their classical formulation have first to be expressed in the Hamiltonian formalism with a set of canonical variables $\{q_i, p_i\}$ for quantum mechanics or $\{\phi_a(x), \tilde{\pi}_a(x)\}$ for quantum field theories, where the a index labels the possible components of the field or the possible multiple fields of the theory considered. The space of the $\{q_i\}$ or $\{\phi_a(x)\}$ is called configuration space. As we are interested in quantising GR, which is a field theory, from now on we will focus on the Hamiltonian formulation of field theories. $\tilde{\pi}^a$ is the conjugate momentum of the configuration variable ϕ_a defined by $\tilde{\pi}^a \equiv \delta L/\delta\dot{\phi}_a$, where δ is the functional derivative. In principle, one can easily go from the Lagrangian formulation of a theory to its Hamiltonian formulation thanks to a mathematical transform called Legendre transform

$$\mathcal{H}(\varphi_a, \tilde{\pi}_a) = \int \mathrm{d}^3x(\tilde{\pi}^a(x)\dot{\phi}_a(x) - \tilde{\mathcal{L}}), \tag{5.2}$$

where $\tilde{\mathcal{L}}(x)$ is the Lagrangian density. In the case of GR, it is given by $\tilde{\mathcal{L}} = \sqrt{-g}R/(16\pi\mathrm{G})$ and the usual Lagrangian is simply $L = \int \mathrm{d}^3x\tilde{\mathcal{L}}$. After all, analytical mechanics is just about finding the right variables. Well, it took a while (about 50 years!) for physicists working in the field of canonical quantisation of gravity to find the right ones, that would ease the calculations. In the following we will catch a glimpse of the path taken to find the variables of LQG.

5.1.2.1 The 3+1 decomposition

If it was so difficult for physicists to find the Hamiltonian formulation of GR, this is because in the Hamiltonian formalism one has to treat differently space and time, while GR puts on an equal footing these two variables. Indeed, the canonical variables introduced above $\{\phi_a(x), \tilde{\pi}_a(x)\}$ are functions of the position x only, given at each time t. Because in the Hamiltonian formalism,

[1] The Feynman path integral formulation is another way to quantise a theory, however way more computationally difficult.

physical quantities evolve in time, that equal footing will unfortunately have to be broken to find a Hamiltonian formulation of GR. This is done through a foliation of space-time, see Fig. 5.1. The topology of space-time is thus chosen to be $\Sigma \times \mathbb{R}$, where Σ is a three-dimensional manifold

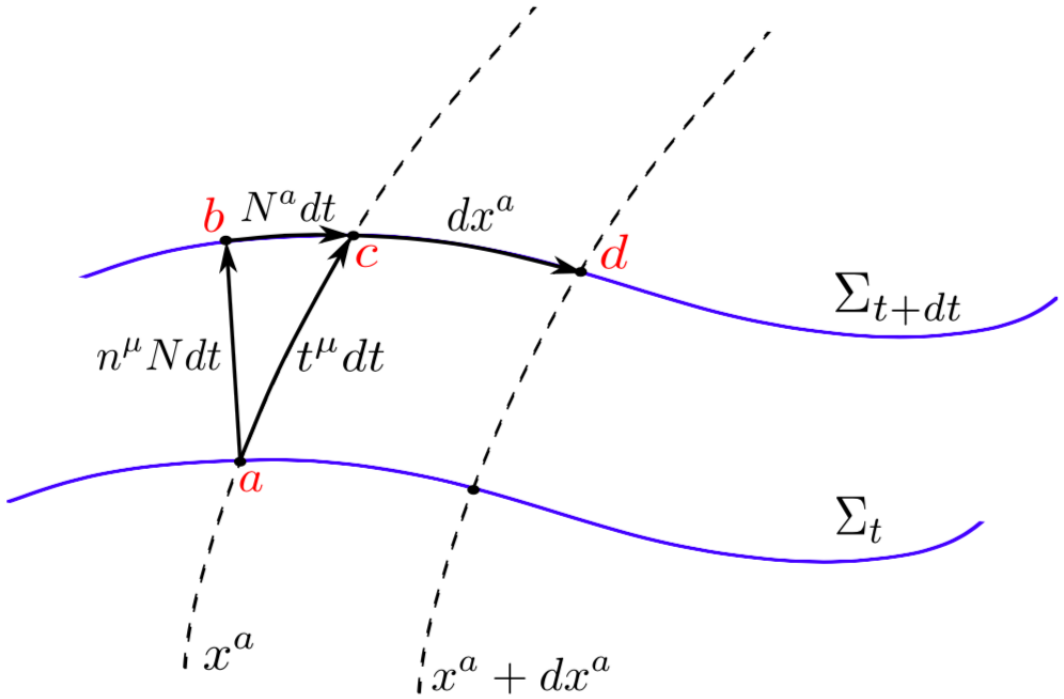

Figure 5.1: A space-time foliation with space-like hypersurfaces Σ_t. Figure taken from Grain (2014).

modeling the space-like surfaces and the real line is the time-like direction. The time-like direction is given by a 4-vector t^μ whose world-line is parameterized by t so that the spatial slices Σ are the t = constant surfaces. We can also introduce a 4-vector field n^μ normal to Σ so that the spatial metric on Σ is given by:

$$q_{ab} \equiv g_{ab} + n_a n_b. \tag{5.3}$$

We recall that the latin indices a, b go from 1 to 3 and the greek indices μ, ν from 0 to 3. We must notice that $t^\mu \neq n^\mu$ so we can decompose t^μ in components normal and tangential to Σ

$$t^a = N n^a + N^a \quad \text{and} \quad t^0 = N. \tag{5.4}$$

N is called the lapse and N^a the shift vector: notice this is a regular 3-vector belonging to Σ. We now have everything needed to write the space-time metric

$$\mathrm{d}s^2 = (-N + N_a N^a)dt^2 + 2N_a \mathrm{d}t\mathrm{d}x^a + q_{ab}\mathrm{d}x^a\mathrm{d}x^b. \tag{5.5}$$

This is called the 3+1, or ADM decomposition, standing for the names of the physicists who first introduced it (Arnowitt et al., 2008).

Another relevant quantity that is central in a Hamiltonian formulation of GR is the extrinsic curvature

$$K_{ab} = \frac{1}{2}\mathcal{L}_n q_{ab}, \tag{5.6}$$

where $\mathcal{L}$ is here the Lie derivative, which is a derivative along a vector n^c. The extrinsic curvature thus tells how the spatial metric q_{ab} evolves along the normal to the spatial surfaces n^μ, so in a sense how the spatial slices evolve when viewed from the whole space-time: this is the concept of extrinsic curvature. It is different from the intrinsic curvature which would tell if the spatial slices are intrinsically curved, like a 2-sphere, but not like a cylinder. The cylinder has an extrinsic curvature that can only be seen when plunged into a higher three-dimensional space. Similarly, the fact that a 2-sphere is expanding in time or not can only be grabbed by the notion of extrinsic curvature, if here the 2-sphere is plunged into a higher 2+1 dimensional space-time. Indeed, as there is a relation between the time-like vector t^μ and the normal n^μ to the spatial slices Eq. (5.4), the extrinsic curvature is related to the time derivative of the spatial metric q_{ab}:

$$\dot{q}_{ab} \equiv \mathcal{L}_t q_{ab} = 2NK_{ab} + \mathcal{L}_{\boldsymbol{N}} q_{ab}. \tag{5.7}$$

We now have the canonical variables to write GR in the Hamiltonian formalism: q_{ab} is the configuration variable and its conjugate momentum is related to the extrinsic curvature K_{ab}. The information of GR is therefore encoded in the spatial metric and its time derivative, or the extrinsic curvature. As we will soon see, the 'loop' in LQG refers to this notion of curvature.

5.1.2.2 GR: a totally constrained system

As I said, analytical mechanics is just about finding the right variables: indeed, a system can be described using different set of canonical variables $\{q_i, p_i\}$ or $\{J_j, \theta_j\}$ where i and j are indices running over the number of configuration variables used. This number can be bigger than the number of degrees of freedom of the system, meaning we are using more variables than what is really necessary. However, the use of a set of canonical variables may turn out to be more convenient than using another one. This might also be due to a lack of knowledge about the degrees of freedom of a system. Anyway, when this is the case, one has to compensate this too high number of variables by adding constraints between them. Constraints are relations between the canonical variables that are always satisfied, for example: $C(\phi_a, \pi_a) = 0$. In this case, the constraint is also a conserved quantity. Now from Noether's theorem, we know that conserved quantities correspond to symmetries in the system or theory. Indeed, if we have m constraints $C_i = 0$, the total Hamiltonian is given by

$$\mathcal{H}_{\text{tot}} = \mathcal{H} + \sum_{i=1}^{m} \lambda_i C_i, \tag{5.8}$$

where $\mathcal{H}$ is the original Hamiltonian of the system and the λ_i are called the Lagrange multipliers which can be time dependent. These Lagrange multipliers are unknowns of the system, like the canonical variables. Suppose one has n configuration variables, one will have $2n$ equations of motion given by the Hamilton equations. Given the $2n$ initial conditions, the solution will depend on m additional unknowns. The solutions are then all related to each other by the symmetries of the system corresponding to the constraints C_i. Note that the total Hamiltonian is a function of the canonical variables, not of the solutions of the Hamilton equations giving the canonical variables. Hence, the C_i appearing in the total Hamiltonian are the relations between the canonical variables but for the constraint to be zero, it has to be taken on the solutions of the Hamilton equations.

In the case of GR, the configuration variable is the spatial metric q_{ab} which is a symmetric tensor, hence the theory has six configuration variables. However we know that GR has only two degrees of freedom, the two possible polarizations of gravitational waves. Thus, formulated with these canonical variables, the theory needs to have four constraints. One of them is called

the Hamiltonian constraint and is associated with the lapse N, which is actually a Lagrange multiplier. It represents the time invariance reparameterisation of the theory: $\mathcal{H} = 0$, or the invariance of the theory under deformations of the spatial surfaces since time can be reparameterised at any point in space. The other three constraints are a vector constraint associated with the shift vector N^a. The related symmetries are spatial diffeomorphisms: GR is indeed invariant under spatial coordinate transformations. The total Hamiltonian of the theory is thus only a sum of the constraints times Lagrange multipliers: GR is what is called a totally constrained system.

We will now move to a new set of canonical variables, the Ashtekar's variables, named after the physicist who introduced them in 1986.

5.1.2.3 Ashtekar's variables

The Ashtekar's variables were introduced to make the theory look like the other three fundamental quantum field theories,[2] in the hope to use the mathematical framework of quantum field theories in order to quantise gravity. Let us recall that in the Hamiltonian formulation of GR, the configuration variables are the spatial metric q_{ab} of the spatial slices Σ and its conjugate momentum is related to the extrinsic curvature K_{ab}. We rewrite the spatial metric like

$$\tilde{\tilde{q}}^{ab} = \det(q) q^{ab} = \tilde{E}^a_i \tilde{E}^b_j \delta^{ij}, \tag{5.9}$$

$\tilde{E}^a_i$ are three vector fields ($i = 1, 2, 3$) that are orthogonal and called the densitised triads. The tilde denotes the absorption of a $\sqrt{\det(q)}$ in the definition of quantities like metric or vectors and gives the attribute of "densitised". What we can see on this last expression is a mapping between a possibly curved space q_{ab} and flat space δ_{ij}. The indices i, j are said to be the internal indices of the theory. Then, instead of using the spatial metric q_{ab} as canonical variables, one can instead use the densitised triads $\tilde{E}^a_i$. These are ones of the Ashtekar's canonical variables, the other ones being related to the extrinsic curvature by:

$$A^i_a = \Gamma^i_a + \beta K^i_a, \tag{5.10}$$

where $\Gamma^i_a = \Gamma_{ajk}\epsilon^{jki}$ and $\Gamma_a{}^j{}_k$ is called the spin connection, $K^i_a = K_{ab}\tilde{E}^{bi}/\sqrt{\det(q)}$ and β is called the Barbero-Immirzi parameter. The spin connection is the same kind of object as the usual connection used in GR, or Christoffel symbol. It is used to define a kind of covariant derivative with respect to spatial coordinates but for objects with internal indices and it is actually completely determined by the usual connection (Christoffel symbol). To complicate a little bit, the A^i_a are also called connections: to be precise, they are $su(2)$ connections. With these variables, the situation is reversed with respect to the Hamiltonian formulation of GR that we introduced above: the A^i_a are the configuration variables and their conjugate momentum are the densitised triads $\tilde{E}^a_i$. There are thus nine configuration variables here, while the theory still has only two degrees of freedom. Thus, in this formulation, there has to be seven constraints. The Hamiltonian constraint is still one of them, so that the total Hamiltonian of the theory is again the sum of the constraints times Lagrange multipliers.

A lot, but not all of the difficulties in quantising gravity came from the Hamiltonian constraint. Indeed, the Hamiltonian itself is a constraint: $\mathcal{H} = 0$. However, the Hamiltonian is always the energy of the system considered. When the Hamiltonian does not depend on time, the energy is therefore conserved and from Noether's theorem it means that the system is invariant in time or stated otherwise, there is no time evolution of the system. As we already noticed, this is

[2] To be more precise, written in terms of these variables, the theory looks like a Yang-Mills theory or gauge theory.

exactly what happens in GR: the theory is invariant under reparametrisation of time, hence it is not surprising that the Hamiltonian is a constraint. However, we should emphasize that the canonical variables we are using here in the 3+1 decomposition are defined on the spatial surfaces Σ. As is always the case for any system, the Hamiltonian generates its time evolution, hence it will not have a simple geometric action on these variables. Therefore, when it comes to quantising gravity, it is difficult to find the wavefunctions of the configuration variables $\Psi[A]$ (these are the states used in the connection representation, where connection here refers to the variable A_a^i) that would be annihilated by the Hamiltonian. So it might be that we have not quite well chosen the variables to work with. This is one of the reasons why the variables of LQG have been introduced; we will present them in the following.

5.1.3 Quantisation using loops

As we have stressed in the introduction, LQG is a non-perturbative quantisation of GR. Even though the quantum version of the three other fundamental field theories is usually worked out perturbatively, their canonical formulation with a Hamiltonian and canonical variables have the same structure as GR formulated with Ashtekar's variables. The quantisation of the theory with these variables led to the connection representation but unfortunately, it came along with some technical difficulties. The loop representation of LQG helped solving these difficulties. We go from the connection representation to the loop one thanks to the loop transform:

$$\Psi[A] = \sum_{\gamma} \Psi[\gamma] W_\gamma[A], \tag{5.11}$$

where we have expanded the state $\Psi[A]$ onto the basis formed by the $\{W_\gamma[A]\}$ which are the traces of holonomies of the connection:

$$W_\gamma[A] = \mathrm{Tr}\left(P\left[\exp\left(-\oint_\gamma \dot{\gamma}^a(s)\mathbf{A}_a(s)\mathrm{d}s\right)\right]\right). \tag{5.12}$$

The integral inside the exponential is the generalisation of the notion the circulation of a vector field on a closed loop γ. $\dot{\gamma}^a(s)$ is the tangent vector of the loop and the vector field is just the $su(2)$ connection A_a^i. The index a translates the fact it is a spatial 3-vector and the bold font reminds us its components are $su(2)$ matrices. The exponential of the resulting matrix is defined by the Taylor expansion of the exponential. However the products of integrals over s have to be ordered by increasing values of the parameter from the right to the left, as the matrices do not commute and this is the reason of the appearance of the P operator, which stands for path ordered. The trace is finally taken and the resulting object is called a holonomy of the connection[3].

In the loop representation, the states basis is almost given by the holonomies $\{W_\gamma[A]\}$. The situation is very similar to quantum mechanics where one goes from the real space representation with wavefunctions of the space variables to the momentum representation where states are wavefunctions of the momentum p by a Fourier transform which is an expansion on the states basis $\{\exp(ikx)\}$. Thus, in the loop representation, the states are wavefunctions of the loop γ: $\Psi[\gamma]$.

Actually the loop basis $\{W_\gamma[A]\}$ is overcomplete, meaning that all the states are not independent from each other. To overcome this problem, one instead uses spin network states basis ψ_s which is based on spin networks s.

[3]It is a particular case of a parallel propagator as it is along a closed curve

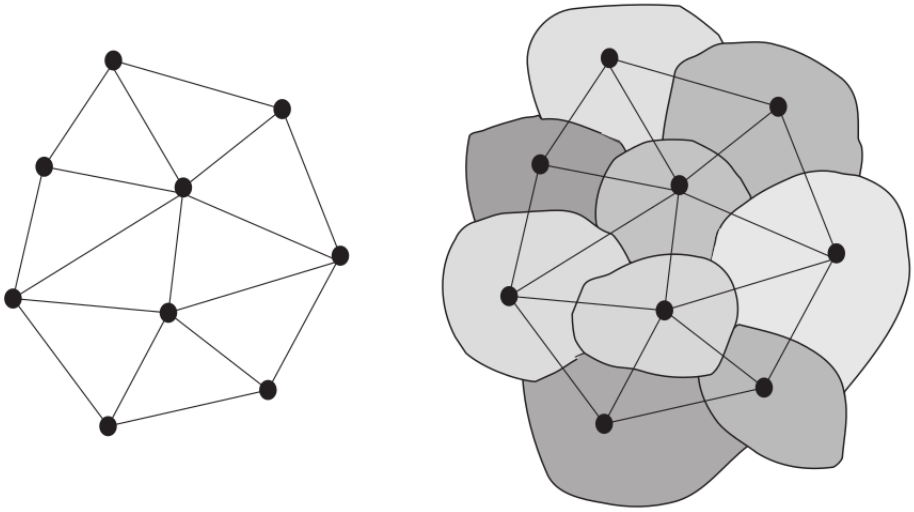

Figure 5.2: On the left is the graph of an abstract spin-network, the nodes of which represent the quanta of space-time illustrated on the right in different shades of grey. Linked nodes indicate adjacent elementary volumes. Figure from Rovelli (2004)

Some of the difficulties encountered during quantisation with the Hamiltonian constraint are solved thanks to the use of this states basis. It also helps us visualise the geometric interpretation of LQG: the spin network is not a discrete version of space but the dual of it. Actually, real space volumes correspond to vertices and areas to lines of the spin network (cf Fig. 5.2). Even though many of the technical problems of LQG have been resolved with these variables, the theory is still incomplete.

5.2 Potential footprints of LQG

Unfortunately, the effects of LQG are expected to be seen at energy, length and time scales orders of magnitude away from the current experiments physicists do: in fact around the Planck scale ($\sim 10^{16}$ TeV) which is fifteen orders of magnitude higher than the energy reached at the LHC (7 TeV). One can have more hope by looking at our observational laboratory being the Universe, where some astrophysical events involve higher energies. For example, historically the photons of gamma ray bursts have been thought to potentially bear traces of quantum gravity effects. Indeed, the discrete nature of space-time would change the dispersion relation for photons so that high energy photons travel faster than lower energy ones and one would see delays in the arrival time of rays of different frequencies in the gamma rays (Amelino-Camelia et al., 1998; Gambini & Pullin, 1999).

Other astrophysical objects to look at when searching for quantum gravity effects are black holes. Hawking (1971) and Bekenstein (1973) computed the entropy of a black hole to be proportional to its area, from GR considerations. The same formula has been computed starting from the more 'fundamental' LQG theory, fixing the value of the Barbero-Immirzi parameter $\beta = 0.274067$. This, is not an observable effect of LQG but the consistency with other classical considerations enables to constrain the parameter of the theory. However, the full study of the

geometry of a black hole horizon in LQG does lead to an observational effect as it predicts quantum gravity corrections to the Hawking radiation of evaporating black holes. The quantum corrections translate into a set of discrete frequencies on top of the thermal radiation spectrum predicted by Hawking for black holes which could potentially be seen if one observed the radiation emanating from a black hole (Bekenstein & Mukhanov, 1995; Barrau et al., 2011). Still about black holes, recent research suggests that due to quantum repulsive effects, there is no singularity inside a black hole but instead what is called a Planck star Rovelli & Vidotto (2014) which could be a transition state between a black hole and a white hole (Barrau et al., 2014b; Barrau & Rovelli, 2014).

Finally, the application of the LQG quantisation techniques to the system Universe with the homogeneity and isotropy symmetries, encoded in the FLRW metric, leads to the field of Loop Quantum Cosmology (LQC) and replaces the big bang singularity by a quantum big bounce. The early Universe is thus another laboratory to test the LQG theory. In particular, the perturbations expected to be produced during inflation in the standard model of cosmology are modified by the pre-inflationary dynamics that contain quantum gravity corrections (Bolliet et al., 2016; Barrau et al., 2014a). Part of this thesis deals with the phenomenology of LQC and its observational effects, and we will explain these last considerations in more details in the next two chapters.

Chapter 6

Application to the early Universe: Loop Quantum Cosmology

Loop quantum cosmology (abbreviated by LQC) is an application of the LQG theory to the particular system Universe. Unlike gravity, cosmology is not a fundamental theory but a science that uses GR and other physical theories to describe the Universe. It is thus natural to apply the LQG theory to the whole Universe, as GR was applied soon after its publication to the whole Universe, in 1917. It later led to its description in terms of the FLRW metric we described in Chapter 1, Section 1.1.1. It is especially natural because this description predicts a singularity at the origin of the Universe, where quantum effects have to be taken into account within the strong field regime of GR. But how do we apply LQG to the whole Universe? One would naturally think we should wait for the theory to be complete in order to apply it to this system. Indeed, GR was well established by the time it was applied to the whole Universe to later lead to the current Standard Model of Cosmology, ΛCDM. In particular, it would require to find the states annihilated by the constraints, and among them the Hamiltonian constraint, and then take the ones that are on average homogeneous and isotropic (because of the Heisenberg uncertainty principle, states can have fluctuations around homogeneity and isotropy but not on average, to stay consistent with the cosmological principle). Such states would describe the Universe as observations tell it is homogeneous and isotropic on large scales and so translates the fact that it was homogeneous and isotropic in the past as the large scales we see today correspond to the Universe scale in the Early Universe.

Finding these states might be difficult and therefore this is not what is done in LQC. In this chapter, we will explain how LQG is applied to the system Universe by considering a scalar field as energy content of the Universe. We will see that the Big-Bang singularity is removed and replaced by a Big Bounce no matter what is the potential of the scalar field. Then we will describe a model of the Universe with a massive scalar field with quadratic potential as energy content, focusing first on the background dynamics of this model, showing that with such a matter content, one is naturally led to inflation in LQC. Secondly, we will describe how perturbations propagate in this model and show the characteristic features of their power spectra, which depend on the scale considered. This chapter shows the strategy followed in the next chapter in the simpler case where one massive scalar field with quadratic potential is considered, where we will present a model of the Universe with two scalar fields.

6.1 The Big Bang singularity replaced by a quantum bounce

6.1.1 Semi-classical description of LQC

The idea of LQC is to start from cosmology and use the same techniques as the ones of LQG to quantize it directly. Another approach would have consisted in quantizing GR and then reduce the resulting LQG theory to homogeneity and isotropy to produce a new cosmological model of the Universe. Instead, one starts with the already reduced version of GR, that is the Universe described by the FLRW metric, and then apply the techniques of LQG to quantize it. This approach is called the mini-superspace approximation.

In order to do so, we will have to go through all the steps we described in the previous chapter. First, write the cosmological theory in the Hamiltonian formulation. With the FLRW metric Eq. (1.7), the Ashtekar's variables for space-time are the following:

$$A_a^i = c\,\delta_a^i \quad \text{and} \quad \tilde{E}_i^a = p\,\delta_i^a, \tag{6.1}$$

with $c = \beta\,\dot{a}$ and $p = a^2$, where a is the scale factor of the ΛCDM model and β is the Barbero-Immirzi parameter we already saw in the previous chapter. This pair of canonically conjugate variables satisfy the Poisson bracket

$$\{c, p\} = \frac{8}{3}\pi G\beta. \tag{6.2}$$

For the FLRW metric not to model the only vacuum which would be represented by a trivial space-time, the Hamiltonian of the theory must be coupled to matter. For a matter content of the Universe described by a homogeneous scalar field φ whose canonical variables are written φ and π_φ with Poisson bracket $\{\varphi, \pi_\varphi\} = 1$, the Hamiltonian constraint for such a cosmology is given by

$$\mathcal{H} = -\frac{3}{8\pi \mathrm{G}\beta^2}c^2\sqrt{p} + \frac{\pi_\varphi^2}{2p^{3/2}} + p^{3/2}V(\varphi), \tag{6.3}$$

where V is the potential of the scalar field. The first term is the Hamiltonian of the geometry of the Universe corresponding to the curvature of space-time and the last two terms correspond to the Hamiltonian of the scalar field which is just the energy density of the matter field. Their sum equals zero as the total Hamiltonian vanishes. Then, it leads to the usual equations of cosmology, the Friedmann's equations, by combining the Hamilton's equations $\dot{p} = \{p, \mathcal{H}\} = -(8\pi G\beta/3)\partial\mathcal{H}/\partial c$ and $\dot{c} = \{c, \mathcal{H}\} = (8\pi G\beta/3)\partial\mathcal{H}/\partial p$ with the constraint equation $\mathcal{H} = 0$. Furthermore, the Hamilton's equations for the field $\dot{\pi}_\varphi = \{\pi_\varphi, \mathcal{H}\} = -\partial\mathcal{H}/\partial\varphi$ and $\dot{\varphi} = \{\varphi, \mathcal{H}\} = \partial\mathcal{H}/\partial\pi_\varphi$ lead to another equation which is the Klein-Gordon equation. Note the different normalisation for the Poisson bracket of the cosmological variables c and p Eq. (6.2) and the Poisson bracket for the field φ and its conjugate momentum π_φ with usual normalisation to 1. Hence we stress that there is nothing quantum at this stage and this is just a reformulation of the classical hamiltonian of the cosmological model with the Ashtekar's variables.

The historical quantum cosmology model was the Wheeler-De Witt quantization and was based on a variant of this set of canonical variables with the spatial metric q^{ab} being the configuration variable, related to the densitised triad $\tilde{E}_i^a$ by Eq. (5.9). Unfortunately, it did not remove the singularity at the origin of the Universe. Anyway, these variables are not the analogous of the variables of LQG. Indeed, we have seen in Eq. (5.12) that the configuration variables are not the Ashtekar's connections but holonomies of the connections. This comes from the fact that the Ashtekar's configuration variables A_a^i are here proportional to the connection curvature (which is a curvature in the internal $SU(2)$ space of LQG, and not curvature of space-time, but is related

to it) and that in LQG-like quantization of theories, space and in particular areas are quantized. The minimum physical surface value is given by the smallest eigenvalue of the physical area operator: $\Delta = 4\pi\sqrt{3}\beta\ell_{\rm Pl}^2$. Thus, it is no longer possible to compute the curvature at a single point, hence the use of holonomies of the connection: instead, curvature is computed along a loop enclosing an elementary space cell. Actually, this connection curvature at a point can be computed classically along such a loop by taking the limit where the surface shrinks to a point. Now in LQC, one cannot take this limit as there is a non-vanishing minimal size for surfaces, so connection curvature is computed by taking the limit where the surface goes to its minimum value and not zero. This procedure is thus a curvature regularisation. The regularisation is made on physical surfaces as otherwise the elementary cells would expand with the Universe. As space homogeneity is assumed in our model of the Universe, we take space to be composed of identical elementary cells with comoving perimeter λ. In full generality, one should compute the curvature at every point but because of homogeneity, its value is the same everywhere. The holonomies of Eq. (5.12) are thus given by $h_\lambda = \exp(i\lambda c)$. The integral in Eq. (5.12) was easy to perform: A_a^i is proportional to a Kronecker delta and thanks to homogeneity c only depends on time. With these variables, the Hamiltonian constraint can be written as an effective Hamiltonian constraint thanks to the regularisation procedure that we will not detail here, which is similar to what is done in LQG to solve the technical difficulty to promote the Hamiltonian constraint to an operator with the Ashtekar's variables. Indeed, one cannot promote Eq. (6.3) to a quantum operator as curvature, hence c cannot be computed at a single point. In the following expression, c is therefore replaced by $\sin(\lambda c)/\lambda$ so that we recover the expression Eq. (6.3) in the limit where $\lambda \to 0$

$$\mathcal{H}_{\rm eff} = -\frac{3}{8\pi {\rm G}\beta^2}\frac{\sin^2(\lambda c)}{\lambda^2}\sqrt{p} + \frac{\pi_\varphi^2}{2p^{3/2}} + p^{3/2}V(\varphi). \tag{6.4}$$

This regularisation is done at an effective level here but at a quantum level one would have to consider space states with real areas encompassed by loops to derive the quantum Hamiltonian and then an effective one starting from it. We see on that expression that only the geometrical part of the Hamiltonian constraint has changed which is not surprising since only the variables associated with the geometry of space-time have changed. The λ parameter is the comoving length of a loop so that the sine function can be expanded in terms of holonomies h_λ. Thus, it is this expression that would be promoted to a quantum operator, even though as areas are quantized in LQG, the loop cannot be shrinked to a point in the quantum theory by taking the limit $\lambda \to 0$. This is the reason why the loop quantum version of cosmology have different properties than the classical theory: this particularity allows us to get rid of the Big Bang singularity. One can compute the minimal value of λ thanks to the smallest eigenvalue of the physical area operator giving $\lambda = \sqrt{\Delta/p}$.

6.1.2 Modified Friedmann's equations and bouncing cosmologies

Instead of entering into the details of the quantization of the constraints and operators, we will work directly with the semiclassical theory of Eq. (6.4). As it is different from the rewriting of classical cosmology given by Eq. (6.3), the equations of motion will be different than the classical Friedmann's equations encountered in Chapter 1, Section 1.1.1. Indeed, the equations of motion give a modified Friedmann equation derived by combining the evolution equation given by the Hamilton's equation $\dot{p} = \{p, \mathcal{H}_{\rm eff}\}$ with the constraint equation $\mathcal{H}_{\rm eff} = 0$

$$H^2 = \frac{8\pi {\rm G}}{3}\rho\left(1 - \frac{\rho}{\rho_c}\right), \tag{6.5}$$

where ρ is the total energy density and ρ_c its critical value obtained thanks to the minimum area value Δ and given by

$$\rho_c = \frac{3}{8\pi \mathrm{G}\beta^2\lambda^2 p} = \frac{3}{8\pi \mathrm{G}\beta^2\Delta}. \tag{6.6}$$

A modified Raychaudhuri equation can be derived likewise

$$\dot{H} = -4\pi \mathrm{G}(\rho + P)\left(1 - \frac{2\rho}{\rho_c}\right), \tag{6.7}$$

where P is the pressure. We stress that H here is the Hubble parameter and not the Hamiltonian constraint. As we said earlier, Hubble's observations in 1929 showed the Universe was expanding. Thus, the backwards evolution of the Universe is a contraction, translating in the scale factor a becoming smaller and smaller and the energy density ρ consequently becoming bigger and bigger, as shown in the standard Friedmann's equation Eq. (1.16). In the Standard Model of Cosmology, nothing prevents the energy density to blow up to infinity as the scale factor reaches 0. Indeed, the classical Raychaudhuri equation Eq. (1.16) shows that $\dot{H} \propto -\rho$ so that the forward expansion of the Universe decelerates. It means that going backwards in time, the contraction never stops and actually accelerates more and more as ρ increases, remembering that H measures the rate of expansion/contraction of the Universe. Thus the Hubble parameter becomes infinite when the scale factor vanishes, as shown for $t = 0^+$ in Fig. 6.1: this is the Big Bang singularity. However,

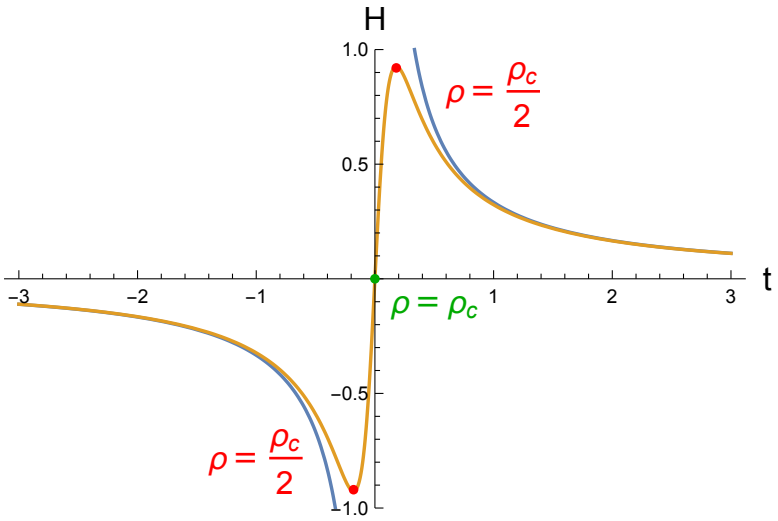

Figure 6.1: The Hubble parameter H in classical cosmology (blue) and in LQC (orange) for a Universe with a massive scalar field for only matter content. For $t > 0$, $H > 0$ meaning the Universe is expanding from $t = 0$. In classical cosmology, at $t = 0^+$, $H \to +\infty$ meaning that looking backwards in time from today, the Universe is contracting faster and faster approaching $t = 0$ so that at this point there is a singularity: this is the Big Bang singularity of the FLRW model of the Universe. We also draw the classical value of H for $t < 0$ for an hypothetical contraction previous to the Big Bang singularity: $H < 0$. The Hubble parameter shows a regular behaviour in LQC with two turning points (in red), occurring when $\rho = \rho_c/2$, and a vanishing value at $t = 0$ (green dot) when $\rho = \rho_c$, replacing the big-bang singularity by a regular big-bounce.

the equation Eq. (6.5) tells a slightly different story that has a drastic change for the origin of the Universe. Of course the backwards evolution of the Universe is a contraction and the scale factor decreases back to the origin. At the same time, the energy density increases until such a point where $\rho = \rho_c$. But at that point, the Hubble parameter H vanishes for a non-zero value of the scale factor. Then, the backwards evolution of the Universe has to expand as $\rho > \rho_c$ would give unphysical solutions of Eq. (6.5) for the scale factor: so ρ has to decrease after reaching ρ_c, meaning the Universe is expanding if one looks backwards in time after the instant when $\rho = \rho_c$. This behaviour is usually called the Big Bounce and replaces the Big Bang singularity at the origin of the Universe: it can be seen as a quantum repulsive effect due to the fact that volumes are quantized with a minimum eigenvalue in LQC, so that the energy density cannot go to infinity. This Big Bounce instant allows to connect the classical contracting branch shown in Fig. 6.1 for $t < 0$ with the classical expanding branch for $t > 0$ with a Hubble factor vanishing at $t = 0$. Therefore, if one goes back in time, there must be two turning points where the derivative of the Hubble parameter vanishes, i.e. the Raychaudhuri equation Eq. (6.7) vanishes, one when $t > 0$ and one when $t < 0$, in order to connect the two branches of Fig. 6.1. These turning points must happen before $\rho = \rho_c$ as this instant corresponds to $H = 0$. As $\rho + P > 0$, the Raychaudhuri equation shows that $\dot{H} = 0$ when $\rho = \rho_c/2$ where H reaches its extremum value given by $\pm 1/(\beta\sqrt{\Delta})$. From this point then, $\dot{H}$ changes sign: while classically the contraction accelerates going back in time, here it stops accelerating when $\rho = \rho_c/2$ and then decelerates. When $\rho = \rho_c$, the Hubble parameter vanishes and changes sign since $\dot{H}$ stays positive even when $t < 0$ while $\rho < \rho_c/2$, and $\dot{H}(0)$ has a finite value: the Big Bounce is said to be regular. Therefore, the Universe is expanding when one goes back in time before $t = 0$ and the expansion accelerates until $\rho = \rho_c/2$ where it starts decelerating.

One can be skeptical about this analysis as we worked with the semiclassical theory. However, the Big Bounce is also the conclusion of the quantized theory of this simple cosmology with the same value of the critical density so that we can effectively work with the semiclassical theory. Actually, the solutions of the semiclassical equations like the scale factor a, are the expectation values of the corresponding operators on the background wavefunction of the Universe. This wavefunction can be decomposed into sharply peaked states of operators around their most probable values. Therefore, making the full quantum gravity treatment whose solutions are sharply peaked states or using the effective semiclassical theory with solutions that are the most probable values of these states, is equivalent.

6.2 LQC with one scalar field

6.2.1 Inflation in LQC

As in the next chapter we will work with two scalar fields as an effective matter content of the Universe, we can get some inspiration by what has already been done with one massive scalar field as matter content, both at the background level and for the matter perturbations. The motivation for incorporating a massive scalar field in the LQC framework comes from inflation. Indeed, the resolution of the initial singularity by the bounce works well with a massless scalar field without potential, but no inflation phase follows the bounce. Thus, one would want to enhance the model by adding a massive scalar field as it is the simplest model of inflation, see Chapter 2, Section 2.2.3, that is not ruled out by CMB observations (Planck Collaboration et al., 2018d). The simplest potential one can choose is the $m^2\varphi^2/2$. We now know it is ruled out by CMB observations (see for example Fig. 12 of Planck Collaboration et al. (2018d) for constraints on the inflation potential that are degenerated with the number of e-folds), but at the time the model was proposed it had not been yet. However, changing the potential does not change the

qualitative features of the model.

The background equations of motion for this simple model of the Universe are given by the modified Friedmann's equation Eq. (6.5) and the Klein-Gordon (K-G) equation for the massive scalar field φ

$$\begin{cases} H^2 = \dfrac{8\pi \mathrm{G}}{3}\rho\left(1-\dfrac{\rho}{\rho_c}\right), \\ \ddot{\varphi} + 3H\dot{\varphi} + m^2\varphi = 0, \end{cases} \tag{6.8}$$

where m is the mass of the scalar field, the dot derivative is here with respect to cosmic time. Indeed, one can show that the K-G equation can be derived by combining the modified Raychaudhuri equation Eq. (6.7) with the derivative of the modified Friedmann equation Eq. (6.5) since $\rho + P = \dot{\varphi}^2$ and $\rho = \dot{\varphi}^2/2 + m^2\varphi^2/2$ by assuming a quadratic potential for the scalar field: $V(\varphi) = m^2\varphi^2/2$. As the motivation for introducing a massive scalar field in our model comes from inflation, it would be good for consistency that inflation is part of our model. Actually, as noticed in Mielczarek (2010), slow-roll inflation seems a natural feature of LQC. Indeed, during the contraction phase previous to the bounce, the Hubble parameter is negative. Therefore, the K-G equation Eq. (6.8) is the equation of an amplified harmonic oscillator as the $3H\dot{\varphi}$ is an antifriction term, so that the oscillations of the field φ are amplified during the contraction. Hence, even if the scalar field is initially at the bottom of its potential well but with a small non-zero velocity $\dot{\varphi}$ in the far past of the contraction, it climbs up the potential through this contraction so that after the bounce, when initial conditions are usually taken for the inflation phase, there is enough potential energy in the field to start a long enough period of inflation, as its duration is given by the number of e-folds is $N \approx 2\pi\frac{\varphi_{\mathrm{ini}}^2}{m_{\mathrm{Pl}}^2}$: the inflationary conditions are thus easily met. This is illustrated in Fig. 6.2; the evolution of the scalar field can be decomposed into four phases. First, the field shows an oscillatory behaviour during the contraction phase where $\rho \ll \rho_c$, $H < 0$ and $H^2 \ll m^2$: the antifriction term is therefore small enough to solve the K-G equation with an oscillatory field with slowly growing amplitude. Then the bounce occurs for $H^2 \gg m^2$ and $\dot{\varphi}^2 \gg m^2\varphi^2$: the large kinetic energy in the field allows it to climb up its potential so that it ends up with a large fraction of potential energy. One notes the hypothesis on the kinetic energy dominated bounce as one would need to take into account quantum backreaction effects otherwise (Bojowald, 2008), so that the effective Hamiltonian would be modified and consequently Eq. (6.5). From there, a phase of slow-roll inflation can follow, characterised by the slow-roll conditions $\rho \ll \rho_c$, $H > 0$, $H^2 \gg m^2$ and $m^2\varphi^2 \gg \dot{\varphi}^2$. Finally, when inflation ends, a phase of post-bounce oscillations similar to the oscillations occurring during the contraction takes place where $\rho \ll \rho_c$, $H > 0$ and $H^2 \ll m^2$. This evolutionary scenario is consequently named the shark-fin evolution because of the shape of the evolution of the field through time. The initial conditions for inflation are thus naturally encountered in LQC thanks to the contraction phase. Actually, this is not surprising as it is not a specific feature of LQC: indeed, people have shown that inflation is an attractor (Bond et al., 1988), even in the classical model of cosmology.

6.2.2 Main phases of the bouncing Universe: contraction, bounce and expansion

This is however not the only possible evolution of the field as the evolution also depends on the initial conditions. However, it has been shown to be the most probable one, as we will see, the dynamics being quite natural as explained above. To see it, analytic approximations have been derived for the solutions of this simple model of the Universe in Linsefors & Barrau (2013).

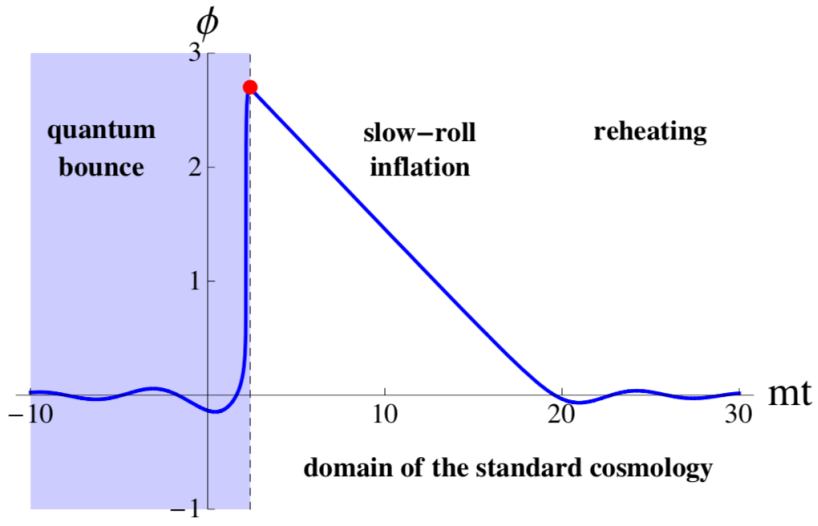

Figure 6.2: A natural evolutionary scenario in LQC: the shark fin-type evolution of a scalar field with $m = 10^{-3} m_{\rm Pl}$. The (red) dot represents the point where the initial conditions in classical cosmology are usually set. Notice the rescaling of time in mt. Figure taken from Mielczarek (2010).

Defining the fractions of potential x and kinetic y energy by

$$\begin{cases} x \equiv \dfrac{m\varphi}{\sqrt{2\rho_c}}, \\ y \equiv \dfrac{\dot{\varphi}}{\sqrt{2\rho_c}}, \end{cases} \tag{6.9}$$

so that the energy density of the matter field is given by

$$\rho = \rho_c (x^2 + y^2), \tag{6.10}$$

the K-G equation for this model of the Universe Eq. (6.8) can be rewritten using these variables as a set of two first order differential equations

$$\begin{cases} \dot{x} = my, \\ \dot{y} = -mx - 3Hy. \end{cases} \tag{6.11}$$

Thanks to these equations, they showed that in full generality, the evolution of the very Early Universe can be decomposed into five phases in this model, where different hypotheses run them.

1. First, the prebounce oscillations. During this phase, $\rho \ll \rho_c$, $H < 0$, $H^2 \ll m^2$ so that the Universe can be described classically by Eq. (1.16). As already noted, one can neglect the second term in the second equation Eq. (6.11) so that x and y are oscillating functions of frequency m with growing amplitudes given by $\sqrt{\rho/\rho_c}$. Then one can introduce an equation for ρ by taking the derivative of Eq. (6.10)

   $$\dot{\rho} = -6H\rho_c y^2, \tag{6.12}$$

   which can be analytically solved. This phase ends when one of the three hypotheses running it is violated, leading to the second following phase.

2. Slow-roll deflation: the condition on the Hubble parameter is violated $H^2 \gg m^2$ but one is still far from the bounce $\rho \ll \rho_c$. If, by chance, at the same time $x^2 \gg y^2$ and $y = \text{sign}(x)\frac{m}{\sqrt{24\pi\rho_c}}$, then y is almost constant and $|x|$ is consequently linearly growing, hence the name slow-roll deflation. It is however not very probable as it occurs for very specific conditions for x and y at the end of the prebounce oscillations: slow-roll deflation is said to be unstable.

3. Superdeflation, bounce and superinflation: as the slow-roll deflation is unstable, it can be that the kinetic energy dominates over the potential energy at some point: $y^2 \gg x^2$. This phase is also characterised by $H^2 \gg m^2$ and $\rho \lesssim \rho_c$: one therefore needs to take into account the quantum effects, i.e. the evolution of the Universe is described by Eq. (6.5). During this phase, $\rho > \rho_c/2$ so even though the equation of state forbids an accelerated expansion, the quantum corrections in the modified Raychaudhuri equation Eq. (6.7) involves that $\dot{H} > 0$. Thus, the Hubble factor H increases rapidly (ρ also increases and $\dot{H} \propto \rho^2$), hence the names 'superdeflation' and 'superinflation', but the slow-roll conditions are not necessarily met. Meanwhile, the fraction of potential energy x grows or decreases rapidly while y decreases to zero, leading to the following fourth phase.

4. Slow-roll inflation: this is the symmetric version of slow-roll deflation with respect to the bounce. Hence, during this phase $\rho \ll \rho_c$, $H > 0$, $H^2 \gg m^2$ and $x^2 \gg y^2$ as $|x|$ grew rapidly during the previous phase so that the condition $y^2 \gg x^2$ is violated. If this condition is violated before the condition on H, one is naturally led to the desired phase of slow-roll inflation by having a large fraction of potential energy in the field not long after the bounce, see Fig. 6.2. Because $y = -\text{sign}(x)\frac{m}{\sqrt{24\pi\rho_c}}$ is an attractor and y is almost constant, $|x|$ is linearly growing: the slow-roll conditions are met. Inflation is therefore stable, until one of the two last conditions is broken.

5. Finally, the condition on the Hubble parameter is violated: $H^2 \ll m^2$ and $\rho \ll \rho_c$, $H > 0$. This signs the end of inflation and starts a post-bounce oscillations phase, similar to the first phase and symmetric to it with respect to the bounce. The field and its derivative oscillate with frequency m and decreasing amplitude given by $\sqrt{\rho/\rho_c}$ with ρ solving Eq. (6.12). If coupled to other (SM) fields, this last phase corresponds to reheating in the standard model of cosmology, the Universe being therefore described classically.

6.2.3 Main classes of cosmic evolution

As we will see and as already explained, inflation is the most probable evolution for such a massive scalar field during the very Early Universe. However, we have also shown a phase called slow-roll deflation can occur after the pre-bounce oscillations during the contraction, even though this phase is unstable. In Fig. 6.3, we show different examples of evolutions of the scalar field through the variable $x \propto \varphi$. The linear behaviour of x for $t > 0$ characterises the slow-roll inflation phase as in the shark-fin evolution. This same linear behaviour for $t < 0$ characterises the slow-roll deflation phase. The bottom left plot shows a solution with deflation but no inflation and is not very probable. Another possible trajectory is a solution with both deflation and inflation as shown in three of the plots, like the upper right one. These trajectories are also unlikely as they contain a deflation phase. One can show as in Mielczarek (2010) that one needs a small fraction of potential energy at the bounce to initiate a long enough phase of slow-roll inflation. This is illustrated in Fig. 6.4: the $x = 0$ case corresponds to no potential energy at the bounce and results in symmetric phases of deflation and inflation. This trajectory is not very probable as it corresponds to a very specific choice of initial condition for x at the bounce $t = 0$. This figure also shows the higher the fraction of potential energy x at the bounce, the higher the value

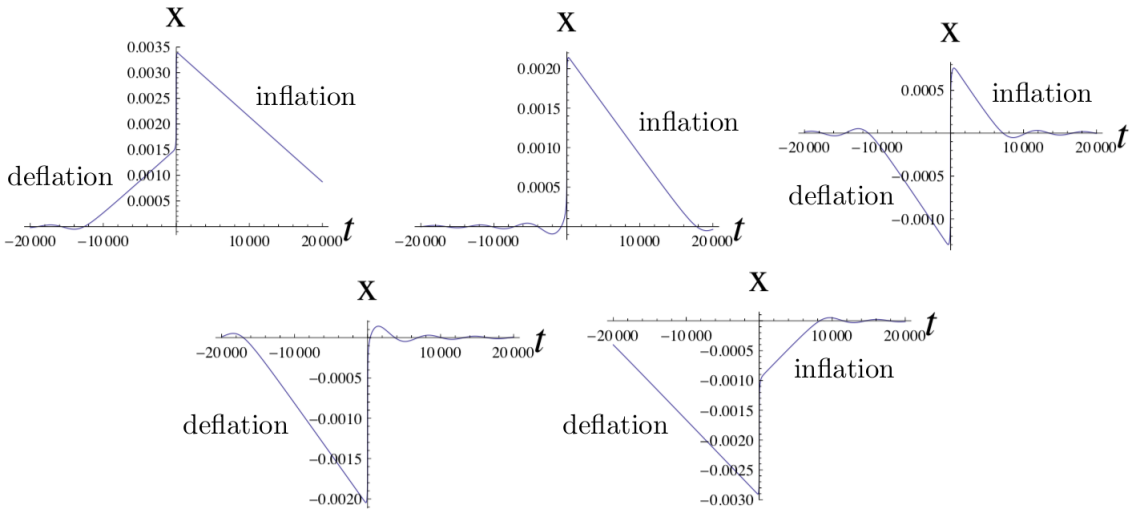

Figure 6.3: Examples of evolutions of the normalised value of the field $x = m\varphi/\sqrt{2\rho_c}$ as a function of time for different solutions. The linear increase (decrease) of $|x|$ is the slow-roll deflation (inflation) phase, and the almost vertical increase or decrease of x is the superdeflation, bounce, and superinflation phase. A solution with no deflation at all like in the upper middle plot is by far the most probable. The mass of the scalar field used here is $m = 10^{-3}$ but the features remain true for any mass. Figure taken from Linsefors & Barrau (2013).

reached by the scalar field after the bounce, and we recall that a high value is needed to start a long enough phase of inflation.

We kept on saying that trajectories with slow-roll deflation were not very probable while those with inflation were extremely probable. Indeed, it has been shown in Linsefors & Barrau (2013) that slow-roll deflation was unstable while slow-roll inflation was stable, see Sec. 6.2.2. But why is it so? One could argue that slow-roll deflation is just slow-roll inflation for a Universe where time is reversed. Indeed, the equations of motion for the Universe are reversible in time so that the inflation phase can be seen as a deflation phase if one evolves the Universe backwards. This is indeed the case, but in our description of the Universe, we chose a direction for time where the Universe evolves causally from the past to the future. This sets the initial conditions for the scalar field in the far past where it behaves like dust during the pre-bounce oscillations. As the time symmetry is broken, slow-roll deflation is therefore unstable and not very probable, while it is the contrary for slow-roll inflation.

6.2.4 Probability of inflation

When one talks about the initial conditions of the scalar field, one actually talks about their Probability Distribution Function (PDF), as one cannot know exactly what would be the value of the scalar field and its derivative initially, so one can at most give it a PDF. As one actually has no guess on what this PDF might be, we will take the uniform PDF in order to be conservative.

As we set the initial conditions in the remote past contracting and oscillating phase, we first

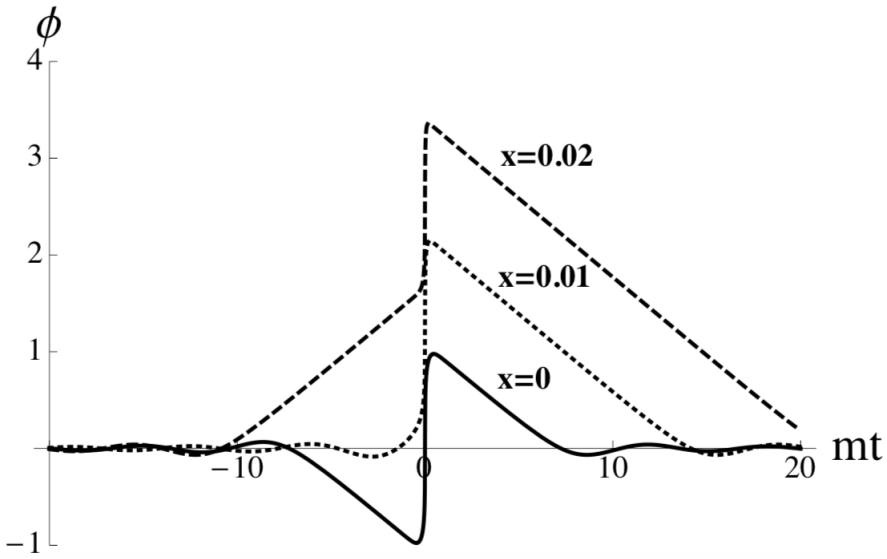

Figure 6.4: Time evolution of the scalar field. Different evolutionary scenarii leading to a slow-roll inflation phase are displayed. The bottom (solid) line represents the symmetric case. The middle (dotted) line represents the shark fin-type evolution. The top (dashed) line corresponds to a larger fraction of potential energy. For all curves $m = 0.01 m_{\rm Pl}$. Figure taken from Mielczarek et al. (2010).

need the analytic approximated solutions for this period (Linsefors & Barrau, 2013)

$$\rho = \rho_0 \left(1 - \frac{1}{2}\sqrt{24\pi \mathrm{G}\rho_0}\left(t + \frac{1}{2m}\sin(2mt + 2\delta)\right)\right)^{-2}, \tag{6.13}$$

and

$$\begin{cases} x = \sqrt{\dfrac{\rho}{\rho_c}}\sin(mt + \delta), \\ y = \sqrt{\dfrac{\rho}{\rho_c}}\cos(mt + \delta), \end{cases} \tag{6.14}$$

where ρ_0 and δ are initial free parameters. One notices that changing the value of ρ_0 just corresponds to a shift in the origin of times and a redefinition of δ. Thus, the only relevant free parameter is δ. Setting the initial conditions for the scalar field during this phase amounts to set their initial PDF and as there is only one free parameter, this is finally equivalent to set the initial PDF for δ. As there is no knowledge of what the value of this parameter should be, a flat probability distribution has been taken. This flat PDF will be preserved during the whole pre-bounce oscillating phase meaning that once the solutions for the field are evolved with time according to Eq. (6.14), δ still have the same flat PDF at any time provided one is still within this phase. Thus, any prediction made from this initial PDF will not depend on the specific choice for the value of ρ_0. This comes from what is explained above: a time shift results in a change in ρ_0 (if we take some later time to be the origin of time, the new initial value of ρ has changed) which redefines δ, but as the flat PDF for δ is preserved during the pre-bounce oscillating phase, the initial value for ρ does not change the predictions made within this choice of initial PDF.

Hence, in addition to being the natural choice of distribution for a process with no knowledge, it is also consistent as it does not require specific knowledge on the value of the energy density at some time.

The fraction of potential energy at the bounce, x_B, and the duration of slow-roll inflation in number of e-folds, N, have been computed with this initial PDF in Linsefors & Barrau (2013) and are given in Fig. 6.5 left and right respectively. They showed that the most probable value for x_B was 3.55×10^{-6} (which scales as $m \log(1/m)$, with $m \ll 1$ in Planck units) which is consistent with the treatment where the bounce is kinetic energy dominated so that one can indeed neglect the quantum backreaction effects. This small fraction of potential energy at the bounce as the most probable value confirms that trajectories with no slow-roll deflation are the most probable ones. Furthermore, the duration of inflation is computed by $N = 4\pi\rho_c(x_{\max}/m)^2$ where $x_{\max}$ is the highest value reached by the scalar field after the bounce, which starts the phase of slow-roll inflation and the most probable value is found to be $N = 145$ e-folds. Thus, trajectories with no slow-roll deflation but with a long enough slow-roll inflation are the most probable ones, as already anticipated in Sec. 6.2.2 where the different phases in the very Early Universe are described. Inflation is thus natural and occurs without fine-tuning in this simple model of LQC.

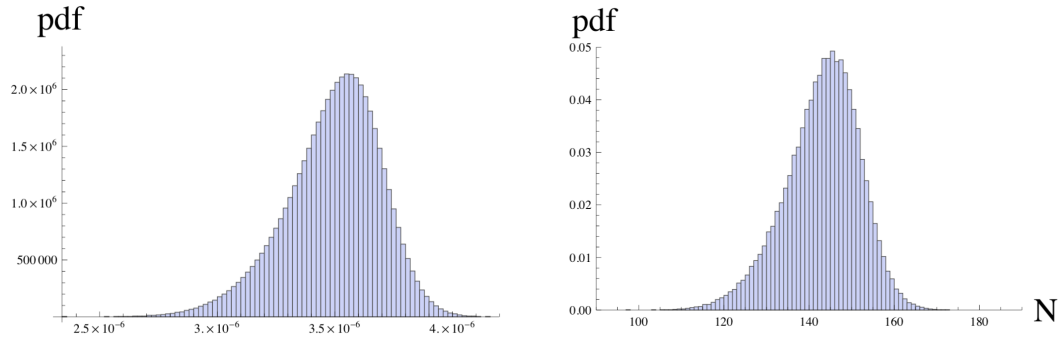

Figure 6.5: PDF of $\text{sign}(y_B)x_B$ on the left and of the number of e-folds of slow-roll inflation N on the right. Figure taken from Linsefors & Barrau (2013).

Taking the initial PDF for the scalar field during the pre-bounce oscillations phase is a choice motivated by the causal evolution of the Universe from the past to the future. The scalar field existing prior to the bounce in this model, it is believed to later lead to a period of slow-roll inflation, so the initial conditions for inflation usually needed in the standard model are pushed back to the pre-bounce oscillations phase. This is however not the choice of Ashtekar & Sloan (2011): the absence of information on what the initial conditions of the scalar field would be led them to consider a flat PDF over the Liouville measure on the phase-space of solutions. This Liouville measure is 'canonical', as they state, and preserved over time so likewise the choice of Linsefors & Barrau (2013), it is consistent. However, as the total measure on the space of solutions is infinite, it requires to choose a time slice to set the initial conditions. In LQC, there is a 'canonical' time slice corresponding to the bounce surface so that initial conditions are specified there. Then they found that the probability of having a slow-roll inflation with a quadratic potential for the inflation field whose initial conditions are compatible with the seven year WMAP data (Komatsu et al., 2011) is greater than 0.999997. The slow-roll inflation compatible with observations does not occur only in the extreme kinetic energy dominated bounce: that is, if the fraction of the total energy density which is in the potential at the bounce x_B^2 is less than 7.35×10^{-6}. Therefore, it confirms the attractor behaviour of slow-roll inflation even in LQC

dynamics when a massive scalar field with quadratic potential dominates its evolution. No fine-tuning is required for a long enough inflation to occur and even for inflation with initial conditions that are compatible with observations. It is then also consistent with the above analysis where initial conditions are set during the pre-bounce oscillating phase, see also Bolliet et al. (2017) for more details.

6.3 Cosmic perturbations in bouncing universes

Even though LQC solves the Big Bang singularity problem and allows to reach high energies in a regular fashion so that the initial conditions for an inflation phase are met (when coupled to a massive scalar field with a quadratic potential), the modified dynamics of this Universe does not provide concrete observables, so the dynamics does not have predictive power. Indeed, one would need to look at our Universe from a 5^{th} dimension in order to do so. Nonetheless, the Universe is not purely homogeneous and isotropic and contains initial perturbations that translate into CMB anisotropies in temperature and polarisation and later into large-scale structures as seen in Chapters 3 and 4. These initial perturbations are thus observable through their effects on cosmological observables. The question is then: could we use these observables to constrain LQC? Stated otherwise: does LQC make predictions different from the Standard Model for these observables? As we will soon see, the answer is yes: the bouncing dynamics of LQC modifies in itself the production of these perturbations and the very equations of motion for the perturbations are different than in the Standard case, all of this translating in different angular power spectra for the perturbations at the end of inflation. The next section is devoted to the two different approaches for deriving the equations of motion for these perturbations within the LQC framework.

6.3.1 Equations of motion for the perturbations

Within the LQC framework, there exists two main approaches to model these cosmological quantum perturbations corresponding to the level at which they are modeled.

6.3.1.1 Deformed algebra approach

One of these approaches is called the deformed algebra approach and operates at the semiclassical level of the theory. Indeed, the strategy consists in starting from the semiclassical Hamiltonian of the quantized FLRW theory and add semiclassical first order perturbations to it. The name 'deformed algebra' stands for the way the perturbations are derived. Indeed, the constraints of the (quantized) FLRW theory form an algebra called the algebra of constraints. When perturbations are added, the constraints no longer form an algebra but anomalies are added on the right-hand-side of the Poisson bracket. The strategy then is to correct these anomalies by changing the structure functions and by adding counter-terms to the perturbed Hamiltonian that correct the anomalies. The semiclassical effective equations of motion for the scalar and tensor perturbations described by the Mukhanov-Sasaki variables as in Chapter 3 are derived thanks to this procedure

$$v'' - \Omega(\eta)\Delta v - \frac{z''}{z}v = 0, \tag{6.15}$$

with

$$\Omega(\eta) = \left(1 - 2\frac{\rho(\eta)}{\rho_c}\right), \tag{6.16}$$

and, as away from the bounce $\rho \ll \rho_c$, $\Omega \to 1$. The derivative $'$ is with respect to conformal time η and Δ is the Laplacian; z is a function of the background given by

$$z_{\rm S}(\eta) = \frac{a^2(\eta)\varphi'(\eta)}{a'(\eta)} \quad \text{or} \quad z_{\rm T}(\eta) = \frac{a(\eta)}{\sqrt{\Omega(\eta)}}, \tag{6.17}$$

for the scalar and tensor perturbations respectively. For the case of the scalar perturbations, this function is exactly the same as classically, see the first equation of Eq. (3.59), but is different for the tensor perturbations.

6.3.1.2 Dressed metric approach

The other approach, developed in Agullo et al. (2013a), works upstream: it uses again techniques of LQG as what was done to build a quantized version of the FLRW model of cosmology in LQC, see Sec. 6.1. Indeed, it starts with a truncated classical phase space of GR coupled to a scalar field corresponding to the homogeneous and isotropic background plus first order inhomogeneous perturbations: the truncation is made to second order in the first order perturbations. The Hamiltonian for this model can be decomposed into two parts: one governing the dynamics of the FLRW background, written H_0, and one governing the dynamics of the perturbations, H_1. Then the quantum Hamiltonian corresponding to this phase-space is worked out by finding the quantum geometry of this model. The quantum Hamiltonian operators are respectively $\hat{H}_0$ and $\hat{H}_1$, and $\hat{H}_0$ is already known from the LQC framework as mentioned in Section 6.1. Then, the approximation that the backreaction of the perturbations on the background is negligible allows to write physical states Ψ as a tensor product between a state describing the background quantum geometry Ψ_0 and a state describing the linear scalar and tensor perturbations ψ: $\Psi = \Psi_0 \otimes \psi$. Thus, the background is quantized separately from the perturbations: this is the Born-Oppenheimer approach. Then, it is shown that the evolution of the quantum gauge perturbations $\hat{\mathcal{Q}}$ and $\hat{\mathcal{T}}$ on the background geometry is equivalent to their evolution on an effective background metric $\tilde{g}_{ab}$ 'dressed' with quantum corrections which, away from the bounce, tends to the FLRW metric. This 'dressed metric' depends on the expectation value of the sharply peaked wavefunction Ψ_0 representing the background geometry and captures some fluctuations of the metric essential for describing the evolution of the quantum perturbations. Thus, finally, the semiclassical effective Hamiltonian for the perturbations is derived to second order in the first order perturbations (in fact, it is quadratic in the linear perturbations, as when one derives the equations of motion, one order is lost). Hence, the semiclassical effective equations of motion for the scalar and tensor perturbations are also derived

$$v'' - \Delta v - \frac{\langle \hat{z}'' \rangle}{\langle \hat{z} \rangle} v = 0, \tag{6.18}$$

where $\langle . \rangle$ gives the quantum expectation value of a quantum operator on the background quantum geometry and $\langle \hat{z} \rangle$ is not necessarily the same as their classical expressions or the ones given by the deformed algebra approach. The 'dressed metric' approach for deriving the quantum cosmological perturbations equations is therefore similar to what is done to find the semiclassical effective Friedmann's equations.

The two frameworks for the quantum perturbations allow us in the end to compute the power spectra of scalar or tensor perturbations. The differences in the two approaches mainly show up at high wavenumbers, i.e. in the Ultra Violet regime. Strictly speaking, in this thesis we have not used either of these approaches but considered the standard equations of motion for

the evolution of the quantum linear perturbations on the classical FLRW model of the Universe. This is motivated by the fact that away from the bounce, both of these approaches reduce to this classical procedure. Only during the bounce we replace the Friedmann's equation by its LQC modified version Eq. (6.5), keeping in mind that for further developments a more consistent LQC treatment should be made of these perturbations. Anyway, in a sense the approach followed in this thesis is close to the dressed metric one as the expectation values of the functions appearing in the equations of motion Eq. (6.18) are computed on the sharply peaked states of the background, and this is what is captured in the semi-classical background function z, as this last one is instead composed of the expectation values of functions taken on the sharply peaked states computed through the effective modified Friedmann's equations Eq. (6.5).

6.3.2 Predicted primordial power spectra

Some work has already been done in LQC for the perturbations of a scalar field with a quadratic potential in Schander et al. (2016) and for the tensor perturbations in Bolliet et al. (2015); Linsefors et al. (2013). The equations of motion are given by Eq. (6.15) and as already stated above, $\Omega \to 1$ away from the bounce, or by Eq. (6.18). Analytic approximations for the perturbations have been derived in the past contracting phase where the initial conditions are set: we will get some inspiration from what has already been done for our work.

In this section, we will focus on the power spectra of the tensor perturbations at the end of inflation in the dressed metric approach, as this is the closest to ours, to describe some of its characteristic features. We illustrate the case of the tensor perturbations as it is simpler but the strategy and the features of the power spectra remain the same for the scalar perturbations. The equations of motion for the tensor modes are given by Eq. (6.18)

$$v_{\mathrm{T}}'' - \Delta v_{\mathrm{T}} - \frac{\langle \tilde{a}'' \rangle}{\langle \tilde{a} \rangle} v_{\mathrm{T}} = 0, \tag{6.19}$$

where $\tilde{a}$ is a dressed scale factor whose expectation value is taken on the background state. Going to Fourier space and introducing the mode functions $v_k(\eta)$, one needs to solve the following equation

$$v_k'' + \left(k^2 - \frac{\langle \tilde{a}'' \rangle}{\langle \tilde{a} \rangle} \right) v_k = 0, \tag{6.20}$$

and one can show that for sharply peaked background states $\langle \hat{a}'' \rangle / \langle \hat{a} \rangle$ is well approximated by a''/a over the whole evolution, including the bounce (Agullo et al., 2013a). The function a is the expectation value of the scale factor operator on the sharply peaked wavefunction describing the background, and is solution of the modified Friedmann equation Eq. (6.5). Because the fluctuations about the value where the wavefunction is maximum are negligible, an effective approach can be taken with effective equations of motion for the perturbations. Thus, Eq. (6.20) simplifies to

$$v_k'' + \left(k^2 - \frac{a''}{a} \right) v_k = 0. \tag{6.21}$$

The primordial tensor power spectrum for the tensor perturbations at the end of inflation is then given by

$$\mathcal{P}_{\mathrm{T}} = \frac{32 \mathrm{G} k^3}{\pi} \left| \frac{v_k(\eta_e)}{a(\eta_e)} \right|^2, \tag{6.22}$$

where η_e is the conformal time at the end of inflation. We will now present the two limits of this power spectrum: the infrared (IR) and the ultraviolet (UV) limit.

The UV limit corresponds to comoving modes k for which $k^2 \gg a''/a$. For small enough wavenumbers, they coincide with modes for which $k \gg aH$ where aH is the inverse of the comoving Hubble radius. In terms of wavelength, it translates into comoving wavelengths smaller than the comoving Hubble radius, thus they are called sub-Hubble modes. The UV modes are oscillating during the prebounce contracting phase and until the start of the slow-roll inflation phase because their equation of motion is now approximated by

$$v_k'' + k^2 v_k = 0. \tag{6.23}$$

They thus do not feel the background curvature during the contracting phase and the bounce, as shown in Fig. 6.6. They then become amplified once $k^2 < a''/a$, that is during the inflation phase. One can easily solve the equation of motion for the mode functions Eq. (6.21) during the contracting phase in this limit. Taking the initial conditions to be the Minkowski vacuum, one shows the power spectrum in the UV limit to be slightly red-tilted, as the power spectrum predicted in the standard inflationary scenario.

The IR limit corresponds to comoving modes k for which $k^2 \ll a''/a$. For small enough wavenumbers, they coincide with modes for which $k \ll aH$. In terms of wavelength, it translates into comoving wavelengths higher than the comoving Hubble radius, thus they are called super-Hubble modes. The IR modes are frozen during the prebounce contracting phase, i.e. they stopped oscillating during this phase because their equation of motion is now approximated by

$$v_k'' - (a''/a) v_k = 0. \tag{6.24}$$

They are thus amplified right in the contracting phase, contrary to the UV modes that keep oscillating during this phase and have to wait until inflation to start being amplified. Now in a model of the Universe with a matter scalar field with quadratic potential as matter content, the analytical approximations for the solutions of the modified Friedmann's equations during the pre-bounce contracting phase Eq. (6.14) allows to compute a''/a analytically which gives

$$\frac{a''}{a} = \frac{2}{\eta^2}. \tag{6.25}$$

As a''/a is increasing during the contraction, if k^2 is initially smaller than a''/a during the contraction, it remains smaller during the whole evolution so that the amplitude of the mode remains frozen almost until the end of inflation, as shown in Fig. 6.6, up to two tiny periods around the bounce. The equation Eq. (6.21) is easy to solve in the IR regime in the contracting phase. Furthermore, one can also choose the Minkowski vacuum as initial conditions for the modes as far enough in the past, all modes are in the UV regime, i.e. they satisfy $k^2 \gg a''/a$. Thus, one can finally show that the power spectrum in the IR regime is scale invariant like the prediction of standard GR.

Finally, the intermediate scales shown in Fig. 6.6 by the middle green line correspond to modes that are amplified during the bounce. It is essentially at these intermediate scales that the power spectrum of the modes differs from the standard prediction of classical cosmology. Indeed, the full power spectrum is obtained numerically and is shown in Fig. 6.7. The left part below the vertical dotted lines corresponds to the IR regime and one can see the scale invariance of the power spectrum. The right part above the vertical dashed line corresponds to the UV regime and one can guess the slightly red-tilted power spectrum as predicted in the inflationary scenario. The intermediate scales show damped oscillations, which are characteristic features of LQC.

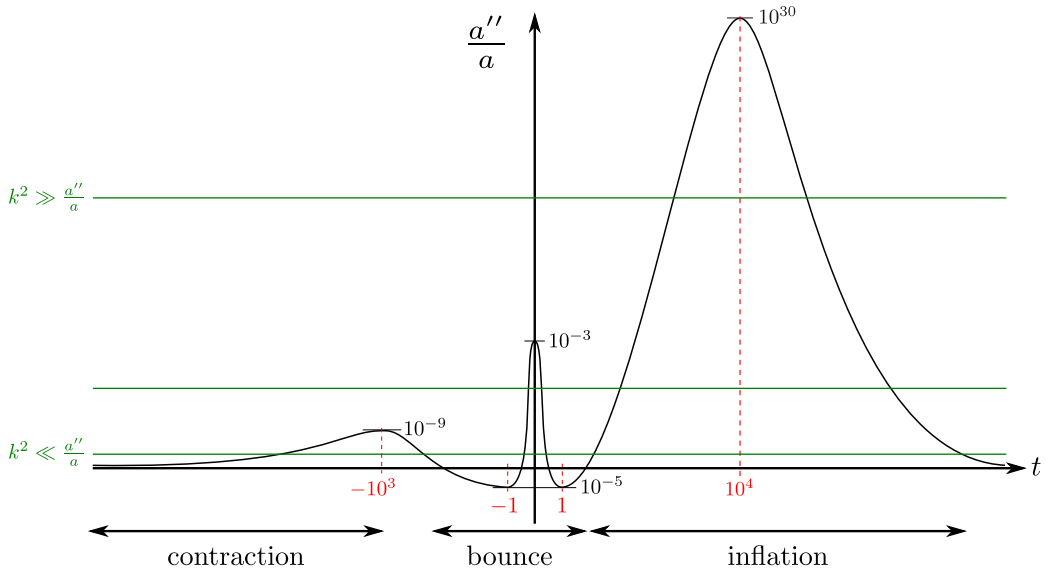

Figure 6.6: Schematic plot of a''/a as a function of cosmic time t. In black are the values taken by the function at the corresponding times given by the vertical dashed lines in red. The many orders of magnitude spanned by the function does not allow us to plot it on a single graph in order to see its different features during the contraction, bounce and inflation. This schematic plot is therefore not to scale. The horizontal plain green lines represent the values of the wavenumber k^2 compared to a''/a. The lower green line corresponds to the IR limit, whose modes are frozen until the end of inflation, while the upper one corresponds to the UV limit whose oscillations are amplified during inflation. The middle line shows an intermediate scale where oscillations are amplified during the bounce.

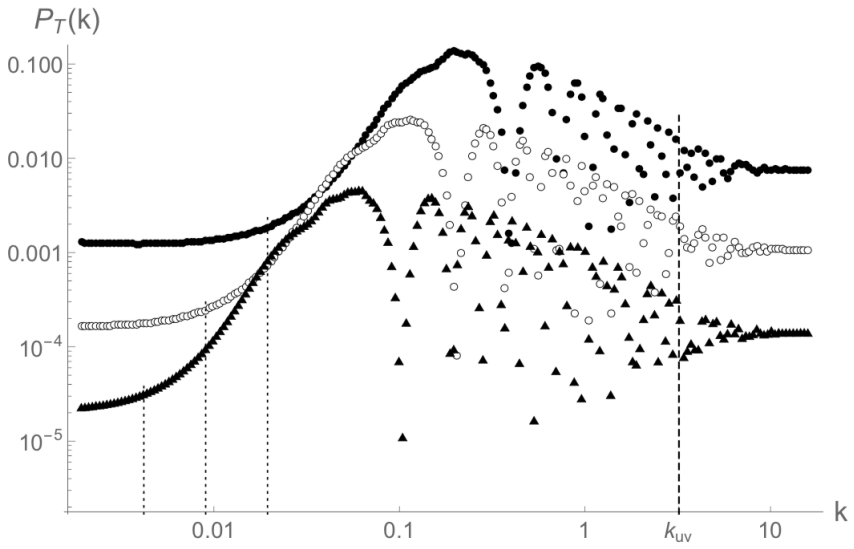

Figure 6.7: Primordial power spectra for tensor modes in the dressed metric approach for different values of the mass of the scalar field: $m = 10^{-3} m_{\rm Pl}$ (triangles), $m = 10^{-2.5} m_{\rm Pl}$ (open disks), and $m = 10^{-2} m_{\rm Pl}$ (black disks). The dotted vertical lines at smaller k delimits the IR regime ($k^2 \ll a''/a$) which scales as $m^{2/3}$: one notices the scale invariant behaviour. It corresponds to modes that are amplified during the contracting phase. The dashed vertical line at large k delimits the UV regime ($k^2 \gg a''/a$) which does not depend on m: one can guess the slightly red-tilted power spectrum as predicted in the standard inflationary scenario. These modes are amplified during the inflation phase. The intermediate scales (between $k^2 \ll a''/a$ and $k^2 \gg a''/a$) show damped oscillations and correspond to modes amplified during the bounce. The figure is taken from Bolliet et al. (2015).

Chapter 7

LQC with two scalar fields

7.1 Motivations

Already in the original classical Hamiltonian formulation of cosmology coupled to a massless scalar field ϕ without potential as content of the Universe, one can show that the field is a monotonic function of time so that it can be used to parameterize the evolution of the variables instead of time t (Gambini & Pullin, 2011): it is a relational clock field. This idea of relational dynamics already has its roots in classical mechanics: one relates events in time to the number of oscillations of a pendulum. At the quantum level of the modeling, as geometry itself is quantized, the theory gives probability amplitudes for the metric and therefore time is no longer properly defined. One can thus use the scalar field ϕ as a relational emergent time (see Ashtekar et al., 2009). More recently, in a paper by Gielen & Oriti (2018), this idea has been generalised in the Group Field Theory approach to quantum gravity which is close to the LQG formalism, to include a total of four reference scalar fields coupled to gravity, used as relational clock and rods. Symmetries are imposed on the dynamics of these fields so that they are used as a physical coordinate system: they form a material reference frame. A beginning of study in this direction within the framework of LQC has been made in Mielczarek (2009), which studied potentials of scalar fields such that the latter behave like fluids, and are shown to have the property of being monotonic. On the contrary, the massive field with quadratic potential studied in the previous chapter has been seen being not monotonic, especially during the contracting phase. However, this field is needed to have an inflation phase after the bounce. Indeed, we have seen that one needs a small fraction of potential energy at the bounce to get such a phase. A massless field alone therefore could not give rise to inflation. Furthermore, adding more fields to an early Universe model would come within the scope of multifield inflation. As LQC allows to study models of the very early Universe even prior to the phase of inflation, it would also be interesting to study these multifield models within this framework. Indeed, actually one can expect the massive scalar field to being coupled to other fields of the SM of particle physics during the contraction phase, by a kind of inverse reheating process. The case of two scalar fields has been considered in Wilson-Ewing (2013) in the ekpyrotic paradigm -an alternative to inflation in which perturbations are produced during a contracting phase prior to the Big-Bang singulartiy- but in the context of LQC. The ekpyrotic scenario is characterised by its potential. In this chapter, in the idea of having a phase of inflation, we will build a model of the very early Universe with the massive scalar field φ with mass m and quadratic potential $V(\varphi) = m^2\varphi^2/2$ described in Section 6.2 that will be the inflaton field, and a massless scalar field ϕ that will be our clock field. Both represent the effective content of the very early Universe. This work could be then

generalised to include three more reference scalar fields to complete the material reference frame. Finally, we will study the perturbations produced by these fields, with an adiabatic and and isocurvature components.

7.2 Background dynamics

7.2.1 Equations of motion

The equations of motion for the background dynamics are given by Eq. (6.8) for the massive scalar field φ, completed with the Klein-Gordon equation for the massless scalar field ϕ

$$\begin{cases} H^2 = \dfrac{8\pi \mathrm{G}}{3}\rho\left(1-\dfrac{\rho}{\rho_c}\right), \\ \dot{H} = -8\pi\rho_c\left(Z^2+Y^2\right)\left(1-2\left(Z^2+Y^2+X^2\right)\right), \\ \ddot{\varphi}+3H\dot{\varphi}+m^2\varphi = 0, \\ \ddot{\phi}+3H\dot{\phi} = 0, \end{cases} \tag{7.1}$$

with $\rho = (\dot{\varphi}^2+\dot{\phi}^2)/2+V$. One notices that the constraint equation on H^2 is unchanged, up to a redefinition of ρ to take into account the energy associated with the massless scalar field. Therefore, the Big-Bang singularity is also removed in this model of the Universe and replaced by a bounce like in the one scalar field model studied in the previous chapter.

In addition to define the fractions of potential X and kinetic Y energy in the massive scalar field, we also define the fraction of kinetic Z energy in the massless scalar field

$$\begin{cases} X \equiv \dfrac{m\varphi}{\sqrt{2\rho_c}}, \\ Y \equiv \dfrac{\dot{\varphi}}{\sqrt{2\rho_c}}, \\ Z \equiv \dfrac{\dot{\phi}}{\sqrt{2\rho_c}}, \end{cases} \tag{7.2}$$

so that the total energy density of the Universe is given by

$$\rho = \rho_c(X^2+Y^2+Z^2). \tag{7.3}$$

The equations of motion for this model of the Universe Eq. (7.1) can be rewritten using these variables as a set of four first order differential equations

$$\begin{cases} \dot{H} = -8\pi\rho_c\left(Z^2+Y^2\right)\left(1-2\left(Z^2+Y^2+X^2\right)\right), \\ \dot{X} = mY, \\ \dot{Y} = -mX-3HY, \\ \dot{Z} = -3HZ, \end{cases} \tag{7.4}$$

ensuring that the contraint on H^2 is satisfied. We recall that away from the bounce one can neglect the term $-2(Z^2+Y^2+X^2)$ in this equation.

Qualitatively, as in the single massive field model H decreases away from the bounce (see Fig. 6.1), one expects the same behaviour for the Hubble factor by adding just one other scalar field (as it can be seen as just having more kinetic energy in the energy content of the Universe).

Thus, far away in the contracting phase, one expects that $|H| \ll m$ so that one would like to neglect the last term in the Klein-Gordon equation for the massive scalar field Eq. (7.1), which then would be approximated by

$$\ddot{\varphi} + m^2\varphi \approx 0. \tag{7.5}$$

Hence, the massive scalar field oscillates with constant amplitude while the massless scalar field decreases like $\phi \propto 1/a^3$ away from the bounce: therefore, one expects that the contraction will always be dominated by the massive scalar field, if one goes back far enough in the past. On the contrary, closer to the bounce, $|H| \gg m$ and this is the second term in the KG equation for the massive scalar field that one would like to neglect. In this phase, the massive field seems to have the same behaviour as the massless one, that is in $1/a^3$. Thus, there should be a transition at the hypersurface $|H| = m$ where the inflaton field transits from a massive field that oscillates with frequency m to a massless one that dilutes as the inverse volume of the Universe. Hence, as the two fields should have the same behaviour close to the bounce, one expects that depending on which field dominates when $|H| = m$, this is the same field that should dominate at the bounce. In the following section, we will check these intuitions more rigorously, both analytically and numerically.

7.2.2 Analytical approximations phase by phase

7.2.2.1 The contraction

Two cases are to be considered: either the massless field dominates the energy content of the Universe at some point during the contraction so that it leads the evolution of the Universe (by virtue of the modified Friedmann's equations), or it is the massive field that does. Let us begin with the first case.

a) The massless scalar field dominates the energy content of the Universe during the contraction well before to the moment when $|H| = m$.

From the reasoning presented in the last section, one expects the massless field not to dominate very far in the remote past. Let us check this is the case. Our hypothesis allows us to neglect the energy density of the massive field $\rho_c(X^2 + Y^2)$ in ρ, so that the equations of motion in this limiting case are given by

$$\begin{cases} \dot{H} = -8\pi\rho_c Z^2, \\ \dot{X} = mY, \\ \dot{Y} = -mX - 3HY, \\ \dot{Z} = -3HZ. \end{cases} \tag{7.6}$$

One first solve the equation for Z independently and then the equation for H and finally the system of equations on X and Y. The solutions are

$$\begin{cases} H(t) = \dfrac{1}{3t}, \\ X(t) = \dfrac{m(AJ_0(mt) + BY_0(-mt))}{\sqrt{2\rho_c}}, \\ Y(t) = \dfrac{BY_1(-mt) - AJ_1(mt)}{\sqrt{2\rho_c}}, \\ Z(t) = -\dfrac{1}{\sqrt{24\pi\rho_c}t}, \end{cases} \tag{7.7}$$

where J and Y are respectively the Bessel functions of the first and second kinds and A and B are constants to be determined given the initial conditions for X and Y. These solutions are plotted in Fig. 7.1 together with the numerical solutions with the same initial conditions, for the energy densities of the fields $\rho_\varphi = \rho_c(X^2(t) + Y^2(t))$ and $\rho_\phi = \rho_c\, Z^2(t)$ as a function of the normalised time $t' = mt$. Now as $J_\alpha(x) = \mathcal{O}\sqrt{2/(\pi x)}$ and similarly for $Y_\alpha(x) = \mathcal{O}\sqrt{2/(\pi x)}$ as $x \to \infty$, one can use these asymptotic behaviours in the infinite past. Thus, the energy density of the massive scalar field ρ_φ behaves like $1/t$ far in the contraction while the energy density of the massless scalar field ρ_ϕ behaves like $1/t^2$ meaning that if at some point the massless scalar field dominates the evolution of the Universe in the past contracting phase, one will always find a remote time when it is not the case and it is the massive field which dominates. This behaviour is also found numerically and Fig. 7.1 shows that indeed, the massive field ends up dominating in the past. Stated otherwise, our hypothesis on the dynamics is broken: we assumed the massless scalar field dominates the energy content of the Universe, translating in the fact that the dynamics of the Universe is ruled by it, see the Raychaudhuri equation in Eq. (7.6). However this is not the case during the whole contraction, as one can find a remote time when this condition is violated. This is the reason why the numerical solutions to the system of equations Eq. (7.4) under this hypothesis deviates from the analytical approximations, as one can see in Fig. 7.1, the analytical approximations overestimating the energy densities of both fields: indeed the true behaviours of the fields far in the contraction fall faster as we shall soon see. Therefore from now on, we will choose initial conditions such that the massive scalar field dominates the energy content of the Universe during the contraction. Let us recall the analytical approximations in such a case.

b) The massive scalar field dominates the energy content of the Universe during the contraction well before to the moment when $|H| = m$.

In this case, I neglect the energy density of the massless field $\rho_c Z^2$ in ρ and the equations of motion simplify to

$$\begin{cases} \dot{H} = -8\pi\rho_c Y^2, \\ \dot{X} = mY, \\ \dot{Y} = -mX - 3HY, \\ \dot{Z} = -3HZ. \end{cases} \tag{7.8}$$

One further assumes that $H^2 \ll m^2$, which is necessarily the case far enough in the contraction as the Hubble factor increases in absolute value during the contraction: $H < 0$ (the Universe is contracting) and $\dot{H} < 0$ given the Raychaudhuri equation, so the Hubble factor becomes more and more negative and it increases in absolute value. With this assumption, one rewrites the third equation like $\dot{Y} = -mX$, and we have already presented the analytical approximations for the massive scalar field in Eq. (6.14) in this limiting case. These approximations can be completed with the solution for the fraction of kinetic energy in the massless scalar field Z

$$\begin{cases} \rho(t) = \rho_0 \left(1 - \frac{1}{2}\sqrt{24\pi\rho_0}\left(t - t_0 + \frac{1}{2m}\sin(2m(t-t_0))\right)\right)^{-2}, \\ X(t) = \sqrt{\frac{\rho}{\rho_c}}\sin(m(t-t_0)), \\ Y(t) = \sqrt{\frac{\rho}{\rho_c}}\cos(m(t-t_0)), \\ Z(t) = Z_0\left(\frac{t_0}{t}\right)^2, \end{cases} \tag{7.9}$$

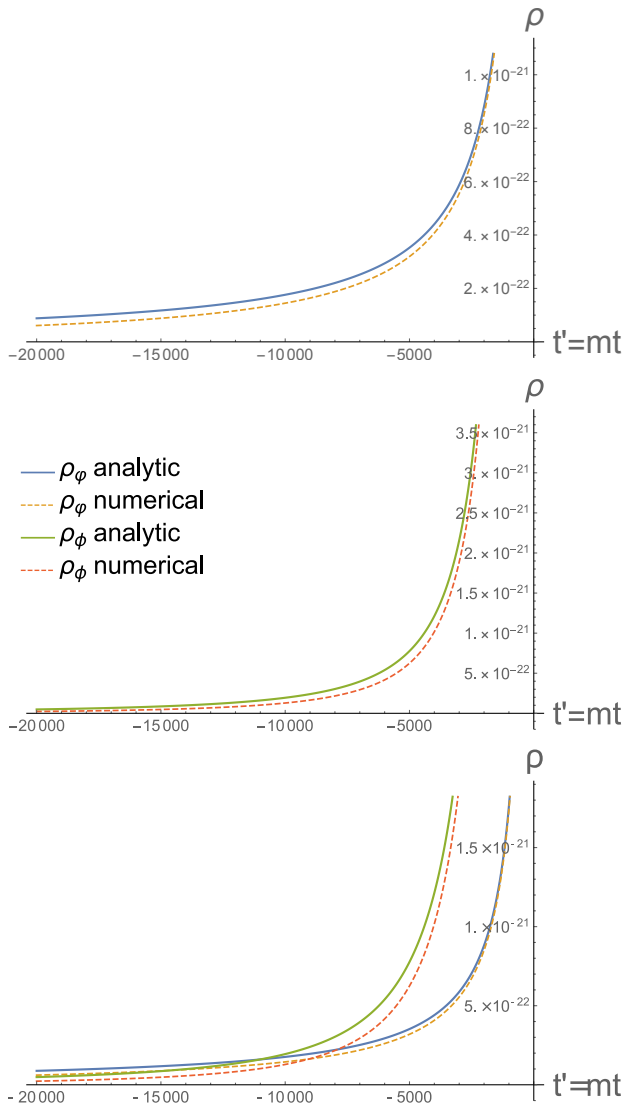

Figure 7.1: Energy densities of the massive scalar field ρ_φ (upper panel) and the massless scalar field ρ_ϕ (middle panel) and their comparison (lower panel) during the contraction, assuming that at some initial time $t'_0 \approx -215$, the massive field dominates the energy content of the Universe. If this is the case, our hypothesis is broken at some point prior to the initial time so that our analytical approximations deviate from the numerical resolution of the dynamics Eq. (7.4). Then, if some part of the contraction is dominated by the massless scalar field, one can always find a remote time when it is the massive field that dominates the evolution of the Universe. Notice the rescaling of time $t' = mt$, where $m = 1.21 \times 10^{-6}\, m_{\rm Pl}$ is the mass of the inflaton field, for numerical convenience. The Big-Bang singularity occurs at $t = 0$.

where we have set $\delta = 0$ and redefine the origin of times so that at some initial time t_0 in the past contracting phase $\rho(t_0) = \rho_0$ and t_0 is chosen so that the bounce occurs at $t = 0$ (on

these solutions, it will be a singularity as we have neglected the effective quantum effect in the Raychaudhuri equation) and Z_0 is the initial condition for Z at t_0. One can notice that the energy density of the massive field behaves like $\rho_\varphi \propto 1/(-t)^2$ and the energy density of the massless field ρ_ϕ like $\rho_\phi \propto 1/(-t)^4$, ensuring that the massive scalar field always dominates the contracting phase as far as we can go in the remote past. These solutions are plotted in Fig. 7.2 together with the numerical solutions with the same initial conditions. One sees good agreement between the analytical approximations and the numerical resolution, supporting the hypotheses we have made.

This study confirms our first intuition that the massive field should always dominate during the contracting phase. Let us now study how the fields behave around the bounce, where quantum gravity effects are taken into account, and see if it changes our qualitative conclusions.

7.2.2.2 The bounce

As for the contraction, two cases are to be considered: either the massless field dominates the energy content of the Universe during the bounce so that it leads the evolution of the Universe, or it is the massive field that does. Let us begin with the first case.

a) The massless field dominates the energy content of the Universe at the bounce, and the massive field is kinetic energy dominated.

First, before deriving the analytical approximations at the bounce under these hypotheses, we want to check the conclusion of Section 7.2.1, that if the massless field dominates when $|H| = m$, it dominates at the bounce. With the initial conditions set during the contracting phase exactly like in a), we check numerically that the massless field stil dominates when $|H| = m$, as expected from the analytical study, since the quantum gravity effects are stil negligible. Then the numerical resolution of the equations of motion, including the bounce, confirms that the massless field dominates at the bounce with $\rho_\phi(0) \approx \rho_c \approx 0.41$ while $\rho_\varphi(0) \approx 10^{-4}$ (in Planck units). Thus, this supports our first intuitions.

Let us now derive the solutions for the background in a bounce dominated by a massless field. Under our assumptions, $Z \gg Y \gg X$ and the system of equations (7.4) reduces to

$$\begin{cases} \dot{H} = -8\pi\rho_c Z^2\left(1-2Z^2\right), \\ \dot{X} = mY, \\ \dot{Y} = -3HY, \\ \dot{Z} = -3HZ, \end{cases} \tag{7.10}$$

whose solutions around the bounce (occurring at $t = 0$) are given by

$$\begin{cases} H(t) = \dfrac{8\pi\rho_c t}{1+24\pi\rho_c t^2}, \\ X(t) = X_B + \dfrac{mY_B}{\sqrt{24\pi\rho_c}}\ \mathrm{arcsinh}\left(\sqrt{24\pi\rho_c}t\right), \\ Y(t) = \dfrac{Y_B}{\sqrt{1+24\pi\rho_c t^2}}, \\ Z(t) = \dfrac{1}{\sqrt{1+24\pi\rho_c t^2}}. \end{cases} \tag{7.11}$$

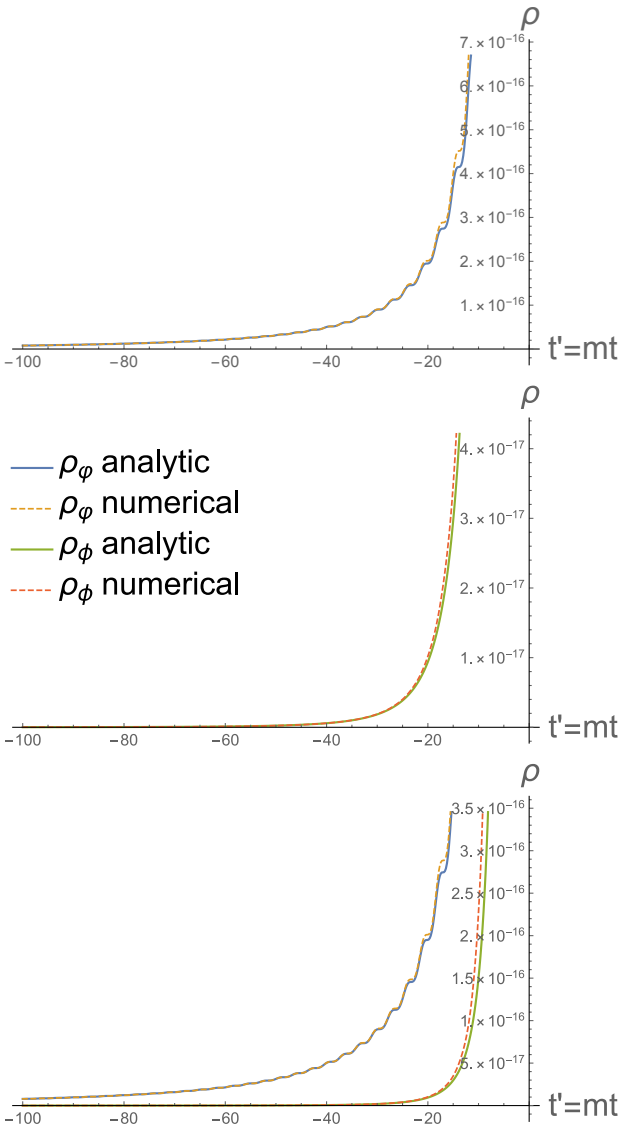

Figure 7.2: Energy densities of the massive scalar field ρ_φ (upper panel) and the massless scalar field ρ_ϕ (middle panel) and their comparison (lower panel) during the contraction, assuming that at some initial time $t'_0 \approx -44$, the massive field dominates the energy content of the Universe. If this is the case, our hypothesis is never broken for times prior to the initial time so that our analytical approximations fit well to the numerical resolution of the dynamics Eq. (7.4). Then, if the contraction is dominated by the massive scalar field, this one dominates the whole evolution of the Universe up to the point where quantum effects have to be taken into account. Notice the rescaling of time $t' = mt$, where $m = 1.21 \times 10^{-6}$ is the mass of the inflaton field, for numerical convenience. The Big-Bang singularity occurs at $t = 0$.

First, as the energy density of the massive field φ is dominated by its kinetic energy, the energy density of the two fields around the bounce are given by

$$\begin{cases} \rho_\varphi(t) = \dfrac{\rho_c Y_B^2}{1+24\pi\rho_c t^2}, \\ \rho_\phi(t) = \dfrac{\rho_c}{1+24\pi\rho_c t^2}, \end{cases} \tag{7.12}$$

so that as expected already in Section 7.2.1, the two fields have the same behaviour when $|H| \gg m$. It is not surprising that we recover this conclusion as we have just implemented in our hypotheses the conditions for having the equations that solved like this. As the massless field dominates at the bounce, one can take $Y_B = 1/10$ and from the above solution, one could be tempted to conclude that if the massless field dominates at the bounce, it always dominates away from it. This is seen not to be the case in Fig. 7.3 right, where we plotted the energy densities of the massive field and the massless field, both with the numerical resolution and the analytical approximations. Indeed, we have seen previously that the massless field cannot dominate the whole evolution of the Universe and that far away enough from the bounce, the massive field ends up dominating because H becomes small enough compared to m so that one can no longer neglect the potentiel term $m^2\varphi$ in the KG equation on the massive field. Here, it has been neglected because we further assumed the massive field was kinetic energy dominated at the bounce. Thus, one does not have to wait that $|H| = m$ for the massive field to dominate over the massless one, which occurs for $t \approx \pm 11$. Actually, away from the bounce, the fraction of potentiel energy X becomes important $X(t) \sim mY_B/\sqrt{24\pi\rho_c}\ln(2\sqrt{24\pi\rho_c}t)$ with respect to $Y(t) \sim -Y_B/(\sqrt{24\pi\rho_c}t)$ so that one of our hypothesis is violated, changing drastically the evolution of the Universe. Indeed, the comparison with numerical simulations in Fig. (7.3) right shows that away from the bounce, the analytical approximation overestimates the energy density of the massless scalar field and that the massive scalar field ends up dominating the evolution of the Universe. Thus, even though the massless scalar field dominates the evolution of the Universe at the bounce if it dominates when $|H| = m$, the reverse is not true: if the massless field dominates at the bounce, it does not necessarily dominate at the hypersurface $|H| = m$.

b) The massive field dominates the energy content of the Universe at the bounce, which is kinetic energy dominated.

Before deriving the analytical approximations in this case, let us check that as for the massless field, if the massive field dominates at the hypersurface $|H| = m$, it dominates at the bounce. By choosing initial conditions there, one imposes that the massive field dominates at the hypersurface. Then, one computes the energy densities of the fields at the bounce and finds $\rho_\varphi(0) \approx 0.3$ while $\rho_\phi(0) \approx 0.1$, confirming again our first conclusion.

Let us now derive the solutions for the background in a bounce dominated by a massive field. Under our assumptions, one can use the analytic approximations of Linsefors & Barrau (2013) for the massive scalar field and complete with the resolution for the additional massless scalar field. Indeed, with our hypotheses $Y \gg X, Z$, and the system of equations (7.4) reduces to

$$\begin{cases} \dot{H} = -8\pi\rho_c Y^2\left(1-2Y^2\right), \\ \dot{X} = mY, \\ \dot{Y} = -3HY, \\ \dot{Z} = -3HZ, \end{cases} \tag{7.13}$$

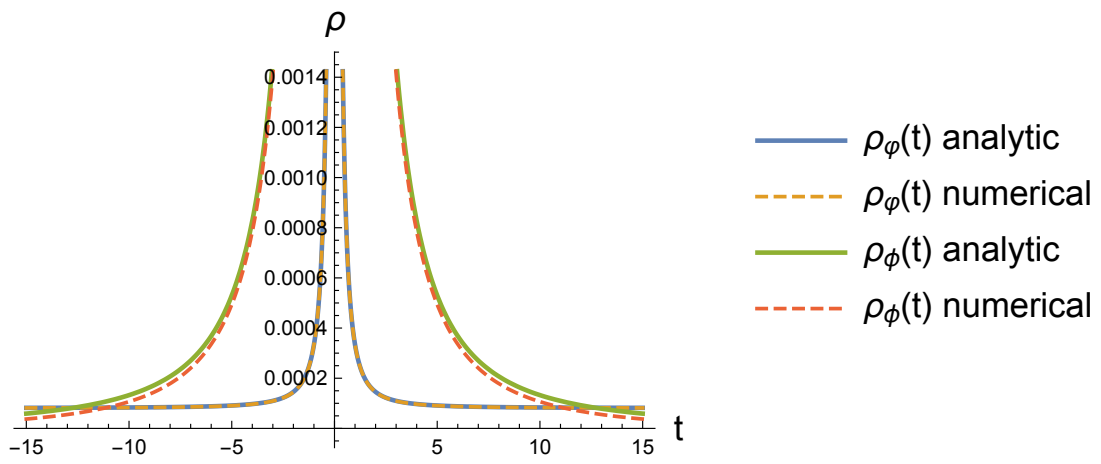

Figure 7.3: Energy densities of the massive scalar field ρ_φ and the massless scalar field ρ_ϕ around the bounce occurring at $t = 0$. Even if the bounce is dominated by the massless scalar field, it will not remain the case away from the bounce.

whose solutions around the bounce (occurring at $t = 0$) are given by

$$\begin{cases} H(t) = \dfrac{8\pi\rho_c t}{1 + 24\pi\rho_c t^2}, \\ X(t) = X_B \pm \dfrac{m}{\sqrt{24\pi\rho_c}} \operatorname{arcsinh}\left(\sqrt{24\pi\rho_c}\, t\right), \\ Y(t) = \pm\dfrac{1}{\sqrt{1 + 24\pi\rho_c t^2}}, \\ Z(t) = \dfrac{Z_B}{\sqrt{1 + 24\pi\rho_c t^2}}. \end{cases} \tag{7.14}$$

Assuming the massless scalar field contributes to the total energy density with a ratio 10^{-1} at the bounce through its only kinetic energy: $Z_B = 10^{-1}$ then $Z(t) = 1/(10\sqrt{1 + 24\pi\rho_c t^2})$. The energy densities of the massive scalar field φ and the massless scalar field ϕ are respectively given by

$$\begin{cases} \rho_\varphi(t) = \dfrac{\rho_c}{1 + 24\pi\rho_c t^2}, \\ \rho_\phi(t) = \dfrac{\rho_c}{100(1 + 24\pi\rho_c t^2)}. \end{cases} \tag{7.15}$$

As for a), one could rapidly conclude that if the massive scalar field dominates the evolution of the Universe at the bounce, it always dominates, either in the past contracting phase or in the future expansion of the Universe. However as for a), one might be skeptical about this conclusion, remembering that the above analytical approximations hold when the bounce is kinetic energy dominated so that it may no longer be the case as one goes away from the bounce. Indeed, the same analysis holds: the potential energy in the massive field becomes important away from the bounce, overcoming the kinetic energy at some point, changing the dynamics. Therefore, our hypothesis on the kinetic energy dominated massive field is also

violated here. This is the reason why the comparison with numerical simulations shows in Fig. (7.4) right that actually, the analytical approximation underestimates the energy density of the massive scalar field away from the bounce. However, even though the fact that at some point the potential energy in the massive scalar field overcomes its kinetic energy changes the dynamics, one can expect from a) that the massive field keeps dominating away from the bounce. Indeed, it is the potential energy of the scalar field which makes it dominate away from the bounce in a) as kinetic energy alone (in the massless field) falls faster. Therefore, here too we expect the same behaviour. Furthermore, we have shown that far enough in the contraction, the massive field dominates. Thus, if it dominates the evolution at the bounce, it always dominates either in the past or future.

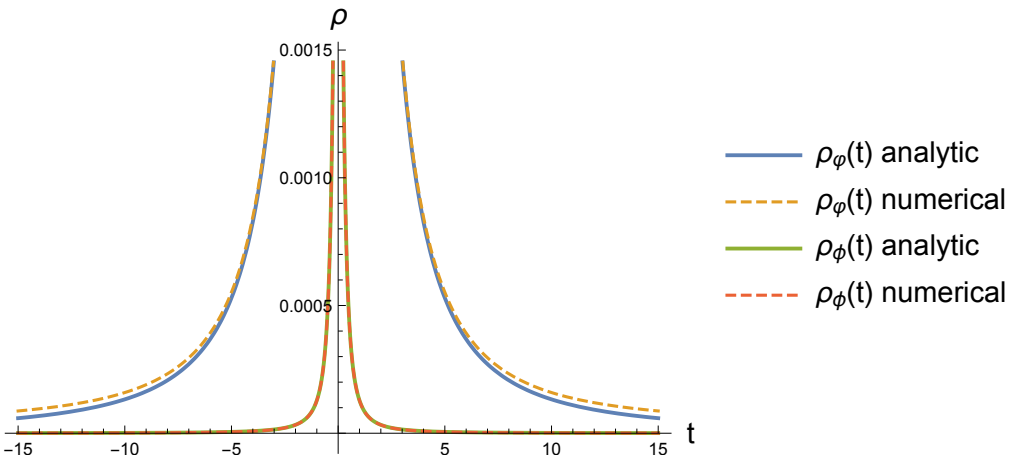

Figure 7.4: Energy densities of the massive scalar field ρ_φ and the massless scalar field ρ_ϕ around the bounce occurring at $t = 0$. If the bounce is dominated by the massive scalar field, it dominates all the evolution of the Universe, in this model.

To conclude this section, we have checked that very close to a kinetic energy dominated bounce, the two fields have the same behaviour in $1/a^3$ and that when one of the two fields dominates at the hypersurface $|H| \ll m$, it also dominates at the bounce. Finally, the massive scalar field dominates the evolution of the Universe away from it. Thus, in Section 7.3 we will focus on a contracting phase dominated by the massive scalar field for the treatment of the quantum perturbations in this model, using the analytic approximations of Eq. (7.9) for the background.

7.2.3 Inflation in two-fields LQC

In Fig. 7.5, we redo the plot of Fig. 6.4 in our two fields model with the same fractions of potential energy at the bounce x and the same mass $m = 10^{-2}$ for the massive scalar field. We find the same behaviours as in the model with one field, that is: a symmetric evolution when there is no potential energy at the bounce $x = 0$ and a longer phase of inflation the bigger x is. However, our massive field do no reach such high values, resulting in shorter phases of inflation. This is explained by the fact that there is more kinetic energy in our model, although the values of the fraction of potential energy are the same, because of the presence of the massless field. Therefore,

inflation is still a feature of our model which happens under quite the same conditions, that is a bit of potential energy at the bounce. However, we expect to have a shorter phase of inflation on average than in the one field model, even though the massless field decreases rapidly away from the bounce.

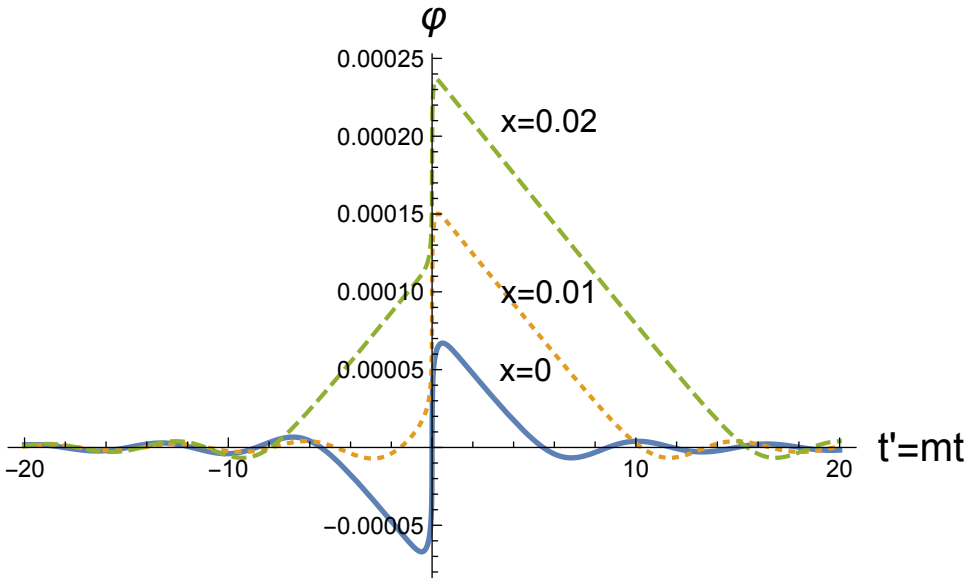

Figure 7.5: Time evolution of the scalar field. Different evolutionary scenarii leading to a slow-roll inflation phase are displayed. The bottom (solid) line represents the symmetric case. The middle (dotted) line represents the shark fin-type evolution. The top (dashed) line corresponds to a larger fraction of potential energy. For all curves $m = 0.01 m_{\mathrm{Pl}}$.

Initial conditions for the background fields

In the previous section, we have just shown that the massless field is always negligible in the past, if one goes far enough in the contracting phase. One can see it as convenient, as if one finds an enough remote time, we can use the analytical approximations in this fields configuration Eq. (7.9). Unfortunately, if with one massive field a natural PDF for the initial conditions of the field arises that is preserved over time, as a PDF on the δ parameter (see Section 6.2.4), there is none in our two fields model. Indeed, in addition of the natural PDF for the massive field, one would need to find a PDF for the initial condition of the massless field, that is, a PDF on Z_0. A PDF for Z_0 could be to take any value uniformly in the interval $[-Z_{0\mathrm{max}}, Z_{0\mathrm{max}}]$ with $Z_{0\mathrm{max}} \ll \sqrt{\rho_0/\rho_c}$. Thus, two problems arise: first, how do you define the fact that the initial value $Z_{0\mathrm{max}}$ is negligible with respect to $\sqrt{\rho_0/\rho_c}$. One could fix a threshold like $10^{-1}\sqrt{\rho_0/\rho_c}$ but there would be some arbitrariness in this choice. Secondly, there is also some arbitrariness in the choice of the initial time t_0, or equivalently, in the choice of ρ_0. In the one field model of the previous chapter and likewise here, the initial time t_0 is determined by ρ_0, such that one has $|H(t_0)| = \sqrt{8\pi\rho_0/3} \ll m$, delimiting the validity of our analytical approximations in the contracting phase. As they hold for the whole contracting phase, one can choose any value for ρ_0 as long as this condition is fulfilled. Therefore, the interval where one can set the initial condition for Z_0, $[-Z_{0\mathrm{max}}, Z_{0\mathrm{max}}]$, shrinks to zero in the infinite past. This

is the reason why it is said that there is no natural PDF for this initial parameter in the past contracting phase. A way to overcome this second issue would be to take the initial conditions at the hypersurface $|H| = m$ in the contracting phase, as it is around there that the massive field changes behaviour, from massive to massless. This also further determines which field dominates at the bounce, and consequently the existence and duration of inflation. It seems therefore 'natural' to put the initial conditions there. Nevertheless, nothing ensures that the massive field dominates at this point (as we have seen in the previous section), so one does not have to require that $Z_{0\max} \ll \sqrt{\rho_0/\rho_c}$ but rather that $Z_{0\max} = \sqrt{3/(8\pi\rho_c)}m$. Then the energy density for the massive field would be fixed by $X_0^2 + Y_0^2 = 3m^2/(8\pi\rho_c) - Z_0^2$ but another problem arises here because there is no more natural PDF for the massive field (previously set on the δ parameter). Therefore the ratio between potential and kinetic energy in the massive field could take any value on the real line, which is not of finite volume. However, one notices that the PDF for the massless field is conserved, by considering the constant of motion $\pi_\phi = a_0\dot{\phi}_0$. Fixing arbitrarily the value of a_0 either at the bounce or during the contraction (as the value of a_0 is not important and changing it is just a rescaling of the Universe), one can choose randomly $\dot{\phi}_0$ within $[-\sqrt{2\rho_c}, \sqrt{2\rho_c}]$ or $[-\sqrt{3/(4\pi)}m, \sqrt{3/(4\pi)}m]$ (if one chooses to put the initial conditions when $|H| = m$), respectively, and the PDF is conserved.

Nonetheless, following Ashtekar & Sloan (2011), it seems that there are natural probability distributions for the initial conditions of X, Y and Z at the bounce. As we do not know the initial conditions for this model of the Universe, the probability distribution is taken to be flat with respect to the Liouville measure. The choice of the Liouville measure is justified by the fact it is preserved over time and 'canonical' (see Ashtekar & Sloan, 2011, for more details). Concretely, as X, Y and Z are ratios of (square-roots of) energy densities, they take values in the interval [-1,1]. Thus, we can parameterize the initial conditions as follows

$$\begin{cases} X(0) = \cos(\gamma_i)\sin(\delta_i), \\ Y(0) = \sin(\gamma_i)\sin(\delta_i), \\ Z(0) = \cos(\delta_i), \end{cases} \tag{7.16}$$

with $\gamma_i \in [0, 2\pi]$ and $\delta_i \in [0, \pi]$, so that they belong the unit sphere 7.6. Now, one can wonder about the relevance of the signs of the initial conditions in Eq. (7.16). Indeed, what seems to be physically relevant is the value of the potential $2\rho_c X(0)^2$ of the massive field at the bounce and the values of the kinetic energies $2\rho_c Y(0)^2$ and $2\rho_c Z(0)^2$ of the massive field and the massless field, respectively. In particular, in this section we are interested in the duration of inflation which only depends on $X^2_{\max}$, among these parameters. Therefore, one could think the sign of X is not a relevant parameter. However, the plain (blue) and dotted (green) curves in Fig. 7.7 which are symmetric with respect to the vertical axis show that it matters. In the first case, one has a slow-roll inflation phase while in the second, one has no slow-roll inflation but a slow-roll deflation phase prior to the bounce. In fact, this graphics shows that what is relevant to determine if an inflation phase occurs or not is the sign of $X(0)Y(0)$. Indeed, the plain (blue) and dot-dashed (orange) curves are symmetric with respect to the horizontal axis, both predicting a slow-roll inflation phase with the same duration, and similarly for the dashed (yellow) and green (dotted) curves predicting a slow-roll deflation phase with the same duration. The left plot is done for $Z(0) > 0$ while the right plot is done for $Z(0) < 0$ and are exactly identical: the trajectory thus do not depend on the sign of this initial parameter. Thus, we can restrict ourselves to the interval $[0, \pi/2]$ for δ_i and $[0, \pi]$ for γ_i.

Although this initial PDF is quite natural, the drawback is that it can pose a problem of consistency. Indeed, one can have a very large fraction of potential energy at the bounce where quantum backreaction effects should be taken into account. Further work thus needs to be made to use this initial PDF in order to be fully consistent.

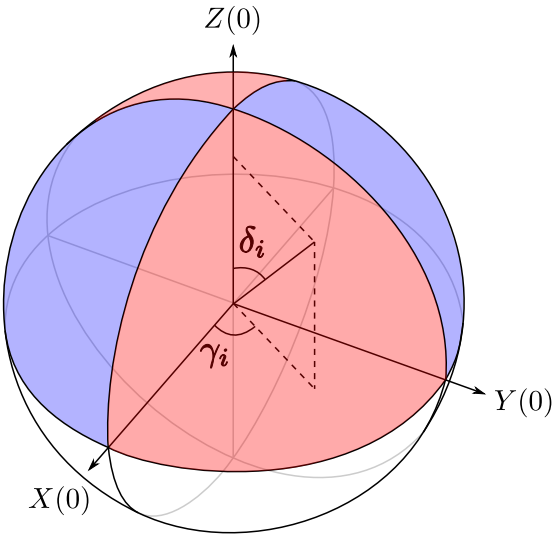

Figure 7.6: The initial conditions for the fields $X(0)$, $Y(0)$ and $Z(0)$ belong to the unit sphere, so they can be parameterised by the spherical coordinates $\delta_i \in [0, \pi]$ and $\gamma_i \in [0, 2\pi]$. The evolution scenarii do not depend on the sign of $Z(0)$ so we restrict ourselves to the north hemisphere to take the initial conditions: $\delta_i \in [0, \pi/2]$. Furthermore, the fact that an inflation phase with given length occurs or not only depends on the sign of $X(0)Y(0)$. The red parts correspond to the inflation phase in the evolution scenarii of Fig. 7.7 while the blue parts to the deflation phase in these same scenarii. We thus further restrict ourselves to a quarter of the sphere to take the initial conditions for the fields, that is taking $\gamma_i \in [0, \pi]$ for example.

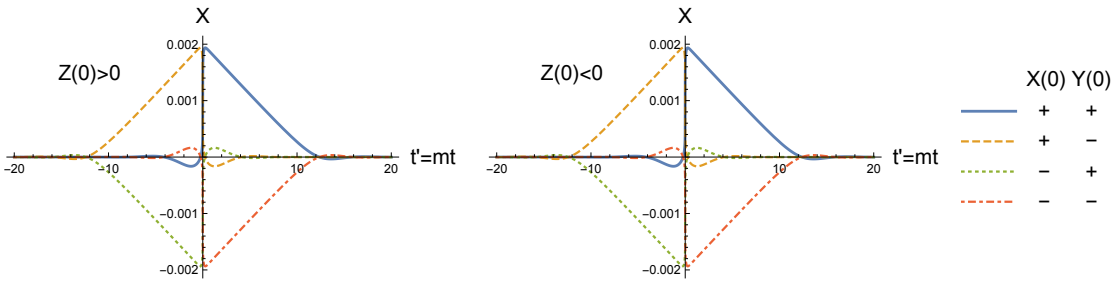

Figure 7.7: The dependence of the evolution scenarii on the sign of the initial conditions for the fields. The fact that an inflation phase with given length occurs or not only depends on the sign of $X(0)Y(0)$. The results are insensitive to $Z(0)$, the initial value of the massless field velocity.

In conclusion, it seems to be difficult to find conserved PDF for the massive and the massless scalar field simultaneously during the contracting phase so setting the initial PDF at the bounce looks like the most convenient choice.

7.3 Adiabatic and isocurvature scalar perturbations

7.3.1 Coupled equations of motion

As explained in Section 6.3.1, we will not use either of the two approaches developed in Grain (2016) or Agullo et al. (2013a) for the equations of motion of the perturbations but use the classical treatment made for the quantum perturbations during the very early Universe. The reason for this is that away from the bounce, either of the two approaches reduces to this treatment and we may need inputs from the mother LQG theory to arrive at a consensus and a clear derivation of these equations. Only during the bounce the equations must include quantum corrections. However, these quantum corrections should not affect modes that are not amplified during the bounce, that is modes in the UV and IR limits. Furthermore, as for the case of a perfectly homogeneous and isotropic Universe, we assume that the effective equations still give the evolution of the expectation values of the sharply peaked states, both for the background and linear perturbations, thus neglecting backreaction effects. Here, we use the framework developed in Langlois & Renaux-Petel (2008) for the treatment of perturbations in generalized multi-field inflation. As explained in Chapter 3, Section 3.3, in multi-field inflation, in addition to the usual adiabatic or curvature perturbations σ one also predicts isocurvature or entropic perturbations s. Their equation of motions are given in conformal time η by Eq. (3.57) which we recall here

$$\begin{cases} v_\sigma'' - \xi v_s' + \left(k^2 - \dfrac{z''}{z}\right) v_\sigma - \dfrac{(z\xi)'}{z} v_s = 0, \\ v_s'' + \xi v_\sigma' + \left(k^2 - \dfrac{a''}{a} + a^2\mu_s^2\right) v_s - \dfrac{z'}{z}\xi v_\sigma = 0. \end{cases} \tag{7.17}$$

Now we can compute the explicit expressions of the background functions appearing in Eq. (7.17) given that here, the pressure is $P = (\dot\varphi(t)^2 + \dot\phi(t)^2)/2 - m^2\varphi(t)^2/2$ (there is no potential energy associated with the massless scalar field ϕ), so that

$$\begin{aligned} P_{,s} &= e_s^I P_{,I} = \frac{m^2\varphi(t)\dot\phi(t)}{\dot\varphi(t)^2 + \dot\phi(t)^2}, \\ P_{,ss} &= e_s^I P_{,sI} = \frac{-m^2\dot\phi(t)^2}{\dot\varphi(t)^2 + \dot\phi(t)^2}, \end{aligned} \tag{7.18}$$

where we recall that $P_{,I}$ is the partial derivative of the pressure with respect to the field ϕ^I (with $\phi^1 = \varphi$ and $\phi^2 = \phi$) and e_s^I is the unit vector orthogonal to the adiabatic direction and gives the entropy direction in field space. Finally

$$\begin{cases} \xi(t) = \dfrac{a(t)}{\dot\varphi(t)^2 + \dot\phi(t)^2} 2m^2\varphi(t)\dot\phi(t), \\ z(t) = \dfrac{a(t)\sqrt{\dot\varphi(t)^2 + \dot\phi(t)^2}}{H}, \\ \mu_s^2(t) = \dfrac{m^2\dot\phi(t)^2}{\dot\varphi(t)^2 + \dot\phi(t)^2}\left(1 - \dfrac{m^2\varphi(t)^2}{\dot\varphi(t)^2 + \dot\phi(t)^2}\right). \end{cases} \tag{7.19}$$

Notice here that the functions of the background appearing in Eq. (7.17) are given with respect to cosmic time t whose derivative is denoted by a dot. Actually, one can rewrite the equations

of motions for the perturbations Eq. (7.17) in cosmic time

$$\begin{cases} \ddot{v}_\sigma + H\dot{v}_\sigma - \dfrac{\xi}{a}\dot{v}_s + \left(\dfrac{k^2}{a^2} - \left(\dfrac{\ddot{z}}{z} + H\dfrac{\dot{z}}{z}\right)\right) v_\sigma - \left(\dfrac{\dot{z}\xi}{az} + \dfrac{\dot{\xi}}{a}\right) v_s = 0, \\ \ddot{v}_s + H\dot{v}_s + \dfrac{\xi}{a}\dot{v}_\sigma + \left(\dfrac{k^2}{a^2} - \left(\dfrac{\ddot{a}}{a} + H^2\right) + \mu_s^2\right) v_s - \dfrac{\dot{z}}{az}\xi v_\sigma = 0, \end{cases} \tag{7.20}$$

with the dot $\dot{}$ meaning derivative with respect to cosmic time. This rewriting with cosmic time will turn out to be more convenient as the numerical resolution of the background was done in cosmic time, see Section 7.2.2. In the following, we will go back and forth between the two formulations of the equations of motion for the perturbations Eq. (7.17) in conformal time η and Eq. (7.20) in cosmic time t because it is easier to get intuitions on the physical properties of the equations of motion in the first formulation while it is easier to deal with the second one numerically. Therefore, we mention here the relation between the two time variables in the dust-like contraction

$$t = \frac{1}{t_0^2}\left(\frac{\eta a_0}{3}\right)^3, \tag{7.21}$$

and the link between the coefficient functions

$$\begin{aligned} \frac{z''}{z} &= a^2\left(\frac{\ddot{z}}{z} + H\frac{\dot{z}}{z}\right), \\ \frac{(z\xi)'}{z} &= a^2\left(\frac{\dot{z}\xi}{az} + \frac{\dot{\xi}}{a}\right), \\ \frac{a''}{a} &= a^2\left(\frac{\ddot{a}}{a} + H^2\right), \quad \text{and} \\ \frac{z'}{z}\xi &= a^2\frac{\dot{z}}{az}\xi. \end{aligned} \tag{7.22}$$

After introducing all these notations, we can go back to the equations of motion for the perturbations (7.17) and comment. As ξ is non-vanishing, the equations of motion for the adiabatic and entropy perturbations are coupled meaning that if ξ is not negligible, they feed each other through all the evolution of the Universe. Indeed, as shown in Fig. (7.8), ξ/a shows growing oscillations as going in the remote past. This system of two coupled second order equations is quickly oscillating during the contraction so that it is particularly difficult to solve in comparison to the inflationary phase where one can find approximations for the functions in terms of the slow-roll parameters (e.g. Byrnes & Wands, 2006), or in comparison to the one-field case where there is no coupling.

Another way to see that the perturbations are coupled is to look at the bakcground trajectory in fields space, see Fig. 7.9. Indeed, we recall that the angle θ characterises the tangent of the trajectory, see Fig. 3.1 and its definition equations Eq. (3.39)

$$\tan\theta = \frac{\dot{\phi}}{\dot{\varphi}}. \tag{7.23}$$

Now, differentiating this equation with respect to cosmic time t and using the KG equations for the fields Eq. (7.1), one finds

$$\dot{\theta} = \frac{\Xi}{2} = \frac{\xi}{2a}. \tag{7.24}$$

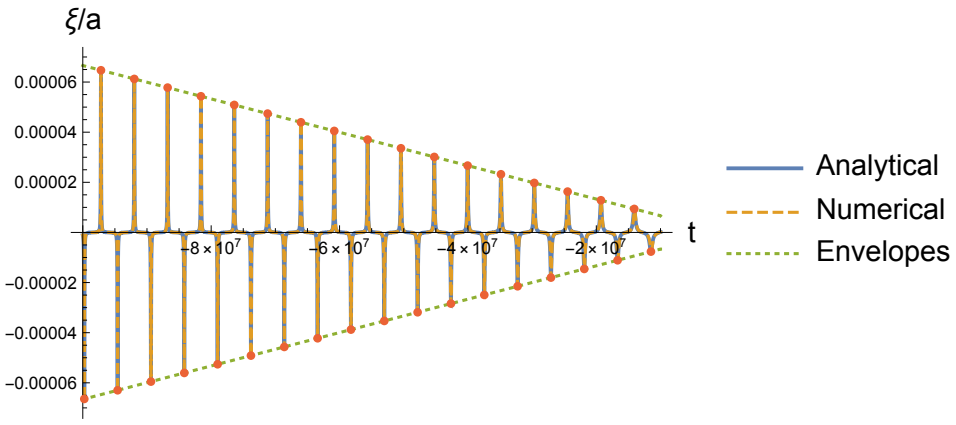

Figure 7.8: The coupling ξ/a during the contracting phase dominated by the massive scalar field. It shows growing oscillations in the remote past. The orange dots indicate the tips of the peaks, whose time position correspond to the orange dots in Fig. 7.9. The bounce is taken at $t = 0$.

Thus, the curvature of the background trajectory, given by $\dot{\theta}$ is another characterisation of the coupling of the adiabatic and isocurvature perturbations. This is illustrated with the orange dots in Fig. 7.8 and Fig. 7.9 that correspond to times when the coupling between the perturbations is the strongest.

7.3.2 Initial conditions during the contraction

We want to set the initial conditions for the perturbations in the remote past when $t \to \infty$. Indeed, these initial conditions must be part of our model so that we can make predictions in terms of power spectra of the perturbations. Hence, we use approximations for the background functions in order to solve analytically the perturbations equations and then find initial conditions.

The $\xi = 0$ case

We will start by considering the simpler case when there is no coupling ξ in the system of equations (7.17)

$$\begin{cases} v_\sigma'' + \left(k^2 - \dfrac{z''}{z}\right) v_\sigma = 0, \\ v_s'' + \left(k^2 - \dfrac{a''}{a} + a^2\mu_s^2\right) v_s = 0, \end{cases} \tag{7.25}$$

and try to solve it. The coefficient functions do not have simple analytic expressions. However, using the analytic approximations for the background Eq. (7.9), we will try to compute the asymptotic approximations in the infinite past for these functions of the background. Doing this, the expressions of the coefficients are still very complicated as they show an oscillatory behaviour because of the oscillatory massive field φ, see Fig. (7.10). We will thus need to approximate them more, by averaging the oscillations, among other things.

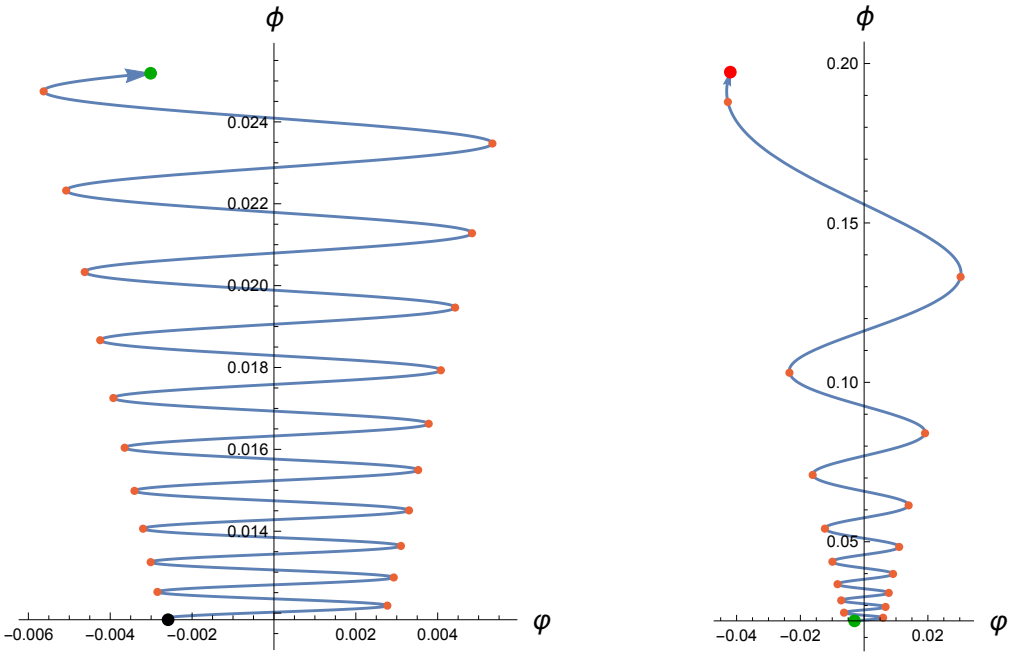

Figure 7.9: The fields trajectory in fields space, during the contracting phase dominated by the massive scalar field. On the left the trajectory is plotted from $t = -10^8$ (black dot) to $t = -4.7 \times 10^7$ (green dot) and on the right from $t = -4.7 \times 10^7$ to $t = -6 \times 10^6$ (red dot), so that the arrow indicates the direction of time, running from bottom to top. The analytical approximations for the fields might break below $t = -6 \times 10^6$ as $H^2 \sim m^2$. One notices that the background trajectory is curved, meaning the adiabatic and isocurvature perturbations are coupled. The orange dots indicate where the trajectory is the most curved, indeed corresponding to the times when the coupling ξ reach its highest values, i.e. the orange dots in Fig. 7.8.

If we write directly these functions in terms of the scalar fields and their derivatives, one gets

$$\begin{aligned}\frac{z''}{z} = a(t)^2 \Bigg[&- \frac{16\pi m^2 \varphi(t)\dot{\varphi}(t)}{H(t)} + \frac{32\pi^2 \left(\dot{\phi}(t)^2 + \dot{\varphi}(t)^2\right)^2}{H(t)^2} + 2H(t)^2 + \frac{m^4 \varphi(t)^2}{\dot{\phi}(t)^2 + \dot{\varphi}(t)^2} \\ &+ \dot{\varphi}(t)^2 \left(- \frac{m^2 \left(m^2 \varphi(t)^2 + \dot{\phi}(t)^2 + \dot{\varphi}(t)^2\right)}{\left(\dot{\phi}(t)^2 + \dot{\varphi}(t)^2\right)^2} + \frac{48\pi \dot{\phi}(t)^2}{\rho_c} - 28\pi \right) \\ &+ \frac{24\pi \dot{\phi}(t)^4}{\rho_c} + \frac{24\pi \dot{\varphi}(t)^4}{\rho_c} - 28\pi \dot{\phi}(t)^2 \Bigg],\end{aligned} \tag{7.26}$$

$$a^2 \mu_s^2 = \frac{a(t)^2 m^2 \dot{\phi}(t)^2}{\dot{\varphi}(t)^2 + \dot{\phi}(t)^2} \left(1 - \frac{m^2 \varphi(t)^2}{\dot{\varphi}(t)^2 + \dot{\phi}(t)^2}\right), \tag{7.27}$$

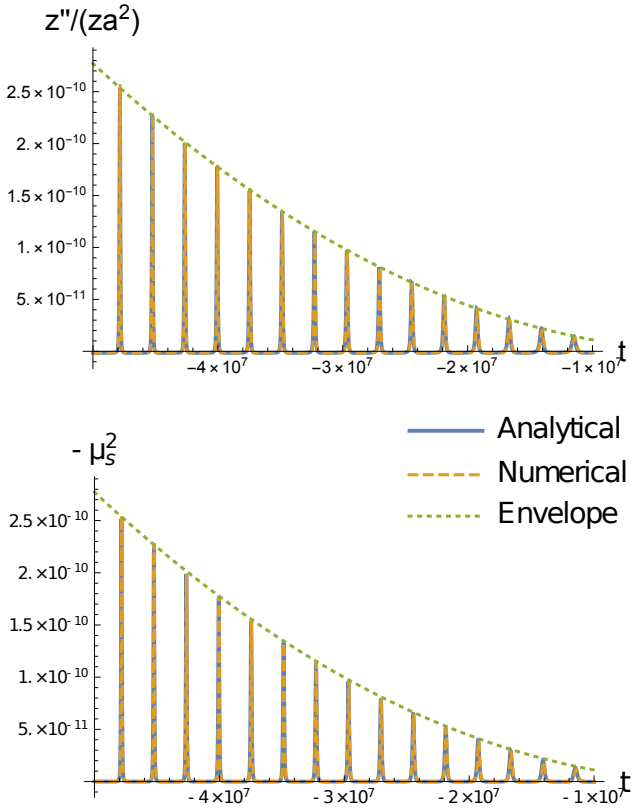

Figure 7.10: The coefficient functions $z''/(za^2) = \ddot{z}/z + H\dot{z}/z$ (upper panel) and $-\mu_s^2$ (lower panel), as a function of time. They show an oscillatory behaviour with growing amplitude in the remote past.

and

$$\frac{a''}{a} = \frac{2}{\eta^2}. \tag{7.28}$$

Notice again the mix between conformal time η on the left-hand side denoted by derivative $'$ and cosmic time t on the right hand-side. This is the term in square brackets in Eq. (7.26) which is plotted in Fig. 7.10 left, which is also equal to $\ddot{z}/z + H\dot{z}/z$ appearing in Eq. (7.20). In Schander et al. (2016) there is only one massive scalar field φ so we recover their equation (50) by setting $\dot{\phi} = 0$ in Eq. (7.26). In their case, they can easily take the average of $z''/(za^2)$ as this is simply a sum of sine and cosine modulated by positive powers of $\sqrt{\rho}$ plus a constant $-m^2$. As $\sqrt{\rho} \propto 1/t$, once the average taken, one is left only with the constant term $-m^2$. In our case, the oscillatory behaviour of our function is not that simple because of the appearance of the derivative of the massive field in the denominators. Nonetheless, the oscillations are still imprinted on top of the constant term $-m^2$, as shown in Fig. 7.11 so that $z''/(za^2)$ is almost always equal to $-m^2$ except in some tiny periods of time. Thus, we will solve the equation for the adiabatic perturbations Eq. (7.25) by approximating z''/z by $-m^2a^2 \propto m^2\eta^4$ (even if in some tiny periods of time the function scales like $z''/z \propto \eta^{10}$), and consider physical modes such that $(k/a)^2 \ll m^2$, as it is

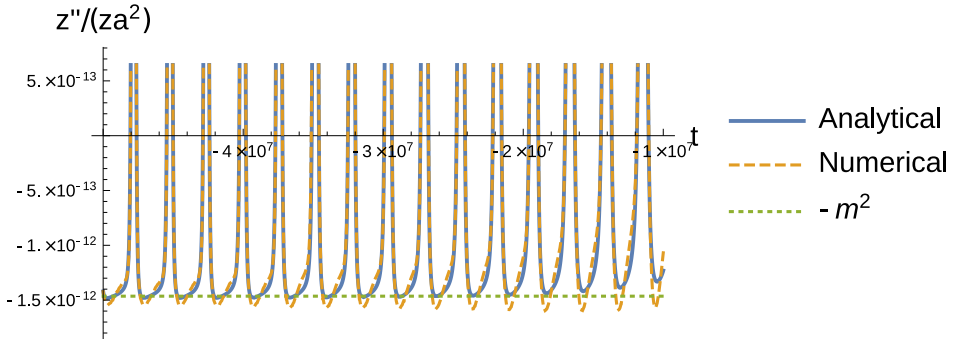

Figure 7.11: The bottom shape of the function $z''/(za^2)$.

the case for all modes in the infinite past. In conformal time, this gives

$$v_\sigma(\eta) = \sqrt{\frac{-a_0\eta}{3}}\left(AH^{(1)}_{1/6}\left(\frac{a_0^3 m\eta^3}{27t_0^2}\right) + BH^{(2)}_{1/6}\left(\frac{a_0^3 m\eta^3}{27t_0^2}\right)\right), \tag{7.29}$$

where $H^{(1)}_{1/6}$ and $H^{(2)}_{1/6}$ are the Hankel functions of the first and second kind of order $1/6$ respectively; t_0 is the initial cosmic time where the initial conditions are set for the background and a_0 is the scale factor at that time. The constants A and B need to be determined to fully specify our initial conditions for the perturbations. First, we use the fact that

$$\begin{cases} H^{(1)}_{1/6}\left(\frac{a_0^3 m\eta^3}{27t_0^2}\right) \underset{\eta\to-\infty}{\sim} \sqrt{\frac{54t_0^2}{\pi a_0^3 m\eta^3}}\exp\left(i\left(\frac{a_0^3 m\eta^3}{27t_0^2} - \frac{\pi}{3}\right)\right), \\ H^{(2)}_{1/6}\left(\frac{a_0^3 m\eta^3}{27t_0^2}\right) \underset{\eta\to-\infty}{\sim} \sqrt{\frac{54t_0^2}{\pi a_0^3 m\eta^3}}\exp\left(-i\left(\frac{a_0^3 m\eta^3}{27t_0^2} - \frac{\pi}{3}\right)\right), \end{cases} \tag{7.30}$$

to set $A = 0$ so that we only keep the solution that propagates in the positive time direction. Then, B is found thanks to the Wronskian condition

$$v_\sigma v_\sigma^{*\prime} - v_\sigma^* v_\sigma' = i, \tag{7.31}$$

which finally gives $|B|^2 = \pi/(4a_0)$ and

$$v_\sigma(\eta) = \sqrt{\frac{-\pi\eta}{12}}H^{(2)}_{1/6}\left(\frac{a_0^3 m\eta^3}{27t_0^2}\right). \tag{7.32}$$

One still has to solve the equation for the entropy perturbations Eq. (7.25). Using the same trick as what was done for the function z''/z, we notice that $a^2\mu_s^2$ behaves like $1/\eta^2$ except in some tiny periods of time where the amplitude of the peaks goes like η^{10}. Thus, we solve this second equation by considering modes such that $k^2 \gg 1/\eta^2$, which again is always the case in the infinite past. The equation is thus just a simple harmonic oscillator with frequency k. Its solution, once normalised with the Wronskian and taken to propagate in the positive time direction, is simply

$$v_s(\eta) = \frac{e^{-ik\eta}}{\sqrt{2k}}, \tag{7.33}$$

which is the Minkowski vacuum, see Section 3.3.

Going back to the full equations Eq. (7.17) in conformal time or Eq. (7.20) in cosmic time, let us see if one can play the same trick to approximate the other coefficient functions. Fig. 7.8 seems to show that ξ/a oscillates around a zero mean value so that it is zero except in some tiny periods of time. Indeed, $\xi \propto 1/\eta$ except for the amplitude of the peaks that go like $\pm\eta^5$. Similarly, one plots in Fig. 7.12 the coefficient functions $\dot{z}\xi/(az) + \dot{\xi}/a = (z\xi)'/(za^2)$ and $\dot{z}\xi/(az) = z'\xi/(za^2)$. The functions are both proportional to η, $(z\xi)'/z \propto \eta$ and $z'\xi/z \propto \eta$, except in those tiny periods of time where they show peaks with growing amplitude in the remote past. Unfortunately, it is not as simple as for the other coefficient functions ξ, z''/z or $a^2\mu_s^2$ to get how the amplitude of the peaks scale. Anyway, one can already draw the conclusion that, even though 'on average', the coupling ξ decreases to zero away from the bounce, the other coefficient functions $(z\xi)'/z$ and $z'\xi/z$ that couples the two equations of motion for the adiabatic and isocurvature perturbations increase away from the bounce. Hence, it turns out to be difficult to neglect them in Eq. (7.17).

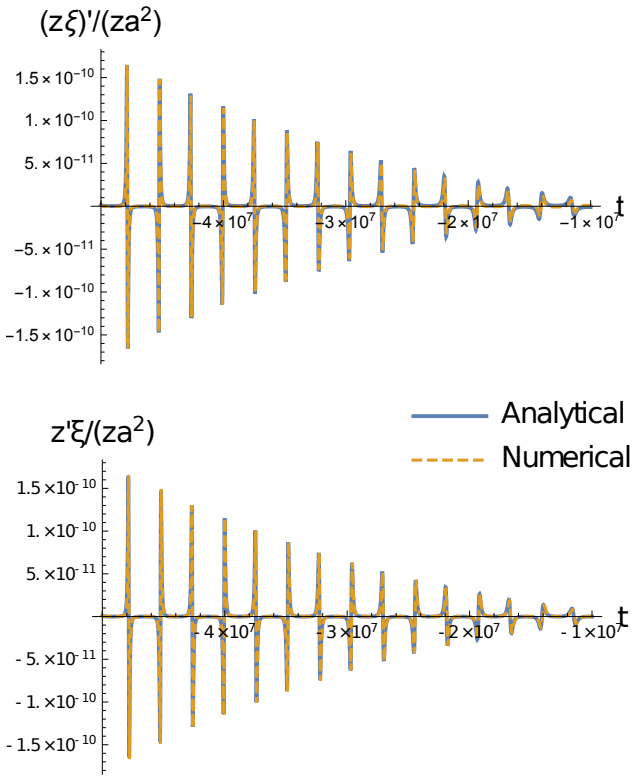

Figure 7.12: The coefficient functions $(z\xi)'/(za^2)$ (upper panel) and $z'\xi/(za^2)$ (lower panel), as a function of time. As for the other coefficient functions, they show an oscillatory behaviour with growing amplitude in the remote past.

In Section 3 of Lalak et al. (2007) which deals with curvature and isocurvature perturbations in two-fields inflationary models, they make a rotation of the adiabatic and isocurvature basis

that allows to rewrite Eq. (7.17) without the first order derivatives of the perturbations. It turns out, as we will soon see, that this rotation is the inverse rotation performed in Eq. (3.38) to go from the fields' space to the adiabatic and entropy basis $\{e_\sigma, e_s\}$. The system of equations for the adiabatic and entropy perturbations Eq. (7.17) will thus be transformed into a system of equations for the fields perturbations. Now, far in the contraction, away from the bounce, gravity no longer couples the two scalar fields together as $H^2 = \kappa Y^2/3 \to 0$, since the energy density is diluted and goes to zero infinitely far in the contraction. We thus expect a vanishing coupling between the two fields perturbations, contrary to the case when one considers adiabatic and isocurvature perturbations, where the coupling is related to the rotation of the adiabatic and isocurvature basis. Thus, one actually factorises out this rotation of the basis by going back to the fields'space, which then lowers the coupling between the perturbations. To see this, we first rewrite Eq. (7.17) in matrix form

$$v''(\eta) + C(\eta)v'(\eta) + D(\eta)v(\eta) = 0, \tag{7.34}$$

with

$$\begin{aligned} v(\eta) = \begin{pmatrix} v_\sigma(\eta) \\ v_s(\eta) \end{pmatrix}, \quad C(\eta) = \begin{pmatrix} 0 & -\xi(\eta) \\ \xi(\eta) & 0 \end{pmatrix}, \\ \text{and} \quad D(\eta) = \begin{pmatrix} k^2 - \frac{z''(\eta)}{z(\eta)} & -\frac{(z(\eta)\xi(\eta))'}{z(\eta)} \\ -\frac{z'(\eta)\xi(\eta)}{z(\eta)} & k^2 - \frac{a''(\eta)}{a(\eta)} + a^2(\eta)\mu_s^2(\eta) \end{pmatrix}. \end{aligned} \tag{7.35}$$

As $C(\eta)$ is an antisymmetric matrix, one can introduce a time-dependent orthogonal matrix which satisfies $R'(\eta) = -C(\eta)R(\eta)/2$. Let

$$R(\eta) = \begin{pmatrix} \cos\Theta(\eta) & -\sin\Theta(\eta) \\ \sin\Theta(\eta) & \cos\Theta(\eta) \end{pmatrix}, \tag{7.36}$$

then

$$R'(\eta) = \begin{pmatrix} -\Theta'(\eta)\sin\Theta(\eta) & -\Theta'(\eta)\cos\Theta(\eta) \\ \Theta'(\eta)\cos\Theta(\eta) & -\Theta'(\eta)\sin\Theta(\eta) \end{pmatrix}. \tag{7.37}$$

Furthermore, see Eq. (7.24),

$$\xi(\eta) = \xi(t) = a(t)\dot{\theta}(t) = 2a(\eta)\frac{\theta'(\eta)}{a(\eta)} = 2\theta'(\eta) \quad \text{i.e.} \quad \xi(\eta) = 2\theta'(\eta), \tag{7.38}$$

and

$$\begin{aligned} \tfrac{C(\eta)}{2}R(\eta) &= \begin{pmatrix} 0 & -\theta'(\eta) \\ \theta'(\eta) & 0 \end{pmatrix} \begin{pmatrix} \cos\Theta(\eta) & -\sin\Theta(\eta) \\ \sin\Theta(\eta) & \cos\Theta(\eta) \end{pmatrix} \\ &= \begin{pmatrix} -\theta'(\eta)\sin\Theta(\eta) & -\theta'(\eta)\cos\Theta(\eta) \\ \theta'(\eta)\cos\Theta(\eta) & -\theta'(\eta)\sin\Theta(\eta) \end{pmatrix}, \end{aligned} \tag{7.39}$$

and $R'(\eta) = -C(\eta)R(\eta)/2$ gives

$$\Theta'(\eta) = -\theta'(\eta), \tag{7.40}$$

so one can choose

$$\Theta(\eta) = -\theta(\eta), \tag{7.41}$$

and one does get $R'(\eta) = -C(\eta)R(\eta)/2$. Then, defining the vector $u(\eta)$ by

$$v(\eta) = R(\eta)u(\eta), \tag{7.42}$$

the choice for the angle Θ makes us identify $R(\Theta(\eta))$ with $M(\theta)$ in Eq. (3.38) so that one can interpret the components of the vector $u(\eta)$ as being the fields perturbations

$$u(\eta) = \begin{pmatrix} \delta\varphi(\eta) \\ \delta\phi(\eta) \end{pmatrix}. \tag{7.43}$$

Then, one has

$$\begin{cases} v'(\eta) = R'(\eta)u(\eta) + R(\eta)u'(\eta), \\ v''(\eta) = R''(\eta)u(\eta) + 2R'(\eta)u'(\eta) + R(\eta)u''(\eta), \end{cases} \tag{7.44}$$

and the matrix equation Eq. (7.34) becomes

$$\begin{aligned} & R''(\eta)u(\eta) + 2R'(\eta)u'(\eta) + R(\eta)u''(\eta) + C(\eta)(R'(\eta)u(\eta) + R(\eta)u'(\eta)) + D(\eta)R(\eta)u(\eta) = 0, \\ \Leftrightarrow\ & R(\eta)u''(\eta) + \left(R''(\eta) - \frac{C(\eta)^2}{2}R(\eta) + D(\eta)R(\eta)\right)u(\eta) = 0, \\ \Leftrightarrow\ & u''(\eta) + R^{-1}(\eta)\left(-\frac{C'(\eta)}{2} - \left(\frac{C(\eta)}{2}\right)^2 + D(\eta)\right)R(\eta)u(\eta) = 0, \end{aligned} \tag{7.45}$$

so that we have eliminated the first order time derivatives in the equations of motion. One is left to compute the matrix $R^{-1}(\eta)\left(-C'(\eta)/2 - (C(\eta)/2)^2 + D(\eta)\right)R(\eta)$ and see if it simplifies the coefficient functions. At first the coefficient functions seem more complicated

$$M(\eta) \equiv R^{-1}(\eta)\left(-\frac{C'(\eta)}{2} - \left(\frac{C(\eta)}{2}\right)^2 + D(\eta)\right)R(\eta) = \begin{pmatrix} m_{11}(\eta) & m_{12}(\eta) \\ m_{21}(\eta) & m_{22}(\eta) \end{pmatrix}, \tag{7.46}$$

with

$$\begin{cases} m_{11}(\eta) = k^2 + \left(\dfrac{\xi(\eta)}{2}\right)^2 - \cos^2\theta(\eta)\dfrac{z''(\eta)}{z(\eta)} + \sin^2\theta(\eta)\left(-\dfrac{a''(\eta)}{a(\eta)} + a^2(\eta)\mu_s^2(\eta)\right) \\ \qquad\qquad + \sin 2\theta(\eta)\left(\dfrac{z'(\eta)}{z(\eta)}\xi(\eta) + \dfrac{\xi'(\eta)}{2}\right), \\ m_{12}(\eta) = -\dfrac{\sin 2\theta(\eta)}{2}\left(\dfrac{z''(\eta)}{z} - \dfrac{a''(\eta)}{a(\eta)} + a^2(\eta)\mu_s^2(\eta)\right) - \cos 2\theta(\eta)\left(\dfrac{z'(\eta)}{z(\eta)}\xi(\eta) + \dfrac{\xi'(\eta)}{2}\right), \\ m_{21}(\eta) = m_{12}(\eta), \\ m_{22}(\eta) = k^2 + \left(\dfrac{\xi(\eta)}{2}\right)^2 - \sin^2\theta(\eta)\dfrac{z''(\eta)}{z(\eta)} + \cos^2\theta(\eta)\left(-\dfrac{a''(\eta)}{a(\eta)} + a^2(\eta)\mu_s^2(\eta)\right) \\ \qquad\qquad - \sin 2\theta(\eta)\left(\dfrac{z'(\eta)}{z(\eta)}\xi(\eta) + \dfrac{\xi'(\eta)}{2}\right), \end{cases} \tag{7.47}$$

but one notices that the matrix is symmetric. Again for numerical convenience, one can rewrite the rotated equations of motion for the perturbations Eq. (7.45) in cosmic time

$$\ddot{u}(t) + H(t)\dot{u}(t) + \frac{M(t)}{a(t)^2}u(t) = 0. \tag{7.48}$$

This makes first order derivatives appear again in the equation, but the Hubble factor just multiplies the components of the vector u so that this term does not couple the two components.

Then, one can approximate the diagonal coefficients far in the contraction, i.e. when $\eta \to -\infty$. This gives

$$\begin{aligned} m_{11}(\eta) - k^2 &\underset{\eta\to-\infty}{\approx} \frac{\eta^4 a_0^6 m^2}{81 t_0^4}, \\ m_{22}(\eta) - k^2 &\underset{\eta\to-\infty}{\approx} -\frac{2}{\eta^2}, \end{aligned} \tag{7.49}$$

where we substracted the k^2 term as these are the functions $m_{11}(\eta) - k^2$ and $m_22(\eta) - k^2$ which have to be compared to the wavenumbers k to determine if the mode oscillates or is frozen. One can compare these functions to their homologues in the equations for the adiabatic and isocurvature perturbations Eq. (3.57), that is the functions $-z''/z$ and $-a''/a + a^2\mu_s^2$. This is done in Fig. 7.13 where on the left is plotted $(k^2 - m_{11}(\eta))/a^2$ and $z''/(za^2)$ with the constant $-m^2$ and on the right the functions $(k^2 - m_{11}(\eta))/a^2$ and $(a''/a - a^2\mu_s^2)/a^2$. The general behaviour of $-z''/z$ and $m_{11}(\eta) - k^2$ are the same: they almost always scale like η^4 but the function $-z''/z$ behaves like η^{10} in some tiny periods of time, while $m_{11}(\eta) - k^2$ oscillates around the general behaviour in η^4. Similarly, the functions $-a''/a + a^2\mu_s^2$ and $m_{22}(\eta) - k^2$ both almost always scale like $1/\eta^2$, but the function $-a''/a + a^2\mu_s^2$ behaves like η^{10} in some tiny periods of time, while $m_{22}(\eta) - k^2$ oscillates around the general behaviour in $1/\eta^2$. To see this more closely, we have plotted in Fig. 7.14, the function $(k^2 - m_{11}(\eta))/a^2$ and its general behaviour in $2/(\eta^2 a^2)$ as a function of time, during the contracting phase.

Finally, we would be lucky if the off-diagonal coefficient vanishes in the contraction. In fact, one can show that

$$m_{12}(\eta) = m_{21}(\eta) \propto \frac{1}{\eta^2}, \text{ except in some tiny periods of time where } m_{12}(\eta) = m_{21}(\eta) \propto \pm\eta^4, \tag{7.50}$$

so that one faces the same kind of issue already encountered in the decoupling case with the coefficient functions z''/z and $a^2\mu_s^2$. However, 'on average', the off-diagonal terms decrease to zero as $1/\eta^2$ far in the contracting phase, which is better than the coupling terms $(z\xi)'/z$ and $z'\xi/z$ that scale like η appearing in the equations of motion in the adiabatic and isocurvature basis Eq. (3.57). This is shown in Fig. 7.15 where the function $m_{12}(\eta)/a^2$ is plotted, with its general behaviour in $1/(\eta^2 a^2)$ and the envelopes in $\eta^4/a^2 =$cst including how it behaves in some tiny periods of time. Thus, one can assume that in this basis, the equations of motion are decoupled, so that it might be easier to set the initial conditions for the perturbations. This makes sense as we already argued that the two fields are independent far away in the contracting phase.

Therefore, one might consider setting the initial conditions for the fields perturbations as we did in the uncoupled case for the adiabatic and isocurvature perturbations, so that

$$\begin{cases} \delta\varphi(\eta) = \sqrt{\dfrac{-\pi\eta}{12}} H^{(2)}_{1/6}\left(\dfrac{a_0^3 m \eta^3}{27 t_0^2}\right), \\ \delta\phi(\eta) = \dfrac{e^{-ik\eta}}{\sqrt{2k}}. \end{cases} \tag{7.51}$$

One notices that in the uncoupled case, the adiabatic perturbation correspond to the perturbation in the massive field $\delta\varphi$ while the isocurvature perturbation correspond to the perturbations in the massless field $\delta\phi$. One then solve numerically for these fields perturbations. Actually, as the coefficient functions for the equations of motion for the fields perturbations are less stiff than for the adiabatic and isocurvature perturbations, it might be easier to solve for them numerically. Then, one can get the adiabatic and isocurvature perturbations by going back to the original

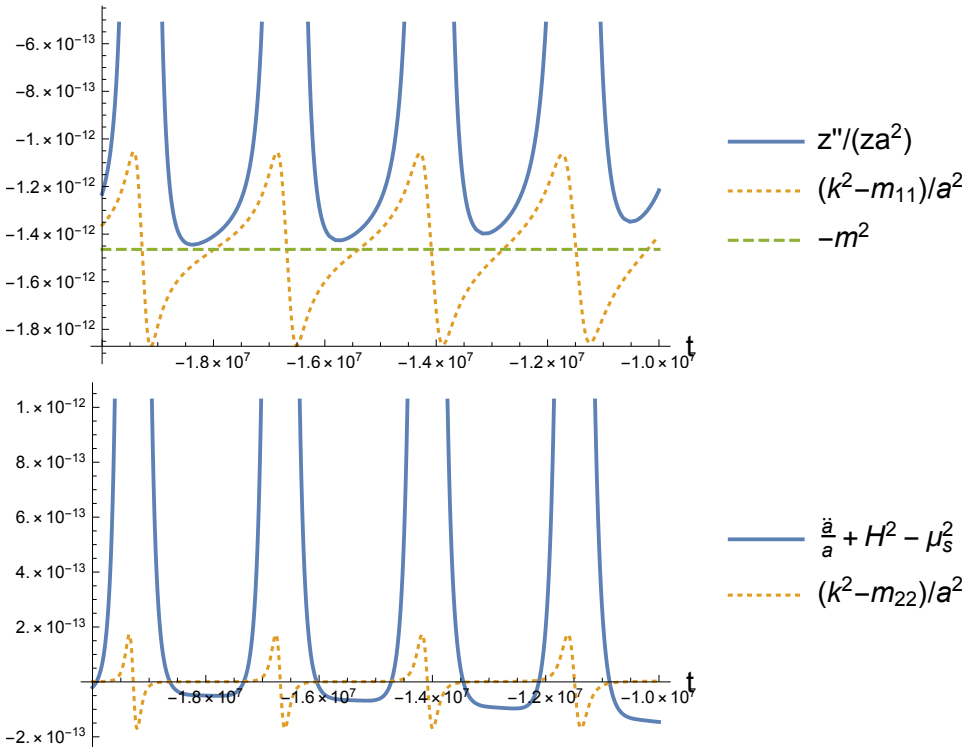

Figure 7.13: The comparison between the functions $z''/(za^2)$ and $(k^2 - m_{11}(\eta))/a^2$ (upper panel) and $(a''/a - \mu_s^2)/a^2$ and $(k^2 - m_{22}(\eta))/a^2$ (lower panel), as a function of time. The functions in the rotated system of equations Eq. (7.45) are less stiff than in the original system Eq. (3.57). They also show an oscillatory behaviour, but instead of being *on top* of a general behaviour, it is *around* it. Thus, the functions $m_{11}(\eta) - k^2$ and $m_{22}(\eta) - k^2$ are on average given by the formula Eq. (7.49).

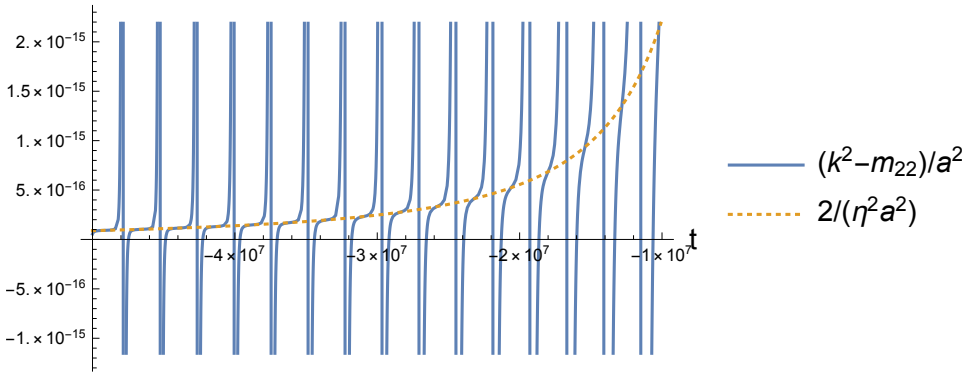

Figure 7.14: The function $(k^2 - m_{11}(\eta))/a^2$ and its general behaviour in $2/(\eta^2 a^2)$ as a function of time, during the contracting phase.

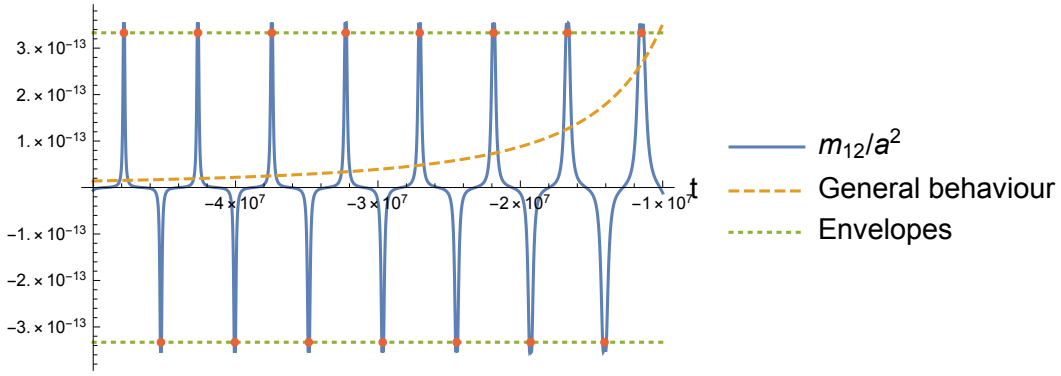

Figure 7.15: The function $m_{12}(\eta)/a^2$ and its general behaviour in $2/(\eta^2 a^2)$ as a function of time with its envelopes being constants, during the contracting phase.

basis thanks to the rotation Eq. (7.42). Thus, one could also turn the initial conditions to get the initial conditions for v_σ and v_s and then solve numerically for them. Finally, the results of the two numerical resolutions could be compared.

Setting the initial conditions elsewhere

In Agullo et al. (2013b), they set the initial conditions for the perturbations of their field at the bounce, in line with Ashtekar & Sloan (2011) where initial conditions for the background are also taken at the bounce. This could also be considered here: the above analysis would need to be redone by taking the analytical approximations for the background variables at the bounce, as derived in Section 7.2.2, in order to find analytical approximations for the perturbations at the bounce that would then allow us to set the initial conditions. However it is argued in Agullo et al. (2013b) that the Bunch-Davies vacuum cannot be taken at the bounce for the perturabtions, as the space-time geometry is far for being the de Sitter one (which is usually the approximation taken for space-time during slow-roll inflation, as H is almost constant). Instead, they ask the initial state for being regular and maximally symmetric with respect to the dressed metric approach they use for the equations of motion for the perturbations, that is invariant under spatial translations and rotations, which leads to a 4^{th} order adiabatic vacuum.

In early studies of Grain & Barrau (2009); Grain et al. (2009), they put initial conditions at the beginning of inflation so they can make use of the slow-roll approximation to derive analytical approximations for the perturbations. One can wonder the relevance of doing this as during inflation, gravitation can be treated classically, and so think this would give the same results as the usual treatment made for inflation within GR. In fact, there is some residual quantum gravity effects at the beginning of inflation so LQC can leave its imprints on the power spectra of perturbations, which are indeed changed with respect to the usual treatment. These considerations could be investigated in future works, although here we have chosen to set the initial conditions in the past, with a view to having a causal evolution from the past to the future.

Perspectives on the power spectra of the perturbations

Finally, power spectra of the perturbations would need to be computed at the end of inflation. Analytical approximations in the IR and UV limits could also be derived, by considering the

evolution of the perturbations during the different phases: contraction, bounce and inflation. These limiting cases will allow us to check our numerical predictions. The comparison of these scalar power spectra with those derived in the case of one field for the scalar and tensor perturbations could give us hints about their impact on the CMB, as this has already been looked at, for example in Grain et al. (2010). The interested reader can find for example in Bojowald et al. (2011) observational constraints on LQC with a single scalar field. Eventually, one would want to propagate our scalar spectra to the CMB to get the angular power spectra of primary anisotropies in temperature and polarisation in order to compare them to the ones predicted by the standard scenario and finally to observations. This would allow us to test or put constraints on our model of the very early Universe and maybe indicate directions to enrich it. The observational constraints on isocurvature modes is promising to do so since our model has the peculiarity to generate such modes. For this to be done thoroughly one may need to run the data analysis with this specific model.

Part III

Secondary polarised anisotropies of the CMB

Chapter 8

Faraday Rotation and Faraday Conversion of the CMB photons in large-scale structures

Other sources of CMB secondary polarised anisotropies are due to magnetised plasmas, in addition to the gravitational lensing (due to the gravitational potential of the virialised structures), which also distort the polarisation image of the CMB. Virialised structures contain a magnetised plasma, which leaves a footprint on the CMB through at least two effects: Faraday Rotation (FR) and Faraday Conversion (FC). To quantify the secondary anisotropies, we need to study the statistical effects of FR and FC. After explaining their mechanisms, and modeling the cosmological structures (Dark Matter halos and their statistical distribution), we will present the computation of their angular power spectra which depend both on cosmological and astrophysical parameters, and then their statistical impact on the CMB polarised anisotropies which inherit of the correlations from the large-scale structures. Finally, estimators are built in order the reconstruct the FR and FC effects in halos over the whole sky.

8.1 The Faraday Rotation and Conversion mechanisms

As light travels through a magnetised medium, its polarisation state is modified through magneto-optical effects. Here we will focus on two of such effects: Faraday rotation and Faraday conversion.

8.1.1 Faraday Rotation

Faraday rotation, also know as Faraday effect, is named after Michael Faraday who discovered it in 1845. It is a magneto-optic or gyromagnetic effect, that is the interaction of an electromagnetic wave with a quasi-static magnetic field in a medium, that rotates the polarization of an incident linearly polarized wave. In such a medium, left and right circularly polarized electromagnetic waves, which are the eigenpolarizations of the medium (see Azzam & Bashara, 1978), have different speeds, so that the phenomenon is similar to optical rotation. Indeed, consider the ideal and simplest case of a transverse monochromatic electromagnetic plane wave of frequency ω propagating in the direction $\hat{\mathbf{e}}_3$ of an orthonormal basis $\{\hat{\mathbf{e}}_1, \hat{\mathbf{e}}_2, \hat{\mathbf{e}}_3\}$ which is linearly polarized

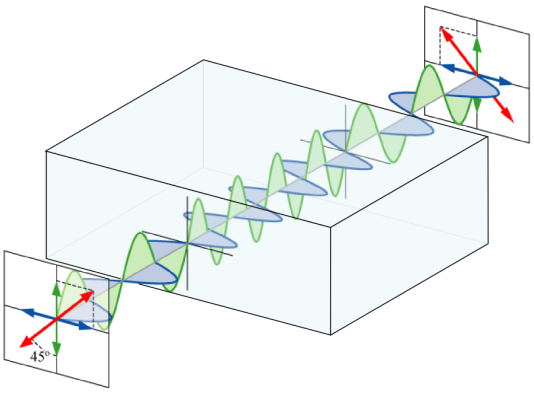

Figure 8.1: Illustration of a linearly polarised light travelling through a half-wave plate. Red arrows indicate the total electric field, while the blue and green arrows correspond to orthogonal projections. These two components have different propagation speeds in the medium, which delays one with respect to the other, such that the polarisation direction of the outgoing light is rotated by 90 degrees compared to the ingoing direction. Image by Bob Mellish.

in the $\{\hat{\mathbf{e}}_1, \hat{\mathbf{e}}_2\}$ plane, i.e.

$$\mathbf{E}(\mathbf{r}, t) = E_1 \cos\left(\frac{\omega}{c} z - \omega t\right) \begin{vmatrix} 1 \\ 1 \end{vmatrix}, \tag{8.1}$$

as any electromagnetic wave can be decomposed onto the basis formed by these kinds of waves. It is indeed a linearly polarized wave, as the electric field vector oscillates with frequency ω along a constant direction given by the unit vector $(1,1)/\sqrt{2}$ in the plane $(\hat{\mathbf{e}}_1, \hat{\mathbf{e}}_2)$. Such a linearly polarized wave can be decomposed into the sum of a right and a left circularly polarized waves

$$\begin{aligned} \mathbf{E}(\mathbf{r}, t) =& \frac{E_1}{2} \begin{vmatrix} 2\cos\left(\frac{\omega}{c} z - \omega t\right) + \sin\left(\frac{\omega}{c} z - \omega t\right) - \sin\left(\frac{\omega}{c} z - \omega t\right) \\ 2\cos\left(\frac{\omega}{c} z - \omega t\right) - \sin\left(\frac{\omega}{c} z - \omega t\right) + \sin\left(\frac{\omega}{c} z - \omega t\right) \end{vmatrix} \\ =& \frac{E_1}{2} \left(\begin{vmatrix} \sqrt{2}\cos\left(\frac{\omega}{c} z - \omega t - \frac{\pi}{4}\right) \\ -\sqrt{2}\sin\left(\frac{\omega}{c} z - \omega t - \frac{\pi}{4}\right) \end{vmatrix} + \begin{vmatrix} \sqrt{2}\cos\left(\frac{\omega}{c} z - \omega t + \frac{\pi}{4}\right) \\ \sqrt{2}\sin\left(\frac{\omega}{c} z - \omega t + \frac{\pi}{4}\right) \end{vmatrix} \right). \end{aligned} \tag{8.2}$$

The first vector corresponds to a right circularly polarized wave and the second one to a left circularly polarized wave. When a linearly polarized wave goes through a gyromagnetic medium as described above, the effect is similar to a wave going through a chiral material, see Fig. 8.1. It is similar in the sense that, as in a chiral material, the polarization direction of a linearly polarized wave is rotated when going through the medium, all the more importantly as the concentration of the chiral molecule in the medium and the path length of the wave are high. As the linearly polarized wave is a superposition of two right and left circularly polarized waves, the phenomenon acts effectively as the medium having a different refractive index n for the two handedness. The difference with optical rotation is that here the rotation angle depends on the sign of the projection of the magnetic field along the direction of propagation so that there is an

assymetry. After going through the gyromagnetic medium, the electric field becomes

$$\widetilde{\mathbf{E}}(\mathbf{r}+L\,\hat{\mathbf{e}}_3,t)=\frac{E_1}{2}\left(\begin{vmatrix}\sqrt{2}\,\cos\left(\frac{\omega}{c}(z+n_rL)-\omega t-\frac{\pi}{4}\right)\\-\sqrt{2}\,\sin\left(\frac{\omega}{c}(z+n_rL)-\omega t-\frac{\pi}{4}\right)\end{vmatrix}+\begin{vmatrix}\sqrt{2}\,\cos\left(\frac{\omega}{c}(z+n_lL)-\omega t+\frac{\pi}{4}\right)\\\sqrt{2}\,\sin\left(\frac{\omega}{c}(z+n_lL)-\omega t+\frac{\pi}{4}\right)\end{vmatrix}\right), \tag{8.3}$$

where L is the length of the medium which is gone through, n_r and n_l are the refractive indices for the right and left circularly polarized waves respectively so that the speed for the right circularly polarized wave in the medium is c/n_r and for the left circularly polarized wave it is c/n_l. Then, it can be rewritten as

$$\begin{aligned}\widetilde{\mathbf{E}}(\mathbf{r}+L\,\hat{\mathbf{e}}_3,t)=&\frac{E_1}{2}\left(\begin{vmatrix}\cos\left(\frac{\omega}{c}(z+n_rL)-\omega t\right)+\sin\left(\frac{\omega}{c}(z+n_rL)-\omega t\right)\\-\sin\left(\frac{\omega}{c}(z+n_rL)-\omega t\right)+\cos\left(\frac{\omega}{c}(z+n_rL)-\omega t\right)\end{vmatrix}\right.\\&\left.+\begin{vmatrix}\cos\left(\frac{\omega}{c}(z+n_lL)-\omega t\right)-\sin\left(\frac{\omega}{c}(z+n_lL)-\omega t\right)\\\sin\left(\frac{\omega}{c}(z+n_lL)-\omega t\right)+\cos\left(\frac{\omega}{c}(z+n_lL)-\omega t\right)\end{vmatrix}\right),\end{aligned} \tag{8.4}$$

and using the sum-to-product identity $\cos(\theta_1)+\cos(\theta_2)=2\cos[(\theta_1+\theta_2)/2]\cos[(\theta_1-\theta_2)/2]$, and its similar expression for sine, we get

$$\widetilde{\mathbf{E}}(\mathbf{r}+L\,\hat{\mathbf{e}}_3,t)=E_1\cos\left(\frac{\omega}{c}z-\omega t+\varphi\right)\left[\cos(\alpha)\begin{vmatrix}1\\1\end{vmatrix}+\sin(\alpha)\begin{vmatrix}-1\\1\end{vmatrix}\right], \tag{8.5}$$

with the phase

$$\varphi=\frac{\omega}{c}\left(\frac{n_l+n_r}{2}\right)L, \tag{8.6}$$

and angle

$$\alpha=\frac{\omega}{c}\left(\frac{n_l-n_r}{2}\right)L. \tag{8.7}$$

The term in brackets can be written as a matrix of rotation, such that finally

$$\widetilde{\mathbf{E}}(\mathbf{r}+L\,\hat{\mathbf{e}}_3,t)=E_1\cos\left(\frac{\omega}{c}z-\omega t+\varphi\right)\begin{pmatrix}\cos(\alpha)&-\sin(\alpha)\\\sin(\alpha)&\cos(\alpha)\end{pmatrix}\begin{vmatrix}1\\1\end{vmatrix}. \tag{8.8}$$

Comparing this expression to its initial state Eq. (8.1), we can see that the electric field is phase-shifted and linearly polarized, but in a direction rotated by an angle α.

As an example, let us consider Faraday rotation in a cold stationary rarefied homogeneous magnetized plasma with incident light frequency ω satisfying $\omega \gg \omega_p$ and $\omega \gg \omega_B$, where $\omega_p=\sqrt{n_e e^2/(m\varepsilon_0)}$ is the plasma frequency and $\omega_B=eB/m$ is the cyclotron frequency. This is relevant for modeling light propagation in the interstellar medium and the intracluster medium. Under such conditions, starting from the expression Eq. (8.7) in differential form (i.e. modeling the path of light as a succession of infinitesimal lengths), Melrose & McPhedran (1991) show that the polarization direction of light traveling from a given source to an observer is rotated by an angle

$$\alpha=\mathrm{RM}\,\lambda^2, \tag{8.9}$$

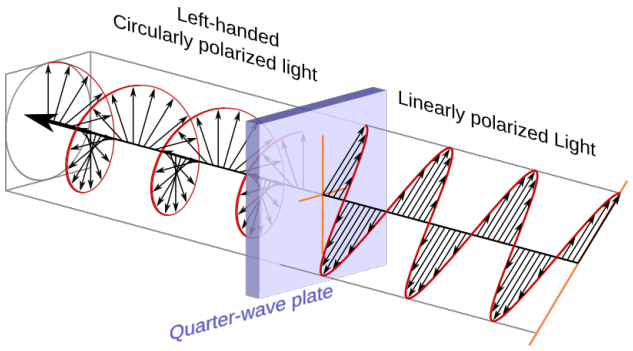

Figure 8.2: Quarter-wave plates transform incoming linearly polarised light (on the right of the figure) into circularly polarised light (on the left). Image from Wikimedia Commons.

with λ the wavelength of the incident light and RM the so-called Rotation Measure. This rotation measure depends on the magnetic field projected along the direction of propagation $B_\parallel$, the cold electron density n_e and the distance d over which the light has travelled in the plasma

$$\mathrm{RM} = \frac{e^3}{8\pi^2\varepsilon_0 m^2 c^3}\int_0^d \mathrm{d}r\ n_e(r)B_\parallel(r), \tag{8.10}$$

where e is the charge of the electron, c is the speed of light, m is the mass of an electron and ε_0 is the vacuum permittivity, the formula being given in SI units.

The physical interpretation of this phenomenon is that the two circularly polarized electromagnetic waves will imprint a force on the charged particles (more importantly on the electrons because of their low mass), resulting in them having circular motion. They will thus create their own magnetic field, adding to the already existing magnetic field. The circular motion of the particles being clockwise or counter-clockwise depending on which of the two circularly polarized waves imprinted the motion, the created magnetic field will then be either in the same direction as the external magnetic field, or in the opposite direction so that the resulting magnetic field is bigger or smaller, respectively. Then, this changes the interaction for each of the two circularly polarized waves, so that one of the two will be slowed down more than the other, hence the phase difference between the two polarizations. The superposition of two circularly polarized waves with an additional phase shift will thus be a linearly polarized wave whose polarization direction is rotated by an angle α (see p. 229 of Rybicki & Lightman, 1979).

8.1.2 Faraday Conversion

Faraday conversion or generalized Faraday rotation (also called circular repolarization (Pacholczyk, 1973) or Faraday pulsation (Pacholczyk & Swihart, 1970)), is the conversion of linear polarization to circular polarization (Sazonov, 1969a; Jones & Odell, 1977; Melrose, 1997b). It is similar to the Cotton-Mouton effect happening in liquids or the action of a quarter-wave plate on linear polarization, see Fig. 8.2. Indeed, one can make a similar demonstration as what we did for Faraday Rotation by decomposing the incoming linearly polarised wave into two linearly polarised waves along the normal axes of the relativistic medium to show that the effect introduces a phase shift between these two components making the outgoing wave having a circular component. In a highly relativistic rarefied stationary homogeneous and weakly anisotropic magnetized plasma, the natural wave modes are linearly polarized (Sazonov, 1969b; Melrose, 1997a).

The conversion of linear to circular polarization is characterized by a conversion rate

$$\phi = \mathrm{RRM}\ \lambda^3, \tag{8.11}$$

where RRM is called the relativistic rotation measure. In SI units

$$\mathrm{RRM} = \frac{e^4}{4\pi^3\varepsilon_0 m^3 c^4}\frac{\beta_E - 1}{\beta_E - 2}\Gamma_{min}\int_0^d \mathrm{d}r\ n_{rel}B_\perp^2, \tag{8.12}$$

with Γ_{min} the minimum Lorentz factor of a power-law distribution of relativistic particles and β_E the power law index. Indeed, the above formula is only valid for a power-law isotropic distribution of relativistic particles

$$N(\Gamma) = \frac{n_{rel}(\beta_E - 1)\Gamma^{-\beta_E}}{\Gamma_{min}^{1-\beta_E} - \Gamma_{max}^{1-\beta_E}}, \tag{8.13}$$

for $\Gamma_{min} \leq \Gamma \leq \Gamma_{max}$ and Eq. (8.12) is derived assuming $\Gamma_{max} \gg \Gamma_{min}$ and for frequencies much larger than the plasma and synchrotron frequencies: $\omega \gg \omega_p \gg \omega_B$ (see e.g. Sazonov, 1969a; Heyvaerts et al., 2013) and is a good approximation for $\Gamma_{min} \leq 100$ (Huang & Shcherbakov, 2011). Precise computations of the Faraday rotation angle and Faraday conversion rate for any particle distribution have been derived in Shcherbakov (2008); Huang & Shcherbakov (2011) and for different frequency regimes (Heyvaerts et al., 2013) but Eq. (8.12) is of most interest for us for the astrophysical plasmas under consideration and for cosmic microwave background frequencies of the order of 100 gigaHertz.

Faraday conversion has first been useful to interpret the circular polarization in compact radio sources (Pacholczyk, 1973) which was not consistent with the frequency dependence of intrinsic circular polarization from synchrotron emitting sources going as $\omega^{-1/2}$. It has later been used in order to probe the magnetic field of the Active Galactic Nuclei (AGN) near the central black hole of our galaxy, Sagittarius A*, through its radio emission, leading to a GR polarized radiative transfer treatment in Huang et al. (2009); Shcherbakov & Huang (2011). Here we will see to what extent it has some effect on the CMB polarized light through galaxy clusters.

8.2 Dark Matter halos

Dark Matter halos are large (up to several Mpc) Dark Matter overdensities that host baryonic matter (constituting roughly 10% of the mass fraction) in the form of galaxies and gas. Hot gas has been probed in these structures by the SZ effect (see Section 4.3.2), and magnetic fields in the intracluster medium of clusters of galaxies are observed through the methods reviewed in for example Govoni (2006). Let us now detail how we model each of these components and most importantly the electron density and magnetic field distribution.

8.2.1 Large-scale structure of dark matter

We have seen in Chapter 3 that there were some tiny quantum fluctuations in the very Early Universe that could therefore be treated as cosmological perturbations around the homogeneous and isotropic FLRW background. In Chapter 4, we have seen these perturbations translated in the anisotropies in temperature and polarization of the CMB at the epoch of recombination. The secondary CMB anisotropies due to large scale structures are another illustration of these primordial perturbations: indeed, how these structures could have been formed if it were not from original seeds at the beginning of the Universe? Roughly speaking, structures form through the

following steps. First an overdense region decouples from the global expansion (a concept called 'turn-around', see e.g. Peebles, 1980) and starts collapsing onto itself. The gravitational collapse overcomes the counteracting effect of pressure, according to Jeans' criterion, and the structure finally reaches a stable state. This process is called virialization and the end state is called the virialized state. Finally, matter at cosmological scales ends up distributed in a filamentary way, called the 'Cosmic Web'. However here we focus on the most virialised structures and choose to describe the distribution of matter at cosmological scales thanks to the halo model, replacing this cosmic web by spherical structures, namely DM halos, the largest of them constituting the nodes of this Web. DM halos are thus the result of the non-linear stages of the evolution of the large scale structure of the Universe, and for simplicity, in the following we model them as spherically symmetric. We will consider halo masses ranging from 10^{10} to $10^{16} M_\odot$. High-mass halos (typically greater than $10^{13} M_\odot$) host so-called 'clusters of galaxies', namely groups of between a hundred to a few thousands of galaxies, while low-mass halos (typically smaller than $10^{13} M_\odot$) host less a hundred of them.

To be a little more quantitative, let us consider the following simple model. A DM halo is assumed to be formed from the spherical collapse of a density perturbation, as a first approximation. The spherical collapse of an initial top-hat density perturbation model (Gunn & Gott, 1972) predicts the mean density of virialized halos to be (Bryan & Norman, 1998)

$$\Delta_{\rm vir} = 18\pi^2 + 82(\Omega_m(z) - 1) - 39(\Omega_m(z) - 1)^2, \tag{8.14}$$

times the critical density at virialization time. This expression is valid in an $\Omega_m + \Omega_\Lambda = 1$ (flat) universe and accurate to 1% for $\Omega_m(z)$ within the range $[0, 1; 1]$. In an Einstein-de Sitter Universe, the expression Eq. (8.14) reduces to the exact $18\pi^2 \approx 178$ value.

Analytical expressions for halo density profiles have been fitted to numerical simulations, and it was found that Navarro et al. (1996)(NFW), Moore et al. (1999)(M99)

$$\rho(r|m) = \frac{\rho_s}{(r/r_s)(1 + r/r_s)^2} \quad \text{(NFW)} \quad \text{or} \quad \rho(r|m) = \frac{\rho_s}{(r/r_s)^{3/2}(1 + (r/r_s)^{3/2})} \quad \text{(M99)}, \tag{8.15}$$

are very good universal descriptions of the density profile around the centre of virialized halos. The parameter r_s is a scale radius fitted to the simulation and ρ_s is the density at that radius determined by the mass m and virial radius $r_{\rm vir}$ of the halos which is predicted by the spherical collapse model Eq. (8.14). For the two above mentioned profiles, one has respectively

$$m = 4\pi\rho_s r_s^3 \left[\ln(1 + c) - \frac{c}{1 + c}\right] \quad \text{and} \quad m = 4\pi\rho_s r_s^3 \frac{2\ln(1 + c^{3/2})}{3}, \tag{8.16}$$

where $c \equiv r_{\rm vir}/r_s$ is the concentration parameter. Therefore, the halo density profile depends only on the mass of the halo and the r_s fitted parameter, although simulations show that even though the distribution at fixed mass of the concentration c depends on mass, its width does not depend on the mass (Sheth & Tormen, 2002; Cooray & Sheth, 2002). Thus, at the end of the day, the halo density profile only depends on the mass. To finish, note that it is still not understood theoretically why the NFW and M99 profiles fit the DM simulations so well (e.g. Huss et al., 1999).

8.2.2 Baryonic and magnetic content

The aim of this part of the manuscript is to study how, and quantify how much, the plasma contained in galaxy halos acts as a source of secondary polarized anisotropies of the CMB, revisiting and amending the first estimates of Cooray et al. (2003) and Tashiro et al. (2008). To

do so, we need to model precisely two characteristics of halos: their free electron density and their magnetic field spatial profiles. Inside large enough DM halos, the baryonic matter collapses and galaxies begin to form.

8.2.2.1 Distribution of free electrons

Two populations of electrons may be distinguished in astrophysical clusters and halos: thermal electrons, which are in particular responsible for the thermal Sunyaev-Zel'dovich (tSZ) effect, and relativistic electrons, generated by AGNs, shocks or cosmic rays. It is crucial to make this distinction because the expressions of the different coefficients in the Faraday effects introduced in section 9.1, as well as their relative amplitude, depend on the nature of free electrons in the magnetized plasma. As already explained in Section 8.1, the two extreme situations are either normal waves of the plasma are circularly polarized, or these normal waves are linearly polarized. In the former case, Faraday rotation is dominant over Faraday conversion, which is the case for a plasma made of non-relativistic electrons (or cold plasma in Sazonov, 1969a). In the latter case, it is Faraday conversion which is dominant. This can occur for a population of relativistic and non-thermal electrons, with some restrictions on their energy distributions (see Sazonov, 1969a).

For the case of thermal electrons, the typical temperature of clusters is $\sim 10^7$K, corresponding to about few keV's, hence much smaller than the electron mass. This population of electrons is thus mainly non-relativistic. A typical value of the number density of thermal electrons for clusters is $n_e \sim 10^3 \mathrm{m}^{-3}$ for a halo mass of $M = 10^{14} M_\odot$ and size $r_{\rm vir} = 1$ Mpc. Historically, the spatial profile for the free electrons was taken to be the β-profile of Cavaliere & Fusco-Femiano (1978) as it matched the X-ray observations, while now the tSZ community relies on a generalisation of the NFW profile defined in Eq. (8.15), the GNFW profile, as it is expected that the baryons follow the DM potentials. Here, as a first estimate, we chose the β-profile as in Tashiro et al. (2008)

$$n_e(r) = n_e^{(c)} \left(1 + \frac{r^2}{r_c^2}\right)^{-3\beta/2}, \tag{8.17}$$

where r and r_c are respectively the physical distance (or comoving as it depends only on the ratio of these two distances) to the halo centre and the typical core radius of the halo. One notes that the physical halo core radius of the order of a tenth of the virial radius

$$r_c \sim \frac{r_{vir}}{10}, \tag{8.18}$$

where the virial radius is

$$r_{vir} = \left(\frac{M}{(4\pi/3)\Delta_c(z)\bar{\rho}(z)}\right)^{1/3}, \tag{8.19}$$

with the spherical overdensity of the virialized halo

$$\Delta_c(z) \approx 18\pi^2 \Omega_m(z)^{0.427}, \tag{8.20}$$

and $\bar{\rho}(z)$ the critical density at redshift z (see Tashiro et al., 2008). The quantity $n_e^{(c)}$ is the central free electron density. For thermal free electrons, it is given by:

$$n_e^{(c)} = 9.26 \times 10^{-4} \mathrm{cm}^{-3} \left(\frac{M}{10^{14} M_\odot}\right) \left(\frac{r_{vir}}{1\mathrm{Mpc}}\right) \left(\frac{\Omega_b}{\Omega_m}\right) \times {}_2F_1^{-1}(3/2, 3\beta/2; 5/2; -(r_{vir}/r_c)^2), \tag{8.21}$$

with ${}_2F_1$ the hypergeometric function.

For relativistic electrons however, the properties inside halos are not well known (see Sec. 5 of Cavaliere & Lapi, 2013, for a brief overview). We consider relativistic electrons to be described by a power-law in the momentum space (following e.g. Colafrancesco et al., 2003, and references therein) with Lorentz factor ranging from $\Gamma_{\rm min} \gg 1$ to $\Gamma_{\rm max}$ and an isotropic spatial distribution of the energy distribution. Assuming for simplicity that $\Gamma_{\rm max} \gg \Gamma_{\rm min}$, the relativistic electron distribution function simplifies to (Colafrancesco et al., 2003)

$$n_e^{(rel)}(r,\Gamma) = n_e^{(r)}(r,\Gamma_{\rm min})(\beta_E - 1)\Gamma_{\rm min}^{\beta_E - 1}\Gamma^{-\beta_E}, \tag{8.22}$$

with $\beta_E > 1$ the spectral index, and $n_e^{(r)}(r,\Gamma_{\rm min})$ the number density of relativistic electrons integrated over the range of Lorentz boost. Typical values for the spectral index is 2.5. We chose the normalisation assumed by Colafrancesco et al. (2003), that is

$$n_e^{(r)}(r,\Gamma_{\rm min} = 100) = 10^{-6}{\rm cm}^{-3}, \tag{8.23}$$

even though the number density of relativistic electrons is largely unknown and we consider here the maximum value we found in the literature. Our results will be easily rescaled for different values of $n_e^{(r)}(r,\Gamma_{\rm min})$. Let us mention that the number density $n_e^{(r)}(r,\Gamma_{\rm min})$ is in full generality taken as a function of $\Gamma_{\rm min}$ so that other choices of normalisation can be made. In fact the total number density of electrons increases for lower values of $\Gamma_{\rm min}$.

8.2.2.2 Modeling the magnetic field

Let us denote by $\boldsymbol{x}$ a given position within the halo, and by $\boldsymbol{x}_i$ the position of the halo centre. The magnetic field $\boldsymbol{B}$ is in full generality a function of both $\boldsymbol{x}$ and $\boldsymbol{x}_i$, as well as a function of the mass and the redshift of the considered halo. In particular, small scale structures of the magnetic field in galaxy clusters have been observed via rotation measures. This can be taken into account as in Murgia et al. (2004); Govoni et al. (2006); Bonafede et al. (2010) by modeling the magnetic field in Fourier space as the convolution of the Fourier transform of a simple radial profile times the Fourier coefficients of a vector potential $\boldsymbol{A}(k)$, described by a statistically isotropic, power-law power spectrum at scales smaller than the cluster scales, i.e. smaller than the virial radius. This models a magnetic field which is coherent on scales smaller than the halo size. For example, in Murgia et al. (2004), the power spectrum is non zero on scales ranging from a hundredth of the core radius, r_c, to almost two times the core radius. This would mean a coherence length of about half the virial radius. This modeling of the magnetic field as a convolution in Fourier space of two components shows that it can be decomposed into two superposed magnetic fields: an average magnetic field over the cluster scale with constant direction and a given radial profile plus small scale fluctuations, i.e. a stochastic component in the magnetic field with coherence length smaller than the virial radius.

However, because we have only a poor knowledge of the magnetic field inside halos, we allow ourselves to choose a model for $\boldsymbol{B}$ that will simplify a bit the calculations of the angular power spectra. Therefore, we assume a magnetic field which is coherent over the halo scale, by taking only the above large-scale average component and we will later see how the model can be made more complex. Thus, in our modeling, the orientation of the magnetic field is roughly constant over the halo scale, but we still allow for potentially radial profile for its amplitude, i.e.

$$\boldsymbol{B}(\boldsymbol{x},\boldsymbol{x}_i) = \boldsymbol{B}(|\boldsymbol{x} - \boldsymbol{x}_i|)\hat{\boldsymbol{b}}(\boldsymbol{x}_i). \tag{8.24}$$

The vector $\hat{\boldsymbol{b}}(\boldsymbol{x}_i)$ is a unit vector labelling the orientation of the magnetic field of a given halo. Therefore it depends on the halo position only and is considered as a random variable. Here,

we also assumed a spherically symmetric profile for the amplitude of the magnetic field. Based on observations (e.g. Hummel et al., 1991; Murgia et al., 2004; Bonafede et al., 2009, 2010), we consider that the radial dependency of the norm of the magnetic field is related to the gas density by a power-law

$$B \propto (n_{gas})^{\mu}, \tag{8.25}$$

and thus choose a β-profile

$$B(r) = B_c(z) \left(1 + \frac{r^2}{r_c^2}\right)^{-3\beta\mu/2}, \tag{8.26}$$

where B_c is the mean central value. As for the time evolution, denoting by B_0 the field strength at t_0 (today), we take as in Widrow (2002)

$$B_c(z) = B_0 \exp\left(-\frac{t_0 - t(z)}{t_d}\right), \tag{8.27}$$

which introduces the timescale

$$t_d = \sqrt{\frac{r_{vir}^3}{GM}}. \tag{8.28}$$

Note that increasing the value of the μ parameter makes the profile fall down more rapidly. Now, the stochastic component of the magnetic field having a coherence length smaller than the virial radius, it induces a large-scale suppression with respect to the case where the magnetic field is coherent over the halo scale. Thus, a smaller coherence length can be taken into account at an effective level by increasing the value of the μ parameter.

In principle the magnetic field strength at the centre B_c depends on the mass of the halo. Inside galaxies (halos with $M < 10^{13} M_\odot$) it may reach $\sim 10\mu$G, while in clusters (halos with $M > 10^{13} M_\odot$) a few μG's are typically expected, though it could rise to 10μG in the most massive ones (Vacca et al., 2012). In fact we expect B to increase with the mass, because of the scaling law (Kunz et al., 2011)

$$B_0 \propto n_e^{1/2} T^{3/4}, \tag{8.29}$$

which, combined with the temperature-mass relation deduced from X-rays observations (Giodini et al., 2013), gives

$$B_0 \propto M. \tag{8.30}$$

As we will see later, the dependence of the angular power spectra of Faraday rotation and conversion on cosmological parameters is impacted by how B scales with the halo mass. Therefore in this study, we will consider three different mass scalings. First, a mass-scale independent magnetic field, which will be our benchmark. The second scaling, suited to model the effects due to clusters, will be

$$B_0(M) = B_p \times \left(\frac{M}{M_p}\right)^{\gamma}, \tag{8.31}$$

with $M_p = 5 \times 10^{14} M_\odot$, $B_p = 3\mu$G, and $\gamma > 0$ for the magnetic field to increase with mass. Third, to take into account galaxies, in which the field is greater than in clusters, we will take

$$B_0(M) = B_p + B_g \times \left\{1 + \tanh\left[\frac{\log(M_g/M)}{\Delta \log M}\right]\right\}, \tag{8.32}$$

with $B_c = 3\mu$G, $B_g = 3.5\mu$G, $M_g = 10^{13} M_\odot$, and $\Delta \log M \simeq 0.43$. This last scaling is convenient because it enables us to consider two regimes with a smooth transition: For low masses ($M < 10^{13} M_\odot$) it becomes $B_0 = 10\mu$G, which is relevant for galaxies, while for high masses ($M >$

$10^{13}M_\odot$) we have $B_0 = 3\mu$G as expected in clusters. This transition is centered at $10^{13}M_\odot$ with a width of about half of an order of magnitude in mass.

For simplicity, as a first approach, throughout our work we consider single profiles for the electron density and magnetic fields in halos. However, we are aware that improving this modeling may affect our results. For example Tashiro et al. (2008) show the effect of taking into account the fact that galaxies have disc structures on which gas from the halo may condense.

8.3 The halo model

The halo model can be used to make a statistical study of various large scale structure physical observables, such as the spatial distribution of galaxies, the nonlinear velocity field, the pressure field, the weak gravitational lensing as well as secondary sources of anisotropies of the CMB such as the thermal and kinetic SZ effects. Therefore, we will use this model to make a statistical study of the FR and FC effects in galaxies and galaxy clusters, so that our treatment will be close to the one of the SZ effect. To use the halo model for other physical observables than the DM density field, it suffices to replace the DM halo density profile Eq. (8.15) with the relevant spatial profile for the considered physical observable and the appropriate clustering.

A review of the halo model is presented in Cooray & Sheth (2002) and most of the content of this chapter on this model is based on it. The halo model is based on the description of the spatial distribution of galaxies by Neyman & Scott (1952). In their modeling, galaxies were discrete points clumped together in clusters of galaxies with different sizes so that the ingredients of the model were the distribution of cluster sizes, the distribution of galaxies around the cluster centre and a model for the clustering of clusters. If one replaces these clusters of galaxies by the DM virialized halos of Section 8.2.1, so that one replaces the distribution of galaxies around the cluster centre by the halo density profile of Eq. (8.15), one is building the halo model of large scale structure describing the spatial statistics of the dark matter density field. The motivation for doing this comes from the fact that 84% of the matter in the Universe is dark (Planck Collaboration et al., 2018b). In the halo model, all the mass of the complex network formed by DM (sheets, filaments and knots) is replaced by the virialized DM halos, see Fig. 8.3.

Then, the distribution of halos in size, that is the distribution of halos in mass, is given by the mass function $n(m,z)$ which is the average comoving number density of halos of mass m at redshift z

$$\frac{m^2 n(m,z)}{\bar{\rho}}\frac{\mathrm{d}m}{m} = \nu f(\nu)\frac{\mathrm{d}\nu}{\nu}, \tag{8.33}$$

with $\bar{\rho}$ the comoving density of the background; $\nu \equiv \delta_{\rm sc}^2(z)/\sigma^2(m)$ where $\delta_{\rm sc}(z)$ is the initial density contrast δ_i (defined in Chapter 3) required for spherical collapse, extrapolated using linear theory to the time of collapse z, and $\sigma^2(m)$ is the variance in the initial density fluctuation field smoothed with a tophat filter on scale R. In fact, mass functions f can be parametrised either by ν or σ. Here we describe the ν parametrisation taken when the virial density is used to define halos, so that it is consistent with our definition of halos with the virial radius as in Eq. (8.19). We have chosen the modelisation of Despali et al. (2016) based on ellipsoidal collapse model (Sheth et al., 2001; Sheth & Tormen, 2002) which gives a good fit to the mass function in DM numerical simulations

$$\nu f(\nu) = A\left(1+\frac{1}{\nu'^p}\right)\left(\frac{\nu'}{2\pi}\right)^{1/2}\mathrm{e}^{-\nu'/2}, \tag{8.34}$$

with $\nu' = b\nu$ and best fit values for (b,p,A) are given in the paper by Despali et al. (2016). The fitting parameters hardly depend on redshift: the mass function is therefore said to be universal.

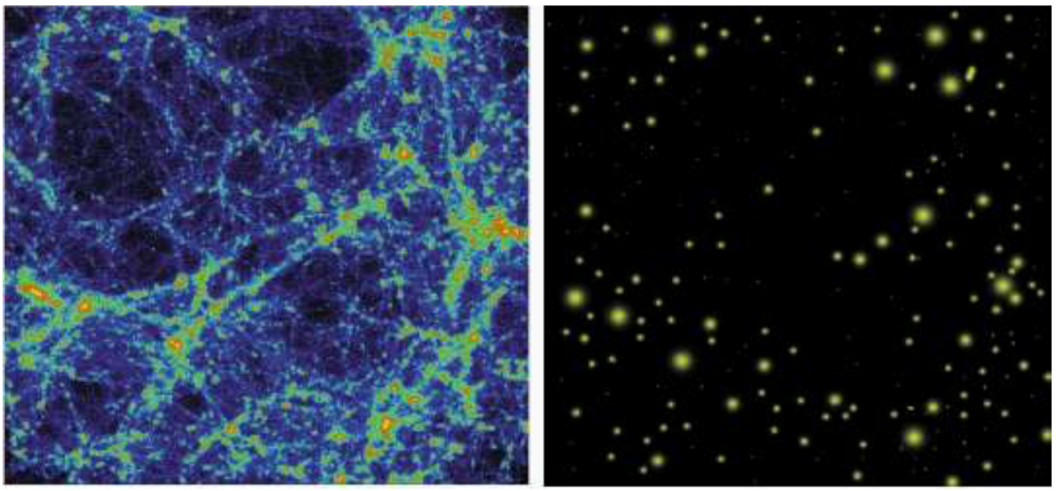

Figure 8.3: The complex distribution of DM as found in numerical simulations, shown on the left, is replaced by the distribution of DM halos shown on the right. All the mass of the Universe is therefore contained in these virialized DM halos. Figure taken from Cooray & Sheth (2002).

Finally, a model for the clustering of halos which takes into account the spatial correlations between halos is related to the perturbation theory describing the clustering of DM (Bernardeau et al., 2015) by the deterministic biasing on large scales

$$\delta_h(m, z_1|M, V, z_0) = \sum_{k>0} b_k(m, z_1)\delta^k, \tag{8.35}$$

where δ_h is the density contrast of halos of mass m which collapsed at z_1 in cells of comoving volume V and mass M at z_0. The sum over k is just an expansion in powers of δ, which is the usual DM density contrast, and the b_k are called the bias parameters which account for the difference between the DM density field one can observe in simulations and its halo description, see Fig. 8.3. This allows us to compute the variance of the halo counts on large scales

$$\langle \delta_h(m, z_1|M, V, z_0)^2 \rangle = \langle \left(\sum_{k>0} b_k(m, z_1)\delta^k \right)^2 \rangle \approx b_1^2(m, z_1)\langle \delta^2 \rangle_V, \tag{8.36}$$

where $\langle \delta^2 \rangle_V$ is the variance of the DM distribution and can be computed using perturbation theory, the average $\langle ... \rangle$ in on large cells of volume V with mass M at z_0. Then, the two-point correlation function ξ of the continuous DM density field normalised to the mean density $\bar{\rho}$ in the model is given by

$$\xi(\boldsymbol{x} - \boldsymbol{x}') = \xi^{1h}(\boldsymbol{x} - \boldsymbol{x}') + \xi^{2h}(\boldsymbol{x} - \boldsymbol{x}'), \tag{8.37}$$

with

$$\xi^{1h}(\boldsymbol{x} - \boldsymbol{x}') = \int \mathrm{d}m \, \frac{n(m)}{\bar{\rho}^2} \int \mathrm{d}^3 y \; \rho(\boldsymbol{y}|m)\rho(\boldsymbol{y} + \boldsymbol{x} - \boldsymbol{x}'|m), \tag{8.38}$$

$$\begin{aligned} \xi^{2h}(\boldsymbol{x} - \boldsymbol{x}') = \int \mathrm{d}m_1 \, \frac{n(m_1)}{\bar{\rho}} \int \mathrm{d}m_2 \, \frac{n(m_2)}{\bar{\rho}} \int \mathrm{d}^3 x_1 \; \rho(\boldsymbol{x} - \boldsymbol{x}_1|m_1) \\ \int \mathrm{d}^3 x_2 \; \rho(\boldsymbol{x}' - \boldsymbol{x}_2|m_2)\xi_{hh}(\boldsymbol{x}_1 - \boldsymbol{x}_2|m_1, m_2). \end{aligned} \tag{8.39}$$

In this continuous description, the above average is transformed by an average over space and an average over the halo mass function. The first term of the two-point correlation function is called the one-halo term (hence the superscript '1h') and represents the contributions coming from the same halo to the two-point correlation function of the DM density field, the second term is called the two-halos term (hence the superscript '2h') and represents contributions coming from two different halos which are correlated. Finally, $\xi_{hh}(\boldsymbol{x}_1 - \boldsymbol{x}_2|m_1, m_2)$ is the two-point correlation function of halos of mass m_1 and m_2 and can be computed using the deterministic biasing on large scales Eq. (8.36)

$$\xi_{hh}(r|m_1, m_2) \approx b(m_1)b(m_2)\xi(r), \tag{8.40}$$

and it has been noticed that using the linear theory for ξ is a good estimation at all scales: $\xi_{hh}(r|m_1, m_2) \approx b(m_1)b(m_2)\xi^{\rm lin}(r)$.

8.4 Angular power spectra of the FR and FC effects by large-scale structures

The purpose of our work in the paper of Chapter 9 was to model the FR and FC effects in large scale structures such as galaxies and galaxy clusters as a first step in order to predict their impact on the anisotropies in polarisation of the CMB. This was an all sky modelisation of the effects, thus we made use of the spherical harmonics formalism of Section 4.3.1, used to describe the anisotropies of the CMB and of the above described halo model of large scale structure.

We have seen in Section 8.3 that the halo model allows us to compute correlation functions of various physical observables of large scale structure, in particular the secondary effects on the CMB such as the thermal and kinetic SZ effects. Similarly in our work of Chapter 9, we have used the two-point correlation function Eq. (8.37) derived in the halo model to study statistically the two FR and FC effects in galaxies and galaxy cluster halos. Thus the DM halo density profile Eq. (8.15) has been replaced by the gas and magnetic field spatial distributions in galaxy clusters Eq. (8.17) and Eq. (8.26) in the above expressions of Eq. (8.38) and Eq. (8.39).

Let ϕ_s be the effect under consideration, either the Faraday Rotation angle or Faraday Conversion rate, with s labelling the spin of the effect (the FR angle is a scalar while the FC rate is a spin 2 quantity). It can be written as an integrated effect over the Line-Of-Sight (L.O.S.) as all clusters along the L.O.S. contribute cumulatively to the effect

$$\phi_s(\boldsymbol{n}) = \int_0^{r_{\rm CMB}} {\rm d}r\ a(r) \int {\rm d}M_i \int {\rm d}^3x_i\ n_h(M_i, \boldsymbol{x}_i) f_s(\boldsymbol{b}(\boldsymbol{x}_i), \boldsymbol{n}) \Phi(M_i, |\boldsymbol{x} - \boldsymbol{x}_i|), \tag{8.41}$$

where $\boldsymbol{n}$ is L.O.S. direction pointing towards the sky such that $\boldsymbol{x} = r\boldsymbol{n}$ and r is the comoving distance along the L.O.S., $\boldsymbol{x}_i$ the position of the centre of a cluster, $n_h(M_i, \boldsymbol{x}_i)$ the abundance of halos, f_s is a function of the projection of the orientation $\boldsymbol{b}(\boldsymbol{x}_i)$ of the magnetic field which depends only on the cluster i through its position, and $\Phi(M_i, |\boldsymbol{x} - \boldsymbol{x}_i|)$ is the dimensional spatial profile of the effect, depending on the magnetic field and electron density profiles, where we have assumed spherical symmetry. We bother writing the effects we considered this way to highlight our statistical modelisation. Indeed, the two-point correlation function of ϕ_s is then

$$\xi^{\phi_s\phi_{s'}}(\boldsymbol{n}_1, \boldsymbol{n}_2) \equiv \langle \phi_s(\boldsymbol{n}_1)\phi_{s'}(\boldsymbol{n}_2)\rangle \propto \langle n_h(M_i, \boldsymbol{x}_i) n_h(M_j, \boldsymbol{x}_j) f_s(\boldsymbol{b}_i, \boldsymbol{n}_1) f_{s'}(\boldsymbol{b}_j, \boldsymbol{n}_2)\rangle, \tag{8.42}$$

and can be split into a one-halo term and a two-halo term following Eq. (8.37). Now assuming the spatial distribution of halos is uncorrelated to the distribution of the magnetic field orientations, the above average can be factorised in two

$$\begin{aligned} &\langle n_h(M_i, \boldsymbol{x}_i) n_h(M_j, \boldsymbol{x}_j) f_s(\boldsymbol{b}_i, \boldsymbol{n}_1) f_{s'}(\boldsymbol{b}_j, \boldsymbol{n}_2)\rangle \\ &= \langle n_h(M_i, \boldsymbol{x}_i) n_h(M_j, \boldsymbol{x}_j)\rangle_c\ \langle f_s(\boldsymbol{b}_i, \boldsymbol{n}_1) f_{s'}(\boldsymbol{b}_j, \boldsymbol{n}_2)\rangle_{SO(3)}, \end{aligned} \tag{8.43}$$

where $\langle ... \rangle_c$ is an average over the spatial distribution of clusters and $\langle ... \rangle_{SO(3)}$ an average over the magnetic fields orientations which are labelled by three Euler angles, or equivalently by a rotation matrix belonging to $SO(3)$. Finally, we assumed the magnetic field orientations to be independent from one halo to another so that

$$\langle f_s(\boldsymbol{b}_i, \boldsymbol{n}_1) f_{s'}(\boldsymbol{b}_{j\neq i}, \boldsymbol{n}_2)\rangle_{SO(3)} = \langle f_s(\boldsymbol{b}_i, \boldsymbol{n}_1)\rangle_{SO(3)} \langle f_{s'}(\boldsymbol{b}_{j\neq i}, \boldsymbol{n}_2)\rangle_{SO(3)}, \tag{8.44}$$

and that these orientations are uniformly distributed over the whole halo population, as is required for a statistically homogeneous and isotropic Universe so $\langle f_s(\boldsymbol{b}, \boldsymbol{n})\rangle_{SO(3)} = 0$. Thus, the two-point correlation of the magnetic field orientations is proportional to a Kronecker delta

$$\langle f_s(\boldsymbol{b}_i, \boldsymbol{n}_1) f_{s'}(\boldsymbol{b}_j, \boldsymbol{n}_2)\rangle_{SO(3)} \propto \delta_{ij}, \tag{8.45}$$

so that it is non-zero only for the same halos, and the two-halos term in the two-point correlation function Eq. (8.42) vanishes.

Finally, the angular power spectrum of the effect is obtained by going to the analog of Fourier space on the sky, i.e. making a spherical harmonic tranform

$$\langle \phi_{s;\ell m} \phi^*_{s';\ell' m'} \rangle = \int \mathrm{d}^3 n_1 \int \mathrm{d}^3 n_2 \; \xi^{\phi_s \phi_{s'}}(\boldsymbol{n}_1, \boldsymbol{n}_2)_s Y^*_{\ell m}(\boldsymbol{n}_1)_{s'} Y_{\ell' m'}(\boldsymbol{n}_2), \tag{8.46}$$

where $\langle \phi_{s;\ell m} \phi^*_{s';\ell' m'} \rangle$ is the correlation matrix of the multipolar coefficients and is expected to be diagonal as the effects are statistically homogeneous and isotropic: $\langle \phi_{s;\ell m} \phi^*_{s';\ell' m'} \rangle = C_\ell^{\phi_s, \phi_{s'}} \delta_{\ell,\ell'} \delta_{m,m'}$, $C_\ell^{\phi_s, \phi_{s'}}$ being the angular power spectrum of the effect. As the two-point correlation function Eq. (8.42) is written as the product of the two-point correlation function for the magnetic field orientations and the two-point correlation function for the amplitude of the effect, the angular power spectrum is actually the convolution of their two respective angular power spectra.

As already mentioned in Section 8.2.2.2, a more realistic magnetic field model would be one with a power spectrum at smaller scales than the virial radius (as in Murgia et al., 2004; Govoni et al., 2006; Bonafede et al., 2010), characterised by a vector potential described by a statistically isotropic, power-law power spectrum on small scales (smaller than the cluster scale). Including such fluctuations, the two-point correlation function Eq. (8.45) of the magnetic field orientations becomes

$$\langle f_s(\boldsymbol{b}_i, \boldsymbol{n}_1) f_{s'}(\boldsymbol{b}_j, \boldsymbol{n}_2)\rangle \to \langle f_s(\boldsymbol{b}'_i, \boldsymbol{n}_1) f_{s'}(\boldsymbol{b}'_j, \boldsymbol{n}_2)\rangle S(r_{1,2}), \tag{8.47}$$

where here $\boldsymbol{b}'$ corresponds to the orientation of the average magnetic field over the halo scale, that is to the large-scale component of the full magnetic field of the halo. This two-point correlation function is non-zero if and only if the two lines-of-sight cross the same clusters (encoded in the δ_{ij}). Finally, the function $S(r_{1,2})$ is the two-point correlation function associated to the power spectrum of magnetic fields at small scales. It is a function of the distance $r_{1,2}$ between the two points at which $B_i(r_1)$ and $B_j(r_2)$ are considered (not to be confused with r_1 and r_2 which are distances of each point from the observer). Such a two-point correlation function drops down to zero beyond a separation Λ_c that is smaller than the size of the halo, i.e. for $r_{1,2} > \Lambda_c$ with $\Lambda_c < r_{\rm vir}$, while it tends to one for $r_{1,2} \to 0$. This drop accounts for the fact that the magnetic field is coherent on scales smaller than the halo size. In Murgia et al. (2004) for instance, the power spectrum is non vanishing on scales ranging from a hundredth of the core radius, r_c, to almost twice the core radius. This corresponds to a coherence length of roughly half the virial radius. Here we assumed that the magnetic fields are coherent over the entire halo, meaning that up to the virial radius the function S equals ~ 1. By assuming a coherence up to the virial radius, it is likely that the angular power spectrum on large scales will be overestimated, in the range from $r_{\rm vir}/2$ to $r_{\rm vir}$ or so.

Let us finally examine how the above result can be modified to include a stochastic component in the magnetic field (as in Murgia et al., 2004; Govoni et al., 2006; Bonafede et al., 2010). It can be shown that adding the 2-point correlation $S(r)$ of the stochastic magnetic field can be accounted for introducing an effective profile, $X \rightarrow X_{eff}$, where X is the profile of the effect considered, i.e. $X \propto n_e(r)B_{\parallel}(r)$ for FR and $X \propto n_{rel}(r)B_{\perp}^2(r)$ for FC. This profile should take into account two effects. First it has to fall down to zero faster than the β-profile in order to include the large scale suppression due to a coherence length smaller than the virial radius. The precise shape of such an additional drop depends on the details of the power spectrum describing the stochastic magnetic field. However, as a simple effective description, one can increase the values of the parameter μ in Eq. (8.26), since the profile drops faster for higher values of μ. Therefore in what follows, the parameter μ should be interpreted as an effective parameter which also (partially) captures the impact of a magnetic field coherent on scales smaller than the virial radius. Second, the correlation $S(r)$ may add a new scaling of the total amplitude of the effect with the mass. Nevertheless this modification can be absorbed completely in the mass scaling of B_c. We will thus consider that the impact of such a stochastic component is effectively captured by an increased value of μ (in terms of shape), and by the mass-scaling we introduced for B_c. This obviously does not capture the details of the power spectrum of the magnetic field, but at least it takes into account its impact at a qualitative level. The other way around, one can also expect that the large-scale suppression induced by the power spectrum description, and the additional scaling in mass, is partially degenerate with the parameter μ and the mass-scaling of B_c.

In our work of Chapter 9, we have computed the angular power spectra of the FR and FC effects for different values of the parameters β and μ of the electron density and magnetic field spatial profiles Eq. (8.17), (8.26), as well as for different models for the amplitude of the magnetic field Eq. (8.31), (8.32) and also for relativistic electrons instead of cold electrons. Fig. 8.4 shows the angular power spectrum of the Faraday Rotation angle α for different models for the amplitude of the magnetic field. The solid red curve is the reference curve representing no mass-scaling of the amplitude of the magnetic field: here, all halos have the same magnetic field amplitude set to $3\mu G$. The dashed blue curve accounts for the galaxy scaling Eq. (8.32): galaxies (i.e. halos with $M < 10^{13}M_{\odot}$) have a higher magnetic field, as high as $10\mu G$ for halos with mass $M = 10^{10}M_{\odot}$, thus the overall amplitude of the angular power spectrum is higher with respect to the no-mass scaling model. However, as galaxy clusters (halos with $M > 10^{13}M_{\odot}$) have a lower magnetic field amplitude, as low as $3\mu G$ for the most massive halos, the galaxies dominate the contribution to the effect: it is reflected by the fact that the dashed blue curve is shifted to higher ℓ, hence to smaller scales, galaxies being smaller scale objects on the sky than galaxy clusters for a given redshift. The dot-dashed orange and dotted green curves correspond to a more refined model of magnetic field amplitude where one has the above galaxy scaling Eq. (8.32) plus a mass-scaling Eq. (8.31) for galaxy clusters. In this model, galaxy clusters have a stronger magnetic field compared to the galaxy scaling only, as strong as $60\mu G$ for the most massive clusters ($M = 10^{16}M_{\odot}$) in the $\gamma = 1$ case. Therefore, the overall amplitude is again greater with respect to the galaxy scaling model, as we add more power through the galaxy clusters: hence, the gain in amplitude is at small ℓ, i.e. large scales, galaxy clusters being larger scale objects on the sky than galaxies. These qualitative features are also found for the angular power spectra of the Faraday Conversion rate with cold electrons, however enhanced because the FC rate scales with the magnetic field to the square.

The different models for the magnetic field strength, electron density and magnetic field profiles change the scaling of the angular power spectra with cosmological parameters. Thus, a precise modeling of the electron density and magnetic field inside galaxies and galaxy clusters is needed if one wants to use these effects to probe the cosmological parameters or inversely,

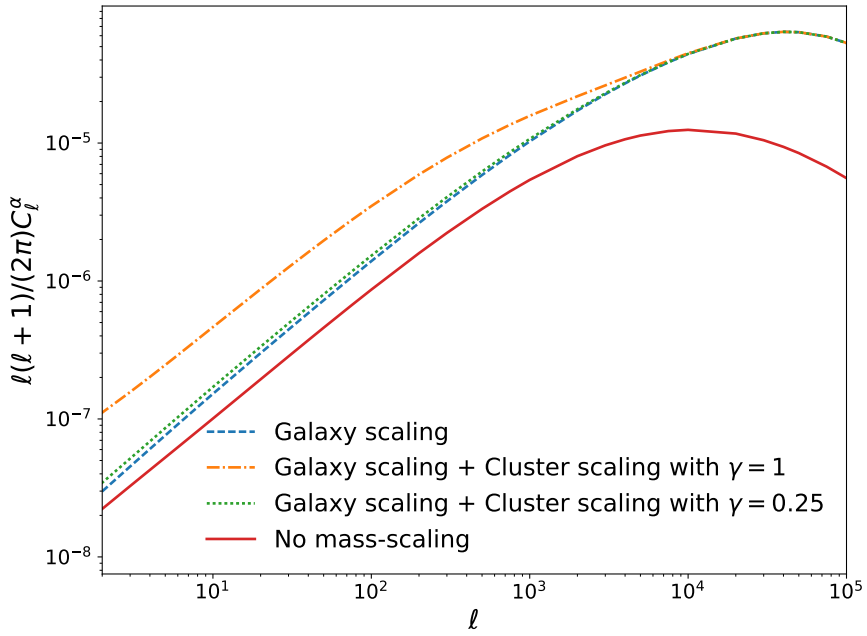

Figure 8.4: The power spectrum of the Faraday Rotation angle α for different models of the magnetic field amplitude inside halos.

knowing precisely the cosmology could allow us to probe the gas and magnetic field properties of galaxy halos. The table 8.1 summarizes our results concerning the scalings with the cosmological parameters σ_8, which is the amplitude of the linear matter power spectrum on scales of $8/h$ Mpc, and Ω_m, the matter density parameter, of the two FR and FC angular power spectra for different models of the magnetic field strength and electron populations. One notices that our effects are above all sensitive to the σ_8 parameter which is strongly linked to the mass function, as the latter gives the abundance of halos in mass and redshift, hence being another manifestation of the density fluctuations. Furthermore, the more the effects depend on mass, the more strongly it scales with σ_8, see the 'no mass' and 'cluster' scalings of the magnetic field strength cases for example. This is due to the fact that the mass function depends more strongly on σ_8 for high masses. For that matter, the scaling with σ_8 at $\ell = 10$ is always stronger than at $\ell = 10000$, as low multipoles correspond to large scales, hence high masses. There is thus a degeneracy between this scaling in σ_8 and the mass dependence of the magnetic field strength. Finally, the effects are almost insensitive to Ω_m when varying Ω_{CDM}. For a comparison, we give the scalings with these cosmological parameters of other probes, the different scaling in σ_8 being explained by a different mass scaling of the effects. When constraining the cosmological parameters, there is usually a degeneracy in the $\sigma_8 - \Omega_m$ plane, see for example Fig. 20 of Planck Collaboration et al. (2018b). The different scalings of our effect as compared to other probes could therefore be used to lift this degeneracy, provided that the magnetic field properties are well known and the other way around, knowing the cosmological parameters from other probes would allow to determine the scaling with mass of the magnetic field strength.

		σ_8	Ω_m
Faraday Rotation power spectrum	No mass-scaling	3.1; 2.1	-0.12; -0.22
	Galaxy scaling	2.0; 0.89	
	Cluster scaling $\gamma = 1$	9.6; 7.6	
	Galaxy scaling + cluster scaling $\gamma = 1$	7.0; 1.0	
Faraday Conversion power spectrum	Thermal electrons	3.1; 1.9	-0.12; -0.21
	Relativistic electrons		1.0; 0.7
Halo number counts from thermal SZ		9	3
Thermal SZ power spectrum at $\ell \simeq 3000$		8.1	3.2
CMB lensing power spectrum at $\ell \simeq 30$		2	0.5

Table 8.1: Scaling of different large-scale-structure probes with σ_8 and Ω_m. The scaling reported here is to be understood as $P \propto \sigma_8^n \, \Omega_m^p$ with P the amplitude of any of the considered probe. They are given for two values of the multipole $\ell = 10$ and $\ell = 10000$ for the Faraday Rotation angle and the Faraday Conversion rate, at the peaking multipole of $\ell(\ell+1)C_\ell$ for the tSZ flux, and the peaking multipole of $\ell^2(\ell+1)^2 C_\ell^{\phi\phi}$ for the lensing potential.

8.5 Impact on the CMB

The impact of the FR and FC effects in galaxy clusters on the CMB is similar to the weak lensing of the background radiation by these very large-scale structures. The weak lensing effect has been mentioned in Section 4.3.2 and consists in the deflection of the background light by the gravitational potential of large-scale structures such as galaxy clusters. It changes the primordial image of the CMB by inducing secondary temperature anisotropies, but also secondary polarised anisotropies, converting some of the primordial E modes patterns into secondary B modes ones, as shown in Fig. 4.12. The FR and FC effects also transforming polarisation, it is this last part of the impact of weak lensing on the CMB that is similar. The CMB being described statistically (cf Chapter 4), the impact of these effects on the CMB translates into a modification of the angular power spectra of the polarised anisotropies $C_\ell^{EE/BB}$. Therefore, similarly to the lensing effect, the observed polarised anisotropies of the CMB can be used to reconstruct the FR and FC fields, containing potentially a lot of astrophysical and cosmological information. The reconstruction of these fields requires to build their estimators, in a similar way to those built for lensing in Hu & Okamoto (2002); Okamoto & Hu (2003), see also Kamionkowski (2009) for the FR angle α.

8.5.1 Secondary polarised anisotropies

Thus, the second step in our work was to predict the impact of such effects on the anisotropies in polarisation of the CMB. The CMB being described statistically, its anisotropies can be characterised by their statistical moments; the angular power spectra for the secondary linearly polarised CMB anisotropies have already been derived elsewhere for the case of gravitational lensing (see Zaldarriaga & Seljak, 1998; Hu, 2000) and Faraday Rotation (see Takada et al., 2001; Scoccola et al., 2004; Kosowsky et al., 2005; Tashiro et al., 2008) with the help of the basis independent non-local E and B modes (see Chapter 4) rather than the Q and U basis dependent Stokes parameters. Therefore, we will only give the expressions of the angular power spectra for the two combined effects and begin with the derivation of the angular power spectrum of the secondary circularly polarized anisotropies of the CMB due to Faraday Conversion, the

derivation being similar but simpler than for the E and B modes due to Faraday Rotation and gravitational lensing.

8.5.1.1 Secondary V Stokes parameter

Contrary to the Q and U Stokes parameters, the V Stokes parameter is invariant under rotations of the coordinate basis. It is however a pseudo-scalar (the intensity I is a real scalar), meaning it gets a minus sign when reversing the handedness of the basis (under a parity transformation). We will therefore use it to characterise the angular power spectrum of circular polarisation. Faraday Conversion transforms the incoming linear polarisation described by the polarisation field $P_{\pm 2}$ (defined in Eq. (4.29)) into circular polarisation described by the V Stokes parameter at a rate $\phi_{\mp 2}$. Formally a perturbative solution for V at the next-to-leading order is given by

$$\begin{aligned}\widetilde{V}^{\mathrm{FR+FC}} = \widetilde{V} + i\left(\int_{r_{\mathrm{CMB}}}^{0} \mathrm{d}r \frac{\mathrm{d}\phi_{-2}(r)}{\mathrm{d}r} e^{-2i\theta_B(r)} e^{-2i\alpha(r,r_{\mathrm{CMB}})}\right)\widetilde{P}_2 \\ - i\left(\int_{r_{CMB}}^{0} \mathrm{d}r \frac{\mathrm{d}\phi_{2}(r)}{\mathrm{d}r} e^{2i\theta_B(r)} e^{2i\alpha(r,r_{\mathrm{CMB}})}\right)\widetilde{P}_{-2},\end{aligned} \tag{8.48}$$

where $\widetilde{V}$ and $\widetilde{P}_{\pm 2}$ are the primary+lensed CMB polarisation fields, assuming lensing occurs before FR and FC [1], r_{CMB} is the comoving distance to the CMB, ϕ is the FC rate of Eq. (8.11), α the FR angle defined in Eq. (8.9) and θ_B is the angle between the magnetic field projected on the plane perpendicular to the L.O.S. $(\boldsymbol{e}_\theta, \boldsymbol{e}_\varphi)$, which is along $\boldsymbol{e}_2$, and the basis vector $\boldsymbol{e}_\theta$, as shown in Fig 8.5. The primordial Stokes V parameter is however expected to be zero in the standard

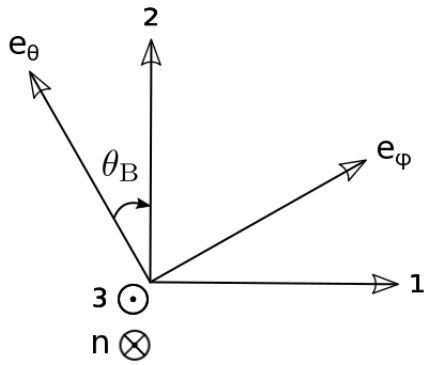

Figure 8.5: The angle θ_B between the magnetic field projected on the plane perpendicular to the L.O.S. direction $\boldsymbol{n}$, which is along $\boldsymbol{e}_2$ as in Sazonov (1969a), and the spherical coordinates basis vector $\boldsymbol{e}_\theta$.

cosmological model, as there is no source of circular polarisation at recombination. Moreover, as the FR angle is small, it is treated like a perturbation and one can expand the exponential in the above integrals. Keeping terms at the lowest order it becomes

$$\widetilde{V}(\boldsymbol{n}) = i\left(\phi_{-2}(\boldsymbol{n}; 0, r_{\mathrm{CMB}})P_2(\boldsymbol{n}) - \phi_2(\boldsymbol{n}; 0, r_{\mathrm{CMB}})P_{-2}(\boldsymbol{n})\right), \tag{8.49}$$

[1] As shown for example in Lewis & Challinor (2006) (cf the right panel of their fig 3) the main contribution to the power spectrum of the lensing potential is due to the cumulative effect of redshifts $z > 0.5$ for all multipoles, while our effects are expected to mainly occur at low redshifts $z \lesssim 1$.

where $\phi_{\pm 2}(\boldsymbol{n}; 0, r_{\rm CMB})$ is the integral over the L.O.S. of $\mathrm{d}\phi(r)/\mathrm{d}r\, e^{\pm 2 i \theta_B(r)}$. Note on this expression that terms involving α do not appear because as it is a small effect, one can Taylor expand the exponential so that these terms are of higher order.

Decomposing $\widetilde{V}$ onto the spherical harmonics gives the following multipolar coefficients

$$\widetilde{V}_{\ell m} = \int \mathrm{d}^3 n\, \widetilde{V}(\boldsymbol{n}) Y^*_{\ell m}(\boldsymbol{n}). \tag{8.50}$$

We can do the same for the spin 2 field $\phi_{\pm 2}(\boldsymbol{n})$

$$\phi_{\pm 2}(\boldsymbol{n}) = \sum_{\ell m} {}_{\pm 2}\phi_{\ell m}\, {}_{\pm 2}Y_{\ell m}(\boldsymbol{n}), \tag{8.51}$$

and define the ϕ^E and ϕ^B modes for $\phi_{\pm 2}$, similarly to what is done for the polarisation field $P_{\pm 2}$ in Section 4.3.1.2,

$${}_{\pm 2}\phi_{\ell m} = -(\phi^E_{\ell m} \pm i \phi^B_{\ell m}). \tag{8.52}$$

With these notations, the $\widetilde{V}$ Stokes parameter is rewritten

$$\begin{aligned}\widetilde{V}(\boldsymbol{n}) = i\Bigg(&\sum_{\ell m} (\phi^E_{\ell m} - i\phi^B_{\ell m})\ {}_{-2}Y_{\ell m}(\boldsymbol{n}) \sum_{l' m'} (E_{\ell' m'} + iB_{\ell' m'})\ {}_{+2}Y_{\ell' m'}(\boldsymbol{n}) \\ &- \sum_{\ell m} (\phi^E_{\ell m} + i\phi^B_{\ell m})\ {}_{+2}Y_{\ell m}(\boldsymbol{n}) \sum_{\ell' m'} (E_{\ell' m'} - iB_{\ell' m'})\ {}_{-2}Y_{\ell' m'}(\boldsymbol{n}) \Bigg),\end{aligned} \tag{8.53}$$

and using the Gaunt integrals

$$\begin{aligned}\int d^2\boldsymbol{n}\ {}_{-2}Y_{\ell' m'}(\boldsymbol{n})\, {}_{+2}Y_{\ell'' m''}(\boldsymbol{n}) Y^*_{\ell m}(\boldsymbol{n}) =& (-1)^m \sqrt{\frac{(2\ell'+1)(2\ell''+1)(2\ell+1)}{4\pi}} \\ & \begin{pmatrix} \ell' & \ell'' & \ell \\ -m' & -m'' & m \end{pmatrix} \begin{pmatrix} \ell' & \ell'' & \ell \\ -2 & +2 & 0 \end{pmatrix},\end{aligned} \tag{8.54}$$

and

$$\begin{aligned}\int d^2\boldsymbol{n}\ {}_{+2}Y_{\ell' m'}(\boldsymbol{n})\, {}_{-2}Y_{\ell'' m''}(\boldsymbol{n}) Y^*_{\ell m}(\boldsymbol{n}) =& (-1)^{\ell'+\ell''+\ell} (-1)^m \sqrt{\frac{(2\ell'+1)(2\ell''+1)(2\ell+1)}{4\pi}} \\ & \begin{pmatrix} \ell' & \ell'' & \ell \\ -m' & -m'' & m \end{pmatrix} \begin{pmatrix} \ell' & \ell'' & \ell \\ -2 & +2 & 0 \end{pmatrix},\end{aligned} \tag{8.55}$$

the multipolar coefficient for V is

$$\begin{aligned}\widetilde{V}_{\ell m} =& i \sum_{\ell' m'} \sum_{\ell'' m''} (-1)^m \sqrt{\frac{(2\ell'+1)(2\ell''+1)(2\ell+1)}{4\pi}} \begin{pmatrix} \ell' & \ell'' & \ell \\ -m' & -m'' & m \end{pmatrix} \begin{pmatrix} \ell' & \ell'' & \ell \\ -2 & +2 & 0 \end{pmatrix} \\ & \Big(\left(\phi^E_{\ell' m'} - i\phi^B_{\ell' m'}\right) \left(E_{\ell'' m''} + iB_{\ell'' m''}\right) - (-1)^{\ell''+\ell'+\ell} \left(\phi^E_{\ell' m'} + i\phi^B_{\ell' m'}\right) \left(E_{\ell'' m''} - iB_{\ell'' m''}\right) \Big).\end{aligned} \tag{8.56}$$

Finally, the covariance matrix of the multipolar coefficients for the circular polarisation $\langle \widetilde{V}_{\ell_1 m_1} \widetilde{V}^*_{\ell_2 m_2} \rangle$ reduces to an angular power spectrum. Indeed, the two processes involved are homogeneous and isotropic (generation of primary linearly polarized anisotropies or Faraday Conversion)

$$\langle X_{\ell_1'' m_1''} Y^*_{\ell_2'' m_2''} \rangle = \delta_{XY} \delta_{\ell_1'' \ell_2''} \delta_{m_1'' m_2''} C^{XX}_{\ell_1''}, \tag{8.57}$$

$$\langle \phi^X_{\ell_1' m_1'} \phi^{Y*}_{\ell_2' m_2'} \rangle = \delta_{XY} \delta_{\ell_1' \ell_2'} \delta_{m_1' m_2'} C^{\phi_X \phi_Y}_{\ell_1'}, \tag{8.58}$$

where X and Y stand either for E or B. There is no $\phi_E\phi_B$ cross-correlation: $C_\ell^{\phi_E\phi_B}=0$ and no primary cross-correlation between E and B modes $C_\ell^{EB}=0$ for symmetry reasons (the CMB is parity invariant, see chapter 4). Thus for example, the sums over m_2', m_2'' in the computation of $\langle\widetilde{V}_{\ell_1 m_1}\widetilde{V}^*_{\ell_2 m_2}\rangle$ disappear. Furthermore, we make use of the Wigner$-3j$ orthogonality relation

$$\sum_{m_1' m_1''}\begin{pmatrix}\ell_1' & \ell_1'' & \ell_1\\ -m_1' & -m_1'' & m_1\end{pmatrix}\begin{pmatrix}\ell_1' & \ell_1'' & \ell_2\\ -m_1' & -m_1'' & m_2\end{pmatrix}=\delta_{\ell_1\ell_2}\delta_{m_1 m_2}\frac{1}{2\ell_1+1}, \tag{8.59}$$

to remove the last sums on m_1' and m_1''. Then, it is given by

$$\begin{aligned}\langle\widetilde{V}_{\ell_1 m_1}\widetilde{V}^*_{\ell_2 m_2}\rangle &= \delta_{\ell_1\ell_2}\delta_{m_1 m_2}\widetilde{C}_{\ell_1}^{VV}\\ &= \delta_{\ell_1\ell_2}\delta_{m_1 m_2}\sum_{\ell_1'}\sum_{\ell_1''}\frac{(2\ell_1'+1)(2\ell_1''+1)}{2\pi}\begin{pmatrix}\ell_1' & \ell_1'' & \ell\\ -2 & +2 & 0\end{pmatrix}^2\\ &\qquad\Big[(C_{\ell_1'}^{\phi^E\phi^E}+C_{\ell_1'}^{\phi^B\phi^B})(C_{\ell_1''}^{EE}+C_{\ell_1''}^{BB})\\ &\qquad-(-1)^{\ell_1'+\ell_1''+\ell_1}(C_{\ell_1'}^{\phi^E\phi^E}-C_{\ell_1'}^{\phi^B\phi^B})(C_{\ell_1''}^{EE}-C_{\ell_1''}^{BB})\Big].\end{aligned} \tag{8.60}$$

One notices on this expression that the angular power spectrum for circular polarization mixes the primary E and B modes (if any) and different multipoles to create a new type of anisotropies: the circularly polarized ones for which there is no primary contribution, as it does not exist a standard way to generate them primarily at recombination. As the Stokes V parameter is a linear combination of products of the Faraday Conversion rate $\phi_{\pm2}$ with the linear polarisation field $P_{\mp2}$, its angular power spectrum is therefore convolutions of the angular power spectra of the Faraday Conversion rate with angular power spectra of the E and B modes.

Observationally, the current most stringent upper limit on CMB circular polarisation has been set by the SPIDER collaboration (Nagy et al., 2017). Based on measurements for multipoles $33<\ell<307$, they obtain that $\ell(\ell+1)C_\ell^{VV}/(2\pi)$ ranges from $141\mu K^2$ to $255\mu K^2$ at 150 GHz at 95% confidence level.

8.5.1.2 Secondary E and B modes

As mentioned at the beginning of this section, the angular power spectra for the secondary E and B modes have already been computed in the literature separately for the gravitational lensing and Faraday Rotation effects. The derivation for the two combined effects is similar, although a bit more complicated, and in particular follows the same steps as the above derivation for the angular power spectrum for secondary circular polarisation. We will thus give only the key ingredients to perform such a derivation.

One starts with the expression of the lensed and Faraday rotated polarisation field

$$\begin{aligned}\widetilde{P}_{\pm2}(\boldsymbol{n}) &= \exp\left(\mp2i\alpha(\boldsymbol{n}+\underline{\nabla\phi})\right)P_{\pm2}(\boldsymbol{n}+\nabla\phi)\\ &= P_{\pm2}+\nabla_a\phi\nabla^a P_{\pm2}+\frac{1}{2}\nabla_a\phi\nabla_b\phi\nabla^a\nabla^b P_{\pm2}\mp2i\alpha P_{\pm2}\\ &\quad-2\alpha^2 P_{\pm2}\mp2i\alpha\nabla_a\phi\nabla^a P_{\pm2}\mp\underline{2i\nabla_a\phi\nabla^a\alpha P_{\pm2}},\end{aligned} \tag{8.61}$$

where ϕ is here the lensing field (and not the FC rate), and the underlined terms are present only if FR happens before lensing. This notation will be kept to keep track of these terms only present in this case. The second equality accounts for the development at the next-to-leading order of the lensed and Faraday rotated polarisation field, in order to take into account both

effects at the same time, as they are same order of magnitude perturbations to the polarisation field.

Now, using the expressions for the multipolar coefficients of the E and B modes given in Section 4.3.1.2 by inverting the polarisation field Eq. (4.29)

$$\begin{aligned} E_{\ell m} &= -\frac{1}{2}\int \mathrm{d}^3 n \left(P_2(\boldsymbol{n})_2 Y^*_{\ell m}(\boldsymbol{n}) + P_{-2}(\boldsymbol{n})_{-2} Y^*_{\ell m}(\boldsymbol{n})\right), \\ B_{\ell m} &= \frac{i}{2}\int \mathrm{d}^3 n \left(P_2(\boldsymbol{n})_2 Y^*_{\ell m}(\boldsymbol{n}) - P_{-2}(\boldsymbol{n})_{-2} Y^*_{\ell m}(\boldsymbol{n})\right), \end{aligned} \tag{8.62}$$

and replacing the transformed polarisation field Eq. (8.61) into these expressions for the $E_{\ell m}$ and $B_{\ell m}$, gives the secondary $\widetilde{E}$ and $\widetilde{B}$ modes. Finally, the angular power spectra of the secondary $\widetilde{E}$ and $\widetilde{B}$ modes are obtained by computing the correlation matrices of the multipolar coefficients $\langle \widetilde{E}_{\ell m} \widetilde{E}^*_{\ell' m'} \rangle$ and $\langle \widetilde{B}_{\ell m} \widetilde{B}^*_{\ell' m'} \rangle$ and are given by

$$\widetilde{C}_\ell^{EE} = \left\{1 + R[C_{\ell_1}^{\phi\phi}, C_{\ell_1}^{\alpha\alpha}]\right\} C_\ell^{EE} + \sum_{\ell_2} C_{\ell_2}^{EE} F^{(+)}_{\ell\ell_2}[C_{\ell_1}^{\phi\phi}, C_{\ell_1'}^{\alpha\alpha}] + \sum_{\ell_2} C_{\ell_2}^{BB} F^{(-)}_{\ell\ell_2}[C_{\ell_1}^{\phi\phi}, C_{\ell_1'}^{\alpha\alpha}], \tag{8.63}$$

$$\widetilde{C}_\ell^{BB} = \left\{1 + R[C_{\ell_1}^{\phi\phi}, C_{\ell_1}^{\alpha\alpha}]\right\} C_\ell^{BB} + \sum_{\ell_2} C_{\ell_2}^{BB} F^{(+)}_{\ell\ell_2}[C_{\ell_1}^{\phi\phi}, C_{\ell_1'}^{\alpha\alpha}] + \sum_{\ell_1} C_{\ell_2}^{EE} F^{(-)}_{\ell\ell_2}[C_{\ell_1}^{\phi\phi}, C_{\ell_1'}^{\alpha\alpha}], \tag{8.64}$$

$$\widetilde{C}_\ell^{EB} = R^{EB}[C_{\ell_1}^{\alpha\phi}]\left(C_\ell^{EE} - C_\ell^{BB}\right) + \sum_{\ell_2}\left(C_{\ell_2}^{EE} - C_{\ell_2}^{BB}\right) F^{EB}_{\ell\ell_2}[C_{\ell_1}^{\alpha\phi}], \tag{8.65}$$

with

$$\begin{aligned} F^{(+)}_{\ell\ell_2}[C_{\ell_1}^{\phi\phi}, C_{\ell_1'}^{\alpha\alpha}] = \sum_{\ell_1} M_{\ell_1,\ell_2} \Bigg[&\frac{1}{8}\left(N_{\ell,\ell_1,\ell_2}\right)^2 \left[1 + (-1)^{\ell+\ell_1+\ell_2}\right]^2 C_{\ell_1}^{\phi\phi} \\ &+ \left[1 - (-1)^{\ell+\ell_1+\ell_2}\right]^2 C_{\ell_1}^{\alpha\alpha}\Bigg] \begin{pmatrix} \ell & \ell_1 & \ell_2 \\ -2 & 0 & 2 \end{pmatrix}^2, \end{aligned} \tag{8.66}$$

$$\begin{aligned} F^{(-)}_{\ell\ell_2}[C_{\ell_1}^{\phi\phi}, C_{\ell_1'}^{\alpha\alpha}] = \sum_{\ell_1} M_{\ell_1,\ell_2} \Bigg[&\frac{1}{8}\left(N_{\ell,\ell_1,\ell_2}\right)^2 \left[1 - (-1)^{\ell+\ell_1+\ell_2}\right]^2 C_{\ell_1}^{\phi\phi} \\ &+ \left[1 + (-1)^{\ell+\ell_1+\ell_2}\right]^2 C_{\ell_1}^{\alpha\alpha}\Bigg] \begin{pmatrix} \ell & \ell_1 & \ell_2 \\ -2 & 0 & 2 \end{pmatrix}^2, \end{aligned} \tag{8.67}$$

$$R[C_{\ell_1}^{\phi\phi}, C_{\ell_1}^{\alpha\alpha}] = -\sum_{\ell_1}\left(\frac{2\ell_1+1}{\pi}\right)\left[\frac{1}{8}\ell_1(\ell_1+1)\left[\ell(\ell+1) - 4\right] C_{\ell_1}^{\phi\phi} + C_{\ell_1}^{\alpha\alpha}\right], \tag{8.68}$$

$$F^{EB}_{\ell\ell_2}[C_{\ell_1}^{\alpha\phi}] = -\sum_{\ell_1}\frac{(-1)^{\ell+\ell_1+\ell_2}}{2}\left(N_{\ell,\ell_1,\ell_2}\right) M_{\ell_1,\ell_2} \begin{pmatrix} \ell & \ell_1 & \ell_2 \\ -2 & 0 & 2 \end{pmatrix}^2 C_{\ell_1}^{\alpha\phi}, \tag{8.69}$$

$$R^{EB}[C_{\ell_1}^{\alpha\phi}] = -\sum_{\ell_1}\left(\frac{2\ell_1+1}{2\pi}\right)\ell_1(\ell_1+1)\left[1 + \underline{(-1)}\right] C_{\ell_1}^{\alpha\phi}, \tag{8.70}$$

where

$$N_{\ell,\ell_1,\ell_2} = \left[\ell_1(\ell_1+1) + \ell_2(\ell_2+1) - \ell(\ell+1)\right], \quad \text{and} \quad M_{\ell_1,\ell_2} = \frac{(2\ell_1+1)(2\ell_2+1)}{4\pi}. \tag{8.71}$$

The quantitative computation of the impact of both FR and lensing, simultaneously taken into account, on the polarisation power spectra of the CMB, is left for future work. The interested reader will find in Fig. 9-13 of Tashiro et al. (2008) the B mode angular power spectrum including the FR effect only, for different values of the model parameters (β and μ), and including the disk structure of galaxies.

8.5.2 Reconstructing the FR angle and FC rate fields

The FR and FC effects can be used as probes for cosmology (being able to constrain the cosmological parameters) or for astrophysical properties of clusters of galaxies (such as the electron density profile or the magnetic field model (see Tashiro et al., 2009) but they also produce secondary polarised anisotropies, as shown in the previous section. In particular, the secondary B modes should be precisely known to be taken into account in the reconstruction of the primordial B mode, which is a direct tracer of the primordial gravitational waves produced during inflation. As these effects take place in galaxy clusters, the secondary B mode due to FR and gravitational lensing is expected to peak at smaller angular scales than the primordial B mode, allowing an easier reconstruction of this primordial component. However, these secondary polarised anisotropies can also be used to reconstruct the lensing field, which is a more efficient way than using the temperature anisotropies (Hirata & Seljak, 2003; Okamoto & Hu, 2003; Ade et al., 2014). The presence of FR could bias this reconstruction as the two effects, FR and lensing, produce secondary B modes starting from the primary E mode.

In this section we introduce and adapt the concept of quadratic estimator used to estimate the lensing potential from polarized maps (see Hu & Okamoto, 2002; Okamoto & Hu, 2003) to the FC rate. Then, we see how FR can impact the estimation of lensing by considering the estimator of the FR angle, as already introduced by Gluscevic et al. (2009); Kamionkowski (2009).

The idea of building estimators of cosmological quantities has already been introduced in Section 4.3.3, with the estimator of the angular power spectra of the CMB anisotropies. Such estimators of statistical quantities are needed because one only has access to a single realisation of the temperature, polarisation or even lensing fields. Thus, making an ensemble average over multiple universe realisations is not possible, but statistical isotropy and homogeneity involves an ergodic hypothesis which tells that it is equivalent to averaging over the whole sky.

Here, similarly to what has already been done for the lensing field, we would like to reconstruct the FR angle and FC rate fields or equivalently, their harmonic coeffcients α_{LM} and $\phi^{E/B}_{LM}$. However one does not directly measure these fields but they are observed by their impact on the CMB polarised anisotropies. These last ones can thus be used to reconstruct them. These effects on the primordial CMB anisotropies are characterised statistically by the angular power spectra of secondary anisotropies Eq. (8.65) and Eq. (8.60). Actually, the CMB spherical harmonic coefficients are given to first order by Eq. (8.56) for circular polarisation, and by

$$\widetilde{X}_{\ell m} = X_{\ell m} + \delta_\phi X_{\ell m} + \delta_\alpha X_{\ell m}, \tag{8.72}$$

for the $X = E$ or B mode, with

$$\begin{aligned}
\delta_\phi E_{\ell m} &= \frac{1}{2}\sum_{\ell_1 m_1}\sum_{\ell_2 m_2} \phi_{\ell_1 m_1}\left(E_{\ell_2 m_2 +}\mathcal{I}^{\ell\ell_1\ell_2}_{m m_1 m_2} + iB_{\ell_2 m_2 -}\mathcal{I}^{\ell\ell_1\ell_2}_{m m_1 m_2}\right),\\
\delta_\alpha E_{\ell m} &= -i\sum_{\ell_1 m_1}\sum_{\ell_2 m_2} \alpha_{\ell_1 m_1}\left(E_{\ell_2 m_2 -}\mathcal{K}^{\ell\ell_1\ell_2}_{m m_1 m_2} + iB_{\ell_2 m_2 +}\mathcal{K}^{\ell\ell_1\ell_2}_{m m_1 m_2}\right),\\
\delta_\phi B_{\ell m} &= \frac{1}{2}\sum_{\ell_1 m_1}\sum_{\ell_2 m_2} \phi_{\ell_1 m_1}\left(B_{\ell_2 m_2 +}\mathcal{I}^{\ell\ell_1\ell_2}_{m m_1 m_2} - iE_{\ell_2 m_2 -}\mathcal{I}^{\ell\ell_1\ell_2}_{m m_1 m_2}\right),\\
\delta_\alpha B_{\ell m} &= -i\sum_{\ell_1 m_1}\sum_{\ell_2 m_2} \alpha_{\ell_1 m_1}\left(B_{\ell_2 m_2 -}\mathcal{K}^{\ell\ell_1\ell_2}_{m m_1 m_2} - iE_{\ell_2 m_2 +}\mathcal{K}^{\ell\ell_1\ell_2}_{m m_1 m_2}\right),
\end{aligned} \tag{8.73}$$

where ${}_\pm\mathcal{I}^{\ell\ell_1\ell_2}_{m m_1 m_2}$ and ${}_\pm\mathcal{K}^{\ell\ell_1\ell_2}_{m m_1 m_2}$ are some kernels, whose precise form is not important here, but one notes that they are coupling induced by ϕ and α: ${}_\pm\mathcal{I}^{\ell\ell_1\ell_2}_{m m_1 m_2}$ only depends on ϕ and

${}_{\pm}\mathcal{K}^{\ell\ell_1\ell_2}_{mm_1m_2}$ only on α. Both harmonic coefficients show a coupling between different primordial CMB multipoles ℓ and it is this coupling between different angular scales that is used to build the estimators of the FR angle and FC rate fields. One could thus think of inverting Eq. (8.65) and Eq. (8.60) to get the angular power spectrum of the fields as a function of the power spectra of secondary CMB anisotropies, but one rather wants to reconstruct the harmonic coefficients of the fields themselves.

The case of FR angle has already been treated in Gluscevic et al. (2009); Kamionkowski (2009) and we will mention it briefly at the end of this section; hence, let us now illustrate how it is done for the case of the FC rate field $\phi^{E/B}$. Because one wants to reconstruct the harmonic coefficients rather than the angular power spectrum of the effect, when computing the covariance matrices of secondary harmonic coefficients, instead of taking a full average over universe realisations, one 'theoretically' averages over the CMB realisations only, as if the FC rate field was fixed and given. This allows to make appear the correlations between the different primordial CMB multipoles. One can show that it leads to the correlators

$$\langle \widetilde{a}_{\ell m}\widetilde{V}_{\ell' m'}\rangle|_{\rm FC} = \sum_{LM}(-1)^M \begin{pmatrix} \ell & \ell' & L \\ m & m' & -M \end{pmatrix} \left(f^{aV,\phi^E}_{\ell L\ell'}\phi^E_{LM} + f^{aV,\phi^B}_{\ell L\ell'}\phi^B_{LM}\right), \tag{8.74}$$

and we insist on the fact that $(\ell, m) \neq (\ell', m')$ as we correlate different multipoles, a can be the temperature field T or the E or B mode. At first order, one actually correlates a primary $a_{\ell m}$ with a 'deformed' $\widetilde{V}_{\ell' m'}$, as V is already a first order quantity. The covariance matrices are now non-vanishing when one does not average over the FC rate field realisations; on the contrary, when taking the full average over CMB and FC rate field realisations, one can show that

$$\widetilde{C}^{aV}_{\ell} = 0. \tag{8.75}$$

Furthermore, the covariance matrices now get off-diagonal terms with $f^{aV,\phi^{E/B}}_{\ell L\ell'}$ weights for the different quadratic pairs aV that are known forms of the 'Faraday unconversed' angular power spectra of the E and B modes

$$\begin{aligned} f^{EV,\phi^E}_{\ell L\ell'} &= iK^-_{\ell L\ell'}C^{EE}_\ell, \quad f^{EV,\phi^B}_{\ell L\ell'} = K^+_{\ell L\ell'}C^{EE}_\ell, \\ f^{BV,\phi^E}_{\ell L\ell'} &= -K^+_{\ell L\ell'}C^{BB}_\ell, \quad f^{BV,\phi^B}_{\ell L\ell'} = iK^-_{\ell L\ell'}C^{BB}_\ell, \\ f^{TV,\phi^E}_{\ell L\ell'} &= iK^-_{\ell L\ell'}C^{TE}_\ell, \quad f^{TV,\phi^B}_{\ell L\ell'} = K^+_{\ell L\ell'}C^{TE}_\ell, \end{aligned} \tag{8.76}$$

with

$$K^{\pm}_{\ell L\ell'} = \sqrt{\frac{(2\ell+1)(2L+1)(2\ell'+1)}{4\pi}} \begin{pmatrix} \ell & L & \ell' \\ -2 & 2 & 0 \end{pmatrix} \left(1 \pm (-1)^{\ell+L+\ell'}\right). \tag{8.77}$$

Note that in Eq. (8.76) do not appear C^{TB}_ℓ or C^{EB}_ℓ as the CMB is assumed to be parity invariant in the standard model of cosmology. If one averages again over a statistical ensemble of FC rate fields, one recovers the vanishing angular power spectra $\widetilde{C}^{aV}_\ell = 0$. Indeed, the off-diagonal terms of the covariance matrices vanish as the FC rate field is assumed to be statistically isotropic so that it has zero mean $\langle \phi^{E/B}_{LM}\rangle = 0$. We however have access to only one realisation of the FC rate field, and we can build two estimators for it (one for ϕ^E and one for ϕ^B) as a weighted average over covariance matrix coefficients as suggested by Eq. (8.74) (Okamoto & Hu, 2003)

$$\widehat{\phi}^{E/B,aV}_{LM} = (2L+1)\sum_{\ell_1 m_1}\sum_{\ell_2 m_2}(-1)^M \begin{pmatrix} \ell_1 & \ell_2 & L \\ m_1 & m_2 & -M \end{pmatrix} g^{aV,\phi^{E/B}}_{\ell_1\ell_2}\widetilde{a}_{\ell_1 m_1}\widetilde{V}_{\ell_2 m_2}, \tag{8.78}$$

with $g^{aV,\phi^{E/B}}_{\ell_1\ell_2}(L)$ some weights that are derived requiring that the estimator is unbiased $\langle\widehat{\phi}^{E/B,aV}_{LM}\rangle|_{\rm FC} = \phi^{E/B}_{LM}$, where we have averaged over primary CMB and noise realisations only, keeping the FC field fixed. This leads to the constraint

$$\sum_{\ell_1\ell_2} g^{aV,\phi^{E/B}}_{\ell_1\ell_2}(L) f^{aV,\phi^{E/B}}_{\ell_1 L\ell_2} = 1. \tag{8.79}$$

Notice that only the aV estimators can be used to reconstruct the FC field, with $a = T$, E or B, as only circular polarisation is impacted by the FC effect at lowest order. The weighted sum Eq. (8.78) is similar to the sum in Eq. (4.63) in the sense that we only have one realisation of the CMB or of the FC rate field, so we estimate them by summing the spherical harmonic coefficients over the multipoles to reconstruct them. Then, the optimal weights are obtained by minimising the Gaussian variance of the estimator $\langle\widehat{\phi}^{E/B,aV}_{LM}\widehat{\phi}^{E/B,aV*}_{LM}\rangle - \langle\widehat{\phi}^{E/B,aV}_{LM}\rangle\langle\widehat{\phi}^{E/B,aV*}_{LM}\rangle = \langle\widehat{\phi}^{E/B,aV}_{LM}\widehat{\phi}^{E/B,aV*}_{LM}\rangle$ with respect to them, where now the ensemble average is made over CMB, noise and FC rate field realisations, so that $\langle\widehat{\phi}^{E/B,aV}_{LM}\rangle = 0$. The two sets of weights for ϕ^E and ϕ^B are finally given by

$$g^{aV,\phi^{E/B}}_{\ell_1\ell_2} = \frac{1}{\displaystyle\sum_{\ell_1'\ell_2'} \frac{\left(f^{aV,\phi^{E/B}}_{L\ell_1'\ell_2'}\right)^2}{\widetilde{C}^{aa}_{\ell_1'\ell_2'}\widetilde{C}^{VV}_{\ell_1'\ell_2'}}} \frac{f^{aV,\phi^{E/B}}_{L\ell_1\ell_2}}{\widetilde{C}^{aa}_{\ell_1\ell_2}\widetilde{C}^{VV}_{\ell_1\ell_2}}. \tag{8.80}$$

The quadratic estimators for the lensing ϕ and the FR angle α fields have already been computed separately in Okamoto & Hu (2003) and Gluscevic et al. (2009) respectively. These estimators are built by taking into account only the effect on lensing (or FR) and noise on the primary E and B modes and not FR (respectively lensing), i.e. $\widetilde{E}$ and $\widetilde{B}$ correspond to secondary anisotropies in polarisation due to lensing (FR) and noise but not FR (lensing). Thus, we can evaluate the impact of Faraday Rotation on lensing by recomputing the covariance matrix $\langle\widetilde{a}_{\ell m}\widetilde{b}_{\ell' m'}\rangle|_{\rm lens}$ (where $a, b = T$, E or B), taking into account the FR effect in the $\widetilde{a}_{\ell m}$, which will add the angular power spectrum of polarised anisotropies due to FR to the expression. The bias induced by FR on the estimated lensing potential is characterised by an estimator

$$\Delta\widehat{\phi}^{ab}_{LM} = \widehat{\phi}^{ab}_{LM} - \phi_{LM}, \tag{8.81}$$

which is in full generality biased $\langle\Delta\widehat{\phi}^{ab}_{LM}\rangle|_{\rm lens} \neq 0$. However, computing it explicitly, with the weights given in Okamoto & Hu (2003) and the full expressions of the angular power spectra at linear order in ϕ and α Eq. (8.65), one can show that it gives vanishing estimators, assuming the primary CMB anisotropies to be parity-invariant as is the case in the standard model of cosmology: $C^{TB}_\ell = C^{EB}_\ell = 0$. This is due to parity reasons: indeed, ${}_+\mathcal{I}^{\ell\ell_1\ell_2}_{mm_1m_2}$, ${}_+\mathcal{K}^{\ell\ell_1\ell_2}_{mm_1m_2}$ and ϕ are even while ${}_-\mathcal{I}^{\ell\ell_1\ell_2}_{mm_1m_2}$, ${}_-\mathcal{K}^{\ell\ell_1\ell_2}_{mm_1m_2}$ and α are odd, and the CMB is parity invariant. The estimators are thus unbiased by FR. Similarly, one can build an estimator for the Faraday Rotation angle α, as is done in Gluscevic et al. (2009); Kamionkowski (2009)

$$\widehat{\alpha}^{ab}_{LM} = (2L+1)\sum_{\ell_1 m_1}\sum_{\ell_2 m_2}(-1)^M \begin{pmatrix} \ell_1 & \ell_2 & L \\ m_1 & m_2 & -M \end{pmatrix} g^{ab,\alpha}_{\ell_1\ell_2}\widetilde{a}_{\ell_1 m_1}\widetilde{b}_{\ell_2 m_2}, \tag{8.82}$$

whose weights $g^{ab,\alpha}_{\ell_1\ell_2}$ are constrained by requiring that $\widehat{\alpha}^{ab}_{LM}$ is unbiased by the lensing potential (which is the case for the symmetry reasons explained above). Unlike for the lensing potential,

there is no TT estimator for the Faraday Rotation angle as FR does not impact the primary temperature anisotropies of the CMB.

Although the expected level of circular polarisation generated by FC is lower than the secondary linear polarisation generated by FR (first estimations give six orders of magnitude difference), it is always higher than the primary component which vanishes. Therefore, in the case of highly sensitive experiments, one could potentially use the anisotropies in circular polarisation to reconstruct the FC field, which in turn can be used to put constraints on cosmological parameters or models of the spatial profile of free electrons and magnetic field models. This is similar to what is done for lensing, where the lensed BB correlation is used to reconstruct the lensing field, as the primary BB correlation is expected to be very small as it is still undetected, with current upper limit on the tensor-to-scalar ratio $r = 0.12$ (see Ade et al., 2015).

Chapter 9

Article

A&A 630, A149 (2019)
https://doi.org/10.1051/0004-6361/201834485

Astronomy & Astrophysics

Secondary CMB anisotropies from magnetized haloes

I. Power spectra of the Faraday rotation angle and conversion rate

N. Lemarchand[1], J. Grain[1], G. Hurier[2], F. Lacasa[3], and A. Ferté[4]

[1] Institut d'Astrophysique Spatiale, UMR8617, CNRS, Univ. Paris-Sud, Univ. Paris-Saclay, Bâtiment 121, 91405 Orsay, France
e-mail: nadege.lemarchand@ias.u-psud.fr
[2] Centro de Estudios de Física del Cosmos de Aragón (CEFCA), Plaza de San Juan, 1, Planta 2, 44001 Teruel, Spain
[3] Département de Physique Théorique and Center for Astroparticle Physics, Université de Genève, 24 quai Ernest Ansermet, 1211 Geneva, Switzerland
[4] Jet Propulsion Laboratory, California Institute of Technology, 4800 Oak Grove Drive, Pasadena, CA, USA

Received 22 October 2018 / Accepted 14 May 2019

ABSTRACT

Magnetized plasmas within haloes of galaxies leave their footprint on the polarized anisotropies of the cosmic microwave background. The two dominant effects of astrophysical haloes are Faraday rotation, which generates rotation of the plane of linear polarization, and Faraday conversion, which induces a leakage from linear polarization to circular polarization. We revisit these sources of secondary anisotropies by computing the angular power spectra of the Faraday rotation angle and the Faraday conversion rate by the large-scale structures. To this end, we use the halo model and we pay special attention to the impact of magnetic field projections. Assuming magnetic fields of haloes to be uncorrelated, we found a vanishing two-halo term, and angular power spectra peaking at multipoles $\ell \sim 10^4$. The Faraday rotation angle is dominated by the contribution of thermal electrons. For the Faraday conversion rate, we found that both thermal electrons and relativistic, non-thermal electrons contribute equally in the most optimistic case for the density and Lorentz factor of relativistic electrons, while in more pessimistic cases the thermal electrons give the dominant contribution. Assuming the magnetic field to be independent of the halo mass, the angular power spectra for both effects roughly scale with the amplitude of matter perturbations as $\sim\sigma_8^3$, and with a very mild dependence with the density of cold dark matter. Introducing a dependence of the magnetic field strength with the halo mass leads to an increase of the scaling at large angular scales (above a degree) with the amplitude of matter fluctuations up to $\sim\sigma_8^{9.5}$ for Faraday rotation and $\sim\sigma_8^{15}$ for Faraday conversion for a magnetic field strength scaling linearly with the halo mass. Introducing higher values of the magnetic field for galaxies, as compared to clusters, instead leads to a decrease of such a scaling at arcminute scales down to $\sim\sigma_8^{0.9}$ for Faraday rotation.

Key words. cosmic background radiation – large-scale structure of Universe – cosmology: theory

1. Introduction

One of the main challenges in observational cosmology is a complete characterization of cosmic microwave background (CMB) polarization anisotropies, targeted by a large number of ongoing, being deployed, or planned experiments either from ground or space-borne missions (see e.g. Simons Observatory Collaboration 2019; Suzuki et al. 2018). In full generality, polarized light (in addition to its total intensity, I) is described by its linear component encoded in the two Stokes parameters Q and U, and its circular component encoded in the parameter V. For CMB anisotropies, there is no source of primordial V in the standard cosmological scenario (however, see e.g. Giovannini 2010, for potential primordial sources) with upper bounds on its rms of $\sim 1\,\mu$K at ten degrees (Mainini et al. 2013; Nagy et al. 2017). Hence, the CMB polarization field is completely described on the sphere by two Stokes parameters, Q and U. In the harmonic domain, this field can be described either by using spin-(2) and spin-(−2) multipolar coefficients or using gradient, E, and curl, B, coefficients. From a physical point of view, the gradient/curl decomposition is more natural as it is directly linked to the cosmological perturbations produced in the primordial Universe. For symmetry reasons, at first order, scalar perturbations can produce E-modes only and the B-modes part of the polarization field is thus a direct tracer of the primordial gravity waves (Zaldarriaga & Seljak 1997; Kamionkowski et al. 1997). Although such a picture is partially spoilt by the presence of a secondary contribution generated by the gravitational lensing of the E-modes polarization (Zaldarriaga & Seljak 1998), its peculiar angular-scale shape and delensing techniques should allow for a reconstruction of the primordial component.

Lensing of the CMB anisotropies is however not the sole source of cosmological and astrophysical E–B conversion. During the propagation of CMB photons from the last scattering surface to our detectors, the plane of linear polarization could be rotated. Such a rotation could be due to Faraday rotation induced by interactions of CMB photons with background magnetized plasmas, with magnetic fields of either cosmological (Kosowsky & Loeb 1996; Kosowsky et al. 2005; Campanelli et al. 2004; Scoccola et al. 2004) or astrophysical origins (Takada et al. 2001; Ohno et al. 2003; Tashiro et al. 2008, 2009), or interactions with pseudo-scalar fields (Carroll 1998). Furthermore, even though primordial circular polarization is not present in the CMB in the standard model of cosmology, secondary circular polarization could be produced by Faraday conversion (Cooray et al. 2003; De & Tashiro 2015) or for example by nonlinear electrodynamics (Sawyer 2015; Ejlli 2018, 2017) (see also Montero-Camacho & Hirata 2018, for other sources).

With the significant increase of sensitivity of the forthcoming observatories aimed at an accurate mapping of the CMB polarization on wide ranges of angular scales, clear predictions for such additional secondary anisotropies are of importance for many reasons. First, these secondary anisotropies contain some cosmological and/or astrophysical informations and could thus be used to probe, for example parity violation in the Universe (Li & Zhang 2008; Lue et al. 1999; Pospelov et al. 2009; Yadav 2009), intra-halo magnetic fields, or gas evolution at early epochs (Takada et al. 2001; Ohno et al. 2003; Tashiro et al. 2008, 2009). Second, such a signal should be known to be correctly taken into account in identifying the primordial component of the B-mode from such secondary anisotropies or at least shown to be subdominant at super-degree scales at which the primordial B-mode is expected to peak above the lensing B-mode. Thirdly, these secondary anisotropies are of importance for lensing reconstruction using CMB polarized data, which has been shown to be more powerful than starting from temperature data in the case of highly sensitive experiments (Okamoto & Hu 2003; Hirata & Seljak 2003; Ade et al. 2014). Secondary polarized anisotropies in addition to lensing-induced anisotropies could indeed mimic contributions from the lensing potential, thus biasing its reconstruction from E- and B-modes. This last point is also of relevance for the delensing, either internal (Seljak & Hirata 2004; Carron et al. 2017) or based on external tracers of the lensing potential such as the cosmic infrared background (Sigurdson & Cooray 2005; Marian & Bernstein 2007; Smith et al. 2012; Sherwin & Schmittfull 2015).

For any possible non-primordial sources of CMB anisotropies, we first have to quantitatively predict the induced CMB anisotropies. Second, we can further investigate the amount of cosmological/astrophysical information they carry, and finally we can estimate how they may bias the reconstruction of the primordial B-mode and the lensing potential reconstruction. In this article we are interested in magnetized plasmas in haloes of galaxies as a source of secondary polarized anisotropies of the CMB, revisiting and amending first estimates in Tashiro et al. (2008) and Cooray et al. (2003). Observations with, for example Faraday rotation measurements from polarized point sources, suggest that they are magnetized with a coherence length of the size of the halo scale and a typical strength ranging from 1 to 10 μG (Kim et al. 1989; Athreya et al. 1998; Bonafede et al. 2010, 2009). This implies that the CMB linear polarization field is rotated – an effect known as Faraday rotation – and converted to circular polarization – referred to as Faraday conversion. The goal of the present paper is to give an accurate computation of the angular power spectra of the Faraday rotation angle and Faraday conversion rate, which is the first mandatory step before estimating its impact on CMB secondary anisotropies.

This article is organized as follows. We first briefly describe in Sect. 2 the propagation of CMB photons through a magnetized plasma. We show that for the specific case of haloes, the two dominant effects are Faraday rotation and Faraday conversion. This section is also devoted to a brief presentation of the physics and statistics of haloes. Second in Sect. 3, we present our calculation of the angular power spectra of the Faraday rotation angle and Faraday conversion rate. This is done using the halo model, and we amend previous analytical calculations giving special attention to the statistics of the projected magnetic fields of haloes. Our numerical results are provided in Sect. 4 in which we discuss the dependence of the angular power spectra with cosmological parameters. We finally conclude in Sect. 5. Throughout this article, we use the Planck Collaboration Int. XLVI (2016, PlanckTTTEEE+SIMlow) best-fit parameters, namely $\sigma_8 = 0.8174$, $\Omega_{\rm CDM}h^2 = 0.1205$, $\Omega_b h^2 = 0.02225$, and $h = 0.6693$.

2. Physics of haloes

2.1. Radiative transfer in a magnetized plasma

Propagation of radio and millimeter waves in a magnetized plasma has been studied in Sazonov (1969), and later reassessed in Kennett & Melrose (1998), Melrose (2005), Heyvaerts et al. (2013), and Shcherbakov (2008). Generalization to the case of an expanding Universe is done in Ejlli (2018, 2019). In Eq. (1.5) of Sazonov (1969), the radiative transfer equation for the four Stokes parameters, (I, Q, U, V), is provided in a specific reference frame in which one of the basis vectors in the plane orthogonal to the direction of light propagation is given by the magnetic field projected in that plane. The Stokes parameters (Q, U, V) are however reference-frame dependent, and it is thus important to get this equation in an arbitrary reference frame, for at least two reasons. First, we are interested in the Stokes parameter of the CMB light and there is a priori no reason for the reference frame chosen to measure the Stokes parameter to be specifically aligned with the magnetic fields of the many haloes CMB photons pass through. We usually make use of $(\boldsymbol{e}_\theta, \boldsymbol{e}_\varphi, \boldsymbol{n})$ with $\boldsymbol{n}$ pointing along the line of sight and $\boldsymbol{e}_\theta$, $\boldsymbol{e}_\phi$ the unit vectors orthogonal to $\boldsymbol{n}$ associated to spherical coordinates, and there is no reason for $\boldsymbol{e}_\theta$ to be aligned with the projection of the many magnetic fields. Second, we are interested in computing the two-point correlation function and there is obviously no reason for the chosen reference frame to coincide at two arbitrary selected directions on the celestial sphere with the specific reference frame used in Sazonov (1969), which clearly differs from direction to direction on the celestial sphere.

The radiative transfer equation is written in an arbitrary reference frame by performing an arbitrary rotation of the basis vectors in the plane orthogonal to the light propagation, or equivalently an arbitrary rotation of the magnetic field projected in such a plane (Huang et al. 2009; Ejlli 2019). We denote by θ_B the angle between the magnetic field projected on the plane orthogonal to the line of sight and the basis vector $\boldsymbol{e}_\theta$. By further introducing the spin-($\pm$2) field for linear polarization, $P_{\pm 2} = Q \pm iU$, this gives

$$\frac{\mathrm{d}}{\mathrm{d}r}\begin{pmatrix} I \\ P_2 \\ P_{-2} \\ V \end{pmatrix} = \left[\mathbf{M}_{\rm abs} + \mathbf{M}_{I\to P} + \mathbf{M}_{P\to P}\right]\begin{pmatrix} I \\ P_2 \\ P_{-2} \\ V \end{pmatrix}, \tag{1}$$

where r is labelled as the path of light. The three matrices encoding the different contributions to radiative transfer are

$$\mathbf{M}_{\rm abs} = \begin{pmatrix} \dot\tau & 0 & 0 & 0 \\ 0 & \dot\tau & 0 & 0 \\ 0 & 0 & \dot\tau & 0 \\ 0 & 0 & 0 & \dot\tau \end{pmatrix}, \tag{2}$$

$$\mathbf{M}_{I\to P} = \begin{pmatrix} 0 & \dot\phi^{I\to P} e^{-2i\theta_B} & \dot\phi^{I\to P} e^{2i\theta_B} & \dot\phi^{I\to V} \\ \dot\phi^{I\to P} e^{2i\theta_B} & 0 & 0 & 0 \\ \dot\phi^{I\to P} e^{-2i\theta_B} & 0 & 0 & 0 \\ \dot\phi^{I\to V} & 0 & 0 & 0 \end{pmatrix}, \tag{3}$$

$$\mathbf{M}_{P\to P} = \begin{pmatrix} 0 & 0 & 0 & 0 \\ 0 & 0 & -2i\dot\alpha & -i\dot\phi^{P\to V} e^{2i\theta_B} \\ 0 & 2i\dot\alpha & 0 & i\dot\phi^{P\to V} e^{-2i\theta_B} \\ 0 & i\dot\phi^{P\to V} e^{-2i\theta_B} & -i\dot\phi^{P\to V} e^{2i\theta_B} & 0 \end{pmatrix}, \tag{4}$$

where $\dot f$ means differentiation with respect to r.

Table 1. Scaling of the radiative transfer coefficients for thermal electrons and relativistic electrons with the projection of the magnetic fields along or orthogonal to the line of sight, the frequency of photons, and the density and temperature of free electrons (adapted from Sazonov 1969).

	$\dot{\tau}$	$\dot{\phi}^{I\to P}$	$\dot{\phi}^{I\to V}$	$\dot{\alpha}$	$\dot{\phi}^{P\to V}$
Thermal electrons	$n_{\rm e}^2/(\nu^2 T_{\rm e}^{3/2})$	$10^{13}(n_{\rm e}B_\perp)^2/(\nu^4 T_{\rm e}^{3/2})$	$10^{6}(n_{\rm e}^2 B_\parallel)/(\nu^3 T_{\rm e}^{3/2})$	$10^{5}(n_{\rm e}B_\parallel)/(\nu^2)$	$10^{11}(n_{\rm e}B_\perp^2)/(\nu^3)$
	$\sim 10^{-36}$ m^{-1}	$\sim 10^{-55}$ m^{-1}	$\sim 10^{-46}$ m^{-1}	$\sim 10^{-23}$ m^{-1}	$\sim 10^{-33}$ m^{-1}
Relativistic electrons	$n_{\rm e}^{(r)}B_\perp^2/\nu^3$	$n_{\rm e}^{(r)}B_\perp^2/\nu^3$	$n_{\rm e}^{(r)}B_n^{5/2}/\nu^{7/2}$	$n_{\rm e}^{(r)}B_\parallel/\nu^2$	$n_{\rm e}^{(r)}B_\perp^2/\nu^3$
	$\sim 10^{-32}$ m^{-1}	$\sim 10^{-32}$ m^{-1}	$\sim 10^{-36}$ m^{-1}	$\sim 10^{-30}$ m^{-1}	$\sim 10^{-31}$ m^{-1}

Notes. For thermal electrons, the numerical constants in front of the reported scalings span a large range of values and we provide their value relative to that for the parameter $\dot{\tau}$. These constants are all of the same order in the case of relativistic electrons. The corresponding values are obtained for the case of haloes with $n_{\rm e} = 10^{-5}\,{\rm cm}^{-3}$, $T_{\rm e} = 10^7$ K for thermal electrons, and $n_{\rm e}^{(r)} = 10^{-5}\,{\rm cm}^{-3}$ for relativistic electrons. In both cases, the magnetic field is set to $B = 3\,\mu$G and the frequency to $\nu = 30$ GHz.

The different coefficients, $\dot{\tau}$, $\dot{\alpha}$, and $\dot{\phi}^{i\to j}$ are real and their expressions can be found in, for example Sazonov (1969), by setting $\theta_B = 0$, which basically corresponds to choosing the specific reference frame adopted in Sazonov (1969). These coefficients are interpreted as follows. First, the coefficient $\dot{\tau}$ in $\mathbf{M}_{\rm abs}$ simply corresponds to absorption of light by the medium. Second in $\mathbf{M}_{I\to P}$, the coefficients $\dot{\phi}^{I\to P}$ and $\dot{\phi}^{I\to V}$ amount to the transfer from total intensity to linear polarization and circular polarization, respectively. Finally in $\mathbf{M}_{P\to P}$, the coefficient $\dot{\alpha}$ corresponds to Faraday rotation which mixes the two modes of linear polarization, while $\dot{\phi}^{P\to V}$ is Faraday conversion which transfers linear polarization in circular polarization.

In an expanding universe, there is an additional contribution because of the dilution, captured by an additional matrix in the right-hand side of Eq. (1), i.e. $\mathbf{M}_{\rm Hubble} = -3H\mathbf{I}_4$ with $\mathbf{I}_4$ the identity matrix (Ejlli 2019). We note that $\mathbf{S}$ is the vector of the 4 Stokes parameters; the solution accounting for the sole impact of dilution by the expansion (i.e. setting all the radiative transfer coefficients to zero) is $\mathbf{S}(t) = [a_i/a(t)]^3\mathbf{I}_4\mathbf{S}_i$. Using an interaction-picture-like approach, the differential equation for $\widetilde{\mathbf{S}}(t) \equiv [a(t)/a_i]^3\mathbf{I}_4\mathbf{S}(t)$ is given by Eq. (1), where all the dilution is accounted for in the Stokes parameters $\widetilde{\mathbf{S}}$ (Ejlli 2019)[1].

The expressions of the different coefficients and their relative amplitude depend on the nature of free electrons in the magnetized plasma. Two extreme situations are either normal waves of the plasma are circularly polarized or these normal waves are linearly polarized. In the former case, Faraday rotation is dominant, which is the case for a plasma made of non-relativistic electrons[2]. In the latter, Faraday conversion is dominant. This can occur for a population of relativistic and non-thermal electrons; there are some restrictions on their energy distributions (see Sazonov 1969).

For the case of astrophysical clusters and haloes as considered as magnetized plasmas, two populations of electrons are at play. First, the thermal electrons which are for example at the origin of the thermal Sunyaev–Zel'dovich (tSZ) effect, and second, relativistic electrons generated by either active galactic nuclei or shocks. For the case of thermal electrons, the typical temperature of clusters is $\sim 10^7$ K, corresponding to about few kiloelectron volts, hence much smaller than the electron mass. This population of electrons is thus mainly non-relativistic. A typical value of the number density of thermal electrons for clusters is $n_{\rm e} \sim 10^3$ m^{-3} for a halo mass of $10^{14}\,M_\odot$. For the case of relativistic electrons, the coefficients depend on the energy distribution of the relativistic electrons in the injected plasma via the minimal Lorentz factor, $\Gamma_{\rm min}$, the spectral index of the energy distribution, i.e. $n_{\rm e}^{(r)}(\Gamma) \propto \Gamma^{-\beta_E}$, and the spatial distribution of the energy distribution of the injected relativistic electrons in the plasma. In this work we follow Cooray et al. (2003) and De & Tashiro (2015) by considering a spectral index of the energy distribution of relativistic electrons of 2, a minimal value of the Lorentz factor of $\Gamma_{\rm min} = 300$, and an isotropic spatial distribution. The number density of relativistic electrons is largely unknown and we consider the maximum value we found in the literature, $n_{\rm e}^{(r)} = 10$ m^{-3} (Colafrancesco et al. 2003).

The expressions of these radiative transfer coefficients from Sazonov (1969) are provided in Table 1 up to numerical constants. We highlight their scaling with the electron number density ($n_{\rm e}$ and $n_{\rm e}^{(r)}$), the magnetic field either projected on the line of sight, $B_\parallel$, or in the plane perpendicular to it, $B_\perp$, the frequency of the radiation light, ν, and, for the case of thermal electrons the temperature of electrons, $T_{\rm e}$. For thermal electrons, the numerical constants in front of the reported scalings span a large range of values and we provide their value relative to that for the parameter $\dot{\tau}$. These constants are all of the same order in the case of relativistic electrons. The values reported are for a magnetic field of $3\,\mu$G and a frequency of 30 GHz.

For linear polarization, the dominant effect is Faraday rotation by thermal electrons. Faraday rotation from relativistic electrons is 7 orders of magnitude smaller, and absorption, $\dot{\tau}$, is 13 (thermal electrons) and 9 (relativistic electrons) orders of magnitude smaller than Faraday rotation. Faraday conversion from V to $P_{\pm 2}$ is zero for CMB since there is no primordial circular polarization. Intensity of the CMB is about 1–2 orders of magnitude higher than the E-mode of linear polarization, and at least 3 orders of magnitude higher than the B-mode. Leakages of I to $P_{\pm 2}$ could thus rapidly become important because of this great hierarchy. However, the transfer coefficient $\dot{\phi}^{I\to P}$ for thermal electrons and relativistic electrons is 32 and 9 (resp.) orders of magnitude smaller than $\dot{\alpha}$. Hence leakages from intensity to linear polarization is totally negligible as compared to Faraday rotation by thermal electrons.

The dominant effect for circular polarization is Faraday conversion from both thermal electrons and relativistic electrons. Absorption is vanishing for zero initial V. Leakages from intensity to circular polarization remains smaller than Faraday conversion. In the most optimistic case for the number density of relativistic electrons $\dot{\phi}^{I\to V}$ indeed remains 5 orders of magnitude smaller than $\dot{\phi}^{P\to V}$, meaning that circular polarization generated through leakages of intensity is about 3 orders of magnitude smaller than that generated through Faraday conversion[3].

[1] We note that this could also be done for the impact of the absorption coefficients since $\mathbf{M}_{\rm abs} = \dot{\tau}\mathbf{I}_4$.

[2] This population is dubbed "cold plasma" in Sazonov (1969).

[3] We note that in this case Faraday conversion and Faraday rotation by relativistic electrons are of equal magnitude. Faraday rotation by this population remains however much smaller than that due to thermal electrons.

An important last comment is in order at this point. The terms $e^{\pm 2i\theta_B}$ naturally appear for preserving the symmetry properties of the four Stokes parameters.

We note that these parameters are defined in the plane $(\boldsymbol{e}_\theta, \boldsymbol{e}_\varphi)$ orthogonal to the line of sight and in a manner that is reference-frame dependent. The total intensity I is independent of rotation and parity transformations of the reference frame (i.e. it is a scalar). Linear polarization, $P_{\pm 2}$, are spin-± 2 fields meaning that they rotate by an angle $(\pm 2\theta)$ by a rotation θ of the reference frame, and spin-$(+2)$ and spin-(-2) are interchanged by a parity transformation. Finally, circular polarization V is unchanged through rotations but changes its sign via a parity transformation of the reference frame (i.e. it is pseudo-scalar).

The coefficients $\dot{\alpha}$ and $\dot{\phi}^{P\to V}$ are independent of the reference frame. The angle θ_B however is reference-frame dependent and the quantities $e^{\pm 2i\theta_B}$ are spin-(± 2) fields. We can then check that indeed all the symmetry properties are properly preserved through radiative transfer. For example, we obtain

$$\dot{V}(\boldsymbol{n}) = i\dot{\phi}^{P\to V}(\boldsymbol{n})\left[e^{-2i\theta_B(\boldsymbol{n})}P_2(\boldsymbol{n}) - e^{2i\theta_B(\boldsymbol{n})}P_{-2}(\boldsymbol{n})\right], \tag{5}$$

where the right-hand side is an appropriate combination of different spin-(± 2) fields leading to a pseudo-scalar field, V. We note that this is in agreement with expressions used in Huang et al. (2009), Ejlli (2018, 2019), Montero-Camacho & Hirata (2018), and Kamionkowski (2018), written as $\dot{V}(\boldsymbol{n}) = \phi_U(\boldsymbol{n})Q(\boldsymbol{n}) - \phi_Q(\boldsymbol{n})U(\boldsymbol{n})$ with $\phi_Q = 2\dot{\phi}^{P\to V}\cos(2\theta_B)$ and $\phi_U = 2\dot{\phi}^{P\to V}\sin(2\theta_B)$.

It is also easily checked that by selecting the specific reference frame adopted in Sazonov (1969), i.e. setting $\theta_B = 0$, the Eq. (1.5) of Sazonov (1969) is recovered. In particular in this reference frame we see that I is transferred into Q only, while V receives contribution from U only, i.e. $\dot{V} = -2\dot{\phi}^{P\to V}U$. We note that this last expression was used in Cooray et al. (2003) and De & Tashiro (2015), which is however valid on a very specific reference frame.

2.2. Impact on CMB polarization

The impact of radiative transfer within magnetized haloes on the CMB is in theory obtained by integrating Eq. (1). Such radiative-transfer distortions of the CMB within haloes are expected to mainly occur at low redshifts, $z \lesssim 1$. We can thus take as initial conditions the lensed CMB fields.

In full generality, the matrix $\left[\mathbf{M}_{\rm abs} + \mathbf{M}_{I\to P} + \mathbf{M}_{P\to P}\right]$ is too complicated to solve the radiative transfer equation given in Eq. (1). Perturbative solutions using Neumann series have been found in Ejlli (2019). The dominant effect in the case considered in this work is the Faraday rotation by thermal electrons. Neglecting the other coefficients, only linear polarization is modified and the solution is

$$\widetilde{P}^{\rm FR}_{\pm 2}(\boldsymbol{n}) = e^{\mp 2i\alpha(0,r_{\rm CMB})}\,\widetilde{P}_{\pm 2}(\boldsymbol{n}), \tag{6}$$

where $P_{\pm 2}$ is the {primary+lensed} CMB linear polarization field, and $\alpha(0, r_{\rm CMB})$ is the integral of $\dot{\alpha}$ over the line of sight from the last scattering surface at $r_{\rm CMB}$, to present time at $r = 0$; we note that the angle is also a function of $\boldsymbol{n}$. Our forthcoming calculations of the Faraday rotation angle integrated over haloes show that a tiny effect remains, and we can Taylor expand the exponential for small α (see also Tashiro et al. 2008).

The next-to-leading order effect is the Faraday conversion whose impact on the CMB can be implemented with a perturbative approach to solve for Eq. (1). Since the initial V parameter is vanishing, this leaves the solution for linear polarization unchanged. Circular polarization generated should in principle be generated by Faraday conversion of the rotated linear polarization, $P^{\rm rot}_{\pm 2}$, integrated over the line of sight, hence mixing the rotation angle and the conversion rate. These effects are however expected to be small. Multiplicative effect of rotation and conversion are thus of higher orders and these can be neglected. A perturbative approach to solve Eq. (1) keeping $\dot{\alpha}$ at the leading order and $\dot{\phi}^{P\to V}$ at the next-to-leading order gives (Ejlli 2018)

$$\widetilde{P}^{\rm FR+FC}_{\pm 2} = e^{\mp 2i\alpha(0,r_{\rm CMB})}\,\widetilde{P}_{\pm 2} \mp i\left[\int_{r_{\rm CMB}}^{0} {\rm d}s\dot{\phi}^{P\to V}(s)e^{\pm 2i\theta_B(s)}e^{\mp 2i\alpha(0,s)}\right]\widetilde{V},$$

and

$$\widetilde{V}^{\rm FR+FC} = \widetilde{V} + i\left[\int_{r_{\rm CMB}}^{0} {\rm d}s\dot{\phi}^{P\to V}(s)e^{-2i\theta_B(s)}e^{-2i\alpha(s,r_{\rm CMB})}\right]\widetilde{P}_2 - i\left[\int_{r_{\rm CMB}}^{0} {\rm d}s\dot{\phi}^{P\to V}(s)e^{2i\theta_B(s)}e^{2i\alpha(s,r_{\rm CMB})}\right]\widetilde{P}_{-2}.$$

The values $P_{\pm 2}$ and V are the {primary+lensed} CMB polarization field. We then set the initial circular polarization to zero, $V = 0$, and keep the leading order in a Taylor expansion of $e^{\pm 2i\alpha(s,r_{\rm CMB})}$. This gives for circular polarization

$$\widetilde{V}(\boldsymbol{n}) = i\left[\phi_{-2}(0, r_{\rm CMB})\widetilde{P}_2(\boldsymbol{n}) - \phi_2(0, r_{\rm CMB})\widetilde{P}_{-2}(\boldsymbol{n})\right], \tag{7}$$

where $\phi_{\pm 2}(0, r_{\rm CMB})$ is the integral over the line of sight of $\dot{\phi}^{P\to V}e^{\pm 2i\theta_B}$. We note that the impact of dilution implicitly contained in $\widetilde{P}_{\pm 2}$ and $\widetilde{V}$ is homogeneous and does not bring additional anisotropies.

2.3. Haloes description

Distortions of the CMB polarized anisotropies by Faraday rotation and Faraday conversion is a multiplicative effect. Their impact on the CMB angular power spectra is thus determined by the angular power spectra of the Faraday rotation angle, α, and the Faraday conversion rate, $\phi_{\pm 2}$.

We make use of the halo model (Cooray & Sheth 2002) to characterize the statistical properties of the radiative transfer coefficients of the haloes as magnetized plasmas. The basic elements in this theoretical framework are first the physics internal to each halo, i.e. its gas and magnetic field distributions, and second the statistical properties of haloes within our Universe. We consider halo masses ranging from 10^{10} to $5\times 10^{16}\,M_\odot$. Such a range covers both clusters of galaxies as described by high-mass haloes (typically masses $M > 10^{13}\,M_\odot$), and galaxies as described by low-mass haloes (typically smaller than $10^{13}\,M_\odot$).

2.3.1. Gas, relativistic electrons, and magnetic field distribution

In the following, we have mainly two characteristics of haloes: their free electron density and magnetic field spatial profiles, which for simplicity are considered as spherically symmetric.

For the profile $n_{\rm e}$ of free electrons we choose to take the β-profile of Cavaliere & Fusco-Femiano (1978) following Tashiro et al. (2008), i.e.

$$n_{\rm e}(r) = n_{\rm e}^{(c)}\left(1 + \frac{r^2}{r_{\rm c}^2}\right)^{-3\beta/2}, \tag{8}$$

where r and $r_{\rm c}$ are the physical distance to the halo centre and typical core radius of the halo, respectively; we note that these

could be comoving distances as only the ratio of these two distances shows up in the expression. The physical halo core radius r_c is related to the virial radius by $r_{vir} \sim 10 r_c$, where $r_{vir} = (M/(4\pi\Delta_c(z)\bar{\rho}(z)/3))^{1/3}$ and $\Delta_c(z) = 18\pi^2\Omega_m(z)^{0.427}$ is the spherical overdensity of the virialized halo, and $\bar{\rho}(z)$ is the critical density at redshift z (see Tashiro et al. 2008). The quantity $n_e^{(c)}$ is the central free electron density. For thermal free electrons, this quantity is given by

$$n_e^{(c)} = 9.26\times10^{-4}\,\mathrm{cm}^{-3}\left(\frac{M}{10^{14}\,M_\odot}\right)\left(\frac{r_{vir}}{1\,\mathrm{Mpc}}\right)\left(\frac{\Omega_b}{\Omega_m}\right) \times {}_2F_1^{-1}(3/2, 3\beta/2; 5/2; -(r_{vir}/r_c)^2), \quad (9)$$

where ${}_2F_1$ is the hypergeometric function.

The properties of relativistic electrons inside haloes are not well known (see Sect. 5, Cavaliere & Lapi 2013, for a brief overview). We consider relativistic electrons to be described by a power law in the momentum space (following e.g. Colafrancesco et al. 2003, and references therein) with Lorentz factor ranging from $\Gamma_{min} \gg 1$ to Γ_{max}. Assuming for simplicity that $\Gamma_{max} \gg \Gamma_{min}$, the relativistic electron distribution function simplifies to (Colafrancesco et al. 2003)

$$n_e^{(rel)}(r,\Gamma) = n_e^{(r)}(r,\Gamma_{min})\,(\beta_E-1)\,\Gamma_{min}^{\beta_E-1}\Gamma^{-\beta_E}, \quad (10)$$

where $\beta_E > 1$ the spectral index and $n_e^{(r)}(r,\Gamma_{min})$ is the number density of relativistic electrons integrated over the range of Lorentz boost. Typical values for the spectral index is 2.5. In Colafrancesco et al. (2003), the number density $n_e^{(r)}(r,\Gamma_{min})$ is taken as a function of Γ_{min} ensuring $n_e^{(r)}(r,\Gamma_{min})\,(\beta_E-1)\,\Gamma_{min}^{\beta_E-1}$ is constant for different values of Γ_{min}, and with a normalization assumed to be $n_e^{(r)}(r,\Gamma_{min}=100) = 10^{-6}\,\mathrm{cm}^{-3}$. This means that the total number density of electrons increases for lower values of Γ_{min}.

Relativistic electrons could be of secondary origin, as decay products of pions produced by collision between a cosmic-ray proton and a proton from the thermal gas (Blasi & Colafrancesco 1999). A rough upper bound on the number density of relativistic electrons can then be derived using the ratios of the energy density in cosmic rays to the thermal energy density of the gas, $\epsilon = \rho_{CR}/\rho_{gas}$. Stacking of clusters observed with *Fermi*-LAT shows that such a ratio ϵ is of the order of few percent on average (Huber et al. 2013) and considering cosmic rays as protons with a kinetic energy of at least 1 GeV. This ratio can be used to set a relation between the number density of relativistic, cosmic-ray protons to the number density of thermal protons. Thermal energy of the gas is $\rho_{gas} = (3/2)n_p^{(c)}k_B T_p$ while the energy density in cosmic rays is $\rho_{CR} = \left(\frac{\beta_p-1}{\beta_p-2}\right)n_p^{(r)}m_p\Gamma_{min}$, where m_p the proton mass. We assume here a similar description for relativistic protons as for relativistic electrons. This gives

$$n_p^{(r)} = \epsilon f(\beta_p)\left(\frac{k_B T_p}{m_p\Gamma_{min}}\right)n_p^{(c)}, \quad (11)$$

where $f(\beta_p)$ is of order unity for values of β_p considered in Huber et al. (2013, Table 2). For the thermal part, the number density of electrons roughly equals that of protons, and they are both thermalized at the same temperature. The proton mass is ~1 GeV while temperatures of clusters are about few kiloelectron volts, hence the number of cosmic-ray protons is highly suppressed by the factor $\epsilon\left(\frac{k_B T_p}{m_p\Gamma_{min}}\right) \sim 10^{-10}$ as compared to the number of thermal electrons. If relativistic electrons are of secondary origin as a result of proton-proton collision, we thus expect their number density to be suppressed by a similar factor as compared to the thermal electrons. In this case, we thus expect the number of relativistic electrons in cosmic rays to be ten orders of magnitude less than the number of relativistic electrons.

The magnetic field, denoted $\boldsymbol{B}$, is in full generality a function of both $\boldsymbol{x}$ and $\boldsymbol{x}_i$ (respectively labelling any position within the halo and the centre of the halo), as well as a function of the mass and redshift of the considered halo. Because we only have only poor knowledge of the magnetic field inside haloes, we allow ourselves to chose a model for $\boldsymbol{B}$ that simplifies the calculations of the angular power spectra a bit. Therefore, the first of our assumptions is that the orientation of the magnetic field is roughly constant over the halo scale, although we still allow for potentially radial profile for its amplitude, i.e. $\boldsymbol{B}(\boldsymbol{x},\boldsymbol{x}_i) = B(|\boldsymbol{x}-\boldsymbol{x}_i|)\,\hat{\boldsymbol{b}}(\boldsymbol{x}_i)$. The vector $\hat{\boldsymbol{b}}(\boldsymbol{x}_i)$ is a unit vector labelling the orientation of the magnetic field of a given halo, thus depending on the halo position only and considered as a random variable. In this work, we also assume a spherically symmetric profile for the amplitude of the magnetic field. Observations suggest that the amplitude of the magnetic field scales radially as the halo matter content, i.e. $B \propto (n_{gas})^\mu$ (see e.g. Hummel et al. 1991; Murgia et al. 2004; Bonafede et al. 2009, 2010). We thus choose the following form for the amplitude of the magnetic field that corresponds to the β-profile:

$$B(r) = B_c(z)\left(1+\frac{r^2}{r_c^2}\right)^{-3\beta\mu/2}, \quad (12)$$

where B_c is the mean magnetic field strength at the centre of the halo. Its time evolution is given by (Widrow 2002)

$$B_c(z) = B_0\exp\left(-\frac{t_0-t(z)}{t_d}\right)\mu\mathrm{G}, \quad (13)$$

where t_0 is the present time and $t_d = \sqrt{r_{vir}^3/GM}$, and B_0 is the field strength at present time.

In full generality, the central value of the magnetic field is expected to depend on the mass of the halo. For clusters, i.e. haloes with $M > 10^{13}\,M_\odot$, typical values of few μG are expected, while for galaxies, i.e. haloes with $M < 10^{13}\,M_\odot$, typical values for the magnetic fields reaches $\sim 10\,\mu$G. The core magnetic field could however increase for most massive clusters up to $10\,\mu$G (Vacca et al. 2012). Theoretical studies suggest that B increases with the mass, since $B_0 \propto n_e^{1/2}T^{3/4}$ (Kunz et al. 2011). For the temperature-mass relation obtained from X-rays observations (Giodini et al. 2013), this would give $B_0 \propto M$.

Scaling of B with the halo masses has key impact on how angular power spectra of Faraday rotation and conversion depends on cosmological parameters, since such scalings weight different regions the halo mass function. Hence in this study, we first consider a magnetic field which is scale-independent to serve as a benchmark. The different mass scaling is then implemented as follows. For clusters, we introduce a power-law scaling with the halo mass, i.e.

$$B_0(M) = B_p\times\left(\frac{M}{M_p}\right)^\gamma, \quad (14)$$

where $M_p = 5\times10^{14}\,M_\odot$, $B_p = 3\,\mu$G, and $\gamma > 0$ ensuring the magnetic field of clusters to increase with the mass.

For galaxies, we introduce a second scaling that takes into account the increase of magnetic fields there as compared to clusters, i.e.

$$B_0(M) = B_c + B_g \times \left\{1 + \tanh\left[\frac{\log(M_g/M)}{\Delta \log M}\right]\right\}, \quad (15)$$

where $B_c = 3\,\mu$G, $B_g = 3.5\,\mu$G, $M_g = 10^{13}\,M_\odot$, and $\Delta \log M \simeq 0.43$. This allows for having a smooth transition from $B_0 = 10\,\mu$G for galaxies, $M < 10^{13}\,M_\odot$, to $B_0 = 3\,\mu$G for clusters $M > 10^{13}\,M_\odot$. This transition is centred at $10^{13}\,M_\odot$ with a width of roughly half of an order of magnitude in mass.

In Sect. 4 we study the effect of the two scalings both separately and in combination.

2.3.2. Statistical distribution of haloes

The spatial distribution of haloes and their abundance in mass and redshift is described using the halo model (Cooray & Sheth 2002). The abundance in mass and redshift is given by the halo mass function, $\mathrm{d}N/\mathrm{d}M$, and their spatial correlation is derived by the matter power spectrum plus halo bias. In this study, we make use of the halo mass function derived in Despali et al. (2016), which is defined using the virial mass. Halo masses range from $10^{10}\,M_\odot$ to $5 \times 10^{16}\,M_\odot$, hence covering galaxies and clusters of galaxies (similar to Tashiro et al. 2008).

The radiative transfer coefficients introduced in Sect. 2.1 depend on the projection of the magnetic field either along the line of sight or in the plane orthogonal to it. We thus need to introduce some statistics for the orientation of magnetic fields of haloes. This statistics of the relative magnetic field orientations of haloes is however poorly known. To motivate our choice (presented latter), we first briefly comment on previous results obtained in the literature.

The angular power spectrum of the Faraday rotation angle has been firstly computed in Tashiro et al. (2008) using an approach adapted from the study of the Sunyaev–Zel'dovich effect developed in Cole & Kaiser (1988), Makino & Suto (1993), and Komatsu & Kitayama (1999). We however believe that this first prediction should be amended. This is motivated by the following intuitive idea, which is most easily formulated using the two-point correlation function.

The Faraday rotation angle is derived from the projection of the magnetic field on the light of sight followed by CMB photons, i.e. $\alpha(\boldsymbol{n}) \propto \boldsymbol{n} \cdot \boldsymbol{B}$, and the correlation function is thus $\xi(\boldsymbol{n}_1, \boldsymbol{n}_2) := \langle\alpha(\boldsymbol{n}_1)\alpha(\boldsymbol{n}_2)\rangle \propto \left\langle(\boldsymbol{n}_1 \cdot \boldsymbol{B}_i)\left(\boldsymbol{n}_2 \cdot \boldsymbol{B}_j\right)\right\rangle$, where the subscripts i, j label the haloes which are crossed by the lines of sight $\boldsymbol{n}_1$ and $\boldsymbol{n}_2$, respectively. A first case is that the lines of sight are such that they cross two distinct haloes, i.e. $i \neq j$, corresponding to the so-called two-halo term in the angular power spectrum. We further assume that magnetic fields in haloes are produced by astrophysical processes. Hence two different haloes are statistically independent (from the viewpoint of magnetic fields), leading to $\xi^{\rm 2h}(\boldsymbol{n}_1, \boldsymbol{n}_2) \propto \langle \boldsymbol{n}_1 \cdot \boldsymbol{B}_i\rangle \left\langle \boldsymbol{n}_2 \cdot \boldsymbol{B}_{j\neq i}\right\rangle$. To be in line with a statistically homogeneous and isotropic Universe, the orientation of the magnetic field of haloes should be uniformly distributed leading to $\langle \boldsymbol{n} \cdot \boldsymbol{B}_i\rangle = 0$[4]. We thus expects the two-halo term to be zero, which is however not the case in Tashiro et al. (2008) in which such a term is not vanishing[5].

Considering then the one-halo term, this is $\xi^{\rm 1h}(\boldsymbol{n}_1, \boldsymbol{n}_2) \propto \langle(\boldsymbol{n}_1 \cdot \boldsymbol{B}_i)(\boldsymbol{n}_2 \cdot \boldsymbol{B}_i)\rangle$ providing that both lines of sight cross the same halo. This is a priori non-zero since $\langle \boldsymbol{B}_i \boldsymbol{B}_i\rangle$ does not vanish. There is however a subtlety which to our viewpoint, has not been considered in Tashiro et al. (2008). These authors considered that the statistical average of the orientation of magnetic fields for the one-halo term is $\left\langle(\boldsymbol{n} \cdot \boldsymbol{B}_i)^2\right\rangle = 1/3$, the value being that corresponding to orientations distributed uniformly. However, the spatial extension of haloes allows for having two different lines of sight crossing the *same* halo, and there is a priori no reason that $(\boldsymbol{n}_1 \cdot \boldsymbol{B}_i) = (\boldsymbol{n}_2 \cdot \boldsymbol{B}_i)$ for a randomly selected halo. As a consequence, this is $\langle(\boldsymbol{n}_1 \cdot \boldsymbol{B}_i)(\boldsymbol{n}_2 \cdot \boldsymbol{B}_i)\rangle$ which enters as a statistical average on the one-halo term, and not $\left\langle(\boldsymbol{n} \cdot \boldsymbol{B}_i)^2\right\rangle$. A similar argument applies for Faraday conversion except that this is the projection of the magnetic field on the plane orthogonal to $\boldsymbol{n}$, which is involved in this case.

We thus suppose that orientations are uniformly distributed in the Universe, independent for two different haloes, and independent of the spatial distribution of haloes. This can be understood as follows: we assume no coherence of the magnetic field orientations of different haloes or, to put it differently, the magnetic field correlation length is smaller than the inter-halo scale. This assumption is clearly in line with the cosmological principle, and it is motivated by the idea that the magnetism of the haloes is a result of processes isolated from other haloes. Thus, this orientation is a random variable which should be zero once averaged over haloes.

Orientations are given by the unit vector, $\boldsymbol{b}$, which is thus labelled by a zenithal angle, $\beta(\boldsymbol{x}_i)$, and an azimuthal angle, $\alpha(\boldsymbol{x}_i)$. In the Cartesian coordinate system, the three components are

$$b^i_x = \sin(\beta(\boldsymbol{x}_i))\cos(\alpha(\boldsymbol{x}_i)), \quad (16)$$

$$b^i_y = \sin(\beta(\boldsymbol{x}_i))\sin(\alpha(\boldsymbol{x}_i)), \quad (17)$$

$$b^i_z = \cos(\beta(\boldsymbol{x}_i)). \quad (18)$$

Any projection of the magnetic field orientation can be written as a function of the two angles, β and α. Our assumption of uniformly distributed orientations translates into the following averaging

$$\left\langle f(\alpha^i, \beta^i)\right\rangle = \frac{1}{4\pi}\int f(\alpha^i, \beta^i)\,\mathrm{d}\alpha^i\,\mathrm{d}(\cos\beta^i), \quad (19)$$

where β^i and α^i are a shorthand notation for $\beta(\boldsymbol{x}_i)$ and $\alpha(\boldsymbol{x}^i)$. Since we assume two haloes to be independent, we do not need to introduce some correlations further and the above fully describe the statistics of orientations of magnetic fields.

Assuming a magnetic field which is coherent over the scales of haloes does not capture the full complexity of magnetic fields in clusters of galaxies, in particular the small-scale structures observed via rotation measure. This can be taken into account for clusters as in Murgia et al. (2004), Govoni et al. (2006), and Bonafede et al. (2010) by modelling the magnetic field in Fourier

[4] We note that for two distinct haloes having however the same mass and are at the same redshift, it may well be that they share the same amplitude for $\boldsymbol{B}$. This remains consistent with a statistically homogeneous and isotropic Universe as long as the orientations of the magnetic fields average down to zero.

[5] We mention that the two-halo term may not be vanishing assuming some correlations between the magnetic fields of two different haloes; for example if these magnetic fields are seeded by a primordial magnetic field. In this case however, the two-halo term should be composed of a convolution of the matter power spectrum with the magnetic field power spectrum, as we could expect from results obtained for the similar case of the kinetic Sunyaev–Zel'dovich effect induced by the peculiar velocity of haloes (Hernandez-Monteagudo et al. 2006).

space as the convolution of the Fourier transform of the β-profile times the Fourier coefficients of a vector potential described by a statistically isotropic, power-law power spectrum at scales smaller than the cluster scales, i.e. smaller than the virial radius.

With such a modelling (including small scale fluctuations), averages over haloes of the two-point correlation are written as

$$\left\langle (\boldsymbol{n}_1\cdot\boldsymbol{B}_i)\left(\boldsymbol{n}_2\cdot\boldsymbol{B}_j\right)\right\rangle = \frac{1}{3}\,(\boldsymbol{n}_1\cdot\boldsymbol{n}_2)\,\delta_{i,j}B(r_1)B(r_2)S\,(r_{1,2})$$

if the two lines of sight cross the same clusters, and zero for two different clusters (encoded in the $\delta_{i,j}$). The function $B(r)$ is given by the β-profile. The function $S\,(r_{1,2})$ is the two-point correlation functions associated with the power spectrum at small scales. It is a function of the distance $r_{1,2}$ between the two points at which $B_i(\boldsymbol{r}_1)$ and $B_j(\boldsymbol{r}_2)$ are considered; this is not to be confused with r_1 and r_2, which are the distances of each point from the centre of the clusters. Such a two-point correlation function tends to one for $r_{1,2}\to 0$. It then drops down to zero above a typical radius, $r^{(s)}$, than the size of the halo, i.e. $s(r_{1,2}>r^{(s)})\to 0$ with $r^{(s)}<r_{\rm vir}$. This drop takes into account the fact that the magnetic field is coherent on scales smaller than the halo size. In for example Murgia et al. (2004), the power spectrum is non-zero on scales ranging from a hundredth of the core radius, $r_{\rm c}$, to almost two times the core radius. This would mean a coherence length of about half the virial radius.

Assuming instead magnetic fields to be coherent over the entire halo (as we did here) supposes that the function S equals ∼1 up to the virial radius. Otherwise stated, in this article we assume a coherence length of the size of the virial radius and the average over orientations simplfies to

$$\left\langle (\boldsymbol{n}_1\cdot\boldsymbol{B}_i)\left(\boldsymbol{n}_2\cdot\boldsymbol{B}_j\right)\right\rangle \simeq \frac{1}{3}\,(\boldsymbol{n}_1\cdot\boldsymbol{n}_2)\,\delta_{i,j}B(r_1)B(r_2)$$

for two lines of sight crossing the same halo, and 0 otherwise. With the simplifying assumption of coherence up to the virial radius, we thus expect to overestimate the angular power spectrum on large scales, roughly in the range $r_{\rm vir}/2$ to $r_{\rm vir}$. We discuss the impact of such an assumption in more detail in the next section.

3. Angular power spectra of Faraday rotation and Faraday conversion

3.1. Faraday rotation angle

The Faraday rotation angle is given by the following integral over the line of sight

$$\alpha(\boldsymbol{n}) = \frac{e^3}{8\pi^2\,m_{\rm e}^2\,c\,\varepsilon_0}\int_0^{r_{\rm CMB}}\frac{a(r){\rm d}r}{\nu^2(r)}\sum_{i=\rm halo}\left[\hat{\boldsymbol{n}}\cdot\boldsymbol{B}(\boldsymbol{x},\boldsymbol{x}_i)\right]\,n_{\rm e}(|\boldsymbol{x}-\boldsymbol{x}_i|), \tag{20}$$

where r stands for the comoving distance on the line of sight, $\boldsymbol{x}=r\boldsymbol{n}$, $r_{\rm CMB}$ is the distance to the last-scattering surface, and $\boldsymbol{x}_i$ is the centre of the ith halo. With our assumption regarding the magnetic field, and further replacing the summation over haloes by integrals over the volume and over the mass range, the above is

$$\alpha(\boldsymbol{n}) = \frac{e^3}{8\pi^2\,m_{\rm e}^2\,c\,\varepsilon_0}\int_0^{r_{\rm CMB}}\frac{a(r){\rm d}r}{\nu^2(r)}\iint{\rm d}M_i{\rm d}^3\boldsymbol{x}_i\left[n_h(\boldsymbol{x}_i)\times\,b(\boldsymbol{n},\boldsymbol{x}_i)X\,(|\boldsymbol{x}-\boldsymbol{x}_i|)\right], \tag{21}$$

where $n_h(\boldsymbol{x}_i)$ is the abundance of haloes, $b(\boldsymbol{n},\boldsymbol{x}_i)=\boldsymbol{n}\cdot\boldsymbol{b}(\boldsymbol{x}_i)$ the projection along the line of sight, and $X\,(|\boldsymbol{x}-\boldsymbol{x}_i|)=B\,(|\boldsymbol{x}-\boldsymbol{x}_i|)\,n_{\rm e}\,(|\boldsymbol{x}-\boldsymbol{x}_i|)$.

Two simplifications result from the different assumptions made about the statistics of the orientation of the magnetic field. To this end, we introduce the notation

$$A^i(\boldsymbol{n}) = \frac{e^3}{8\pi^2\,m_{\rm e}^2\,c\,\varepsilon_0}\int_0^{r_{\rm CMB}}\frac{a(r){\rm d}r}{\nu^2(r)}\,X\,(|\boldsymbol{x}-\boldsymbol{x}_i|)\,,$$

where we stress that the impact of orientation is omitted in the above. It can basically be interpreted as the maximum amount of rotation the halo i can generate. We note that this is also a function of the mass of the halo.

In the halo model first, the angular power spectrum, or equivalently the two-point correlation function, is composed of a one-halo term and a two-halo term. This gives for the one-halo term

$$\langle\alpha(\boldsymbol{n}_1)\alpha(\boldsymbol{n}_2)\rangle_{\rm 1h} = \iint{\rm d}M_i{\rm d}^3\boldsymbol{x}_i\left(\frac{{\rm d}N}{{\rm d}M}\right)A^i(\boldsymbol{n}_1)A^i(\boldsymbol{n}_2)\times\langle b(\boldsymbol{n}_1,\boldsymbol{x}_i)b(\boldsymbol{n}_2,\boldsymbol{x}_i)\rangle\,, \tag{22}$$

where we use $\left\langle n_h^2(\boldsymbol{x}_i)\right\rangle = {\rm d}N/{\rm d}M$[6]. The two-halo term then is

$$\langle\alpha(\boldsymbol{n}_1)\alpha(\boldsymbol{n}_2)\rangle_{\rm 2h} = \iint{\rm d}M_i{\rm d}^3\boldsymbol{x}_i\iint{\rm d}M_j{\rm d}^3\boldsymbol{x}_j\left\langle n_h(\boldsymbol{x}_i)n_h(\boldsymbol{x}_j)\right\rangle\times A^i(\boldsymbol{n}_1)A^j(\boldsymbol{n}_2)\left\langle b(\boldsymbol{n}_1,\boldsymbol{x}_i)b(\boldsymbol{n}_2,\boldsymbol{x}_j)\right\rangle, \tag{23}$$

where in the above the halo j is necessarily different from the halo i[7]. The two-halo term is however vanishing because of averaging over the orientation of magnetic field. Since two different haloes have uncorrelated magnetic fields, one has $\left\langle b(\boldsymbol{n}_1,\boldsymbol{x}_i)b(\boldsymbol{n}_2,\boldsymbol{x}_j)\right\rangle = \left\langle b(\boldsymbol{n}_1,\boldsymbol{x}_i)\right\rangle\left\langle b(\boldsymbol{n}_2,\boldsymbol{x}_j)\right\rangle$, which is finally equal to zero since magnetic orientations have a vanishing ensemble average.

Second, the two-point correlation function is described by an angular power spectrum, i.e.

$$\langle\alpha(\boldsymbol{n}_1)\alpha(\boldsymbol{n}_2)\rangle = \sum_\ell C_\ell^\alpha\,Y_{\ell m}(\boldsymbol{n}_1)\,Y^\star_{\ell m}(\boldsymbol{n}_2). \tag{24}$$

As detailed in Appendix A, this angular power spectrum, C_ℓ^α, is given by the convolution of two angular power spectra and is written as

$$C_\ell^\alpha = \frac{1}{4\pi}\sum_{L,L'}(2L+1)\,(2L'+1)\begin{pmatrix} L & L' & \ell\\ 0 & 0 & 0\end{pmatrix}^2 D_L^A\,D_{L'}^{\parallel}, \tag{25}$$

where D_L^A is the angular power spectrum associated with the two-point functions of the maximum of the rotation angle, i.e.

$$\iint{\rm d}M_i{\rm d}^3\boldsymbol{x}_i\left(\frac{{\rm d}N}{{\rm d}M}\right)A^i(\boldsymbol{n}_1)A^i(\boldsymbol{n}_2),$$

and $D_{L'}^{\parallel}$ is the angular power spectrum associated with the correlation function of orientations, $\langle b(\boldsymbol{n}_1,\boldsymbol{x}_i)b(\boldsymbol{n}_2,\boldsymbol{x}_i)\rangle$. Finally, the term

$$\begin{pmatrix} L & L' & \ell\\ 0 & 0 & 0\end{pmatrix}$$

[6] We note that abundances are given by a Poisson staistics for which $\left\langle n_h^2\right\rangle = \langle n_h\rangle$.

[7] We note that in the above

$$\left\langle n_h(\boldsymbol{x}_i)n_h(\boldsymbol{x}_j)\right\rangle = \left(\frac{{\rm d}N}{{\rm d}M_i}\right)\left(\frac{{\rm d}N}{{\rm d}M_j}\right)\left[1+b(M_i,z_i)b(M_j,z_j)\xi_{\rm m}\left(\boldsymbol{x}_i-\boldsymbol{x}_j\right)\right],$$

with $b(M,z)$ the bias and $\xi_{\rm m}$ the two-point correlation function of the matter density field.

corresponds to Wigner-3js. The expression in Eq. (25) means that the total angular power spectrum is obtained as the angular power spectrum for the maximum amount of the effect, D_L^A, modulated by the impact of projecting the magnetic field on the line of sight, hence the convolution with $D_{L'}^{\parallel}$.

It is shown in Appendix B that the angular power spectrum D_L^A is using Limber's approximation

$$D_L^A = \int_0^{z_{\rm CMB}} {\rm d}z \left(\frac{r}{\nu^2(r)}\right)^2 \frac{{\rm d}r}{{\rm d}z} \int {\rm d}M \, \frac{{\rm d}N}{{\rm d}M} \left[\alpha_{(c)}\alpha_L\right]^2, \tag{26}$$

with $\alpha_{\rm c}(M,z)$ the rotation angle at the core of the halo given by

$$\alpha_{\rm c} = \left(\frac{e^3}{m_{\rm e}^2 c\varepsilon_0\sqrt{8\pi}}\right) n_{\rm e}^{(c)}(M,z)\, B_{\rm c}(B_0,z). \tag{27}$$

This core angle depends on the mass, the redshift and the magnetic field amplitude of the considered haloes. The projected Fourier transform of the profile is

$$\alpha_\ell = \sqrt{\frac{2}{\pi}} \left(\frac{r_{\rm c}^{(\rm phys)}}{\ell_{\rm c}^2}\right) \int_0^\infty {\rm d}x\, x^2 U(x)\, j_0((\ell+1/2)x/\ell_{\rm c}), \tag{28}$$

where $\ell_{\rm c} = D_{\rm ang}(z)/r_{\rm c}$ the characteristic multipole for a halo of size $r_{\rm c}$ at a redshift z, and $D_{\rm ang}(z)$ the angular diameter distance. The normalized profile $U(x)$ for a β-profile is $U(x) = (1+x)^{-3\beta(1+\mu)/2}$ where $x = r/r_{\rm c}$.

Similarly in Appendix C, the angular power spectrum for the orientation of the magnetic field projected on the line of sight is

$$D_{L'}^{\parallel} = \frac{4\pi}{9}\,\delta_{L',1}. \tag{29}$$

Using the triangular conditions for the Wigner-3j (see e.g. Varshalovich et al. 1988), the angular power spectrum of the Faraday rotation angle boils down to

$$C_\ell^\alpha = \frac{1}{3}\left[\left(\frac{\ell}{2\ell+1}\right) D_{\ell-1}^A + \left(\frac{\ell+1}{2\ell+1}\right) D_{\ell+1}^A\right]. \tag{30}$$

We note that the above does not assume Limber's approximation in the sense that the involved D_ℓ^As can be either the expression obtained from the Limber's approximation, Eq. (26), or the non-approximated expression as given in Eq. (B.6).

The impact of projecting the magnetic fields on the line of sight translates into the modulation of the angular power spectra for the maximum amount of rotations haloes can generate. In the limit of high values of ℓ, the two lines of sights, $\boldsymbol{n}_1$ and $\boldsymbol{n}_2$, can be considered as very close to each other. This leads to $\langle b(\boldsymbol{n}_1,\boldsymbol{x}_i) b(\boldsymbol{n}_2,\boldsymbol{x}_i)\rangle \simeq \left\langle b^2(\boldsymbol{n}_1,\boldsymbol{x}_i)\right\rangle = 1/3$ and one should recover the same result as derived in Tashiro et al. (2008), restricted to the one-halo term however. In this high-ℓ limit, Eq. (30) simplifies to $C_\ell^\alpha = D_\ell^A/3$. From the expression of D_ℓ^A using Limber's approximation, we can check that this is identical to the one-halo term derived in Tashiro et al. (2008).

We finally discuss how the above result can be amended to take into account a stochastic component in the magnetic field as described in Murgia et al. (2004), Govoni et al. (2006), and Bonafede et al. (2010). In Appendix B, we show that adding the two-point correlation $S(r)$ of the stochastic magnetic field can be accounted for introducing an effective profile, $X \to X^{\rm eff}$. This profile should take into account two effects. First it has to decrease to zero more rapidly than the β-profile so as to take into account the large-scale suppression introduced by a coherence length smaller than the virial radius. The precise shape of such an additional drop depends on the details of the power spectrum describing the stochastic magnetic field. At an effective level however, we can simply increase the values of the parameter μ in Eq. (12), since the profile drops more rapidly for higher values of μ. In the following then, the parameter μ should be interpreted as an effective parameter which also (partially) captures the impact of a magnetic field coherent on scales smaller than the virial radius[8]. Second, the correlation $S(r)$ may add a new scaling of the total amplitude of the effect with the mass. This change can however be entirely absorbed in the mass scaling of $B_{\rm c}$.

In this paper, we consider that the impact of such a stochastic component is effectively captured by an increased value of μ (in terms of shape), and by the mass scaling we introduced for $B_{\rm c}$. This obviously does not capture the details of the power spectrum of the magnetic field, but at least it takes into account its impact at a qualitative level. Conversely, we can also expect that the large-scale suppression induced by the power spectrum description, and the additional scaling in mass, is partially degenerate with the parameter μ and the mass scaling of $B_{\rm c}$.

3.2. Faraday conversion

For the Faraday conversion, we first recall that irrespective of the nature of free electrons (either from a thermal distribution or from a relativistic, non-thermal distribution) the conversion rate is proportional to $B_\perp^2 e^{\pm 2{\rm i}\theta_B}$, where $B_\perp$ is the norm of the projected magnetic field on the plane orthogonal to $\boldsymbol{n}$, and θ_B is the angle between the projected magnetic field and the first basis vector in the plane orthogonal to $\boldsymbol{n}$. This defines the spin-($\pm$2) structure of these conversion coefficients which can be conveniently rewritten using projections of the magnetic field on the so-called helicity basis in the plane orthogonal to $\boldsymbol{n}$, i.e.

$$B_\perp^2 e^{\pm 2{\rm i}\theta_B} = B^2\left(|\boldsymbol{x}-\boldsymbol{x}_i|\right)\left[\boldsymbol{b}(\boldsymbol{x}_i)\cdot\left(\boldsymbol{e}_\theta \pm {\rm i}\boldsymbol{e}_\varphi\right)\right]^2, \tag{31}$$

where we note in the equation above that the norm of the magnetic field is a radial function and its orientation depends on the haloes location only.

3.2.1. Thermal electrons

The radiative transfer coefficients integrated over the line of sight is defined as $\phi_{\pm 2}(\boldsymbol{n}) = \int a(r){\rm d}r \sum_{\rm haloes} \dot{\phi}_i^{P\to V}(\boldsymbol{n},r) e^{\pm 2{\rm i}\theta_B^{(i)}(\boldsymbol{n},r)}$. For thermal electrons, this explicitly is

$$\phi_{\pm 2}(\boldsymbol{n}) = \frac{e^4}{16\pi^3 m_{\rm e}^3\, c\,\varepsilon_0} \int_0^{r_{\rm CMB}} \frac{a(r)}{\nu^3(r)}{\rm d}r \iint {\rm d}M_i {\rm d}\boldsymbol{x}_i \left[n_h(\boldsymbol{x}_i) \times b_{\pm 2}(\boldsymbol{n},\boldsymbol{x}_i) X\left(|\boldsymbol{x}-\boldsymbol{x}_i|\right)\right], \tag{32}$$

where now $X\left(|\boldsymbol{x}-\boldsymbol{x}_i|\right) = n_{\rm e}\left(|\boldsymbol{x}-\boldsymbol{x}_i|\right) B^2\left(|\boldsymbol{x}-\boldsymbol{x}_i|\right)$, and $b_{\pm 2}(\boldsymbol{n},\boldsymbol{x}_i) = \left[\boldsymbol{b}(\boldsymbol{x}_i)\cdot\left(\boldsymbol{e}_\theta \pm {\rm i}\boldsymbol{e}_\varphi\right)\right]^2$.

Apart from the spin-($\pm$2) structure encoded in $b_{\pm 2}$, the above has exactly the same structure as the Faraday rotation angle, Eq. (21), and we adopt the same strategy as for the Faraday rotation angle. The key difference for Faraday conversion lies in the spin structure and we have to compute three correlations (two autocorrelations and one cross-correlation). We can either

[8] This is obviously a very simple approach. It is also possible to replace the profile $U(x)$ by $U(x)\times s(x)$ so as to account for a more complex shape of the correlation function of the stochastic magnetic field; see for example Tashiro et al. (2008, 2009).

use spin fields or more conveniently, E and B decompositions which is reference frame independent (see e.g. Kamionkowski et al. 1997; Zaldarriaga & Seljak 1997). We first compute the correlation for spin fields, defined as

$$\left\langle \phi_{\pm2,\ell m}\phi^{\star}_{\pm2,\ell' m'}\right\rangle = C_{\ell}^{\pm2,\pm2}\,\delta_{\ell,\ell'}\delta_{m,m'}, \tag{33}$$

$$\left\langle \phi_{2,\ell m}\phi^{\star}_{-2,\ell' m'}\right\rangle = C_{\ell}^{2,-2}\,\delta_{\ell,\ell'}\delta_{m,m'}. \tag{34}$$

These angular power spectra are easily transformed into angular power spectra for the E and B field associated to $\phi_{\pm2}$ using $\phi^{E}_{\ell m} = -(\phi_{2,\ell m} + \phi_{-2,\ell m})/2$ and $\phi^{B}_{\ell m} = i(\phi_{2,\ell m} - \phi_{-2,\ell m})/2$.

As the case for Faraday rotation, the two-halo term is vanishing because of the orientations of the magnetic fields averages down to zero, i.e.

$$\left\langle b_{\pm2}(\boldsymbol{n}_1,\boldsymbol{x}_i)b_{\pm2}(\boldsymbol{n}_2,\boldsymbol{x}_{j\neq i})\right\rangle = \left\langle b_{\pm2}(\boldsymbol{n}_1,\boldsymbol{x}_i)\right\rangle\left\langle b_{\pm2}(\boldsymbol{n}_2,\boldsymbol{x}_{j\neq i})\right\rangle$$

for two different haloes, and for uniformly random orientations it is found that $\langle b_{\pm2}(\boldsymbol{n},\boldsymbol{x}_i)\rangle = 0$.

Following Appendix A then, we show that

$$C_{\ell}^{\pm2,\pm2} = \frac{1}{4\pi}\sum_{L,L'}(2L+1)(2L'+1)\begin{pmatrix} L' & L & \ell \\ \mp2 & 0 & \pm2\end{pmatrix}^2 D_L^{\Phi}\,D_{L'}^{\perp}, \tag{35}$$

and

$$C_{\ell}^{2,-2} = \frac{1}{4\pi}\sum_{L,L'}(2L+1)(2L'+1)\,D_L^{\Phi}\,D_{L'}^{\perp}, \times\begin{pmatrix} L' & L & \ell \\ -2 & 0 & 2\end{pmatrix}\begin{pmatrix} L' & L & \ell_1 \\ 2 & 0 & -2\end{pmatrix}. \tag{36}$$

The above is interpreted in a very similar way to C_{ℓ}^{α}. It is the power spectrum of the maximum of the effect of Faraday conversion, D_L^{Φ}, which is further modulated by the impact of projecting the magnetic field in the plane orthogonal to the line of sight, which is encoded in $D_{L'}^{\perp}$.

The angular power spectrum of the amplitude of the effect is derived using the standard technique described in Appendix B and by selecting the appropriate profile, $n_E B^2$ instead of $n_E B$. This gives with the Limber's approximation

$$D_L^{\Phi} = \int_0^{z_{\rm CMB}}\mathrm{d}z\left(\frac{r}{\nu^3(r)}\right)^2\frac{\mathrm{d}r}{\mathrm{d}z}\int\mathrm{d}M\,\frac{\mathrm{d}N}{\mathrm{d}M}\left[\Phi_{(\mathrm{c})}\phi_L\right]^2, \tag{37}$$

where the amplitude of the conversion at the core of the halo is given by

$$\Phi_{(\mathrm{c})} = \left(\frac{e^4}{2(2\pi)^{3/2}m_{\mathrm{e}}^3\,c\,\varepsilon_0}\right)n_{\mathrm{e}}^{(c)}\,B_{\mathrm{c}}^2. \tag{38}$$

The Fourier-transformed normalized profile is

$$\phi_{\ell} = \sqrt{\frac{2}{\pi}}\left(\frac{r_{\mathrm{c}}^{(\mathrm{phys})}}{\ell_{\mathrm{c}}^2}\right)\int_0^{\infty}\mathrm{d}x\,x^2U(x)\,j_0((\ell+1/2)x/\ell_{\mathrm{c}}), \tag{39}$$

where the profile is now given by $U(x) = (1+x)^{-3\beta(1+2\mu)/2}$. The angular power spectrum for the orientation contribution is detailed in Appendix D. It is non-zero for a multipole of two only and it is $D_{L'}^{\perp} = (32\pi/75)\,\delta_{L',2}$.

The last step consists in deriving the angular power spectrum in the E and B decomposition of the spin-(±2) of the Faraday conversion coefficients. This first shows that the $\langle EB\rangle$ cross-spectrum is vanishing, i.e. $C_{\ell}^{\phi^E\phi^B} = 0$. The autospectra are given by

$$C_{\ell}^{\phi^E\phi^E} = \frac{4}{15}\left[\frac{(\ell+1)(\ell+2)}{2(2\ell-1)(2\ell+1)}D_{\ell-2}^{\Phi} + \frac{3(\ell-1)(\ell+2)}{(2\ell-1)(2\ell+3)}D_{\ell}^{\Phi} + \frac{\ell(\ell-1)}{2(2\ell+1)(2\ell+3)}D_{\ell+2}^{\Phi}\right], \tag{40}$$

and

$$C_{\ell}^{\phi^B\phi^B} = \frac{4}{15}\left[\left(\frac{\ell+2}{2\ell+1}\right)D_{\ell_1-1}^{\Phi} + \left(\frac{\ell-1}{2\ell+1}\right)D_{\ell+1}^{\Phi}\right]. \tag{41}$$

In the above, we made use of the triangular conditions for the Wigner-3js. We note that the above angular power spectra are spin-(±2) and they are nonvanishing for $\ell \geq 2$. In the high-ℓ limit, the two autospectra are identical and equal to $C_{\ell}^{\phi_E\phi_E} \simeq C_{\ell}^{\phi_B\phi_B} \simeq (4/15)D_{\ell}^{\Phi}$.

3.2.2. Relativistic electrons

For relativistic electrons, the rate of Faraday conversion integrated over the line of sight is

$$\phi_{\pm2}(\boldsymbol{n}) = \frac{e^4\Gamma_{\min}}{8\pi^3m_{\mathrm{e}}^3\,c\,\varepsilon_0}\left(\frac{\beta_E-1}{\beta_E-2}\right)\int_0^{r_{\rm CMB}}\frac{a(r)}{\nu^3(r)}\mathrm{d}r \times\iint\mathrm{d}M_i\mathrm{d}\boldsymbol{x}_i\left[n_h(\boldsymbol{x}_i)\,b_{\pm2}(\boldsymbol{n},\boldsymbol{x}_i)X\left(|\boldsymbol{x}-\boldsymbol{x}_i|\right)\right], \tag{42}$$

where $\Gamma_{\min}$ is the minimum Lorentz factor of the relativistic electrons, and β_E is the spectral index of the energy distribution of relativistic electrons. The profile is $X = n_{\mathrm{e}}^{(r)}\,B^2$, i.e. the same as for thermal electrons replacing the number density of thermal electrons by the number density of relativistic ones.

The angular power spectrum for the Faraday conversion rate due to relativistic electrons has exactly the same form as for thermal electrons, i.e. Eqs. (40) and (41) for the E and B autospectra. The expression for D_{ℓ}^{Φ} also is the same. It is given by Eq. (37) where we only have to replace $\Phi_{(c)}$ by

$$\Phi_{(r)} = \left(\frac{e^4\Gamma_{\min}}{4(2\pi)^{3/2}m_{\mathrm{e}}^3\,c\,\varepsilon_0}\right)\left(\frac{\beta_E-1}{\beta_E-2}\right)n_{\mathrm{e}}^{(r)}\,B_{\mathrm{c}}^2. \tag{43}$$

3.3. Remarks on cross-correlation

We briefly comment on possible cross-correlation. The first point is that in this approach, the cross-correlation between the Faraday rotation angle with any tracer of haloes which is not correlated with the projection of magnetic fields on the line of sight is vanishing. This is because the cross-correlation is proportional to either $\langle\boldsymbol{b}\cdot\boldsymbol{n}\rangle$ or $\left\langle\left[\boldsymbol{b}\cdot\left(\boldsymbol{e}_\theta \pm \mathrm{i}\boldsymbol{e}_\varphi\right)\right]^2\right\rangle$, both of which average down to zero. This is indeed the case for cross-correlation with the thermal and relativistic Sunyaev–Zel'dovich effect, the lensing potential, or the cosmic infrared background fluctuations. This is also the case for cross-correlation with the absorption coefficients, μ.

Finally, we checked that the averages $\left\langle[\boldsymbol{b}\cdot\boldsymbol{n}_1]\left[\boldsymbol{b}\cdot\left(\boldsymbol{e}_\theta^{(2)}\pm\mathrm{i}\boldsymbol{e}_\varphi^{(2)}\right)\right]^2\right\rangle$ equals to zero. This yields a vanishing cross-correlation between the Faraday rotation angle and Faraday conversion.

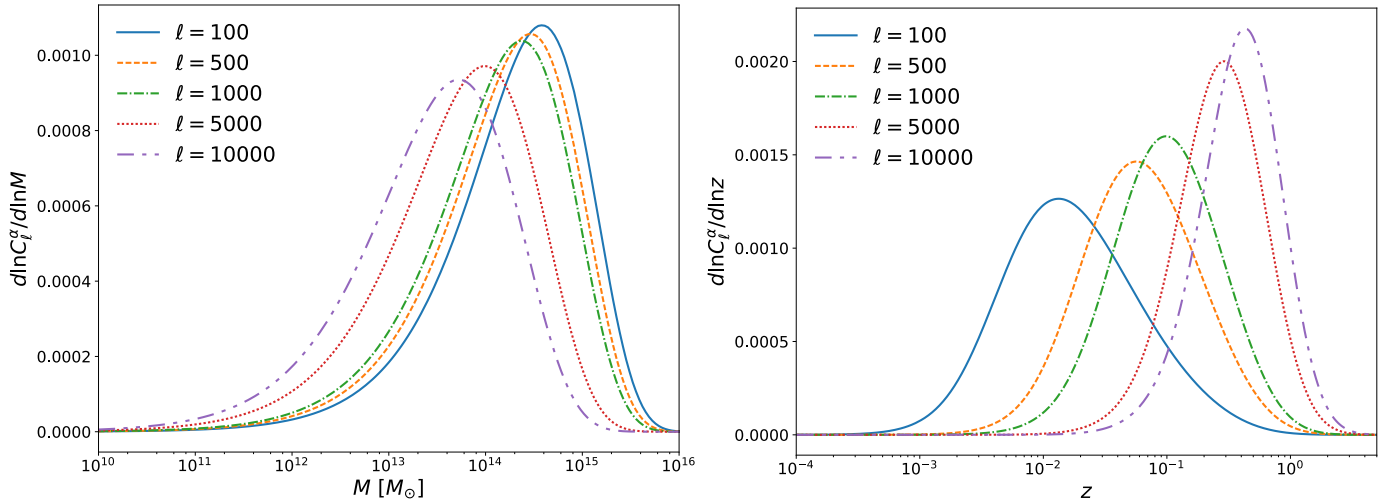

Fig. 1. *Left*: mass distribution of the Faraday rotation effect for various ℓ modes. *Right*: redshift distribution of the Faraday rotation effect for various ℓ modes.

4. Numerical results

Our results are shown for a frequency of observation $\nu_0 = 30\,\mathrm{GHz}$, and a field strength at present time $B_0 = 3\,\mu\mathrm{G}$. The angular power spectrum for the Faraday rotation angle scales as $C_\ell^\alpha \propto B_0^2/\nu_0^4$. The angular autospectra of the E and B modes of Faraday conversion scale as $C_\ell^{\phi^E\phi^E(\phi^B\phi^B)} \propto B_0^4/\nu_0^6$. Unless specified, the parameters for the β-profile are $\beta = \mu = 2/3$, which would correspond to a magnetic field frozen into matter.

All the numerical results reported in this work are obtained using the universal mass function from Despali et al. (2016). For consistency, we checked that similar results are obtained using the mass function of Tinker et al. (2008). In particular, we found similar scaling with cosmological parameters, despite a small variation regarding the overall amplitude of the angular power spectra.

4.1. Power spectrum of the Faraday rotation angle

Figure 1 shows the mass and redshift distributions of the Faraday rotation angle power spectrum for different multipoles ℓ, with, on the left, $\mathrm{d}\ln C_\ell^\alpha/\mathrm{d}\ln M$ as a function of mass and, on the right, $\mathrm{d}\ln C_\ell^\alpha/\mathrm{d}\ln z$ as a function of redshift. Compared to Tashiro et al. (2008) (Figs. 4 and 3, respectively), we note that our distributions are slightly shifted to higher masses and lower redshifts. This results in the Faraday rotation effect being more sensitive to higher mass values and lower redshift galaxy haloes than their Faraday rotation angle, so that its power spectrum seems to be slightly shifted to lower ℓ values as compared to that in Tashiro et al. (2008). Indeed, low multipoles correspond to high angular scales, hence to high masses or low-redshift haloes because these haloes appear bigger on the sky than low masses and high-redshift haloes.

Figure 2 shows the angular power spectrum of the Faraday rotation angle for different values of the parameters β and μ of the spatial distribution profiles of the free electrons density and magnetic field, respectively. First, we note a shift of power to higher multipoles when increasing β or μ. Indeed the profile of free electrons and magnetic fields then becomes steeper so that they are more concentrated in the centre of the halo, which consequently appears smaller on the sky. This result is consistent with Tashiro et al. (2008). We also see that the difference in amplitudes is more significant when we change β rather than μ because β appears both in the free electrons and magnetic field profiles. However, the trend is different when changing β or μ. Indeed, when increasing μ, the amplitude decreases, as expected from the magnetic field profile Eq. (12). On the contrary, when increasing β, the amplitude also increases. This is because as the profile of free electrons is steeper, keeping the number of electrons constant; their concentration increases in Eq. (9), as does the amplitude.

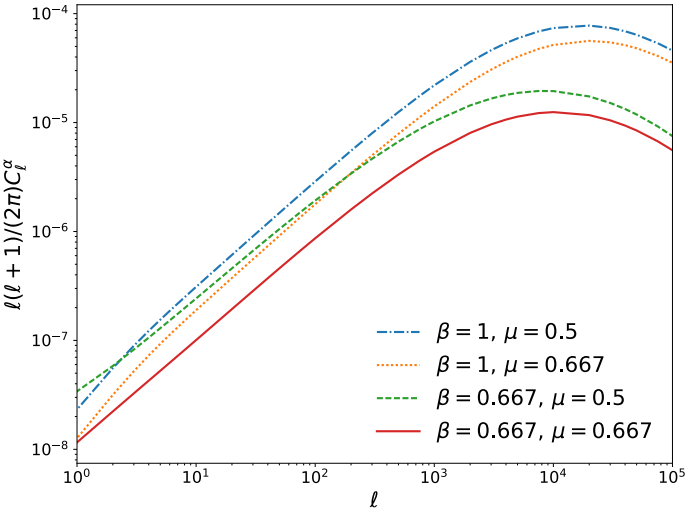

Fig. 2. Angular power spectra of the Faraday rotation angle, C_ℓ^α, for different values of the parameter β of the β-profile and different values of the parameter μ of the magnetic field profile.

Figure 3 shows two different representations of the dependence of the angular power spectrum of the Faraday rotation angle on the amplitude of density fluctuation σ_8: on the left we plot the angular power spectrum for different values of σ_8 and on the right we plot the logarithmic derivative of the angular power spectrum with respect to σ_8 as a function of ℓ. The latter gives the scaling of C_ℓ^α with σ_8, i.e. by writing $C_\ell^\alpha \propto \sigma_8^{n(\ell)}$ then $n(\ell) = \mathrm{d}\ln(C_\ell^\alpha)/\mathrm{d}\ln(\sigma_8)$.

The angular power spectrum C_ℓ^α is composed of the one-halo term only. Hence its scaling with σ_8 is driven by the mass

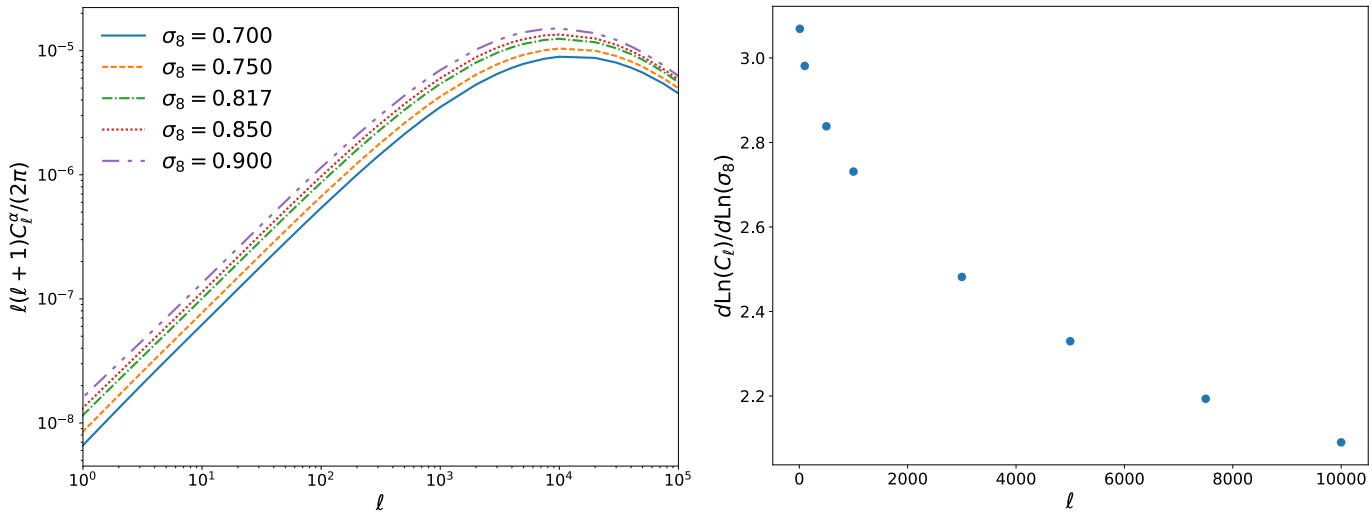

Fig. 3. *Left*: angular power spectra of the Faraday rotation angle, C_ℓ^α, for different values of the density fluctuations amplitude σ_8. *Right*: scaling of the angular power spectra with σ_8, $\mathrm{d}\ln C_\ell^\alpha/\mathrm{d}\ln\sigma_8$, as a function of ℓ.

function, $\mathrm{d}N/\mathrm{d}M$, and the rotation angle at the core of haloes, α_c. The latter does not explicitly depends on σ_8. However, the scaling of $\mathrm{d}N/\mathrm{d}M$ with σ_8 is mass-dependent. Then the mass dependence of α_c probes different mass ranges of the mass function, and as a consequence, different scaling of $\mathrm{d}N/\mathrm{d}M$ with the amplitude of matter perturbations.

We find a dependence as $C_\ell^\alpha \propto \sigma_8^{3.1} - \sigma_8^{2.1}$ for $\ell = 10$ and $\ell = 10^4$, respectively. The power spectrum of the Faraday rotation angle is more sensitive to σ_8 for low ℓ values than for high ℓ values because as seen above, the angular power spectrum is sensitive to higher mass at low ℓ and in this mass regime the mass function is more sensitive to σ_8. We noticed that reducing the mass integration range from $M = 10^{13}\,M_\odot$ to $M = 5\times10^{16}\,M_\odot$ (where it was $[10^{10}\,M_\odot, 5\times10^{16}\,M_\odot]$ before) slightly increases the power in σ_8. This may be because the Faraday rotation effect is mainly sensitive to galaxy haloes with masses in the range $M = 10^{13}$ to $M = 10^{15}\,M_\odot$ (see Fig. 1) and that our mass function depends on σ_8 more strongly from $M = 10^{14}\,M_\odot$.

We note that the scaling in σ_8 of the angular power spectrum is different than that for the tSZ angular power spectrum, which scales with $\sigma_8^{8.1}$ (see e.g. Hurier & Lacasa 2017). The reason is a different scaling in mass of the rotation angle at the core of haloes as compared to the tSZ flux; we note that the tSZ angular power spectrum is dominated by the one-halo contribution. Indeed, $|\alpha_c|^2$ scales as M^2, whereas the square of the tSZ flux at the core scales as $M^{3.5}$. This results in a different weighting of the mass function, which is more sensitive to σ_8 for high-mass values, the tSZ effect giving more weight to high masses than the Faraday rotation angle.

The dependence with σ_8 found in this work is however different from that reported in Tashiro et al. (2008), the difference being mainly due to the presence of a two-halo term in Tashiro et al. (2008). The mass range $\left[M = 10^{13}\,M_\odot, 5\times10^{16}\,M_\odot\right]$ is first considered in Tashiro et al. (2008) for which the angular power spectrum is dominated by its one-halo contribution[9]. In this case, the obtained scaling is σ_8^5. The difference with the scaling found in this case lies in the reduced mass range, which gives more weight to the total effect to higher mass haloes. Second the mass range is extended in Tashiro et al. (2008) down to $10^{11}\,M_\odot$, leading then to a scaling as $\sigma_8^{5.5}$. In the mass range $[10^{11}\,M_\odot, 10^{13}\,M_\odot]$, the two-halo term present in Tashiro et al. (2008) is not negligible anymore. This two-halo term then gives much more contribution to low-mass haloes as compared to ours (see Fig. 7 of Tashiro et al. 2008). However, the scaling of the two-halo term with σ_8 is not driven anymore by

$$\sim \int \mathrm{d}M \frac{\mathrm{d}N}{\mathrm{d}M}\alpha_\mathrm{c}^2,$$

but instead by

$$\sim \left(\int \mathrm{d}M \frac{\mathrm{d}N}{\mathrm{d}M} b(M,z)\alpha_\mathrm{c}\right)^2 P_\mathrm{m}(\ell/r,z),$$

where $P_\mathrm{m}(k,z)$ is the matter power spectrum (proportional to σ_8). The steeper scaling with σ_8 found in Tashiro et al. (2008) is thus mainly due to the non-negligible contribution of the two-halo term in their work.

We now want to study whether the Faraday rotation angle is sensitive to the matter density parameters. Keeping other cosmological parameters fixed, we have two possibilities to vary Ω_m: either by varying the density of cold dark matter, Ω_CDM, or that of baryons, Ω_b.

We found that the Faraday rotation effect is almost independent of Ω_m, when Ω_b is kept fixed while varying Ω_CDM, i.e.

$$C_\ell^\alpha \propto \Omega_\mathrm{CDM}^{-0.1} - \Omega_\mathrm{CDM}^{-0.2}$$

for $\ell = 10$ and $\ell = 10^4$, respectively. This translates into a similar scaling with Ω_m for a varying density of dark matter, i.e.

$$C_\ell^\alpha \propto \Omega_m^{-0.1} - \Omega_m^{-0.2}$$

for $\ell = 10$ and $\ell = 10^4$, respectively.

However, when keeping Ω_CDM fixed and varying Ω_b, the dependence is clearly different and is written as

$$C_\ell^\alpha \propto \Omega_b^{2.0} - \Omega_b^{1.9}$$

for $\ell = 10$ and $\ell = 10^4$, respectively. The resulting scaling with Ω_m by varying the density of baryons is then

$$C_\ell^\alpha \propto \Omega_m^{13} - \Omega_m^{12}$$

[9] The angular power spectra derived in Tashiro et al. (2008) has a non-zero two-halo contribution.

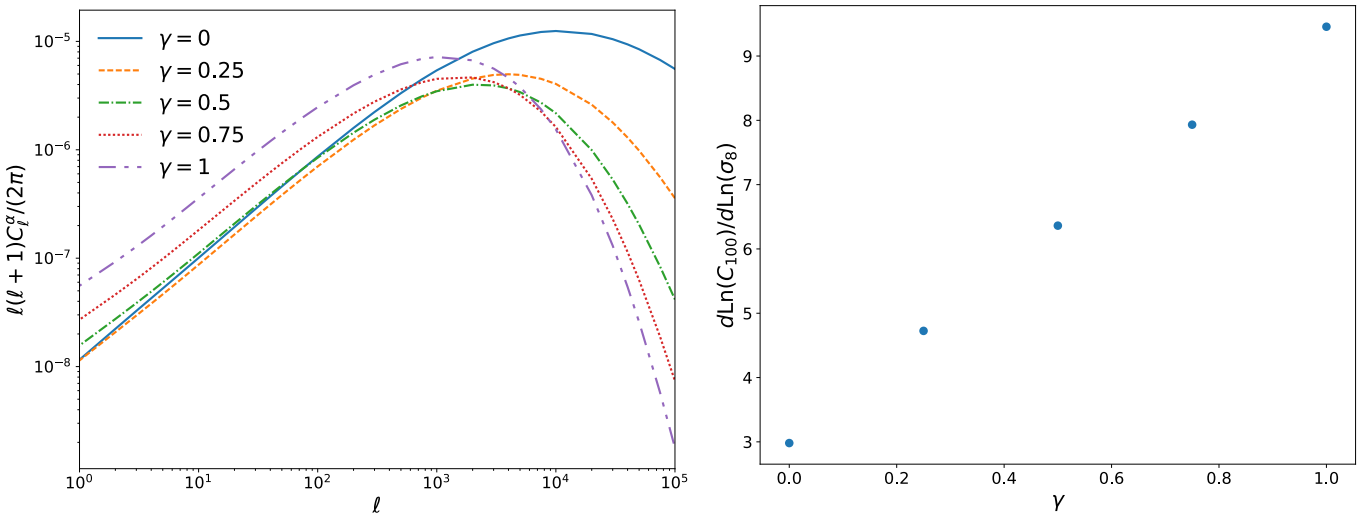

Fig. 4. *Left*: angular power spectra of the Faraday rotation angle, C_ℓ^α, when adding a mass dependence for the magnetic field strength at the centre scaling as $B = B_p(M/M_p)^\gamma$, where $M_p = 5 \times 10^{14} M_\odot$, $B_p = 3\,\mu$G, and for different values of γ. *Right*: scaling of the angular power spectra with σ_8, $\mathrm{d}\ln C_{100}^\alpha/\mathrm{d}\ln\sigma_8$, as a function of γ. We chose to plot this effect for $\ell = 100$ as C_ℓ^α depends more strongly on σ_8 for low ℓ values.

for $\ell = 10$ and $\ell = 10^4$, respectively. The dependence with Ω_b and $\Omega_{\rm CDM}$ is simply understood by the fact the angular power spectrum scales with the fraction of baryons to the square. The effect is almost Ω_m-independent when varying $\Omega_{\rm CDM}$, as compared to the tSZ effect, which scales as $\sim\Omega_m^3$ (Komatsu & Kitayama 1999). We can thus hope to use the Faraday rotation as a cosmological probe, by combining it with another physical effect having a different degeneracy in the $\Omega_m - \sigma_8$ plane, such as the tSZ effect.

We finally study the effect of having a mass dependence of the (central) magnetic field strength owing to either an increase of this magnetic field strength with the mass of clusters, or by considering the higher values of magnetic fields for galaxies.

For the scaling with clusters mass first, we introduce $B_0(M) = B_p \times (M/M_p)^\gamma$, where $M_p = 5 \times 10^{14} M_\odot$, $B_p = 3\,\mu$G, and we let γ to vary from 0 to 1. The global amplitude of the power spectrum now scales with $(B_{\rm p})^2$ while the mass scaling impacts the shape of the spectrum. We note that a change of $B_{\rm p}$ only changes the global amplitude of the power spectrum and not its scale dependence nor its response to changes in the cosmological parameters. The left panel of Fig. 4 shows C_ℓ^α for five different values of γ. When increasing γ, the power spectrum is increased and the peak is shifted to lower ℓ values. Increasing the value of γ indeed leads to a higher contribution of massive haloes, which appears larger once projected on the sky, hence a peak at smaller multipoles. This shift to lower ℓ values and the difference in amplitude of the Faraday rotation angle could give insight into the scaling of the magnetic field strength with mass.

Figure 4 (right) shows how this mass dependence affects the dependence on σ_8 of the Faraday rotation effect by plotting $\mathrm{d}\ln C_{100}^\alpha/\mathrm{d}\ln\sigma_8$ with respect to γ. For $\ell = 100$, when $\gamma = 1$, we find $C_\ell^\alpha \propto \sigma_8^{9.5}$ and we recover $C_\ell^\alpha \propto \sigma_8^{3.0}$ for $\gamma = 0$. In between, $C_\ell^\alpha \propto \sigma_8^{4.7} - \sigma_8^{6.4} - \sigma_8^{7.9}$ for $\gamma = 0.25,\ 0.5,\ 0.75$, respectively. We stated a few lines above that our different scaling with σ_8 of the angular power spectrum as compared to the thermal SZ effect came from a different scaling in mass. Indeed, the angular power spectrum of our effect scales as M^2, where it scales as $M^{3.5}$ for the tSZ effect, hence we recover the same scaling in σ_8 for $\gamma = 0.75$. From this we also see that if we could model the magnetic field with a power-law mass dependence, the more it would depend on mass, the more the effect would be sensitive to σ_8, allowing for a better determination of this cosmological parameter. Hence there is a correlation between the uncertainty on σ_8 and the mass dependence of the magnetic field strength. The Faraday rotation angle still almost does not depend on Ω_m (when varying $\Omega_{\rm CDM}$ only). Indeed, $C_\ell^\alpha \propto \Omega_m^{-0.1} - \Omega_m^{-0.0} - \Omega_m^{-0.0} - \Omega_m^{-0.1} - \Omega_m^{-0.1}$ for $\gamma = 0,\ 0.25,\ 0.5,\ 0.75$, and 1, respectively.

Second, the impact of a higher magnetic field in galaxies is taken into account using the hyperbolic tangent introduced in Eq. (15). We first only account for the increase in B for galaxies, i.e. no power-law scaling for clusters. This is shown as the dashed blue curve in Fig. 5, to be compared to the solid red curve where there is no mass scaling. It first increases the total power as a result of a globally higher magnetic field. The main impact is in the smallest scales since galaxies (which are low masses, hence smaller sized objects) now have an increased contribution because of the higher value of $B_0(M < 10^{13}\ M_\odot)$. In this case, the scaling of C_ℓ^α with σ_8 is shifted to lower values as follows:

$$C_\ell^\alpha \propto \sigma_8^{1.99} - \sigma_8^{0.89},$$

for $\ell = 10$ and $\ell = 10^4$, respectively. This change is because more weights are now attributed to lower haloes, hence probing a region of the mass function less sensitive to σ_8[10].

We finally consider the two types of mass scaling simultaneously, i.e. an increase in the galaxy-mass range using tanh modelling, and an increase for massive cluster using a power law at masses above $5 \times 10^{14}\ M_\odot$. This is depicted in Fig. 5 considering two values for the power law, i.e. $\gamma = 0.25$ in dotted green, and $\gamma = 1$ in dash-dotted orange. The scaling of the angular power spectra with the parameter σ_8 now is

$$C_\ell^\alpha \propto \begin{cases} \sigma_8^{2.56} - \sigma_8^{0.90} & \text{for } \gamma = 0.25, \\ \sigma_8^{7.00} - \sigma_8^{1.01} & \text{for } \gamma = 1, \end{cases}$$

[10] This is, once again, to be compared with the scaling obtained in Tashiro et al. (2008). Accounting for galaxies with a central magnetic field of $10\,\mu$G, the scaling obtained in Tashiro et al. (2008) is $\sigma_8^{5.5}$. The authors of Tashiro et al. (2008) however have a non-negligible contribution of the two-halo term which is vanishing in our study, hence the different scaling.

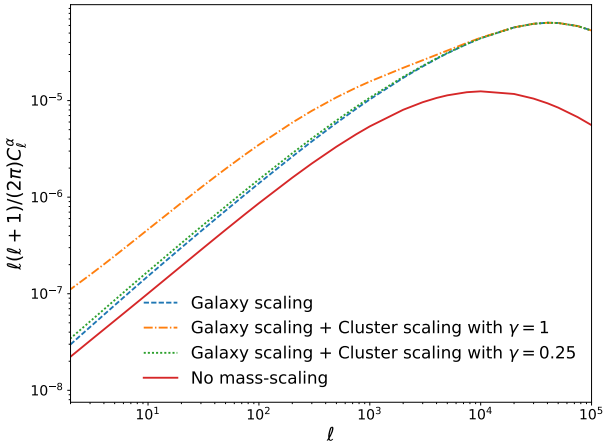

Fig. 5. Angular power spectrum for four models of the scaling of the magnetic field with the halo masses: (i) B_0 = const. in solid red; (ii) an increase of the magnetic field for galaxies, i.e. at masses lower than 10^{13} $M_\odot$ as given by Eq. (15) (dashed blue); and a combination of increased magnetic field for galaxies, Eq. (15), with a power law for massive clusters, Eq. (14), where (iii) $\gamma = 0.25$ (dotted green), and (iv) $\gamma = 1$ (dash-dotted orange).

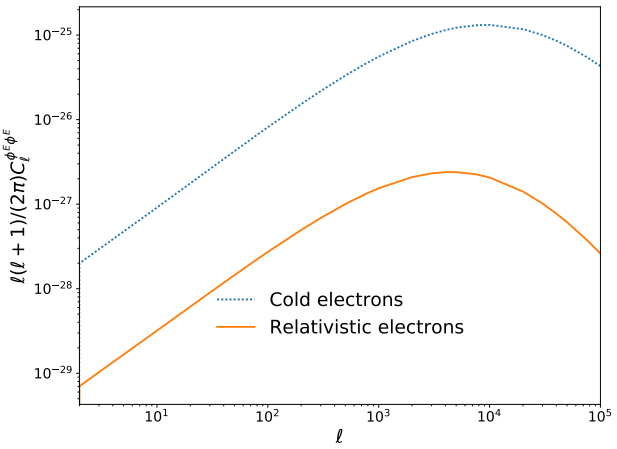

Fig. 6. Angular power spectra of the Faraday conversion rate $C_\ell^{\phi^E\phi^E}$ for thermal electrons (dotted-blue) and for relativistic electrons (solid-orange). For relativistic electrons, one set of $n_{\rm e}^{(r)} = 10^{-6}\,{\rm cm}^{-3}$ and $\Gamma_{\rm min} = 100$.

for $\ell = 10$ and $\ell = 10^4$, respectively. The case $\gamma = 1$ is particularly instructive. At large scales, dominated by massive cluster, we recover the scaling with σ_8 mainly driven by the high-mass region of the mass function. At small scales however, the scaling is dominated by low-mass objects, hence much less sensitive to σ_8. This has to be contrasted with the case of a magnetic field independent of the mass, for which the scaling with σ_8 ranges from $\sigma_8^{3.1}$ to $\sigma_8^{2.1}$ for $\ell = 10$ and $\ell = 10^4$.

4.2. Power spectra of the Faraday conversion rate

First, we found no significative difference between the two angular power spectra of the Faraday conversion rate, $C_\ell^{\phi^E\phi^E}$ and $C_\ell^{\phi^B\phi^B}$. Hence, for simplicity we now show results for the $C_\ell^{\phi^E\phi^E}$ power spectrum only.

In Fig. 6, we compare the angular power spectra of the Faraday conversion rate for two populations of free electrons, either thermal or relativistic. In the case of the relativistic electrons, the central density in the halo is taken to be constant, contrary to the cold case which follows Eq. (9). We took the value $n_e^{(r)} = 10^{-6}\,{\rm cm}^{-3}$ corresponding to $\Gamma_{\rm min} = 100$ and $\beta_E = 2.5$ (Colafrancesco et al. 2003). We note that with this specific choice for the spectral index we gets $n_{\rm e}^{(r)}\Gamma_{\rm min}^{1.5} = $ const. (see Sect. 2.3 and Colafrancesco et al. 2003). Since the amplitude of the angular power spectrum of the Faraday conversion rate is $\propto \left(n_{\rm e}^{(r)}\Gamma_{\rm min}\right)^2$, we obtain $C_\ell^{\phi^E\phi^E}$, which scales as $\propto (n_{\rm e}^{(r)})^{2/3}$ or conversely in terms of the Doppler factor as $\propto 1/\Gamma_{\rm min}$. For such values describing relativistic electrons, we find that $C_\ell^{\phi^E\phi^E}$ is $\sim$2 orders of magnitude higher in the thermal electron case compared to the relativistic case. This means that the number density of relativistic electrons should be pushed towards the unrealistic values of $\sim 10^{-3}\,{\rm cm}^{-3}$ for the relativistic contribution to equal those of thermal electrons. This would correspond to a minimal Lorentz factor of $\Gamma_{\rm min} \sim 1$, which is far below the values of $\sim$100 derived from the lifetime of relativistic electrons in the intracluster medium (Rephaeli 1979; Sarazin 1999).

The values of $n_{\rm e}^{(r)}$ used above are already over-optimistic with respect to the upper bound obtained on the number of cosmic rays (see Sect. 2.3). The contribution of relativistic electrons shown in Fig. 6 is thus a conservative upper bound, and we can safely neglect the case of relativistic electrons as compared to the contribution of thermal electrons.

4.2.1. Thermal electrons

The dependence of the angular power spectra of the Faraday conversion rate from thermal electrons on the density fluctuation amplitude σ_8 is similar to that of the Faraday rotation angle: i.e. $C_\ell^{\phi^E\phi^E} \propto \sigma_8^{3.1} - \sigma_8^{1.9}$ for $\ell = 10$ and $\ell = 10^4$, respectively; the difference between low ℓ and high ℓ values has already been explained. The small differences with Faraday rotation come from the fact that the Faraday conversion rate for the angular power spectra scales as $1/(1+z)^6$, where the conversion rate scales as $1/(1+z)^4$ for the Faraday rotation angle.

As for the Faraday rotation effect, there is almost no variation of the Faraday conversion rate with Ω_m, when varying $\Omega_{\rm CDM}$ and Ω_b kept fixed, the dependence is written as

$$C_\ell^{\phi^E\phi^E} \propto \Omega_m^{-0.1} - \Omega_m^{-0.2} \quad \text{or} \quad C_\ell^{\phi^E\phi^E} \propto \Omega_{\rm CDM}^{-0.1} - \Omega_{\rm CDM}^{0.2}$$

for $\ell = 10$ and $\ell = 10^4$, respectively.

When varying Ω_m via Ω_b instead ($\Omega_{\rm CDM}$ kept fixed), the dependence is not very different from Faraday rotation either, i.e.

$$C_\ell^{\phi^E\phi^E} \propto \Omega_m^{13} - \Omega_m^{12} \quad \text{or} \quad C_\ell^{\phi^E\phi^E} \propto \Omega_b^{2.0} - \Omega_b^{1.9}$$

for $\ell = 10$ and $\ell = 10^4$, respectively. Although these scalings are not very different from Faraday rotation, the same remark on the σ_8 scaling differences applies here, which is that the two effects scale differently with redshift.

We also investigate the degeneracy between a scaling in mass of the magnetic field at the centre of the halo and the σ_8 scaling, as what we have done for the Faraday rotation angle; see Fig. 7. The dependence in σ_8 is $C_\ell^{\phi^E\phi^E} \propto \sigma_8^{15}$ when $\gamma = 1$, $C_\ell^{\phi^E\phi^E} \propto \sigma_8^{12}$ when $\gamma = 0.75$, $C_\ell^{\phi^E\phi^E} \propto \sigma_8^{9.5}$ when $\gamma = 0.5$, and $C_\ell^{\phi^E\phi^E} \propto \sigma_8^{6.4}$ when $\gamma = 0.25$. When $\gamma = 0.5$ the angular power spectra scales with the mass to the four. This results in a scaling with σ_8 to the power 9.5. For a comparison, it was also 9.5 for the Faraday rotation angle when it scaled with the mass to the four, corresponding for this case to $\gamma = 1$, so that our analysis is consistent.

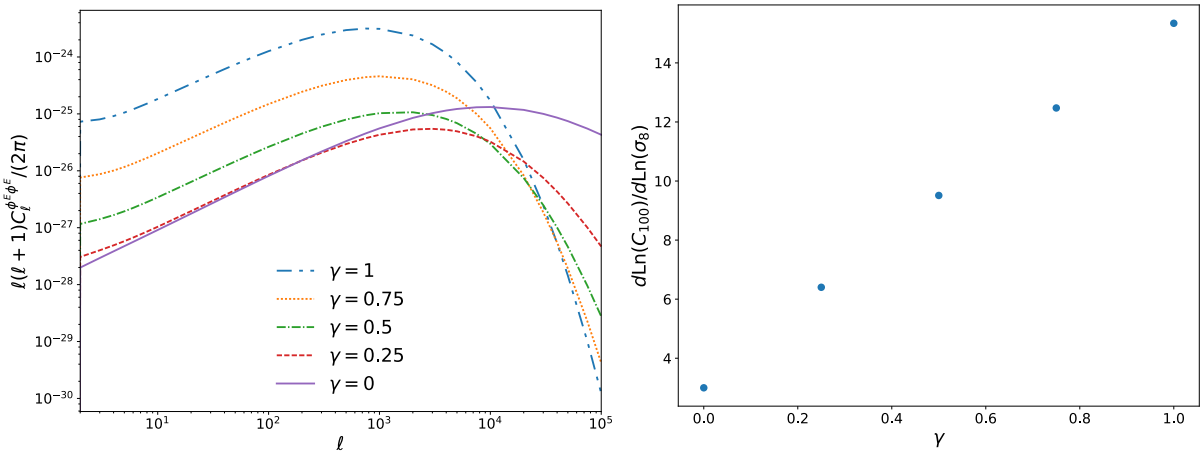

Fig. 7. *Left*: angular power spectra of the Faraday conversion rate, $C_\ell^{\phi^{E/B}\phi^{E/B}}$ when adding a mass dependence for the magnetic field strength at the centre scaling as $\sim(M/M_\mathrm{p})^\gamma$, where $M_\mathrm{p} = 5{\times}10^{13}\ M_\odot$ for different values of γ. *Right*: scaling of the angular power spectra with σ_8, $\mathrm{d}\ln C_{100}^\alpha/\mathrm{d}\ln\sigma_8$, as a function of γ. We chose to plot this effect for $\ell = 100$ as $C_\ell^{\phi^{E/B}\phi^{E/B}}$ depends more strongly on σ_8 for low ℓ values.

Table 2. Scaling of different large-scale-structure probes with σ_8 and Ω_m.

	σ_8	Ω_m
Faraday rotation power spectrum at $\ell \simeq 10^4$	2.1	−0.1
Faraday conversion power spectrum at $\ell \simeq 10^4$ (thermal electrons)	2.1	−0.1
Faraday conversion power spectrum at $\ell \simeq 10^4$ (relativistic electrons)	2.1	1
Halo number counts from thermal SZ	9	3
Thermal SZ power spectrum at $\ell \simeq 3000$	8.1	3.2
CMB lensing power spectrum at $\ell \simeq 30$	2	0.5

Notes. The scaling reported is to be understood as $P \propto \sigma_8^\mathrm{n}\,\Omega_m^\mathrm{p}$ with P any of the considered probe. These values are given at the peaking multipole of $\ell(\ell+1)C_\ell$ for the Faraday rotation angle, the Faraday conversion rate, the tSZ flux, and the peaking multipole of $\ell^2(\ell+1)^2C_\ell^{\phi\phi}$ for the lensing potential.

4.2.2. Relativistic electrons

We mention the case of Faraday conversion with relativistic electrons because the dependence of the angular power spectra with cosmological parameters is a bit different.

Indeed, when varying Ω_CDM and Ω_b kept fixed, the dependence is written as

$$C_\ell^{\phi^E\phi^E} \propto \Omega_m^{1.0} - \Omega_m^{0.7} \quad \text{or} \quad C_\ell^{\phi^E\phi^E} \propto \Omega_\mathrm{CDM}^{0.9} - \Omega_\mathrm{CDM}^{0.6}$$

for $\ell = 10$ and $\ell = 10^4$, respectively.

When varying Ω_b and Ω_CDM kept fixed, the dependence is written as

$$C_\ell^{\phi^E\phi^E} \propto \Omega_m^{0.9284} - \Omega_m^{0.2} \quad \text{or} \quad C_\ell^{\phi^E\phi^E} \propto \Omega_b^{0.1} - \Omega_b^{0.0}$$

for $\ell = 10$ and $\ell = 10^4$, respectively.

This difference in dependence compared to the thermal electron case is explained by the constant value for the density of relativistic free electrons at the centre of the halo, whereas the density of cold free electrons at the centre scales with the fraction of baryons f_b as well as the critical density ρ_c and the spherical overdensity Δ of the virialized haloes.

5. Conclusions

We revisited the derivation of the angular power spectrum of the Faraday rotation angle using the halo model and extended it to the case of Faraday conversion with an emphasis on the assumptions made for the statistics and orientations of magnetic fields inside haloes. Indeed, we first assumed the magnetic field of a halo to have a spherically symmetric profile but the same orientation over the halo scale. Second, the orientations are supposed to be uniformly distributed in the Universe to be consistent with the cosmological principle. Third, the orientations of magnetic fields in different haloes are independent from each other; the underlying idea is that magnetism is produced within halo in a local physical process. We also made the hypothesis that the distribution of the orientations of the magnetic fields inside haloes are independent from the abundance in mass and the spatial distribution of haloes. All of these hypotheses simplified the derivation of the angular power spectra: in particular, only the one-halo term remains because of the independence of the orientations from one halo to another.

We then explored the dependence of the angular power spectra with astrophysical and cosmological parameters. In Table 2, we report the scaling of the angular power spectra of the Faraday rotation angle and the Faraday conversion rate with the parameters σ_8 and Ω_m, assuming in this case that Ω_m would vary by a change of the cold dark matter density. We also reported in this table the scaling for three other probes of the large-scale structures, namely halo number counts as observed through the tSZ effect, the tSZ angular power spectrum, and the angular power spectrum of CMB lensing potential.

In particular, the angular power spectra of both Faraday rotation and Faraday conversion scale with the amplitude of the

density fluctuations as σ_8^3 while it scales with σ_8^8 to σ_8^9 for the other probes. However, this scaling with σ_8 is degenerated with a mass-dependent magnetic field[11]. Still the scaling with the matter density parameter Ω_m is in contrast to the tSZ and lensing probes: while for the SZ there is a scaling with Ω_m^3, in this case it is almost independent of this parameter. Thus the two effects could be combined to lift the degeneracy in the $\sigma_8 - \Omega_m$, assuming nonetheless the magnetic field mass-dependence model to be known. Conversely, a joint analysis could be used so as to infer the scaling of the magnetic fields with the masses of haloes.

Although other physical effects happen in the magnetized plasmas in haloes of galaxies, the dominant contributions are from Faraday rotation and Faraday conversion with thermal electrons as stated in Sect. 2. Indeed, an estimation of the angular power spectra of secondary anisotropies suggests that at 1 GHz, where a magnetic field of $10\,\mu$G and a density of relativistic electrons of $n_{\rm rel} = 10^{-5}\,{\rm cm}^{-3}$ for the absorption coefficients; there are 18 orders of magnitude between the secondary linearly polarized anisotropies produced thanks to Faraday rotation and those produced by absorption of intensity. Similarly, there are 9 orders of magnitude between the secondary circularly polarized anisotropies produced thanks to Faraday conversion and those produced by absorption of intensity. These differences in orders of magnitude do not change significantly when changing the frequency to 30 GHz and the magnetic field to $3\,\mu$G. Moreover, this is an ultra-conservative upper bound on such spectra since we consider in this paper a largely overestimated values for the number density of relativistic electrons. Thus, we can safely conclude that the secondary anisotropies induced by absorption would be negligible compared to the Faraday rotation and Faraday conversion induced anisotropies.

Acknowledgements. The authors would like to thank G. Fabbian, S. Ilic, M. Douspis, and the entire COSM!X team for helpful discussions. J.G. acknowledges funding by the ByoPiC project from the European Research Council (ERC) under the European Union's Horizon 2020 research and innovation programme grant agreement ERC-2015-AdG 695561. Part of the research described in this paper was carried out at the Jet Propulsion Laboratory, California Institute of Technology, under a contract with the National Aeronautics and Space Administration (NASA).

References

Ade, P. A. R., POLARBEAR Collaboration, et al. 2014, Phys. Rev. Lett., 113, 021301
Athreya, R. M., Kapahi, V. K., McCarthy, P. J., & van Breugel, W. 1998, A&A, 329, 809
Blasi, P., & Colafrancesco, S. 1999, Astropart. Phys., 12, 169
Bonafede, A., Feretti, L., Giovannini, G., et al. 2009, A&A, 503, 707
Bonafede, A., Feretti, L., Murgia, M., et al. 2010, A&A, 513, A30
Campanelli, L., Dolgov, A. D., Giannotti, M., & Villante, F. L. 2004, ApJ, 616, 1
Carroll, S. M. 1998, Phys. Rev. Lett., 81, 3067
Carron, J., Lewis, A., & Challinor, A. 2017, JCAP, 1705, 035
Cavaliere, A., & Fusco-Femiano, R. 1978, A&A, 70, 677
Cavaliere, A., & Lapi, A. 2013, Phys. Rep., 533, 69
Colafrancesco, S., Marchegiani, P., & Palladino, E. 2003, A&A, 397, 27
Cole, S., & Kaiser, N. 1988, MNRAS, 233, 637
Cooray, A., & Sheth, R. K. 2002, Phys. Rept., 372, 1
Cooray, A., Melchiorri, A., & Silk, J. 2003, Phys. Lett. B, 554, 1
De, S., & Tashiro, H. 2015, Phys. Rev. D, 92, 123506
Despali, G., Giocoli, C., Angulo, R. E., et al. 2016, MNRAS, 456, 2486
Ejlli, D. 2017, Phys. Rev. D, 96, 023540
Ejlli, D. 2018, Nucl. Phys. B, 935, 83
Ejlli, D. 2019, Eur. Phys. J. C, 79, 231
Giodini, S., Lovisari, L., Pointecouteau, E., et al. 2013, Space Sci. Rev., 177, 247
Giovannini, M. 2010, Phys. Rev. D, 81, 023003
Govoni, F., Murgia, M., Feretti, L., et al. 2006, A&A, 460, 425
Hernandez-Monteagudo, C., Verde, L., Jimenez, R., & Spergel, D. N. 2006, ApJ, 643, 598
Heyvaerts, J., Pichon, C., Prunet, S., & Thiébaut, J. 2013, MNRAS, 430, 3320
Hirata, C. M., & Seljak, U. 2003, Phys. Rev. D, 68, 083002
Huang, L., Liu, S., Shen, Z.-Q., et al. 2009, ApJ, 703, 557
Huber, B., Tchernin, C., Eckert, D., et al. 2013, A&A, 560, A64
Hummel, E., Beck, R., & Dahlem, M. 1991, A&A, 248, 23
Hurier, G., & Lacasa, F. 2017, A&A, 604, A71
Kamionkowski, M. 2018, Phys. Rev. D, 97, 123529
Kamionkowski, M., Kosowsky, A., & Stebbins, A. 1997, Phys. Rev. D, 55, 7368
Kennett, M., & Melrose, D. 1998, PASA, 15, 211
Kim, K. T., Kronberg, P. P., Giovannini, G., & Venturi, T. 1989, Nature, 341, 720
Komatsu, E., & Kitayama, T. 1999, ApJ, 526, L1
Kosowsky, A., & Loeb, A. 1996, ApJ, 469, 1
Kosowsky, A., Kahniashvili, T., Lavrelashvili, G., & Ratra, B. 2005, Phys. Rev. D, 71, 043006
Kunz, M. W., Schekochihin, A. A., Cowley, S. C., Binney, J. J., & Sanders, J. S. 2011, MNRAS, 410, 2446
Li, M., & Zhang, X. 2008, Phys. Rev. D, 78, 103516
LoVerde, M., & Afshordi, N. 2008, Phys. Rev. D, 78, 123506
Lue, A., Wang, L.-M., & Kamionkowski, M. 1999, Phys. Rev. Lett., 83, 1506
Mainini, R., Minelli, D., Gervasi, M., et al. 2013, JCAP, 1308, 033
Makino, N., & Suto, Y. 1993, ApJ, 405, 1
Marian, L., & Bernstein, G. M. 2007, Phys. Rev. D, 76, 123009
Melrose, D. B., & McPhedran, R. C. 2005, Electromagnetic Processes in Dispersive Media, 431 (Cambridge: Cambridge University Press),
Montero-Camacho, P., & Hirata, C. M. 2018, JCAP, 1808, 040
Murgia, M., Govoni, F., Feretti, L., et al. 2004, A&A, 424, 429
Nagy, J. M., Ade, P. A. R., Amiri, M., et al. 2017, ApJ, 844, 151
Ohno, H., Takada, M., Dolag, K., Bartelmann, M., & Sugiyama, N. 2003, ApJ, 584, 599
Okamoto, T., & Hu, W. 2003, Phys. Rev. D, 67, 083002
Planck Collaboration Int. XLVI. 2016, A&A, 596, A107
Pospelov, M., Ritz, A., Skordis, C., Ritz, A., & Skordis, C. 2009, Phys. Rev. Lett., 103, 051302
Rephaeli, Y. 1979, ApJ, 227, 364
Sarazin, C. L. 1999, ApJ, 520, 529
Sawyer, R. F. 2015, Phys. Rev. D, 91, 021301
Sazonov, V. N. 1969, Sov. Ast., 13, 396
Scoccola, C., Harari, D., & Mollerach, S. 2004, Phys. Rev. D, 70, 063003
Seljak, U., & Hirata, C. M. 2004, Phys. Rev. D, 69, 043005
Shcherbakov, R. V. 2008, ApJ, 688, 695
Sherwin, B. D., & Schmittfull, M. 2015, Phys. Rev. D, 92, 043005
Sigurdson, K., & Cooray, A. 2005, Phys. Rev. Lett., 95, 211303
Simons Observatory Collaboration (Ade, P., et al.) 2019, JCAP, 1902, 056
Smith, K. M., Hanson, D., LoVerde, M., Hirata, C. M., & Zahn, O. 2012, JCAP, 1206, 014
Suzuki, A., Ade, P. A. R., Akiba, Y., et al. 2018, J. Low Temp. Phys., 193, 1048
Takada, M., Ohno, H., & Sugiyama, N. 2001, [arXiv:astro-ph/0112412]
Tashiro, H., Aghanim, N., & Langer, M. 2008, MNRAS, 384, 733
Tashiro, H., Silk, J., Langer, M., & Sugiyama, N. 2009, MNRAS, 392, 1421
Tinker, J., Kravtsov, A. V., Klypin, A., et al. 2008, ApJ, 688, 709
Vacca, V., Murgia, M., Govoni, F., et al. 2012, A&A, 540, A38
Varshalovich, D., Moskalev, A., & Khersonskiĭ, V. 1988, Quantum Theory of Angular Momentum: Irreducible Tensors, Spherical Harmonics, Vector Coupling Coefficients, 3nj Symbols (World Scientific Pub.)
Widrow, L. M. 2002, Rev. Mod. Phys., 74, 775
Yadav, A. P. S., Biswas, R., Su, M., & Zaldarriaga, M. 2009, Phys. Rev. D, 79, 123009
Zaldarriaga, M., & Seljak, U. 1997, Phys. Rev. D, 55, 1830
Zaldarriaga, M., & Seljak, U. 1998, Phys. Rev. D, 58, 023003

[11] The impact of the scaling of B with the mass can be viewed as the equivalent of the mass bias in the analysis of the tSZ number counts and angular power spectrum.

Appendix A: Formal derivation of the angular power spectra for any effect considered

A.1. Radiative transfer coefficients

Looking at the expressions of the different radiative transfer coefficients reveals that they can assume two possible forms. These forms are first of scalar type as the Faraday rotation angle, and they read as an integral over the line of sight and over the halo distribution as follows:

$$\alpha(\boldsymbol{n}) = \int_0^{r_{\rm CMB}} a(r)\mathrm{d}r \iint \mathrm{d}M_i \mathrm{d}^3\boldsymbol{x}_i\, n_h(\boldsymbol{x}_i) \times [\boldsymbol{b}(\boldsymbol{x}_i)\cdot\boldsymbol{n}]\, A\left(M_i, |\boldsymbol{x}-\boldsymbol{x}_i|\right). \tag{A.1}$$

In the above, the dependence over orientations is encoded in $[\boldsymbol{b}(\boldsymbol{x}_i)\cdot\boldsymbol{n}]$, which is a scalar function. The function A is the profile of the effect, which is for Faraday rotation by thermal electrons

$$A\left(M_i, |\boldsymbol{x}-\boldsymbol{x}_i|\right) = \left(\frac{e^3}{8\pi^2\, m_{\rm e}^2\, c\, \varepsilon_0 \nu^2(r)}\right) n_{\rm e}\left(|\boldsymbol{x}-\boldsymbol{x}_i|\right) B\left(|\boldsymbol{x}-\boldsymbol{x}_i|\right). \tag{A.2}$$

Since projection effects can only reduce the impact of the effect, the quantity A can be interpreted as the maximum of the effect a given halo can generate. Finally, $n_{\rm h}$ is the halo distribution. The above scalar-type of coefficients are the Faraday rotation angle and the conversion from intensity to circular polarization, $\phi^{I\to V}$.

The second type of coefficients are those which are proportional to $B_\perp^2 e^{\pm 2\mathrm{i}\gamma}$, where $B_\perp$ is the amplitude of the projected magnetic field on the plane orthogonal to the line of sight, and γ the angle between the projected magnetic field with the basis vector $\boldsymbol{e}_\theta$ in that plane. This is typical of the coefficients for Faraday conversion, $\phi^{P\to V}$, or conversion from intensity to linear polarization, $\phi^{I\to P}$. In terms of the amplitude of the magnetic field, B, and its orientation $\boldsymbol{b}$, the phase is $B_\perp^2 e^{\pm 2i\gamma} = B\left[\boldsymbol{b}\cdot\left(\boldsymbol{e}_\theta \pm \mathrm{i}\boldsymbol{e}_\varphi\right)\right]^2$. We thus have spin-(±2) coefficients reading as an integral over the line of sight as follows:

$$i\phi^{P\to V}(\boldsymbol{n}) e^{\pm 2\mathrm{i}\gamma(\boldsymbol{n})} = \int_0^{r_{\rm CMB}} a(r)\mathrm{d}r \iint \mathrm{d}M_i \mathrm{d}^3\boldsymbol{x}_i\, n_h(\boldsymbol{x}_i) \times \left[\boldsymbol{b}\cdot\left(\boldsymbol{e}_\theta \pm \mathrm{i}\boldsymbol{e}_\varphi\right)\right]^2 P\left(M_i, |\boldsymbol{x}-\boldsymbol{x}_i|\right). \tag{A.3}$$

The spin structure of the above is entirely encoded in projection coefficients $\left[\boldsymbol{b}\cdot\left(\boldsymbol{e}_\theta \pm \mathrm{i}\boldsymbol{e}_\varphi\right)\right]^2$. The other terms are identical to those in scalar coefficients, except that the profile of the effect, $P\left(r, |\boldsymbol{x}-\boldsymbol{x}_i|\right)$, admits a different explicit expression, for example for Faraday conversion by thermal electrons

$$P\left(M_i, |\boldsymbol{x}-\boldsymbol{x}_i|\right) = \left(\frac{e^4}{16\pi^2 m_{\rm e}^2 c^3 \nu^3(r)}\right) n_{\rm e}\left(|\boldsymbol{x}-\boldsymbol{x}_i|\right) B^2\left(|\boldsymbol{x}-\boldsymbol{x}_i|\right). \tag{A.4}$$

Apart from the explicit expression of P, the formal expression of the coefficient remains the same for relativistic electrons or for conversion from intensity to linear polarization.

A formal expression for all the above radiative transfer coefficients can be abstracted from that above. On denoting ϕ_s any such coefficients, where $s = 0$ for scalar coefficients and $s = \pm 2$ for the spin coefficients, this is given by

$$\phi_s(\boldsymbol{n}) = \int_0^{r_{\rm CMB}} a(r)\mathrm{d}r \times \iint \mathrm{d}M_i \mathrm{d}^3\boldsymbol{x}_i\, n_h(\boldsymbol{x}_i)\, f_s(\boldsymbol{b}_i, \boldsymbol{n}) \Phi\left(M_i, |\boldsymbol{x}-\boldsymbol{x}_i|\right), \tag{A.5}$$

where $\Phi\left(r, |\boldsymbol{x}-\boldsymbol{x}_i|\right)$ the profile amounting the maximum amount of the effect, which is a scalar function, and $f_{\rm s}(\boldsymbol{b}_i, \boldsymbol{n})$ the function encoding the impact of projecting the magnetic field; the subscript i reminds us that the orientation is a priori a function of the haloes positions, $\boldsymbol{x}_i$. This is this last function which contains the spin structure of the considered coefficients.

A.2. Angular power spectrum

To compute the angular power spectrum, the usual approach consists in first computing the multipolar coefficients of $\phi_s(\boldsymbol{n})$ thanks to $\phi_{s,\ell,m} = \int \mathrm{d}\boldsymbol{n}\phi_s(\boldsymbol{n}) {}_sY^\star_{\ell m}(\boldsymbol{n})$, and then to consider the two-point correlation between these multipolar coefficients, $\left\langle \phi^{(1)}_{s,\ell m} \phi^{(2)\,\star}_{s',\ell' m'} \right\rangle$ (superscripts 1, 2 labels two possibly different radiative transfer coefficients). The fields ϕ_s being statistically homogeneous and isotropic, the two-point correlation of multipolar coefficients is entirely described by an angular power spectrum, i.e. $\left\langle \phi^{(1)}_{s,\ell m} \phi^{(2)\,\star}_{s',\ell' m'} \right\rangle = C_\ell^{(1,2)}\, \delta_{\ell,\ell'} \delta_{m,m'}$.

We adopt a slightly different path (totally equivalent though) by first considering the two-point correlation function on the sphere, denoted $\xi_{1,2}(\boldsymbol{n}_1, \boldsymbol{n}_2) = \left\langle \phi_s^{(1)}(\boldsymbol{n}_1) \phi_{s'}^{(2)}(\boldsymbol{n}_2) \right\rangle$, which is further simplified thanks to our assumption about the statistics of the magnetic fields orientations. The two-point correlation of the multipolar coefficients is secondly derived from the two-point correlation function via $\left\langle \phi_{s,\ell m} \phi^\star_{s',\ell' m'} \right\rangle = \int \mathrm{d}\boldsymbol{n}_1 \int \mathrm{d}\boldsymbol{n}_2\, \xi_{1,2}(\boldsymbol{n}_1, \boldsymbol{n}_2) {}_sY^\star_{\ell m}(\boldsymbol{n}_1) {}_{s'}Y_{\ell m}(\boldsymbol{n}_2)$.

Assuming that orientations of the magnetic fields is not correlated to the spatial distribution of haloes leads to

$$\xi_{1,2}(\boldsymbol{n}_1, \boldsymbol{n}_2) = \int_0^{r_{\rm CMB}} [a(r_1)\mathrm{d}r_1]\,[a(r_2)\mathrm{d}r_2] \times \iint \left[\mathrm{d}M_i \mathrm{d}^3\boldsymbol{x}_i\right]\left[\mathrm{d}M_j \mathrm{d}^3\boldsymbol{x}_j\right] \Phi^{(1)} \times \left(M_i, |\boldsymbol{x}_1 - \boldsymbol{x}_i|\right) \Phi^{(2)}\left(M_j, \left|\boldsymbol{x}_2 - \boldsymbol{x}_j\right|\right) \times \left\langle n_{\rm h}(\boldsymbol{x}_i) n_{\rm h}(\boldsymbol{x}_j) \right\rangle \left\langle f_s(\boldsymbol{b}_i, \boldsymbol{n}_1) f_{s'}(\boldsymbol{b}_j, \boldsymbol{n}_2) \right\rangle. \tag{A.6}$$

Since the orientation of the magnetic fields of two different haloes is uncorrelated, this gives $\left\langle f_s(\boldsymbol{b}_i, \boldsymbol{n}_1) f_{s'}(\boldsymbol{b}_j, \boldsymbol{n}_2) \right\rangle \propto \delta_{i,j}$, and only the one-halo term contributes to the two-point cross-correlation function. In addition, these orientations are statistically homogeneous and isotropic, meaning that $\left\langle f_s(\boldsymbol{b}_i, \boldsymbol{n}_1) f_{s'}(\boldsymbol{b}_j, \boldsymbol{n}_2) \right\rangle$ is a function of $\left|\boldsymbol{x}_i - \boldsymbol{x}_j\right|$ only. Because there is only the one-halo term, this relative distance is zero and $\left\langle f_s(\boldsymbol{b}_i, \boldsymbol{n}_1) f_{s'}(\boldsymbol{b}_j, \boldsymbol{n}_2) \right\rangle$ is a function of $\boldsymbol{n}_1$ and $\boldsymbol{n}_2$, i.e. $\left\langle f_s(\boldsymbol{b}_i, \boldsymbol{n}_1) f_{s'}(\boldsymbol{b}_j, \boldsymbol{n}_2) \right\rangle = \xi^O_{s,s'}(\boldsymbol{n}_1, \boldsymbol{n}_2)\, \delta_{i,j}$. Hence the two-point correlation function boils down to

$$\xi_{1,2}(\boldsymbol{n}_1, \boldsymbol{n}_2) = \xi^O_{s,s'}(\boldsymbol{n}_1, \boldsymbol{n}_2) \times \int_0^{r_{\rm CMB}} [a(r_1)\mathrm{d}r_1]\,[a(r_2)\mathrm{d}r_2] \times \iint \mathrm{d}M_i \mathrm{d}^3\boldsymbol{x}_i \frac{\mathrm{d}N}{\mathrm{d}M} \Phi^{(1)}\left(M_i, |\boldsymbol{x}_1 - \boldsymbol{x}_i|\right) \Phi^{(2)} \times \left(M_i, |\boldsymbol{x}_2 - \boldsymbol{x}_i|\right), \tag{A.7}$$

where the mass function arises from the one-halo average of the abundance $\left\langle n_{\rm h}^2(\boldsymbol{x}_i) \right\rangle = \mathrm{d}N/\mathrm{d}M$. The function $\xi^O_{s,s'}(\boldsymbol{n}_1, \boldsymbol{n}_2)$ is interpreted as the correlation function of orientations, while the remaining term is the one-halo contribution of the two-point correlation function of the amplitude of the radiative transfer coefficient. Let us denote this second correlation function $\xi^\Phi_{1,2}$.

The full correlation function is thus a product of two correlation functions, one for the orientation and one for the amplitude of the coefficient, i.e.

$$\xi_{1,2}(\boldsymbol{n}_1,\boldsymbol{n}_2) = \xi^{O}_{s,s'}(\boldsymbol{n}_1,\boldsymbol{n}_2) \times \xi^{\Phi}_{1,2}(\boldsymbol{n}_1,\boldsymbol{n}_2). \tag{A.8}$$

The correlation function of the amplitude, $\xi^{\Phi}_{1,2}$, is formally identical to the one-halo term of the correlation function of, for example the tSZ effect, which is well known to be described by an angular power spectrum, i.e.

$$\xi^{\Phi}_{1,2}(\boldsymbol{n}_1,\boldsymbol{n}_2) = \sum_{L,M} D^{\Phi}_L \, Y_{LM}(\boldsymbol{n}_1) Y^{\star}_{LM}(\boldsymbol{n}_2), \tag{A.9}$$

where D^{Φ}_L is the angular power spectrum. Similarly, the correlation function of orientations is described by an angular power spectrum, $D^{O}_{L'}$, since this is a statisically homogeneous and isotropic field, i.e.

$$\xi^{O}_{s,s'}(\boldsymbol{n}_1,\boldsymbol{n}_2) = \sum_{L'M'} D^{O}_{L'} \, {}_sY_{L'M'}(\boldsymbol{n}_1) {}_{s'}Y^{\star}_{L'M'}(\boldsymbol{n}_2). \tag{A.10}$$

We note that in the above, spin-weighted spherical harmonics are used to take into account the non-zero spins of the projected orientations.

Plugging Eqs. (A.9) and (A.10) into Eq. (A.8), and then taking the spherical harmonic transforms of $\xi_{1,2}$, we show that $\left\langle \phi^{(1)}_{s,\ell m} \phi^{(2)\,\star}_{s',\ell' m'} \right\rangle$ can be expressed as a function of Gaunt integrals, the latter being defined as

$$G^{\ell_1 m_1 s_1}_{\ell_2 m_2 s_2; \ell_3 m_3 s_3} = \int \mathrm{d}\hat{\boldsymbol{n}} \, {}_{s_1}Y_{\ell_1 m_1}(\hat{\boldsymbol{n}}) \times {}_{s_2}Y_{\ell_2 m_2}(\hat{\boldsymbol{n}}) \times {}_{s_3}Y_{\ell_3 m_3}(\hat{\boldsymbol{n}}). \tag{A.11}$$

Gaunt integrals can be casted as products of Wigner-3j symbols. By then using triangular conditions and symmetries of the Wigner symbols (Varshalovich et al. 1988), we find

$$\begin{aligned}\left\langle \phi^{(1)}_{s,\ell m} \phi^{(2)\,\star}_{s',\ell' m'} \right\rangle = \frac{\sqrt{(2\ell+1)(2\ell'+1)}}{4\pi} \sum_{L,L'} (2L+1)(2L'+1) \\ \times D^{\Phi}_L \, D^{O}_{L'} \begin{pmatrix} L' & L & \ell \\ -s & 0 & s \end{pmatrix} \begin{pmatrix} L' & L & \ell' \\ -s' & 0 & s' \end{pmatrix} \\ \times \sum_{M,M'} \begin{pmatrix} L' & L & \ell \\ M' & M & -m \end{pmatrix} \begin{pmatrix} L' & L & \ell' \\ M' & M & -m' \end{pmatrix}.\end{aligned} \tag{A.12}$$

The last summation over M and M' of two Wigner-3js is equal to $(2\ell+1)^{-1}\,\delta_{\ell,\ell'}\,\delta_{m,m'}$. We thus finally obtain that the correlation matrix of the multipolar coefficients is diagonal (as expected for statistically homogeneous and isotropic process), i.e.

$$\left\langle \phi^{(1)}_{s,\ell m} \phi^{(2)\,\star}_{s',\ell' m'} \right\rangle = C^{(1,2)}_{\ell} \, \delta_{\ell,\ell'} \, \delta_{m,m'}, \tag{A.13}$$

where the angular power spectrum of the Faraday effect is given by

$$\begin{aligned}C^{(1,2)}_{\ell} = \frac{1}{4\pi} \sum_{L,L'} (2L+1)(2L'+1) \begin{pmatrix} L' & L & \ell \\ -s & 0 & s \end{pmatrix} \\ \times \begin{pmatrix} \ell & L & \ell \\ -s' & 0 & s' \end{pmatrix} D^{\Phi}_L \, D^{O}_{L'}.\end{aligned} \tag{A.14}$$

Since the two-point correlation function is the product of two two-point correlation functions, we consistently find that the angular power spectrum is the convolution of the respective two angular power spectra D^{Φ}_L and $D^{O}_{L'}$.

Appendix B: Derivation of D^A_L

B.1. Uniformly oriented magnetic field

We describe the derivation of the expression of D^A_ℓ. This is very reminiscent to the calculation of the angular power spectrum of, for example the tSZ effect (see e.g. Cole & Kaiser 1988; Makino & Suto 1993; Komatsu & Kitayama 1999), simplified in this work since we only need to derive the one-halo term. To this end let us define $A(\hat{\boldsymbol{n}})$ such that

$$\begin{aligned}A(\hat{\boldsymbol{n}}) = \frac{e^3}{8\pi^2 \, m_{\rm e}^2 \, c \, \varepsilon_0} \int_0^{r_{\rm CMB}} \frac{a(r)\mathrm{d}r}{\nu^2(r)} \\ \times \iint \mathrm{d}M_i \mathrm{d}^3\boldsymbol{x}_i n_{\rm h}(\boldsymbol{x}_i) X\left(|\boldsymbol{x}-\boldsymbol{x}_i|\right).\end{aligned} \tag{B.1}$$

Then D^A_L is the angular power spectrum of the above quantity restricted to its one-halo contribution.

The integral over $\boldsymbol{x}_i$ in $A(\boldsymbol{n})$ is the convolution of the halo abundance, $n_{\rm h}$, where the profile of the halo, X. This is then written as a product in Fourier space to get

$$\begin{aligned}A(\boldsymbol{n}) = \frac{e^3}{8\pi^2 \, m_{\rm e}^2 \, c \, \varepsilon_0} \int_0^{r_{\rm CMB}} \frac{a(r)\mathrm{d}r}{\nu^2(r)} \\ \times \iint \mathrm{d}M_i \, \mathrm{d}^3\boldsymbol{k} \, \widetilde{n}_h(\boldsymbol{k}, M_i) \, \widetilde{X}(\boldsymbol{k}) e^{\mathrm{i}\boldsymbol{k}\cdot\boldsymbol{x}},\end{aligned} \tag{B.2}$$

where $\tilde{f}(\boldsymbol{k})$ means the three-dimensional Fourier transform of $f(\boldsymbol{x}_i)$. Because the radial profile is spherically symmetric, it only depends on the norm of the wavevector $k \equiv |\boldsymbol{k}|$ and can be expressed using spherical Bessel functions

$$\widetilde{X}(\boldsymbol{k}) = \widetilde{X}(k) = \sqrt{\frac{2}{\pi}} \int_0^{\infty} \mathrm{d}R \, R^2 \, X(R) \, j_0(kR), \tag{B.3}$$

where $R \equiv |\boldsymbol{x}-\boldsymbol{x}_i|$ and j_0 is the spherical Bessel function at order $\ell = 0$. We further make use of the Rayleigh formula to express the $e^{\mathrm{i}\boldsymbol{k}\cdot\boldsymbol{x}}$ using spherical Bessel functions and spherical harmonics. The multipolar coefficients are then obtained through $A_{LM} = \int \mathrm{d}\boldsymbol{n} \, A(\boldsymbol{n}) Y^{\star}_{LM}(\boldsymbol{n})$ leading to

$$\begin{aligned}A_{LM} = \frac{e^3}{8\pi^2 \, m_{\rm e}^2 \, c \, \varepsilon_0} \int_0^{r_{\rm CMB}} \frac{a(r)\mathrm{d}r}{\nu^2(r)} \iint \mathrm{d}M_i \, \mathrm{d}^3\boldsymbol{k} \, \widetilde{n}_h(\boldsymbol{k}, M_i) \, \widetilde{X}(k) \\ \times (4\pi)(i)^L \, j_L(kr) \, Y^{\star}_{LM}(\boldsymbol{k}/k).\end{aligned} \tag{B.4}$$

The two-point correlation of the above set of multipolar coefficients involves the auto-correlation of the Fourier transform of the halo abundance. The Poisson part of the two-point correlation of the halo density field is $\left\langle n^2_{\rm h}(\boldsymbol{x}_i, M_i) \right\rangle = (\mathrm{d}N/\mathrm{d}M_i)\,\delta(M_i - M_j)\,\delta^3(\boldsymbol{x}_i - \boldsymbol{x}_j)$, where $\mathrm{d}N/\mathrm{d}M_i$ is the mass function. The corresponding power spectrum is constant (independent of scale): $\left\langle \widetilde{n}_{\rm h}(\boldsymbol{k}) \widetilde{n}^{\star}_{\rm h}(\boldsymbol{q}) \right\rangle = (\mathrm{d}N/\mathrm{d}M_i)\,\delta(M_i - M_j)\,\delta^3(\boldsymbol{k}-\boldsymbol{q})$. Thanks to the scale independence of this power spectrum and to the fact that the Fourier-transformed profile of the angle depends on k only, we can perform the integral over $(\boldsymbol{k}/k)$ to get

$$\left\langle A_{LM} A^{\star}_{L'M'} \right\rangle = D^A_L \, \delta_{L,L'} \, \delta_{M,M'}, \tag{B.5}$$

where the angular power spectrum is written as

$$\begin{aligned}D^A_L = \left(\frac{e^3}{2\pi \, m_{\rm e}^2 \, c \, \varepsilon_0}\right)^2 \int_0^{r_{\rm CMB}} \frac{a(r_1)\,\mathrm{d}r_1}{\nu^2(r_1)} \int_0^{r_{\rm CMB}} \frac{a(r_2)\,\mathrm{d}r_2}{\nu^2(r_2)} \\ \times \int \mathrm{d}M \, \frac{\mathrm{d}N}{\mathrm{d}M} \int k^2 \, \mathrm{d}k \, \left|\widetilde{X}(k)\right|^2 \, j_L(kr_1) \, j_L(kr_2).\end{aligned} \tag{B.6}$$

The numerical evaluation of the angular power spectrum D_L as derived above is still prohibitive because of the presence of the highly oscillating Bessel functions. It is however built from expressions of the form

$$\iint \mathrm{d}r_1\,\mathrm{d}r_2\,H_1(r_1)\,H_2(r_2)\int\frac{2k^2\,\mathrm{d}k}{\pi}\,P(k)\,j_\ell(kr_1)\,j_\ell(kr_2),$$

which can be simplified using the Limber approximation (LoVerde & Afshordi 2008). Using this approximation, we obtain

$$D_L^A=\left(\frac{e^3}{m_\mathrm{e}^2\,c\,\varepsilon_0\,\sqrt{8\pi}}\right)^2\int_0^{r_\mathrm{CMB}}\mathrm{d}r\frac{a^2(r)}{r^2\,\nu^4(r)}\times\int\mathrm{d}M\,\frac{\mathrm{d}N}{\mathrm{d}M}\left|\widetilde{X}\left(\frac{L+1/2}{r}\right)\right|^2. \tag{B.7}$$

We finalize our expression of the angular power spectrum D_L^A by introducing the projected Fourier transform of the profile. To this end, we first note that $X(R)=X^{(c)}(M,z,B_c)\,U(R/R_c)$, where B_c is the mean magnetic field strength at the centre of the halo (which can also depend on M and z; see Tashiro et al. (2008)), and U is a normalized profile which only depends on the ratio of the comoving distance from the centre, R, to the typical comoving radius of the halo, R_c, which is also a function of z and M. For a β-profile, this is written as $X^{(c)}=n_\mathrm{e}^{(c)}B_\mathrm{c}$ and $U(R/R_\mathrm{c})=(1+R/R_\mathrm{c})^{-3\beta(1+\mu)/2}$.

Introducing the variable $x=R/R_\mathrm{c}$ and physical radius of the halo, $r_\mathrm{c}^{(\mathrm{phys})}=a(z)R_\mathrm{c}$, we find

$$\widetilde{X}\left(\frac{\ell+1/2}{r}\right)=\left(\frac{r^2}{a(r)}\right)X^{(c)}\times\sqrt{\frac{2}{\pi}}\left(\frac{r_\mathrm{c}^{(\mathrm{phys})}}{\ell_\mathrm{c}^2}\right)\times\int_0^\infty U(x)\,j_0\left((\ell+1/2)x/\ell_\mathrm{c}\right)\,x^2\,\mathrm{d}x,$$

where $\ell_\mathrm{c}=D_\mathrm{ang}(z)/r_\mathrm{c}^{(\mathrm{phys})}$, which is the typical multipole associated with the typical size of the halo (the latter being also a function of M and z through $r_\mathrm{c}^{(\mathrm{phys})}$), and $D_\mathrm{ang}(z)$ the angular diameter distance. By defining the projected Fourier transform of the profiles

$$\alpha_\ell(M,z)=\sqrt{\frac{2}{\pi}}\left(\frac{r_\mathrm{c}^{(\mathrm{phys})}}{\ell_\mathrm{c}^2}\right)\int_0^\infty U(x)\,j_0((\ell+1/2)x/\ell_\mathrm{c})\,x^2\,\mathrm{d}x, \tag{B.8}$$

the angular power spectrum D_L is then written as

$$D_L^A=\left(\frac{e^3}{m_\mathrm{e}^2\,c\,\varepsilon_0\,\sqrt{8\pi}}\right)^2\int\frac{\mathrm{d}z}{\nu^4(z)}\frac{\mathrm{d}r}{\mathrm{d}z}\,r^2\int\mathrm{d}M\,\frac{\mathrm{d}N}{\mathrm{d}M}\,\left|X^{(c)}\right|^2\,\alpha_L^2. \tag{B.9}$$

B.2. Adding a stochastic contribution to the magnetic field

Adding a contribution of a stochastic component to the magnetic field is done by amending Eq. (B.4) as follows: we replace the Fourier transform of the profile $X([\boldsymbol{x}-\boldsymbol{x}_i|)$ by

$$\widetilde{X}(\boldsymbol{k})\rightarrow\widetilde{\mathcal{X}}(\boldsymbol{k})=\int\mathrm{d}^3q\widetilde{X}(\boldsymbol{q})\widehat{b}\,(\boldsymbol{k}-\boldsymbol{q}), \tag{B.10}$$

where $\hat{b}$ is a stochastic variable described by a statistically isotropic power spectrum. This is just the convolution of the profile with some random component described by a power spectrum. This gives for the two-point correlation of the multipolar coefficients

$$\left\langle A_{LM}A^\star_{L'M'}\right\rangle=\left(\frac{e^3}{2\pi\,m_\mathrm{e}^2\,c\,\varepsilon_0}\right)^2\int_0^{r_\mathrm{CMB}}\frac{a(r_1)\,\mathrm{d}r_1}{\nu^2(r_1)}\int_0^{r_\mathrm{CMB}}\frac{a(r_2)\,\mathrm{d}r_2}{\nu^2(r_2)}\times\int\mathrm{d}M\,\frac{\mathrm{d}N}{\mathrm{d}M}\times\int\mathrm{d}^3k\left\langle\left|\widetilde{\mathcal{X}}(\boldsymbol{k})\right|^2\right\rangle(i)^{L-L'}\times j_L(kr)\,j_{L'}(kr)\,Y^\star_{LM}(\boldsymbol{k}/k)\,Y_{L'M'}(\boldsymbol{k}/k). \tag{B.11}$$

We note that only the diagonal of the spectrum, i.e. $\left\langle\left|\widetilde{\mathcal{X}}(\boldsymbol{k})\right|^2\right\rangle$, is involved here, and not the off-diagonal terms, i.e. $\left\langle\widetilde{\mathcal{X}}(\boldsymbol{k})\widetilde{\mathcal{X}}(\boldsymbol{k}')\right\rangle$ with $\boldsymbol{k}\neq\boldsymbol{k}'$. This is because the statistical average of the halo abundance, i.e. $\left\langle\widetilde{n}_h(\boldsymbol{k})\widetilde{n}_h^\star(\boldsymbol{k}')\right\rangle$, is proportional to $\delta^3(\boldsymbol{k}-\boldsymbol{k}')$. Although in this case we are only interested in the one-halo term, this would equally apply to the two-halo term with the addition, however, of the matter power spectrum.

It can be shown that the power spectrum of the random variable $\widetilde{\mathcal{X}}$ is also isotropic, i.e. a function of k only, as follows: We first note

$$\left\langle\left|\widetilde{\mathcal{X}}(\boldsymbol{k})\right|^2\right\rangle=\int\mathrm{d}^3q\,\left|\widetilde{X}(q)\right|^2\widetilde{S}\,(|\boldsymbol{k}-\boldsymbol{q}|), \tag{B.12}$$

where we use the fact that $\widehat{b}$ is a statistically isotropic random field, i.e. $\left\langle\widehat{b}(\boldsymbol{k})\widehat{b}^\star(\boldsymbol{k}')\right\rangle=\widetilde{S}(k)\delta^3(\boldsymbol{k}-\boldsymbol{k}')$. Hence $\left\langle\left|\widetilde{\mathcal{X}}(\boldsymbol{k})\right|^2\right\rangle$ is the convolution of the Fourier coefficients of two functions which are spherically symmetric, since both $\left|\widetilde{X}(q)\right|^2$ and $\widetilde{S}(k)$ are functions of the wavenumber only. Hence we rewrite this in real-space (leading then to a product of two spherically symmetric functions) as follows:

$$\left\langle\left|\widetilde{\mathcal{X}}(\boldsymbol{k})\right|^2\right\rangle=\int\frac{\mathrm{d}^3r}{(2\pi)^{3/2}}e^{\mathrm{i}\boldsymbol{k}\boldsymbol{r}}X_2(r)S(r)=\sqrt{\frac{2}{\pi}}\int_0^\infty\mathrm{d}r\,r^2\,X_2(r)S(r)\,j_0(kr), \tag{B.13}$$

where the inverse-Fourier transform introduced above reads

$$X_2(r)=\int\frac{\mathrm{d}^3k}{(2\pi)^{3/2}}\left|\widetilde{X}(k)\right|^2e^{-\mathrm{i}\boldsymbol{k}\boldsymbol{r}}=\sqrt{\frac{2}{\pi}}\int_0^\infty\mathrm{d}k\,k^2\,\left|\widetilde{X}(k)\right|^2\,j_0(kr), \tag{B.14}$$

$$S(r)=\int\frac{\mathrm{d}^3k}{(2\pi)^{3/2}}\widetilde{S}(k)e^{-\mathrm{i}\boldsymbol{k}\boldsymbol{r}}=\sqrt{\frac{2}{\pi}}\int_0^\infty\mathrm{d}k\,k^2\,S(k)\,j_0(kr). \tag{B.15}$$

We note that r can be understood as a mere dummy variable. We also stress that $X_2(r)$ should not be confused with $|X(r)|^2$. Finally, the function $S(r)$ is no more than the correlation function introduced in Sect. 2.3.

It is then clear that $\left\langle\left|\widetilde{\mathcal{X}}(\boldsymbol{k})\right|^2\right\rangle$ can be replaced by $\left\langle\left|\widetilde{\mathcal{X}}(k)\right|^2\right\rangle$ where it is now a function of the wavenumber only. We can thus perform in Eq. (B.11) the integral over $(\boldsymbol{k}/k)$ to get $\delta_{L,L'}\delta_{M,M'}$. We thus obtain $\left\langle A_{LM}A^\star_{L'M'}\right\rangle=D_L^A\,\delta_{L,L'}\delta_{M,M'}$;the amended angular power spectrum reads

$$D_L^A=\left(\frac{e^3}{2\pi\,m_\mathrm{e}^2\,c\,\varepsilon_0}\right)^2\int_0^{r_\mathrm{CMB}}\frac{a(r_1)\,\mathrm{d}r_1}{\nu^2(r_1)}\int_0^{r_\mathrm{CMB}}\frac{a(r_2)\,\mathrm{d}r_2}{\nu^2(r_2)}\int\mathrm{d}M\,\frac{\mathrm{d}N}{\mathrm{d}M}\times\int k^2\,\mathrm{d}k\,\left\langle\left|\widetilde{\mathcal{X}}(k)\right|^2\right\rangle\,j_L(kr_1)\,j_L(kr_2), \tag{B.16}$$

where the new power spectrum of haloes, $\left\langle\left|\widetilde{\mathcal{X}}(k)\right|^2\right\rangle$, is obtained from the Fourier transform of the β-profile, $\widetilde{X}(k)$, and the power

spectrum of the stochastic component, $\widetilde{S}(k)$, using the set of Eqs. (B.13)–(B.15)[12].

Let us now discuss how this impact D_L^A as compared to the simplifying assumption of uniform orientation of the magnetic field up to the virial radius. This basically consists in comparing $\left\langle\left|\widetilde{\mathcal{X}}(k)\right|^2\right\rangle$ to $\left|\widetilde{X}(k)\right|^2$. We first note to ease the comparison that the latter is directly derived from the former by setting $S(r) = 1$. Hence we need to compare

$$\left\langle\left|\widetilde{\mathcal{X}}(\boldsymbol{k})\right|^2\right\rangle = \sqrt{\frac{2}{\pi}}\int_0^\infty \mathrm{d}r\, r^2\, X_2(r) S(r)\, j_0(kr), \tag{B.17}$$

to

$$\left|\widetilde{X}(k)\right|^2 = \sqrt{\frac{2}{\pi}}\int_0^\infty \mathrm{d}r\, r^2\, X_2(r)\, j_0(kr). \tag{B.18}$$

Assuming self-similarity, we can write $S(r) = S_\mathrm{c}(M) \times s(r/r_\mathrm{c})$, where S_c is some amplitude (potentially mass-dependent), and $s(r/r_\mathrm{c})$ a shape function depending on the ratio r/r_c only, and which decreases to zero at scales smaller than the virial radius. At a qualitative level then, adding the stochastic contribution leads to two effects. First, the shape function introduces a universal smoothing hence suppressing power at large scales. The second impact comes from the peculiar scaling with the mass which might give more or less weights for haloes with different masses. This additional scaling however can be fully incorporated within the mass scaling of B_c.

The function $X_2(r)$ is no more than the convolution of the profile $X(r)$ with itself. Hence we can introduce an effective profile, $X^\mathrm{eff}(r)$, accounting for the stochastic contribution as the function such its auto-convolution product equals $X_2(r)S(r)$, i.e. $\int \mathrm{d}x\, X^\mathrm{eff}(r)X^\mathrm{eff}(r-x) = X_2(r)S(r)$. This effective profile should then account for the additional smoothing introduced by $s(r)$ plus some potential additional scaling of the total amplitude of the effect with the mass; the latter is however easily absorbed into the scaling $B_\mathrm{c}(M)$. Armed with such an effective profile, all the analytical expressions derived in the previous section of this appendix can be directly used replacing X by X^eff.

Appendix C: Derivation of $D_L^\parallel$ for Faraday rotation

The angular power spectrum $D_L^\parallel$ for Faraday rotation is obtained through the computation of the correlation $\left\langle b(\boldsymbol{n}_1,\boldsymbol{x}_i)b(\boldsymbol{n}_2,\boldsymbol{x}_j)\right\rangle$. We note that $b(\boldsymbol{n},\boldsymbol{x}_i) = \boldsymbol{n}\cdot\boldsymbol{b}(\boldsymbol{x}_i)$. We use the vector basis $(\boldsymbol{e}_z,\boldsymbol{e}_+,\boldsymbol{e}_-)$, where $\boldsymbol{e}_\pm = (\boldsymbol{e}_x \pm i\boldsymbol{e}_y)/\sqrt{2}$ and $(\boldsymbol{e}_x,\boldsymbol{e}_y,\boldsymbol{e}_z)$ is the standard Cartesian basis of $\mathbb{R}^3$. The components of the orientation of the magnetic field $\boldsymbol{b}$ and the line-of-sight direction $\boldsymbol{n}$ are given by

$$\boldsymbol{b} = \begin{pmatrix} \cos(\beta(\boldsymbol{x}_i)) \\ \frac{1}{\sqrt{2}}\sin(\beta(\boldsymbol{x}_i))e^{\mathrm{i}\alpha(\boldsymbol{x}_i)} \\ \frac{-1}{\sqrt{2}}\sin(\beta(\boldsymbol{x}_i))e^{-\mathrm{i}\alpha(\boldsymbol{x}_i)} \end{pmatrix}, \quad \text{and,} \quad \boldsymbol{n} = 2\sqrt{\frac{\pi}{3}}\begin{pmatrix} Y_1^0(\boldsymbol{n}) \\ Y_1^{-1}(\boldsymbol{n}) \\ Y_1^1(\boldsymbol{n}) \end{pmatrix}. \tag{C.1}$$

We note that in the specific reference frame adopted in this case, the components of the line-of-sight unit vector are expressed using the spherical harmonics for $\ell = 1$. This way of expressing the components of the unit vector of the line of sight is appropriate for further reading the angular power spectrum from the two-point correlation function; see Eq. (A.10).

[12] This computation requires only three one-dimensional Fourier transforms.

For uniformly distributed unit vectors, we obtain the following average:

$$\left\langle \boldsymbol{b}(\boldsymbol{x}_i)\boldsymbol{b}(\boldsymbol{x}_j)\right\rangle = \begin{pmatrix} 1/3 & 0 & 0 \\ 0 & 0 & -1/3 \\ 0 & -1/3 & 0 \end{pmatrix}\delta_{i,j}\,, \tag{C.2}$$

which is only non-zero for the same haloes. This is also constant in space because, as explained in Appendix A, it results from an homogeneous and isotropic process. The two-point correlation function finally is writen as

$$\left\langle b(\boldsymbol{n}_1,\boldsymbol{x}_i)b(\boldsymbol{n}_2,\boldsymbol{x}_j)\right\rangle = \frac{4\pi}{9}\delta_{i,j}\sum_{m=-1}^{1} Y_{1,m}(\hat{\boldsymbol{n}}_1)\, Y^\star_{1,m}(\hat{\boldsymbol{n}}_2), \tag{C.3}$$

from which the angular power spectrum is easily obtained to be $D_L^\parallel = (4\pi/9) \times \delta_{L,1}$.

Appendix D: Derivation of $D_L^\perp$ for Faraday conversion

In this appendix we compute the following two-point correlation functions: $\left\langle b_{\pm2}(\boldsymbol{n}_1,\boldsymbol{x}_i)b_{\pm2}(\boldsymbol{n}_2,\boldsymbol{x}_j)\right\rangle$ and $\left\langle b_{\pm2}(\boldsymbol{n}_1,\boldsymbol{x}_i)b_{\mp2}(\boldsymbol{n}_2,\boldsymbol{x}_j)\right\rangle$ where we note that $b_{\pm2}(\boldsymbol{n},\boldsymbol{x}_i) \equiv [\boldsymbol{b}(\boldsymbol{x}_i)\cdot(\boldsymbol{e}_\theta \pm i\boldsymbol{e}_\varphi)]^2$. Working in the basis $(\boldsymbol{e}_z,\boldsymbol{e}_+,\boldsymbol{e}_-)$ as used in Appendix B, squares of inner-dot products $b_{\pm2}(\boldsymbol{n},\boldsymbol{x}_i)$ are conveniently expressed as

$$b_{\pm2}(\boldsymbol{n},\boldsymbol{x}_i) = \sum_{\mu=1}^{5} b_\mu(\boldsymbol{x}_i)\, e_\mu^{(\pm)}(\boldsymbol{n}), \tag{D.1}$$

where the five coefficients b_μ depend on the orientations of the magnetic fields only (i.e. they are functions of $\beta(\boldsymbol{x}_i)$ and $\alpha(\boldsymbol{x}_i)$ only). They are given by

$$b_\mu(\boldsymbol{x}_i) = \begin{cases} \sqrt{\frac{2}{3}}(2\cos(\beta(\boldsymbol{x}_i))^2 - \sin(\beta(\boldsymbol{x}_i))^2), \\ -2\sin(\beta(\boldsymbol{x}_i))\cos(\beta(\boldsymbol{x}_i))e^{-\mathrm{i}\alpha(\boldsymbol{x}_i)}, \\ 2\sin(\beta(\boldsymbol{x}_i))\cos(\beta(\boldsymbol{x}_i))e^{\mathrm{i}\alpha(\boldsymbol{x}_i)}, \\ \sin(\beta(\boldsymbol{x}_i))^2 e^{-2\mathrm{i}\alpha(\boldsymbol{x}_i)}, \\ \sin(\beta(\boldsymbol{x}_i))^2 e^{2\mathrm{i}\alpha(\boldsymbol{x}_i)}. \end{cases} \tag{D.2}$$

The five coefficients $e_\mu^{(\pm)}(\boldsymbol{n})$ are functions of the line of sight only and with our choice of the reference frame, they are expressed using spin-weighted spherical harmonics for $s = \pm2$ and $\ell = 2$, i.e.

$$e_\mu^{(\pm)}(\boldsymbol{n}) = \sqrt{\frac{4\pi}{5}}\begin{cases} {}_{\pm2}Y_{2,0}(\hat{\boldsymbol{n}}), \\ {}_{\pm2}Y_{2,1}(\hat{\boldsymbol{n}}), \\ {}_{\pm2}Y_{2,-1}(\hat{\boldsymbol{n}}), \\ {}_{\pm2}Y_{2,2}(\hat{\boldsymbol{n}}), \\ {}_{\pm2}Y_{2,-2}(\hat{\boldsymbol{n}}). \end{cases} \tag{D.3}$$

Ensemble averages are done for the b_μ coefficients, which for a uniform distribution of orientations gives $\left\langle b_\mu(\boldsymbol{x}_i)\, b_\nu(\boldsymbol{x}_j)\right\rangle = \delta_{\mu,\nu}\,\delta_{i,j}$. The different correlation functions are then given by

$$\left\langle b_{\pm2}(\boldsymbol{n}_1,\boldsymbol{x}_i)b_{\pm2}(\boldsymbol{n}_2,\boldsymbol{x}_j)\right\rangle = \frac{32\pi}{75}\delta_{i,j}\sum_{m=-2}^{2} {}_{\pm2}Y_{2,m}(\boldsymbol{n}_1)\, {}_{\pm2}Y^\star_{2,m}(\boldsymbol{n}_2), \tag{D.4}$$

$$\left\langle b_{\pm2}(\boldsymbol{n}_1,\boldsymbol{x}_i)b_{\mp2}(\boldsymbol{n}_2,\boldsymbol{x}_j)\right\rangle = \frac{32\pi}{75}\delta_{i,j}\sum_{m=-2}^{2} {}_{\pm2}Y_{2,m}(\boldsymbol{n}_1)\, {}_{\mp2}Y^\star_{2,m}(\boldsymbol{n}_2). \tag{D.5}$$

All these correlation are thus described by the angular power spectrum (which is non-zero for the one-halo term only) written as $D_\ell^\perp = (32\pi/75)\,\delta_{\ell,2}$.

Conclusion and prospects

Today, the CMB anisotropies still make up an important observable for the whole cosmology as they are made of both primary and secondary anisotropies, tracing respectively the origin of the cosmic inhomogeneities as well as their evolved state in the late-time Universe, namely the large-scale structures, through their interaction with the primordial light. Actually, they are even essential to probe the early Universe physics. Although the hot big bang model is in remarkable agreement with the observation of the CMB anisotropies, it does not provide any explanation about the conditions in which the Universe is found (its homogeneity and flatness for example) and it asks a question of fundamental physics by predicting a singularity at the origin of the Universe. The inflationary paradigm set the Universe in the right conditions for the hot big bang scenario but does not solve the initial singularity problem. It is thought that a modification of Einstein's theory of gravitation would do, and more precisely its quantisation. An attempt to do so is the LQG theory whose application to cosmology led to the LQC field, replacing the initial big bang singularity by a quantum big bounce. In order to have a more complete picture of the Universe, it is thus needed to link very early Universe models like the ones of LQC to the inflationary scenario. All of this remains very theoretical and our only observables to test these models are the perturbations produced during the very early Universe, as different models of the very early Universe might change the production of the inhomogeneities, later leaving their imprints in the temperature and polarisation anisotropies of the CMB. For example, the B modes polarisation patterns are the unique signature of the gravitational waves produced and amplified during inflation so that their detection would support the paradigm, and enable to put tighter constraints on the different early Universe models and discriminate between them. The primordial B modes have not been detected yet because of their very low signal, although a secondary component coming from the lensing of the CMB by large-scale structures has. Lensing transforms some of the primordial (detected) E modes into B modes. It is therefore important to model precisely all the possible sources of secondary B modes -and of secondary anisotropies in general- in order to have access to the primordial signal and to put constraints on the early Universe physics. Conversely, the secondary anisotropies (in temperature and polarisation) of the CMB induced by lensing, among others, contain information both about the evolution of the cosmic inhomogeneities (and therefore about the Universe) since the last scattering surface and the parameters of the Λ CDM model of cosmology. Other sources of secondary anisotropies are due to magneto-optic effects taking place in large-scale structures because of the presence of magnetised plasmas within them, like FR of the primordial linear polarisation, turning some E modes into B modes. These magnetised plasmas also lead to FC of the primordial linear polarisation into circular polarisation, which has no primordial component in the standard model of cosmology. My thesis work has consisted in studying two sides of the cosmic inhomogeneities: on one side, their production in an extension of the inflationary scenario within the LQC framework and on the other side the modelisation of the impact of magnetic fields in their evolved state, namely the large-scale structures, on the CMB polarised anisotropies.

I have checked that the model of the very early Universe presented in Part II with a massless and a massive scalar field is still compatible with the inflationary scenario. I have shown both analytically and numerically that in the remote past of the contraction, the massive field dominates the energy content and thus the evolution of the Universe. Therefore, the analytical approximations of the one field model can be used for the background in this regime. However, at the perturbation level, the perturbations of both fields must be taken into account. Indeed, the scalar perturbations of the two fields are combined into two components: an adiabatic and an isocurvature one, which have been shown to be strongly coupled during the contraction. I have demonstrated how to set the initial conditions for the perturbations there, by making a rotation of basis to go back to the fields' space, since far enough in the contraction, gravity no longer couples the two fields so that the coupling between the two fields' perturbations thus becomes negligible. The perturbations now remain to be propagated through the bounce down to the end of inflation to get the primordial power spectrum of scalar perturbations which would be split in three with an adiabatic, an isocurvature and a cross power spectrum. The two fields model thus presents the distinctive feature of isocurvature perturbations, for which Planck has put upper limits. Hence, as a prospect of the present work, to see if the model lies within the current constraints on isocurvature perturbations, one would need to propagate these primordial power spectra to the CMB, by modifying an early Universe radiative transfer code like CAMB or CLASS, to compute the induced temperature and polarisation anisotropies.

Other prospects have to do with theoretical considerations. At the background level, in addition to the holonomy corrections to the Friedmann's equations, one might want to add the so-called inverse volume corrections which are not clearly established, and are due to the fact that the Hamiltonian of GR contain terms inversely proportional to the volume, and then to fully study the background dynamics with all the corrections. Still at the background level, quantum back-reaction effects should be taken into account when the initial conditions for the fields are set at the bounce, in order to consistently study the probability and duration of an inflation phase. This raises a question about the moment when to put the initial conditions for the fields and their perturbations. As what is done for the fields themselves, it might be relevant to put the initial conditions for the perturbations during the bounce. Then, a related consideration is about the equations of motion for the perturbations to be used: either in the deformed algebra or dressed metric approach, quantum modifications to the equations of motion for the perturbations may need to be taken into account if the initial conditions were to be set at the bounce. Finally, prospects more about the physics such a model describes are to be considered. Indeed, the only known massive scalar field is the Higgs field but it is also known that it cannot trigger the required inflation phase. Maybe a more physical model would include other kinds of more realistic fields than a scalar field. Furthermore, as for reheating where the inflaton is coupled to the other fields of the SM of particle physics, one could wonder why our massive field is not coupled to other fields during the contraction, following some kind of inverse reheating process. Thus, a more realistic and refined model would take into account more fields during both the contraction and the inflation but also during the bounce if a total of four fields are needed to make up a material reference frame.

The primary anisotropies of the CMB are used to extract information about the primordial Universe. However, the observed CMB contains much more information: proper foreground emission by astrophysical sources or secondary anisotropies due to the interaction of the primordial light with large-scale structures. In Part II, I have revisited two sources of secondary polarised anisotropies which are the FR and FC effects, by computing their angular power spectra by the large-scale structures, using the halo model and paying special attention to the projections of the magnetic fields of halos. Assuming magnetic fields of haloes to be uncorrelated, I have found that the two-halo term of the angular power spectra vanishes, and that the latter peak at

multipoles $\ell \sim 10^4$. I have shown that the FR angle is dominated by the contribution of cold thermal electrons, while both cold and relativistic electrons contribute equally to the FC rate in the most optimistic case and in less optimistic situations, the cold electrons dominate the contribution. Both angular power spectra show astrophysical and cosmological dependencies. In particular, when the magnetic field is independent of the halo mass, the angular power spectra scale with the amplitude of matter perturbations σ_8 as $C_\ell \propto \sigma_8^3$, while it almost does not depend on the matter density parameter Ω_m. This scaling with σ_8 is degenerated with a mass-dependent magnetic field. Indeed, introducing a dependence of the magnetic field strength with the halo mass leads to an increase of the scaling at large angular scales (above a degree) with the amplitude of matter fluctuations up to $\sim \sigma_8^{9.5}$ for FR and $\sim \sigma_8^{15}$ for FC for a magnetic field strength scaling linearly with the halo mass. Introducing higher values of the magnetic field for galaxies, as compared to clusters, instead leads to a decrease of such a scaling at arcminute scales down to $\sim \sigma_8^{0.9}$ for FR. There is however a degeneracy in the $\Omega_\mathrm{m} - \sigma_8$ plane which could be lifted by combining these effects with other large-scale structure probes that scale differently with those parameters, like the tSZ effect or lensing for example, assuming nonetheless the magnetic field mass-dependence model to be known. Conversely, a joint analysis could be used so as to infer the scaling of the magnetic fields with the masses of haloes.

The FR and FC effects could thus be used to probe the late-time Universe and for this purpose we have built quadratic estimators of the FR and FC fields to reconstruct them, thanks to their induced secondary anisotropies. The FR and lensing effects impact the primordial CMB similarly by turning some primordial E modes into B modes, so that they could potentially bias each other's reconstruction, but this is not the case for symmetry reasons. Only correlators involving polarised anisotropies can be used to reconstruct the FR angle and FC rate fields, as both of these effects have no impact on the temperature anisotropies of the CMB. Finally, a rough estimate shows that the secondary polarised anisotropies due to the FR effect are expected to be of the same order of magnitude as the lensing effect although at smaller angular scales ($\ell \sim 10^4$) for a CMB frequency of $\nu = 30$ GHz, while the secondary 'V mode' is expected to be 6 orders of magnitude lower. However, no primordial circular component of polarisation is expected in the CMB, so that its detection would be made easier. The precise quantification of the secondary polarised anisotropies is the natural next step and the full power spectra can be computed by taking the input primordial angular power spectra of CMB anisotropies computed in simulations like CAMB or CLASS. These secondary polarised anisotropies could potentially be detected by small-scale CMB S4 missions and for this purpose a signal-to-noise ratio analysis remains to be made. This all-sky detection could also be completed with single observations of clusters. For the case of circular polarisation, observational constraints already exist on the V Stokes parameter (see Nagy et al., 2017, for upper bounds) and its comparison with the value computed by a numerical simulation might already put upper limits on the magnetic field strength or the density of relativistic electrons. To finish, in order to have additional observables that could potentially lift the degeneracy among cosmological parameters or between cosmology and cluster astrophysics, the predictions could also be completed by computing higher order correlations, and cross-correlations with other cosmological probes like the tSZ effect. Note that because of the statistical independence of the magnetic fields from one halo to another, one needs to correlate an even number of FR or FC fields so that higher-order correlation functions are needed when considering cross-correlations with other observables.

Bibliography

Ade, P. A. R., Akiba, Y., Anthony, A. E., et al. 2014, Phys. Rev. Lett., 113, 021301

Ade, P. A. R., et al. 2015, Phys. Rev. Lett., 114, 101301

Aghanim, N., Majumdar, S., & Silk, J. 2008, Reports on Progress in Physics, 71, 066902

Agullo, I., Ashtekar, A., & Nelson, W. 2013a, Physical Review D, 87, 043507

—. 2013b, Classical and Quantum Gravity, 30, 085014

Amelino-Camelia, G., Ellis, J., Mavromatos, N. E., Nanopoulos, D. V., & Sarkar, S. 1998, Nature, 393, 763

Arnowitt, R., Deser, S., & Misner, C. W. 2008, General Relativity and Gravitation, 40, 1997

Ashtekar, A., Kaminski, W., & Lewandowski, J. 2009, Physical Review D, 79, 064030

Ashtekar, A., & Sloan, D. 2011, General Relativity and Gravitation, 43, 3619

Azzam, R. M. A., & Bashara, N. M. 1978, Ellipsometry and Polarized Light, North-Holland Personal Library (North Holland; 3rd reprint 1999 edition)

Barrau, A., Cailleteau, T., Cao, X., Diaz-Polo, J., & Grain, J. 2011, Phys. Rev. Lett., 107, 251301

Barrau, A., Cailleteau, T., Grain, J., & Mielczarek, J. 2014a, Classical and Quantum Gravity, 31, 053001

Barrau, A., & Rovelli, C. 2014, Physics Letters B, 739, 405

Barrau, A., Rovelli, C., & Vidotto, F. 2014b, Physical Review D, 90, 127503

Bekenstein, J. D. 1973, Physical Review D, 7, 2333

Bekenstein, J. D., & Mukhanov, V. F. 1995, Physics Letters B, 360, 7

Bernardeau, F., Codis, S., & Pichon, C. 2015, Monthly Notices of the Royal Astronomical Society, 449, L105

Bianchi, E., & Rovelli, C. 2010, arXiv e-prints, arXiv:1002.3966

Birkinshaw, M. 1999, Physics Reports, 310, 97

Birrell, N. D., & Davies, P. C. W. 1984, Quantum Fields in Curved Space (Cambridge Monographs on Mathematical Physics)

Bojowald, M. 2008, Phys. Rev. Lett., 100, 221301

Bojowald, M., Calcagni, G., & Tsujikawa, S. 2011, Phys. Rev. Lett., 107, 211302

Bolliet, B., Barrau, A., Grain, J., & Schand er, S. 2016, Physical Review D, 93, 124011

Bolliet, B., Barrau, A., Martineau, K., & Moulin, F. 2017, Classical and Quantum Gravity, 34, 145003

Bolliet, B., Grain, J., Stahl, C., Linsefors, L., & Barrau, A. 2015, Physical Review D, 91, 084035

Bonafede, A., Feretti, L., Murgia, M., et al. 2010, Astron. Astrophys., 513, A30

Bonafede, A., Feretti, L., Giovannini, G., et al. 2009, Astron. Astrophys., 503, 707

Bond, J. R., Salopek, D., & Bardeen, J. M. 1988, Can scale invariance be broken in inflation?, ed. V. C. Rubin & G. V. Coyne, 385–395

Brax, P. 2018, Reports on Progress in Physics, 81, 016902

Bryan, G. L., & Norman, M. L. 1998, The Astrophysical Journal, 495, 80

Byrnes, C. T., & Wands, D. 2006, Physical Review D, 74, 043529

Carlstrom, J. E., Holder, G. P., & Reese, E. D. 2002, Annual Review of Astronomy and Astrophysics, 40, 643

Cavaliere, A., & Fusco-Femiano, R. 1978, Astronomy & Astrophysics, 70, 677

Cavaliere, A., & Lapi, A. 2013, Physics Reports, 533, 69

Challinor, A. 2013, in IAU Symposium, Vol. 288, Astrophysics from Antarctica, ed. M. G. Burton, X. Cui, & N. F. H. Tothill, 42–52

Challinor, A., & Peiris, H. 2009, in American Institute of Physics Conference Series, Vol. 1132, American Institute of Physics Conference Series, ed. M. Novello & S. Perez, 86–140

Clifton, T., Ferreira, P. G., Padilla, A., & Skordis, C. 2012, Physics Reports, 513, 1

Colafrancesco, S., Marchegiani, P., & Palladino, E. 2003, Astron. Astrophys., 397, 27

Cooray, A., Melchiorri, A., & Silk, J. 2003, Physics Letters B, 554, 1

Cooray, A., & Sheth, R. 2002, Physics Reports, 372, 1

Despali, G., Giocoli, C., Angulo, R. E., et al. 2016, Monthly Notices of the Royal Astronomical Society, 456, 2486

Fixsen, D. J., Cheng, E. S., Gales, J. M., et al. 1996, The Astrophysical Journal, 473, 576

Gambini, R., & Pullin, J. 1999, Physical Review D, 59, 124021

—. 2011, A First Course in Loop Quantum Gravity (Oxford University Press)

Gielen, S., & Oriti, D. 2018, Physical Review D, 98, 106019

Giodini, S., Lovisari, L., Pointecouteau, E., et al. 2013, Space Science Reviews, 177, 247

Gluscevic, V., Kamionkowski, M., & Cooray, A. 2009, Phys. Rev., D80, 023510

Gordon, C., Wands, D., Bassett, B. A., & Maartens, R. 2001, Physical Review D, 63, 023506

Govoni, F. 2006, Astronomische Nachrichten, 327, 539

Govoni, F., Murgia, M., Feretti, L., et al. 2006, Astronomy & Astrophysics, 460, 425

Grain, J. 2014, Habilitation à diriger des recherches, Université Paris Sud

Grain, J. 2016, International Journal of Modern Physics D, 25, 1642003

Grain, J., & Barrau, A. 2009, Phys. Rev. Lett., 102, 081301

Grain, J., Barrau, A., Cailleteau, T., & Mielczarek, J. 2010, Physical Review D, 82, 123520

Grain, J., Barrau, A., & Gorecki, A. 2009, Physical Review D, 79, 084015

Gunn, J. E., & Gott, J. Richard, I. 1972, The Astrophysical Journal, 176, 1

Hawking, S. W. 1971, Phys. Rev. Lett., 26, 1344

Heyvaerts, J., Pichon, C., Prunet, S., & Thiébaut, J. 2013, Monthly Notices of the Royal Astronomical Society, 430, 3320

Hirata, C. M., & Seljak, U. 2003, Physical Review D, 68, 083002

Hollands, S., & Wald, R. M. 2002, General Relativity and Gravitation, 34, 2043

Hoyle, C. D., Kapner, D. J., Heckel, B. R., et al. 2004, Physical Review D, 70, 042004

Hu, W. 2000, Phys. Rev., D62, 043007

Hu, W., & Okamoto, T. 2002, Astrophys. J., 574, 566

Huang, L., Liu, S., Shen, Z.-Q., et al. 2009, The Astrophysical Journal, 703, 557

Huang, L., & Shcherbakov, R. V. 2011, Monthly Notices of the Royal Astronomical Society, 416, 2574

Hubble, E. 1929, Proceedings of the National Academy of Science, 15, 168

Hummel, E., Beck, R., & Dahlem, M. 1991, Astronomy & Astrophysics, 248, 23

Huss, A., Jain, B., & Steinmetz, M. 1999, The Astrophysical Journal, 517, 64

Ijjas, A., Steinhardt, P. J., & Loeb, A. 2013, Physics Letters B, 723, 261

Jones, T. W., & Odell, S. L. 1977, The Astrophysical Journal, 214, 522

Joyce, A., Jain, B., Khoury, J., & Trodden, M. 2015, Physics Reports, 568, 1

Kamionkowski, M. 2009, Phys. Rev. Lett., 102, 111302

Kolb, E. W., & Turner, M. S. 1990, The early universe, Vol. 69

Komatsu, E., Smith, K. M., Dunkley, J., et al. 2011, Astrophysical Journal, Supplement Series, 192, 18

Kosowsky, A., Kahniashvili, T., Lavrelashvili, G., & Ratra, B. 2005, Physical Review D, 71, 043006

Kowalski, M., Rubin, D., Aldering, G., et al. 2008, The Astrophysical Journal, 686, 749

Kunz, M. W., Schekochihin, A. A., Cowley, S. C., Binney, J. J., & Sanders, J. S. 2011, Monthly Notices of the Royal Astronomical Society, 410, 2446

Lalak, Z., Langlois, D., Pokorski, S., & Turzyński, K. 2007, JCAP, 2007, 014

Lamarre, J. M., Puget, J. L., Ade, P. A. R., et al. 2010, Astronomy & Astrophysics, 520, A9

Langlois, D. 2012, in Journal of Physics Conference Series, Vol. 405, Journal of Physics Conference Series, 012003

Langlois, D., & Renaux-Petel, S. 2008, Journal of Cosmology and Astro-Particle Physics, 2008, 017

Lewis, A., & Challinor, A. 2006, Physics Reports, 429, 1

Liddle, A. R., & Lyth, D. H. 2000, Cosmological Inflation and Large-Scale Structure

Limber, D. N. 1953, The Astrophysical Journal, 117, 134

Linsefors, L., & Barrau, A. 2013, Physical Review D, 87, 123509

Linsefors, L., Cailleteau, T., Barrau, A., & Grain, J. 2013, Physical Review D, 87, 107503

LoVerde, M., & Afshordi, N. 2008, Phys. Rev., D78, 123506

Maldacena, J. 2003, Journal of High Energy Physics, 2003, 013

Markevitch, M., Gonzalez, A. H., Clowe, D., et al. 2004, The Astrophysical Journal, 606, 819

Melrose, D. B. 1997a, Phys. Rev. E, 56, 3527

—. 1997b, Journal of Plasma Physics, 58, 735

Melrose, D. B., & McPhedran, R. C. 1991, Electromagnetic processes in dispersive media (Cambridge University Press)

Mielczarek, J. 2009, Physics Letters B, 675, 273

—. 2010, Physical Review D, 81, 063503

Mielczarek, J., Cailleteau, T., Grain, J., & Barrau, A. 2010, Physical Review D, 81, 104049

Milgrom, M. 1983, The Astrophysical Journal, 270, 365

Moore, B., Quinn, T., Governato, F., Stadel, J., & Lake, G. 1999, Monthly Notices of the Royal Astronomical Society, 310, 1147

Murgia, M., Govoni, F., Feretti, L., et al. 2004, Astronomy & Astrophysics, 424, 429

Nagy, J. M., et al. 2017, Astrophys. J., 844, 151

Nagy, J. M., Ade, P. A. R., Amiri, M., et al. 2017, The Astrophysical Journal, 844, 151

Navarro, J. F., Frenk, C. S., & White, S. D. M. 1996, The Astrophysical Journal, 462, 563

Newman, E. T., & Penrose, R. 1966, Journal of Mathematical Physics, 7, 863

Neyman, J., & Scott, E. L. 1952, The Astrophysical Journal, 116, 144

Nozawa, S., Itoh, N., & Kohyama, Y. 1998, The Astrophysical Journal, 508, 17

Okamoto, T., & Hu, W. 2003, Phys. Rev., D67, 083002

Pacholczyk, A. G. 1973, Monthly Notices of the Royal Astronomical Society, 163, 29P

Pacholczyk, A. G., & Swihart, T. L. 1970, The Astrophysical Journal, 161, 415

Peacock, J. A. 1999, Cosmological Physics

Peebles, P. J. E. 1980, The large-scale structure of the universe (Princeton University Press)

Penrose, R. 1989, Annals of the New York Academy of Sciences, 571, 249

Perlmutter, S., Aldering, G., Goldhaber, G., et al. 1999, The Astrophysical Journal, 517, 565

Peter, P., & Uzan, J. 2009, Primordial cosmology, Oxford graduate texts (Oxford University Press)

Planck Collaboration, Ade, P. A. R., Aghanim, N., et al. 2016, Astronomy & Astrophysics, 594, A17

Planck Collaboration, Akrami, Y., Ashdown, M., et al. 2018a, arXiv e-prints, arXiv:1807.06208

Planck Collaboration, Aghanim, N., Akrami, Y., et al. 2018b, arXiv e-prints, arXiv:1807.06209

—. 2018c, arXiv e-prints, arXiv:1807.06210

Planck Collaboration, Akrami, Y., Arroja, F., et al. 2018d, arXiv e-prints, arXiv:1807.06211

Poincaré, H. 1892, Les méthodes nouvelles de la mécanique céleste

Pralavorio, P. 2013, arXiv e-prints, arXiv:1311.1769

Rephaeli, Y., & Lahav, O. 1991, The Astrophysical Journal, 372, 21

Riess, A. G., Filippenko, A. V., Challis, P., et al. 1998, The Astronomical Journal, 116, 1009

Rovelli, C. 2004, Quantum Gravity

Rovelli, C., & Vidotto, F. 2014, International Journal of Modern Physics D, 23, 1442026

Rybicki, G. B., & Lightman, A. P. 1979, Radiative processes in astrophysics (Wiley-VCH)

Santos, M. G., Cooray, A., Haiman, Z., Knox, L., & Ma, C.-P. 2003, The Astrophysical Journal, 598, 756

Sasaki, M. 1986, Progress of Theoretical Physics, 76, 1036

Sazonov, V. N. 1969a, Soviet Ast., 13, 396

—. 1969b, Soviet Journal of Experimental and Theoretical Physics, 29, 578

Schander, S., Barrau, A., Bolliet, B., et al. 2016, Physical Review D, 93, 023531

Scoccola, C., Harari, D., & Mollerach, S. 2004, Phys. Rev., D70, 063003

Shcherbakov, R. V. 2008, The Astrophysical Journal, 688, 695

Shcherbakov, R. V., & Huang, L. 2011, Monthly Notices of the Royal Astronomical Society, 410, 1052

Sheth, R. K., Mo, H. J., & Tormen, G. 2001, Monthly Notices of the Royal Astronomical Society, 323, 1

Sheth, R. K., & Tormen, G. 2002, Monthly Notices of the Royal Astronomical Society, 329, 61

Smoot, G. F., & Scott, D. 2000, European Physical Journal C, 15, 145

Sunyaev, R. A., & Zeldovich, Y. B. 1972, Comments on Astrophysics and Space Physics, 4, 173

Takada, M., Ohno, H., & Sugiyama, N. 2001

Tashiro, H., Aghanim, N., & Langer, M. 2008, Mon. Not. Roy. Astron. Soc., 384, 733

Tashiro, H., Silk, J., Langer, M., & Sugiyama, N. 2009, Mon. Not. Roy. Astron. Soc., 392, 1421

Vacca, V., Murgia, M., Govoni, F., et al. 2012, Astronomy & Astrophysics, 540, A38

Verlinde, E. 2011, Journal of High Energy Physics, 2011, 29

—. 2017, SciPost Physics, 2, 016

Widrow, L. M. 2002, Reviews of Modern Physics, 74, 775

Will, C. M. 2014, Living Reviews in Relativity, 17, 4

Wilson-Ewing, E. 2013, JCAP, 2013, 015

Zaldarriaga, M., & Seljak, U. 1997, Physical Review D, 55, 1830

—. 1998, Physical Review D, 58, 023003

Zhang, P., Pen, U.-L., & Trac, H. 2004, Monthly Notices of the Royal Astronomical Society, 347, 1224

Appendix A

The formalism of the Poincaré sphere

A.1 Preliminaries

A single temporally, spatially and spectrally coherent electromagnetic wave can be polarised, and the most general case is that the two components $E_1(\boldsymbol{r},t)$ and $E_2(\boldsymbol{r},t)$ obey an ellipse equation

$$\left(\frac{E_1(\boldsymbol{r},t)}{a}\right)^2+\left(\frac{E_2(\boldsymbol{r},t)}{b}\right)^2=1, \tag{A.1}$$

where a and b are the semi-major axis and the semi-minor axis of the ellipse respectively, being along the 1- and 2-directions for convenience, so that we say the wave is elliptically polarized: the electric field describes an ellipse as time goes by, see Fig. A.1.

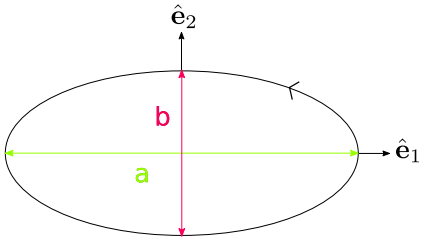

Figure A.1: The ellipse drawn by the electric field components over time. This is a left-handed polarisation.

Depending on whether the ellipse is drawn over time in the right(left) direction, we respectively talk about right(left)-handed elliptical polarisation. Hence to fully describe the polarisation state of the electromagnetic field, one must know the values of the axes a and b of the ellipse as well as its sense of rotation. Linear polarisation is a degenerate case of elliptical polarisation when one of the axes of the ellipse is considered to be null. Another degenerate case is when $a=b$ so that the ellipse is actually a circle: then we talk about circular polarization. Actually, any polarisation of an electromagnetic wave can be decomposed either into two perpendicular linearly polarized waves, or into right- and left-handed circular polarized waves. Knowing that,

such an electromagnetic wave can be parametrized by

$$\boldsymbol{E}(\boldsymbol{r},t) = \left| \begin{array}{l} E_{01}\cos(\boldsymbol{k}\cdot\boldsymbol{r} - 2\pi\nu t) \\ E_{02}\cos(\boldsymbol{k}\cdot\boldsymbol{r} - 2\pi\nu t + \phi) \\ 0 \end{array} \right. , \tag{A.2}$$

ν being the frequency at which the ellipse is drawn and $\boldsymbol{k} = 2\pi n/\lambda\ \hat{\boldsymbol{e}}_3$ so that the wave indeed propagates in the $\hat{\boldsymbol{e}}_3$-direction, λ being its wavelength. n is the refractive index of the medium in which the wave propagates, so that its speed is c/n. The phase ϕ, only in the 2-component, will determine the polarization of the wave. If $\phi > 0$, the wave is left-handed, and conversely if $\phi < 0$. In the case of Eq. (A.1) and Fig. A.1, $\phi = \pi/2$. [1] For a temporally coherent wave, this phase is constant over time. In real life, no waves are perfectly coherent, this phase is actually changing over a timescale called the coherence time of the source τ_c which can be up to $10^{-6}s$ for a helium-neon laser.

Another property of the electromagnetic wave describing light one might want to measure is its amplitude. Because of the short durations of the wave packets, one cannot measure the amplitude of the two components of the electric field over time, hence what we actually measure is a kind of mean value over time of the amplitude: the intensity of light. It is given by

$$I = \langle |E_1|^2 \rangle + \langle |E_2|^2 \rangle = a^2 + b^2. \tag{A.3}$$

Physically, it is the energy of the light (up to a constant factor), the brackets corresponding to time average. It is thus uniquely related to the scalar component of light described in Chapter 4: its temperature.

A.2 The Poincaré sphere

The Poincaré sphere is a formalism developed in Poincaré (1892) to describe the properties of light and the action of optical media. Contrary to the Jones formalism which only describes fully polarized light, it can describe a partially polarized light which is what we more commonly encounter in nature. In the previous section, in describing our electromagnetic wave, we chose a particular coordinate system in which we did not distinguish between the axes of the ellipse and the axes of our basis. Let us now describe this wave in a basis where the axes of the ellipse and those of the basis $(\hat{\boldsymbol{e}}_1, \hat{\boldsymbol{e}}_2, \hat{\boldsymbol{e}}_3)$ are not degenerate. Going now to another orthonormal basis $(\hat{\boldsymbol{e}}'_1, \hat{\boldsymbol{e}}'_2, \hat{\boldsymbol{e}}_3)$ rotated by an angle ψ with respect to the original basis $(\hat{\boldsymbol{e}}_1, \hat{\boldsymbol{e}}_2, \hat{\boldsymbol{e}}_3)$ around the $\hat{\boldsymbol{e}}_3$-direction in a right-handed sense (see Fig. A.2), so that the axes of the ellipse are degenerate with the axes of the new basis, the components of the electric field become

$$\begin{cases} E'_1 = E_1\cos(\psi) + E_2\sin(\psi), \\ E'_2 = E_2\cos(\psi) - E_1\sin(\psi), \end{cases} \tag{A.4}$$

ψ is therefore the tilt of the ellipse with respect to the basis in which the electric field is measured: it is called the azimuth angle of the ellipse. Earlier we said that to fully describe the polarisation state, we needed to know the parameters a, b and the sense of rotation of the ellipse. With the parameterization given in Eq. (A.2) in a random basis, this was equivalent to know E_{01}, E_{02} and the sign of ϕ. However, we cannot really rely on the E_{01} and E_{02} parameters as they depend on our choice of coordinate system. Therefore, we must specify in which system of coordinates

[1] Note that it was arbitrary to put this phase in the 2-component and not into the 1 or split it into both of the components: what is important here is the polarization of the wave, not the amplitude at each instant of this wave. Indeed, changing the way we introduce this phase will just consist in redefining the origin of times.

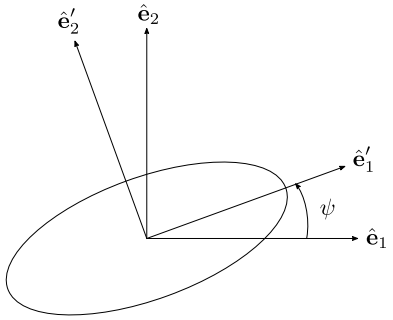

Figure A.2: Change of basis in describing the electromagnetic wave where $(\hat{\boldsymbol{e}}_1', \hat{\boldsymbol{e}}_2')$ are now undistinguishable from the proper axes of the ellipse drawn by the electric field over time.

we describe the polarisation, or equivalently give the tilt ψ of the ellipse with respect to the basis where polarisation is described. Given that, two parameters are missing to fully describe the polarisation. These two remaining parameters are independent on the chosen system of coordinates and are intrinsic to the polarisation. One such parameter is the intensity of the light

$$I = E_{01}^2 + E_{02}^2 = E_{01}^{'2} + E_{02}^{'2} = a^2 + b^2, \tag{A.5}$$

which is indeed the same regardless of the coordinate system. We then need another parameter to fully describe our polarization state. This is given by the ellipticity of the ellipse:

$$\tan(\chi) = \pm\frac{b}{a}. \tag{A.6}$$

A partially polarized light is described by an additional parameter: the degree of polarization p. It is defined as the ratio between the intensity of the polarized light I_p and the total intensity I of the light

$$p \equiv \frac{I_p}{I}, \tag{A.7}$$

so that it is comprised between 0 and 1. Thus, any real light can be described by these four parameters

$$p,\ I,\ \psi,\ \chi. \tag{A.8}$$

We then represent it thanks to the Poincaré sphere. It is a sphere of radius I centered on the origin O of a coordinate system $(O; x, y, z)$ where the polarization properties of the light parametrised by these four parameters are translated into spherical coordinates: the angle ψ is defined with respect to the x-axis while χ is defined with respect to the (Oxy) plane, see Fig. A.3. The coordinates of a point corresponding to a given light beam are

$$\begin{cases} x = Ip\cos(2\psi)\cos(2\chi), \\ y = Ip\sin(2\psi)\cos(2\chi), \\ z = Ip\sin(2\chi), \end{cases} \tag{A.9}$$

so that any light with $\chi = 0$, i.e. any linearly polarized light, will lie in the (Oxy) plane and any light with $\chi = \pm\pi/2$, corresponding respectively to left(right)-handed circularly polarized light will be located at the poles. The northern hemisphere corresponds to left-handed polarisation while the southern one is the right-handed polarization. A fully polarized light thus having $p = 1$ will be represented *on* the sphere while a partially polarized light *within* the sphere. The factors of 2 in front of ψ & χ are respectively related to the facts that one cannot distinguish an ellipse from its rotation by π or from a $\pi/2$ rotation plus a swapping of its axes.

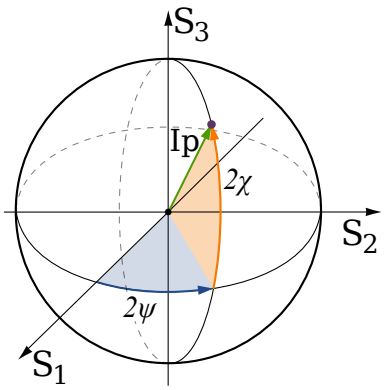

Figure A.3: A point in the Stokes parameters (S_1, S_2, S_3) space, with spherical coordinates given by (Ip, χ, ψ). The Poincaré sphere has its radius equal to I (corresponding to maximal polarisation $p = 1$), and for $p < 1$ this point will lie within the Poincaré sphere. Figure from Inductiveload.

A.3 The Stokes parameters

With the above, we may define the Stokes parameters as

$$\begin{cases} S_0 = I, \\ S_1 = Q = Ip\cos(2\psi)\cos(2\chi), \\ S_2 = U = Ip\sin(2\psi)\cos(2\chi), \\ S_3 = V = Ip\sin(2\chi). \end{cases} \tag{A.10}$$

Note that the total polarized intensity can then be written $I_p = Ip = \sqrt{Q^2 + U^2 + V^2}$.

Allowing for a rotation by an angle α of the coordinate system in a right-handed sense, as was done with the ψ angle, the Q and U parameters are changed according to:

$$\begin{cases} Q' = Ip\cos(2(\psi+\alpha))\cos(2\chi) \\ \quad = Ip\,(\cos(2\psi)\cos(2\alpha) - \sin(2\psi)\sin(2\alpha))\cos(2\chi) \\ \quad = Q\cos(2\alpha) - U\sin(2\alpha), \\ \\ U' = Ip\sin(2(\psi+\alpha))\cos(2\chi) \\ \quad = Ip\,(\sin(2\psi)\cos(2\alpha) + \cos(2\psi)\sin(2\alpha))\cos(2\chi) \\ \quad = U\cos(2\alpha) + Q\sin(2\alpha). \end{cases} \tag{A.11}$$

The Q and U parameters therefore depend on our choice of coordinate system, while I and V are unchanged when rotating this coordinate system. This last equation can be rewritten in complex notation as

$$Q' \pm iU' = (Q \pm iU)e^{\pm 2i\alpha}, \tag{A.12}$$

showing that $Q \pm iU$ is a spin 2 quantity. Although V is unchanged when rotating the coordinate system, which is consistent with the fact that it quantifies the circularly polarized component of light, it is however not a scalar quantity but rather a *pseudo*-scalar one. Indeed, when doing a parity transformation of the coordinate system, V changes according to

$$V' = -V. \tag{A.13}$$

This property of the V parameter will be useful to recall when we will deal with the Faraday Conversion effect in Chapter 8.

université PARIS-SACLAY

ÉCOLE DOCTORALE
Astronomie et Astrophysique d'île-de-France

Titre : Impact des inhomogénéités cosmiques sur le FDC : perturbations primordiales dans les cosmologies en rebond à deux champs et champs magnétiques dans les structures récentes

Mots clés : Univers en rebond, inflation multichamp, champs magnétiques dans les amas de galaxies, fond diffus cosmologique, polarisation, cosmologie

Résumé : Le Fond Diffus Cosmologique (FDC) est une sonde cosmologique clé mettant des contraintes étroites sur le modèle ΛCDM de l'Univers. Emis 380000 ans après le big bang, il montre de petites anisotropies en température et en polarisation qui tracent les inhomogénéités cosmiques à différentes époques de l'Univers. D'une part, les anisotropies primaires donnent accès à l'inflation durant laquelle les perturbations primordiales sont générées. D'autre part, les anisotropies secondaires tracent les inhomogénéités dans l'Univers récent, qui ont évolué en grandes structures sous l'action de la gravité, à partir des inhomogénéités primordiales. Ainsi les anisotropies du FDC sont une sonde puissante à la fois de l'origine des inhomogénéités dans l'Univers très jeune, et de leur état évolué dans l'Univers récent. Cette thèse porte sur deux aspects des inhomogénéités: d'abord leur production dans une extension du scénario inflationnaire, puis la prédiction de l'impact des champs magnétiques des grandes structures sur les anisotropies secondaires polarisées du FDC.

Malgré ses succès, l'inflation ne résout pas le problème de la singularité initiale du big bang, où la gravité pourrait être quantique. En Cosmologie Quantique à Boucles (CQB), cette singularité est remplacée par un rebond quantique. La CQB à un champ avec potentiel quadratique a déjà été étudiée et prédit une phase d'inflation suivant le rebond. Les perturbations primordiales ne sont plus seulement produites pendant l'inflation, mais aussi pendant le rebond et la contraction le précédant. Ici, j'ai consideré une extension à deux champs de la CQB avec un champ massif comme inflaton, et un champ sans masse servant d'horloge interne. J'ai d'abord étudié l'évolution globale de l'Univers de manière analytique et numérique, montrant que loin dans la contraction, le champ massif domine le contenu énergétique. J'ai aussi vérifié que l'inflation reste probable, malgré la présence du champ sans masse. Puis, j'ai examiné la production de perturbations: contrairement au cas à un champ, en plus de la composante adiabatique standard, elles sont ici décrites par une composante isocourbe, caractéristique des modèles multi-champs et pour laquelle Planck a mis des limites supérieures. Loin dans la contraction, ces deux composantes sont hautement couplées. J'ai montré comment fixer leurs conditions initiales en utilisant des variables combinant les deux types de perturbations, rendant le couplage sous-dominant. Il reste maintenant à les propager à travers le rebond jusqu'à la fin de l'inflation pour obtenir leurs spectres de puissance (croisé), à comparer ensuite aux contraintes observationnelles.

Depuis son émission, le FDC a voyagé à travers les grandes structures avant de nous atteindre. Son interaction avec les structures engendre des anisotropies secondaires, comme celles dues à l'effet SZ dans les amas. Des plasmas magnétises ont été observés dans les galaxies et les grandes structures. Cela devrait engendrer de la Rotation Faraday (RF) de la polarisation linéaire primordiale, transformant des modes E en B, et de la Conversion Faraday (CF) de la polarisation linéaire en circulaire. J'ai revisité ces sources d'anisotropies en calculant les spectres de puissance angulaires de l'angle de RF et du taux de CF par les grandes structures. J'ai utilisé le modèle de halo en prêtant attention à l'impact des projections des champs magnétiques. Les spectres piquent à des multipoles $\ell \sim 10^4$ et sont proportionnels à σ_8^3, en supposant un champ magnétique indépendant de la masse du halo. Cette dépendance est cependant dégénérée avec celle qui existe entre les champs magnétiques et la masse des halos. Puis, je détaille le calcul des spectres de puissance angulaires totaux des anisotropies polarisées, à partir de ceux de la RF et de la CF. Enfin, je montre comment reconstruire les champs de RF et de CF à partir du FDC en adaptant les estimateurs développés pour la reconstruction du lentillage gravitationnel.

université PARIS-SACLAY

ÉCOLE DOCTORALE
Astronomie et Astrophysique d'île-de-France

Title : Impacts of cosmic inhomogeneities on the CMB: primordial perturbations in two-field bouncing cosmologies and cosmic magnetism in late-time structures

Keywords : bouncing Universe, multifield inflation, magnetic fields in galaxy clusters, cosmic microwave background, polarisation, cosmology

Abstract : The Cosmic Microwave Background (CMB) is a key cosmological probe, that sets tight constraints on the ΛCDM model of the Universe. Released 380000 years after the big bang, it exhibits tiny anisotropies in temperature and polarisation which trace the cosmic inhomogeneities at different epochs of the Universe. On the one hand, primary anisotropies give access to inflation, during which the primordial perturbations are generated. On the other hand, secondary anisotropies trace inhomogeneities in the recent Universe, which have evolved into large scale structures through gravity, starting from the primordial ones. Hence CMB anisotropies are a powerful probe of both the origin of inhomogeneities in the very early Universe, and their evolved state in the late-time Universe. This thesis deals with two aspects of inhomogeneities by first considering their production in an extension of the inflationary scenario, and second by predicting the impact of magnetic fields in large scale structures on the secondary CMB polarised anisotropies.

Despite its successes, inflation does not solve the initial big bang singularity issue, where gravity might need to be quantised. In Loop Quantum Cosmology (LQC), this singularity is replaced by a quantum bounce. Single field LQC with quadratic potential has already been studied and predicts an inflation phase following the bounce. Then, primordial inhomogeneities are not only produced during inflation, but also during the bounce and the contraction preceding it. Here, I considered a multifield extension of LQC with two fields: a massive one as being the inflaton, and a massless one used as an internal clock. I first studied the background evolution of the Universe both analytically and numerically. I showed that far in the contraction, the massive field dominates the energy budget. I have also checked that inflation remains likely to happen, despite the presence of the massless field. Secondly, I investigated how perturbations are produced. Unlike the one-field case, they are now described by an isocurvature component in addition to the standard adiabatic one, the former being characteristic of multifield models, for which Planck has put upper limits. In the remote past of the contraction, these two kinds of perturbations are highly coupled. I showed how to set their initial conditions by using appropriate variables mixing both kinds of perturbations, making the coupling subdominant. These perturbations remain to be propagated through the bounce down to the end of inflation to get their primordial (cross)spectra, to be subsequently compared to observational constraints.

Since its released, the CMB traveled through large scale structures before reaching us. This leads to secondary anisotropies by its interaction with these structures, like e.g. gravitational deflection or the SZ effect in clusters. Magnetic fields have been observed in galaxies and larger structures. Since these structures are also filled with free electrons, this should lead to the Faraday Rotation (FR) effect which rotates the primordial linear polarisation, turning E into B modes, and to the Faraday Conversion (FC) effect which converts linear into circular polarisation. I revisited these sources of secondary anisotropies by computing the angular power spectra of the FR angle and the FC rate by large-scale structures. I used the halo model paying special attention to the impact of magnetic field projections. I found angular power spectra peaking at multipoles $\ell \sim 10^4$. Assuming a mass-independent magnetic field, the angular power spectra scale with the amplitude of matter perturbations as $\sim \sigma_8^3$. This scaling is however degenerated with the one of the magnetic field with halos' mass. I finally detail how to compute the full angular power spectra of polarised anisotropies, starting from the FR and FC power spectra. I also show how to reconstruct the FR and FC fields from the CMB adapting the estimators developed for lensing reconstruction.

Université Paris-Saclay
Espace Technologique / Immeuble Discovery
Route de l'Orme aux Merisiers RD 128 / 91190 Saint-Aubin, France